

Chemical Reactions as Control Mechanisms for Biomolecular Condensates

Dissertation

for the award of the degree
"Doctor rerum naturalium"
at the Georg-August-Universität Göttingen

within the doctoral degree programme

Physics of Biological and Complex Systems
of the Göttingen Graduate School of Neurosciences, Biophysics, and
Molecular Biosciences (GGNB)
of the Georg-August University School of Sciences (GAUSS)

submitted by

Jan Kirschbaum
from Münster, Germany
Göttingen 2022

Thesis advisory committee

Dr. David Zwicker

Theory of Biological Fluids
Max Planck Institute for Dynamics and Self-Organization

Prof. Dr. Marcus Müller

Institute for Theoretical Physics
Georg-August-Universität Göttingen

Prof. Dr. Karen Alim

Physics Department
Technical University Munich

Members of the examination board:

Referee: Dr. David Zwicker

Theory of Biological Fluids
Max Planck Institute for Dynamics and Self-Organization

Co-referee: Prof. Dr. Marcus Müller

Institute for Theoretical Physics
Georg-August-Universität Göttingen

Other Members of the Examination Board:

Prof. Dr. Karen Alim

Physics Department
Technical University Munich

Prof. Dr. Timo Betz

Third Institute of Physics - Biophysics
Georg-August-Universität Göttingen

Prof. Dr. Stefan Klumpp

Institute for Dynamics of Complex Systems
Georg-August-Universität Göttingen

Dr. Johannes Söding

Quantitative and Computational Biology
Max Planck Institute for Multidisciplinary Sciences

Date of the oral examination: 23.05.2022

Acknowledgments

First, I want to thank David for introducing me to the physics of living systems and giving me the opportunity to work on this topic for almost four years. In particular, I want to thank him for being an amazing supervisor who was always approachable, but also allowed me to work independently. I always enjoyed the scientific discussions with him and the whole group and the atmosphere he created in the group. Then, I want to thank my TAC members, Prof. Karen Alim and Prof. Marcus Müller for their support and co-supervision. Especially, I want to thank Prof. Marcus Müller for reviewing this thesis as a Co-referee.

I want to thank Davide Michieletto, Nick Gilbert, and Mattia Marena as well as Salma Sohrabi-Jahromi, Mark Boehning, and Johannes Söding for the scientific discussions in zoom meetings and lunch breaks. During those, I learned a lot about biomolecular condensates and biology in general.

Furthermore, I want to thank the whole Zwicker group for the nice atmosphere in the office. In particular, I am grateful to Lucas, Noah and Tefa for proofreading this thesis and their constructive feedback. Also, thanks to Ajinkya, who started his PhD, shared an office for 4 years, and will finish his PhD with me. Then, I want to thank all my friends at the institute, especially Antoine and Hansol, who made the time in Göttingen very enjoyable. I also want to thank the people from Münster, in particular Mathe Mensa and my P&P group, Frank, Henrik, Nils and Stefan, the meetings during Corona lockdowns were a very welcome diversion. Robin, for being a great friend although we rarely get the chance to meet. Tefa for the emotional support, in particular during lockdowns, the trips through Germany and Europe, the high quality jokes and traditional pre-christmas meetings. Finally, I want to thank my parents, Malte, Franca and Zoe for their support, not only during this PhD, but also during my studies and pretty much everything else.

Abstract

Biological cells need to structure their interior in space and time. One way this is done are containers enclosed by a membrane as a physical barrier that can control which molecules enter and leave the container. Another, recently discovered, class are biomolecular condensates. These are liquid like droplets that form via liquid liquid phase separation. Although they have no membrane, they do have distinctly different composition from the surrounding. Weak attractive interactions between the molecules in the condensate prevent them from diffusing out of the condensate. To control the formation and dissolution of these condensates, the cell can change the attractive interaction between molecules via chemical reactions.

In this thesis, we develop a theory of phase separation with chemical reactions based on thermodynamic arguments. The chemical reactions switch between two states of a protein, one state phase separates and forms droplets, while the other state is soluble in the solvent. The aim of this thesis was to analyze how such simple reactions can control the phase separation process, for example, the formation, dissolution, and size control of droplets.

In the first part of the thesis, we investigate equilibrium reactions. In this case, the system relaxes to thermodynamic equilibrium. Unlike two component fluids, fluids consisting of multiple components with equilibrium reactions can form droplets, depending on the system parameters. We find that equilibrium reactions introduce a new parameter to control phase separation, the internal energy difference between the two protein states. This internal energy difference can control how much protein is in the phase separating state and thereby, if droplets form or not. We show that the droplet size is very sensitive to changes in the internal energy difference. However, the parameter range for control of droplets is narrow. In addition, the internal energy difference is an equilibrium property of the proteins, thus, it can not be changed fast or in a specific manner.

In the second part of the thesis, we extend our model to non-equilibrium reactions. In this case, the reaction is coupled to fuel molecules, which introduce external energy into the system and drive the reaction away from thermodynamic equilibrium. The external driving strength is a new parameter, which describes how strong the system is driven from equilibrium. We find, that driven reactions alone can be mapped onto an effective equilibrium system with rescaled internal energy difference that depends on the driving strength. This is different if both reaction pathways, the driven and equilibrium reaction, are present. In this case, the total amount of phase separating proteins depends on the reaction kinetics, i.e. on the relative reaction rates of the two pathways. We show that this allows precise, fast and specific control over droplet formation and dissolution. The reason is, that the kinetic parameters can be tuned by enzymes that act only on specific reactions. Finally, motivated by experimental observations, we investigate what happens if enzymes that catalyze the driven reaction are enriched in the droplet phase. We find that the enzymatic enrichment can control individual droplet size and stabilize multiple droplets of the same size against their thermodynamic tendency to form one big droplet.

We show that size control of droplets by reactions is based on three specific features of

the reactions. **(i)** A protein exists in a soluble and a phase separating state and the transition between the two states can be described as a chemical reaction. **(ii)** There are at least two reaction pathways for the transition and at least one has to be driven out of equilibrium. **(iii)** The reaction rates in droplet and solvent phase need to be different, for example, due to enrichment of enzymes in the droplet.

More generally, our results highlight that chemical reactions in phase separating environments can not be described by standard mass action kinetics. The reason is that phase separating systems are inherently non-ideal and mass action kinetics are only valid in ideal, dilute solutions. Instead, a thermodynamic treatment of reactions is necessary, which takes into account that droplets formed by phase separation are chemically different from the solvent phase due to enthalpic interactions.

Contents

| | |
|---|------------|
| Acknowledgments | iii |
| Abstract | v |
| Contents | vii |
| 1 Introduction | 1 |
| 1.1 Biomolecular condensates | 2 |
| 1.2 Chemical Reactions control droplets | 7 |
| 1.3 Reaction Diffusion Systems | 12 |
| 1.4 Outline of thesis | 12 |
| 2 Theory of reactive fluid mixtures | 15 |
| 2.1 Multicomponent fluid mixtures | 15 |
| 2.2 Non-Equilibrium Thermodynamics | 18 |
| 2.3 Multicomponent regular solution theory | 27 |
| 2.4 Liquid-liquid phase separation | 30 |
| 2.5 Simulations | 40 |
| 2.6 Summary | 41 |
| 3 Passive Reactions | 43 |
| 3.1 Chemical Equilibrium | 43 |
| 3.2 Phase separation and chemical reactions | 47 |
| 3.3 SAF-A Phase separation | 56 |
| 3.4 Droplets control chemical reactions | 68 |
| 3.5 Summary | 71 |
| 4 Active Reactions | 75 |
| 4.1 Non-equilibrium reaction | 77 |
| 4.2 Enzymatic reactions | 87 |
| 4.3 Binary active droplets | 91 |
| 4.4 Multicomponent active droplets | 103 |
| 4.5 Reactions as a switch for Droplet | 109 |
| 4.6 Summary | 111 |
| 5 Conclusion and Outlook | 115 |
| 5.1 Passive reactions | 115 |
| 5.2 Active reactions | 117 |

| | |
|---|------------|
| Appendix | 121 |
| A Entropy production | 123 |
| B Flory Huggins Free Energy | 127 |
| C Linear Stability of a ternary mixture | 133 |
| D Partition Coefficient | 135 |
| E Chemical Equilibrium ratio | 137 |
| F Steady state of a reaction cycle | 139 |
| G Steady state of the non-equilibrium dynamics | 141 |
| Bibliography | 147 |

Biological cells are complex objects consisting of various biomolecules like proteins, RNA, and lipids, but also ions like potassium or calcium and metabolites, for example, alcohols. The cell cytosol mass is $\sim 70\%$ water, so the cytosol is best described as a crowded, multicomponent fluid mixture[1]. A schematic example of a minimal cell, developed on the basis of *Mycoplasma mycoides* cells[2], is shown in fig. 1.1. The figure shows the crowded environment in the cytosol and the large variety of different biomolecules. For simplicity, only large molecules are shown and small molecules like water and salt ions are omitted. But the cell is not just a well mixed container with a homogeneous fluid. Instead, to fulfill its function, the cell has to organize its interior in space and time. Spatial structure is achieved in cells via compartments, that control the local concentration of particles[3]. The best known way to do this is via membranes that enclose an area in the cell, so called membrane-bound organelles¹, for example, the nucleus or mitochondria. The membrane forms a physical barrier that controls which particles can enter the organelle and thereby the composition inside the membrane enclosed area. But recently another class, called membraneless organelles or **biomolecular condensates**, has been discovered[4]. These condensates form compartments without membranes but have a different composition than the surroundings[5]. Oftentimes, such condensates form via **Liquid-Liquid Phase Separation (LLPS)**, a phase transition driven by weak enthalpic interactions between proteins[6].

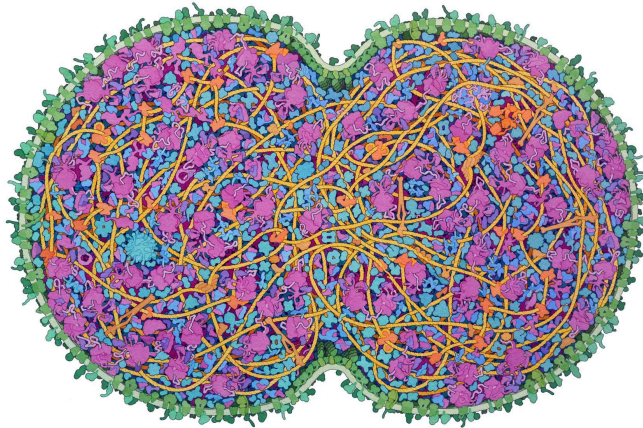
LLPS is an equilibrium phenomenon that does not require external energy input. But biological cells are out of equilibrium systems and use external energy to drive processes inside cells. The energy is supplied in the form of chemical energy via fuel molecules. This chemical energy is used to power virtually all processes in cells, for example, the movement of molecular motors, biochemical reactions, or the pumping of molecules through membranes. It is natural to assume that non-equilibrium processes affect biomolecular condensates as well, but how is not well understood yet[7].

Biomolecular condensates are an example of biological cells using phase transitions to perform functions, which makes them an interesting object of study in biophysics. The aim of this thesis is to elucidate how biochemical reactions can control the formation, size, and number of biomolecular condensates in cells

| | |
|---|--------------|
| 1.1 Biomolecular condensates | 2 |
| Liquid like properties | . . . 3 |
| Condensate function | . . . 4 |
| Modelling condensates | . . . 6 |
| 1.2 Chemical Reactions control droplets | 7 |
| Enrichment inhibition | . . 10 |
| Localization induction | . 10 |
| Other control mechanisms | 12 |
| 1.3 Reaction Diffusion Systems | 12 |
| 1.4 Outline of thesis | 12 |

1: The term organelle describes a specific subunit of the cell and is used in analogy to organ, i.e. an organelle is to a cell what an organ is to the body.

Figure 1.1: Cells are complex assemblies of thousands of molecules that have to be arranged in space. The schematic shows a cross-section through a cell during division. The schematic is based on a minimal cell and depicts the entire known proteome as well as RNA (magenta) and DNA (yellow). Illustration by David S. Goodsell, RCSB Protein Data Bank. Reprinted from [8] under the Creative Commons CC-BY-4.0 license.



based on thermodynamic arguments.

1.1 Biomolecular condensates

As mentioned, biomolecular condensates are organelles without a membrane, that form inside cells. After the original discovery² in Ref.[4], many different types of condensates have been found inside cells³; see fig. 1.2 for a collection of examples. But condensates do not only appear in different places, they come in different sizes as well. From small condensates inside the nucleus with radii of $R \sim 10 - 100 \text{ nm}$ [12, 14], to large condensate up to $R \sim 400 \mu\text{m}$ in *Xenopus laevis* oocytes[15].

There are several experimental indications that many of these biomolecular condensates form via liquid-liquid phase separation[16] and can thus be described as complex liquids[17]. For example, condensates merge upon contact[4], i.e. coalesce, dissolve upon a certain temperature[16], and form only above a critical concentration of specific proteins[18]. The idea is, that weak, multivalent, attractive interactions between biomolecules drive the formation of condensates, very similar to phase separation in polymer melts[19]. Oftentimes these interaction sites lie in **Intrinsically Disordered Regions** (IDRs) of the proteins[5, 20]. In addition, for long molecules, for example certain RNA and DNA, very weak attractive interactions are enough to induce phase separation because the entropy of mixing is small[21–23].

While there has been criticism of the concept of biomolecular condensates forming via LLPS[24, 25]⁴ it is mostly agreed in the literature[17] that liquid-liquid phase separation plays an important role in the formation of at least some biomolecular condensates. Therefore, we next discuss the liquid properties of condensates in cells.

2: Although the idea of protein phase separation in cells is older, see for example Refs.[9, 10] in the context of the origin of life. In addition, phase separation in membranes has long been investigated in the context of lipid rafts[11]

3: Condensates appear not only in the cytosol, but also in the nucleoplasm[12] and in membranes[13].

4: Especially for the very small condensates. A condensate with $R \sim 10 \text{ nm}$ would contain on the order of 10 proteins, is this already a condensate or rather a cluster? When do you start calling it a condensate? In a way, this comes down to the Sorites paradox or how many grains of sand make a heap? See Ref.[26] as well for a discussion on what is a biomolecular condensate.

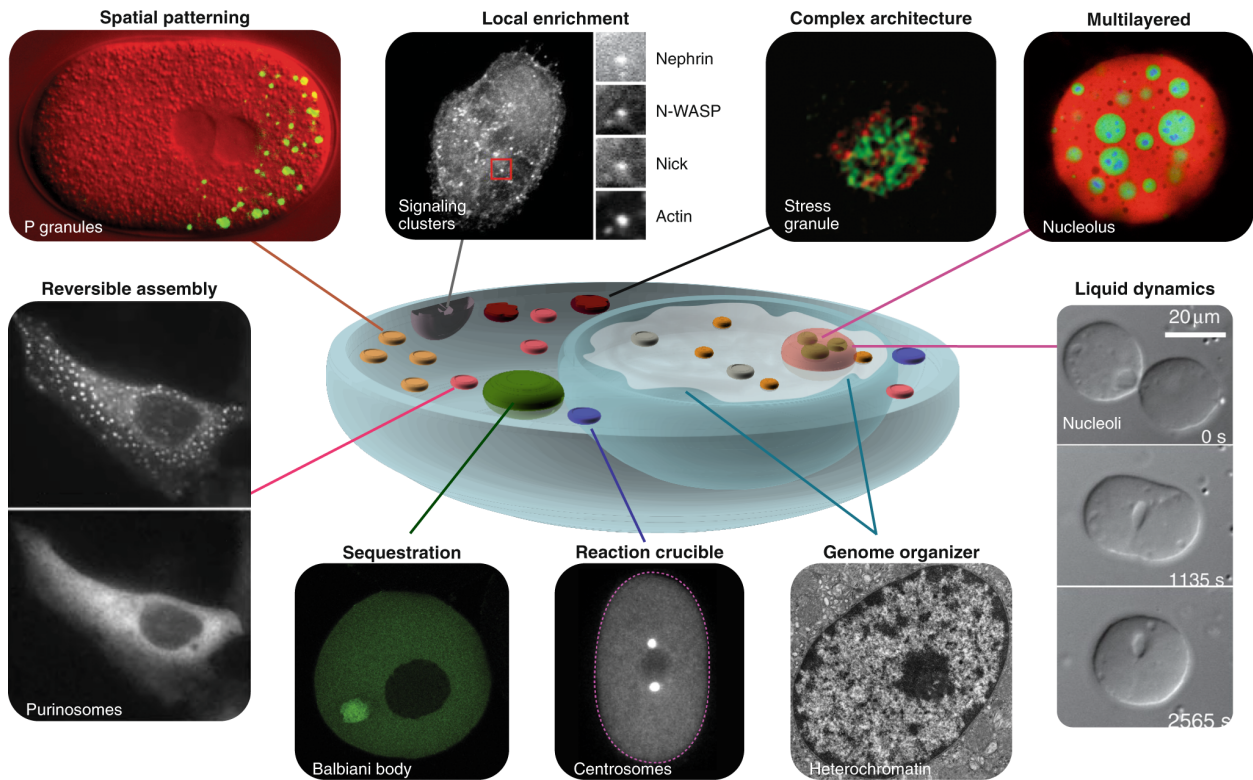


Figure 1.2: Biomolecular condensates appear everywhere in cells. The schematic of a cell is shown in the center and organelles that contain biomolecular condensates are highlighted. Several experimental examples of biomolecular condensates are shown around the schematic with lines indicating where they appear in cells. The white text in the experimental pictures indicates the names of the condensates, while the black text indicates either properties associated with LLPS, for example, ‘Liquid dynamics’ or the function of the condensate, for example, ‘Reaction crucible’. Reprinted from Bracha, et al., “Probing and engineering liquid-phase organelles”, *Nature Biotechnology*, Vol.37(2019)[27] with permission from the publisher under license number 5271401142499.

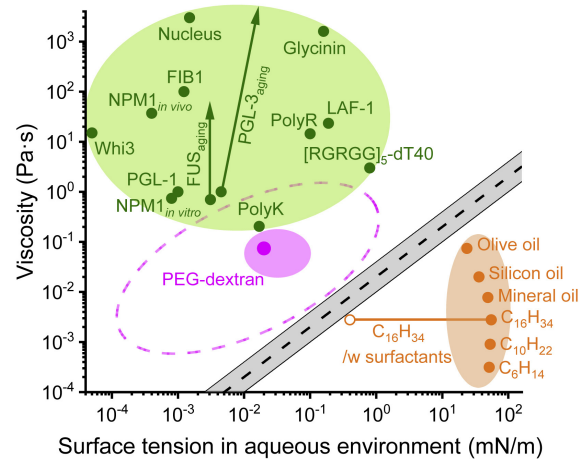
Liquid like properties

Many condensates behave in a way that is consistent with LLPS as a mechanism of condensate formation[17]. In Ref.[7] the authors state six properties that indicate LLPS behavior: **(i)** Due to the surface tension between phases the condensates are usually spherical objects; see fig. 1.2. **(ii)** They show coalescence, i.e. they fuse upon contact; see fig. 1.2 lower right panel. **(iii)** They exchange particles with the surrounding via diffusion. **(iv)** They show wetting or multiphase behaviors; see fig. 1.2 top right panel. **(v)** Although behaving like a liquid, the condensate does not mix with the surroundings but keeps a distinctly different composition from its surrounding. **(vi)** Condensates need a certain concentration threshold of specific proteins to form⁵. Because of their round shape and small size, we will use the term **Droplet** for biomolecular condensates as well throughout this thesis.

But biomolecular condensates have different fluid properties than everyday examples of LLPS like oil in water emulsions; see fig. 1.3. The condensates investigated in Ref.[29] have significantly lower surface tension, but higher viscosity than water

⁵: This is more complex for multicomponent condensates because the threshold depends on the concentration of all components that make up the condensate in principle[18, 28].

Figure 1.3: Biomolecular condensates show higher viscosity and lower surface tension than oil in water. The viscosity and surface tension of different biomolecular condensates in an aqueous buffer (green area, top left) and common oils in water (orange area, bottom right) as a comparison are shown. The green arrows indicate time dependent fluid properties due to aging. Reprinted from Wang, et al.[29] under the Creative Commons CC-BY-4.0 license.



oil emulsions; see fig. 1.3. As a result, the diffusive dynamics in condensates are slow compared to the everyday examples⁶. Low surface tension indicates that particle exchange with the surrounding is fast since there is less resistance to enter or leave the droplet. At the same time, processes like Ostwald ripening are slow⁷. In addition, biomolecular condensates are not simple liquids but are better described as viscoelastic materials[30, 31]. For example, in vitro FUS condensates in Ref.[31] could be described well by a Maxwell model with time dependent viscosity and elasticity, which implies that condensates show aging as well⁸. Furthermore, Ref.[32] found, in FUS condensates as well, that condensates can undergo a liquid to solid transition that has been linked to disease[33]. Taken together, biomolecular condensates are not just simple liquids but show complex material properties that can depend on time as well. The last example indicates that the material properties can influence the function of condensates as well. Therefore, we discuss the possible function of biomolecular condensates in cells next.

Condensate function

Although there has been a lot of work already, see for example Ref.[34], the functions of biomolecular condensates are still not well understood. While the function will depend on the context, it is useful to investigate what kind of functions are possible in theory. Certain properties of condensates that follow directly from liquid-liquid phase separation are potentially useful to cells⁹: **(i)** The formation and dissolution of condensates are very sensitive to external parameters around the critical point[35]. This makes them a perfect tool to sense differences in environmental conditions, which happens, for example, in stress granules[36, 37] or receptor clusters[38, 39]; see fig. 1.4 left panel. **(ii)** The high local concentration of certain molecules can speed up reactions and suppress certain reaction

6: Because the diffusivity D scales inversely with the viscosity $D \propto \eta^{-1}$, according to the Stokes-Einstein relation.

7: Ostwald ripening is a process that minimizes the surface area in an emulsion of droplets. The surface energy scales with the surface tension and thus, the driving force to minimize surface area is smaller for lower surface tension.

8: Aging is a term used in the description of glasses and complex liquids to indicate that the material properties are not constant, but time dependent.

9: Some of these examples are taken from Ref.[34].

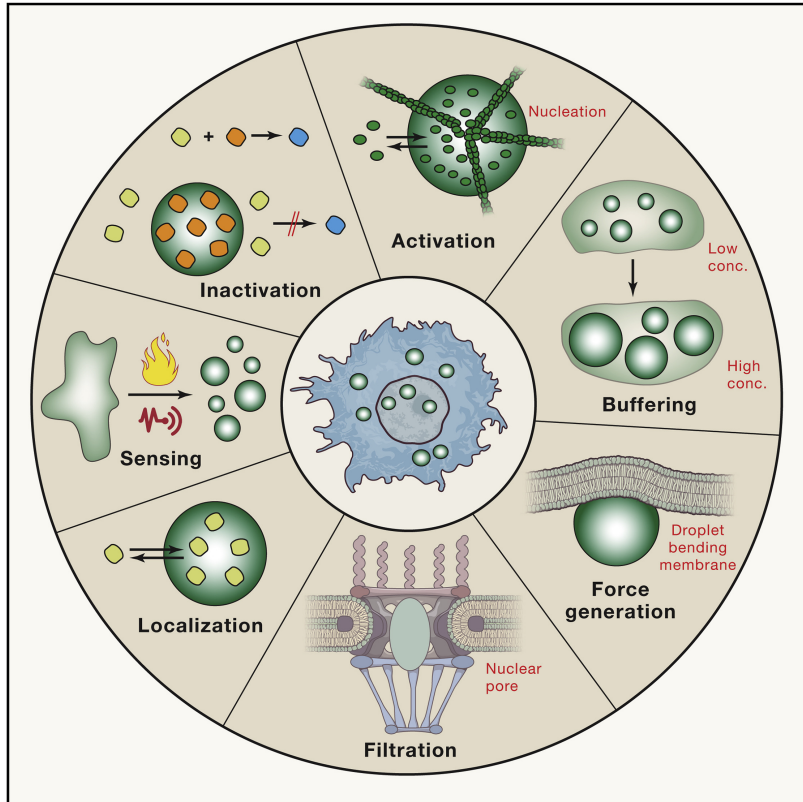


Figure 1.4: Biomolecular condensates can fulfill a variety of functions in cells. The figure depicts an incomplete list of condensate functions related to the properties of liquid-liquid phase separation. For more details see the text in Sec. 1.1. Reprinted from Alberti, et al., "Considerations and Challenges in Studying Liquid-Liquid Phase Separation and Biomolecular Condensates", *Cell*, Vol.176(2019)[34] with permission from the publisher under license number 5271400623500.

pathways, by keeping reactants in different phases[40, 41]; see fig. 1.4 upper left panel. In addition, the high concentration of molecules can enable processes that would be impossible¹⁰ in a well mixed cytosol. For example, microtubule nucleation can be induced in condensates by concentrating tubulin[42, 43]; see fig. 1.4 top panel. Thereby, microtubules only nucleate above a threshold concentration of tubulin, which is exceeded in condensates, but not in the cytosol. Furthermore, condensates can keep molecules together that act cooperatively to fulfill functions. For example, in the transcription machinery condensates combine proteins that fulfill different functions in transcription[44, 45].

(iii) The wetting behavior can be used to control condensate nucleation at specific locations, for example in microtubules[43].

(iv) The two phases formed by LLPS have fixed compositions. Thus, changing the total amount of protein in the two phase region will change the condensate size, but the composition in the condensate and surrounding phase remains the same. It has been suggested in Ref.[46] that condensates can buffer the protein expression noise in the cytosol¹¹; see fig. 1.4 upper right panel.

(v) Another putative function of condensates is force generation; see fig. 1.4 lower right panel. Because of their surface tension, but also elastic properties, condensates can exert forces, for example on the cytoskeleton[47].

(vi) In multiphase systems, condensates can be used to 'sort' proteins. Thereby, molecules partitioning in different phases according to their affinity[48, 49].

¹⁰: Or just extremely slow.

¹¹: This is more complicated in multicomponent systems[18] and it has been argued in Ref.[28], that this mechanism is only possible for certain interaction regimes.

Finally, recently it has been suggested, that a hierarchy of interactions that act on different time scales can be used in condensates to form a biological clock[50].

While some functions are well understood, for example, the nucleation of microtubules[43] and the formation of stress granules as a response to external stimuli[36], others are only putative functions and have not been shown experimentally, for example, the use of condensates as clocks. As a result, there are still a lot of open questions about why condensates form and what their role is in detail. Modeling can help understand what kind of behavior is physically possible and so we will give a short overview of physical models used to understand condensates in cells next.

Modelling condensates

Standard tools from statistical physics and polymer physics have been applied to describe biomolecular condensates[6]. And although those theories fall short in describing the complexity of cells, they have been remarkably successful in describing the phase separation of condensates, for example, of Cajal bodies and stress granules[18] as well as P granules[16]. Of course, there are important differences between standard phase separation and condensates in cells. First, most phase separation studies deal with few components, while the cell is made up of thousands of different molecules. Second, the total number of a certain type of biomolecule is rather low, so thermal noise and small number effects are important. Third, the cell is a crowded environment and contains multiple sub-structures, for example, the cytoskeleton and membrane bound organelles, that influence the diffusive dynamics, and condensates can interact with those sub-structures. Finally, cells are out of equilibrium systems[51]. How active processes, for example driven reactions[40] or the interaction with the cytoskeleton[43], influence phase separation in cells is ongoing research[7, 52] and an important part of this thesis.

The models commonly used to describe biomolecular condensates can be roughly divided into two classes, field theoretical models (like this thesis) and particle based models. Particle based models contain more molecular details, for example, they can investigate the influence of protein sequences[53, 54]. They have been used to investigate which interactions are important in condensate formation[55, 56] and predict how amino acid distribution and protein length can influence condensate formation[55, 57]. Furthermore, molecular dynamics studies can give insight into the material properties of condensates, for example, the plasticity[58] and the formation of networks in the conden-

sate[59]. Thus, particle based theories are particularly useful to study the molecular details, for example, which specific proteins phase separate and how they interact with other biomolecules. Unfortunately, particle based simulations are limited to small length and time scales. For example, in Ref.[59] up to 6000 particles, which corresponds to simulation volumes of $\sim 10^3 \text{ nm}^3$, are simulated for total simulation times of $0.5 \mu\text{s}$.

The field theoretical approach contains fewer molecular details but can be used to study longer length and time scales, for example coarsening behavior[60] or the effect of large scale concentration gradients[61]. For example, in Refs.[62, 63] equilibrium field theory was used to show that mixtures with many components and random interactions are likely to undergo phase separation. In addition, they showed how phase separation is linked to the average and standard deviation of the random interactions. Furthermore, recent studies investigate how tuned interactions, for example via evolution, influence the formation of multiple phases[49, 64]. Along these lines, in Refs.[65, 66] it was shown how the interaction of multiple phases can be described in terms of their relative surface tensions, which can explain wetting as well as multiphase condensates[34]; see fig. 1.4 top right panel. Furthermore, the viscoelastic properties of condensates can be included in field theories as well, for example, ref.[52] investigates condensates that form and grow in an elastic surrounding. Another application for field theories are reaction diffusion models. Refs.[67, 68] use a non-equilibrium reaction diffusion model to investigate the formation of centrioles around the centrosome[42]. In Ref.[69], a reaction diffusion model is used to investigate how transcriptional condensates interact with RNA. And refs.[70, 71] show how first-order reactions can control individual droplet size. Field theories are particularly useful to understand emerging behavior and how different processes interact with each other, for example how reactions and diffusion together can lead to pattern formation[72].

Since we want to investigate the interplay of phase separation and reaction on a thermodynamic basis, we will use field theoretical reaction diffusion models during this thesis as well. To motivate this further, we will next discuss experimental indications that biochemical reactions are important regulators of condensates and two different hypotheses from Ref.[73] on how size control of condensates could be achieved in cells.

1.2 Chemical Reactions control droplets

This section is based on Soeding, et. al. ‘Mechanisms for Active Regulation of Biomolecular Condensates’, Trends in Cell Biology (2020)[73], but rewritten. Our contribution to this pa-

12: We discuss the example of a phase separating protein. But it is similar for RNA or DNA or, in the case of associating phase separation of multiple molecules, a mixture of RNA, DNA, and proteins.

per was to develop the theoretical models and the mechanisms for active regulation of condensates.

Like many other processes in cells, droplet formation and dissolution are controlled by biochemical reactions. An important control parameter for condensate formation is the total amount of phase separating protein¹² because condensates only form above a certain threshold concentration[7]. The total amount of protein can change either due to production or degradation of proteins, but also by modifying already existing proteins via **Post-Translational Modifications** (PTMs)[74, 75]. These PTMs, for example, phosphorylations or methylations, add functional groups to already existing proteins and thereby change the interaction with other molecules, for example, by changing the charge[76]. Oftentimes, these modifications lie in disordered regions[77], which are important for condensate formation[55]. Thus, by controlling the PTMs, the cell can control if a protein forms droplets or not.

The PTMs are biochemical reactions that are oftentimes catalyzed by enzymes, for example, kinases catalyze phosphorylation reactions[78]. Thus, enzyme activity can control PTMs and thereby condensate formation or dissolution[73]. In contrast to other control mechanisms like temperature or protein production, this mechanism is fast because enzymatic reactions are much faster than protein production and specific because the enzyme acts on a specific protein and does not influence other cellular processes the way temperature does.

Signs of this mechanism controlling condensate formation and dissolution are found in several experiments; see Ref.[73] and references therein. For example, in Ref.[79] the authors show that the DEAD-box ATPase family regulates RNA condensates both in prokaryotes and eukaryotes. Thereby, the ATPase can exist in two states, an ATP-bound state, and an ATP free state. In the ATP-bound state, the ATPase promotes phase separation of RNA condensates. But, upon ATP hydrolysis of the ATPase, the condensates dissolve. Another example is shown in fig. 1.5 and taken from Ref.[80]. In this study, the protein CTD forms droplets in vitro; green dots in the lower panels of fig. 1.5. Adding the kinase CDK7, which phosphorylates the CDK protein, dissolves the droplets over time; see time course from left to right in fig. 1.5. This shows that slight changes in the protein properties can dissolve droplets.

Besides condensates in cells, controlling phase separation with chemical reactions is interesting in the context of complex coacervates as well. Complex coacervates are phase separated compartments that form because of electrostatic interactions between oppositely charged molecules[81]¹³. Recent studies use complex coacervation of biomolecules in vitro to study how chem-

13: Some biomolecular condensates form via attractive electrostatic interactions as well[82], so some biomolecular condensates fall into the class of complex coacervates.

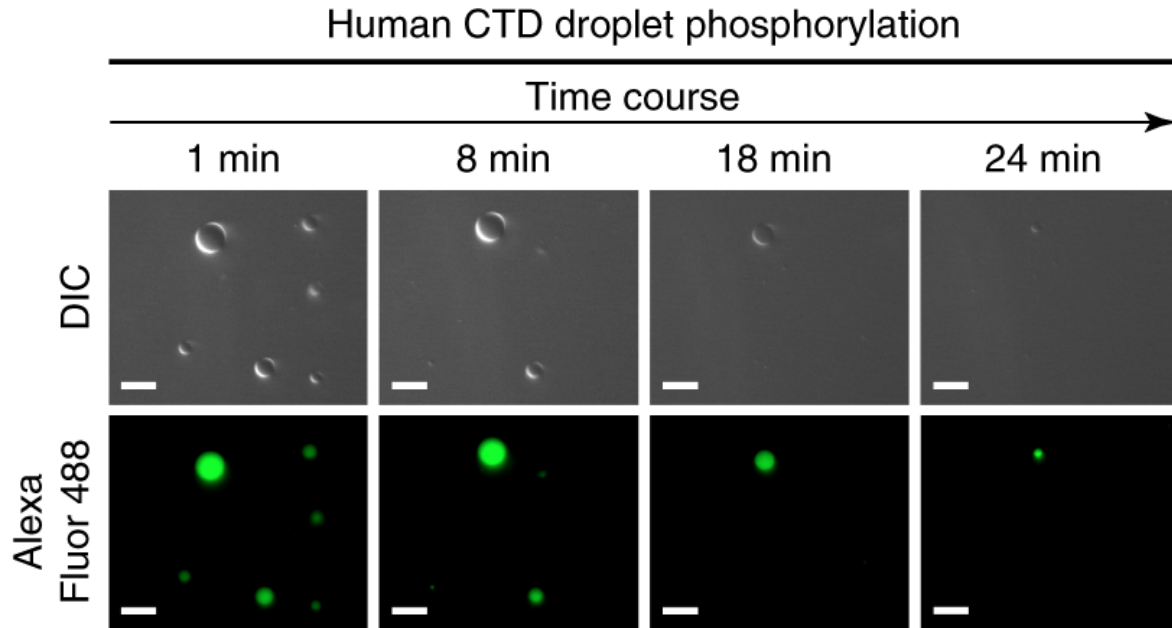


Figure 1.5: Enzyme activity in droplets can dissolve droplets over time. The kinase CDK7 phosphorylates the CTD protein and thereby dissolves CTD droplets (green in the lower panels) over time in vitro. Reprinted from Boehning, et al., "RNA polymerase II clustering through carboxy-terminal domain phase separation", *Nature Structural and Molecular Biology*, Vol.25(2018)[80] with permission from the publisher under license number 5271391421873.

ical reactions get influenced by the presence of coacervates[83, 84] and vice versa. For example, Ref.[85] shows how actively driven reactions can be used to increase the growth rate of coacervates by autocatalytic reactions¹⁴.

In some biological contexts controlling the formation and dissolution of condensates is not enough. It can be necessary to control where droplets form, how big they are, and how many coexist. For example, multiple transcription condensates can be necessary to activate multiple genes[14, 86] and they have to form at the right DNA sites[12]. Size control of condensates formed by liquid-liquid phase separation is tricky because the tendency to minimize surface energy will lead to coarsening of condensates via Ostwald ripening[87] and coalescence[88] until only one large condensate remains. Ostwald ripening is driven by diffusive fluxes between droplets, thus, to suppress ripening, those diffusive fluxes have to be either prevented or compensated by other fluxes to achieve size control. In Ref.[73], we proposed two mechanisms for size control of condensates via chemical reactions, which we briefly introduce next. The main idea for both mechanisms is to introduce reactions that limit droplet growth and thus compensate the diffusive fluxes that control droplets growth dynamics.

¹⁴: In autocatalytic reactions, the reactant catalyzes the reaction itself, for example, in the reaction $A + A \rightleftharpoons A + B$, A catalyzes its own conversion to B .

Enrichment inhibition

We call the first mechanism the enrichment inhibition model and it is based on four traits [73]: **(i)** A protein that is essential for droplet formation gets phosphorylated by a kinase and the proteins do not phase separate in the phosphorylated form. **(ii)** Increasing the kinase activity dissolves the droplet. **(iii)** The kinase is enriched in the droplet together with its substrate¹⁵. **(iv)** The concentration of the phase separating protein is above the condensation threshold in the surrounding, so the mixture is supersaturated and droplets can form spontaneously.

15: Because the kinase is enriched in the droplet and destroys droplet material, the enrichment inhibits the growth, hence the name.

The mechanism of size control then follows from a simple scaling argument: The diffusive influx J into a droplet in a supersaturated environment is proportional to the droplet radius $J \propto R$. Assuming that the droplet phase is homogeneous and the phosphorylation rate is k , the total phosphorylation rate S is proportional to the droplet volume $S \propto kR^3$. As a result, the droplet gains material proportional to R but loses material proportional to kR^3 and the droplet growth stops at a specific radius R_* , where $J = S$. The scaling explains as well that droplets do not form at all if the rate k , i.e. the kinase activity, becomes too large. This reasoning does not explain why the kinase has to enrich in the droplet phase to achieve size control though. We will show in this thesis that the enrichment of the kinase in the droplet phase is essential for size control.

Ref.[73] collects several examples in cells which fulfill all or most of the four traits introduced above. Here, we repeat only one example, P granules in *Caenorhabditis elegans* embryos discussed in Ref.[89]. **(i)** The MEG protein, which has intrinsically disordered domains, gets phosphorylated by the MBK-2 kinase and dephosphorylated by the PPTR-1 phosphatase. **(ii)** P granules can be dissolved by MBK-2 activity and formation can be induced by PPTR-1. **(iii)** MBK-2 is enriched in P granules. **(iv)** P granules form in vivo. Similar evidence was found for stress granules[36], synaptic vesicles[90] and others.

Localization induction

The second control mechanism is the localization induction model and it has three characteristic properties: **(i)** A kinase is localized at a specific position in the cell, for example by binding to a membrane. **(ii)** The localized kinase phosphorylates specific proteins important for droplet formation, such that the phosphorylated protein promotes condensate formation¹⁶. **(iii)** The protein concentration is below the condensation threshold in the surrounding medium, so no droplets form spontaneously.

16: Because the localized enzyme produces the droplet material, droplet formation gets induced locally, hence the name.

The general argument is similar to the enrichment inhibition model. But because the fluid is subsaturated, droplet ma-

terial has to be produced locally, to increase the local concentration above the condensation threshold. In this case, the area that produces droplet material is fixed, and thus the production of droplet material Q is independent of droplet size. At the same time, the subsaturation far away from the droplet leads to a diffusive outflux proportional to the droplet radius $J \propto -R$. The different scalings suggest that a stable droplet size R_* exists if the protein production Q is strong enough to form droplets, to begin with. In this case, increasing the reaction rate should increase droplet size instead of decreasing it as in the enrichment inhibition model, so the reaction has opposite effects in the two mechanisms.

Because this mechanism allows precise control about where droplets form, it is not surprising that the evidence found for this mechanism in Ref.[73] comes from examples that require spatial control, for example, transcription and transmembrane signaling. An example of a condensate that might work according to this mechanism is condensates involved in DNA repair that form around DNA double strand breaks[91]. **(i)** A PARP-1 enzyme localizes around damaged DNA sites. **(ii)** PARP-1 attracts other PAR proteins as well as FUS, a protein known to promote phase separation[92] and forms condensates around the DNA damage. **(iii)** These droplets do not form at any other place than the DNA damage sites. Furthermore, reducing the degradation of PAR proteins by removing PAR degrading enzymes enhances the formation of these condensates[93].

The examples show that chemical reactions play an important role in the formation, dissolution, and control of biomolecular condensates in cells. While the scaling arguments above give an intuition of how size control can be achieved, a thorough theoretical analysis of phase separation and chemical reactions is necessary to understand if the simple scaling holds. In addition, theoretical investigations can help determine the minimal ingredients necessary to achieve size control and control over condensate formation and dissolution. One other important detail is that posttranslational modifications usually require external energy input, for example, phosphorylation reactions involve the hydrolysis of an ATP molecule. Therefore, the control mechanism of condensates via PTMs is an out of equilibrium process. Therefore, for a full understanding, an equilibrium theory is not sufficient, although phase separation is an equilibrium phenomenon. Instead, a non-equilibrium description of the reactions will be necessary.

Other control mechanisms

Of course, chemical reactions are not the only way to control phase separation in cells. In an *in vitro* system, polymer droplets forming inside a hydrogel can be controlled by the elasticity of the gel[94]. Similar effects could appear in cells, where the condensates interact with the cytoskeleton[47, 52].

Furthermore, the aging of condensates can reduce the condensate dynamics and thus arrest them at a certain size[95]. Also, undergoing a liquid to solid transition can arrest droplet growth and even prevent dissolution[32]. But this can have negative health effects as well[34], suggesting that the fluid state is necessary for cellular function.

1.3 Reaction Diffusion Systems

Above, we introduced enzymatically driven reactions as a control mechanism for biomolecular condensates formed by phase separation. This falls into the general class of reaction diffusion systems for pattern formation in biological systems[96, 97]. In the classical form introduced by Alan Turing in Ref.[72], patterns can emerge in a two species model, if the two species diffusion coefficient is different and if the reactions are non-linear¹⁷. These reaction diffusion models have been successfully applied in biological systems, for example in describing oscillations in minD-minE protein systems[98, 99] or morphogenesis[100, 101].

Liquid-liquid phase separation is an equilibrium phase transition, driven by interacting particles. Thus, it can be described in the context of critical phenomena and phase transitions described in Refs.[35, 102].

The combination of LLPS and driven chemical reactions forms a new crossover between phase transitions and reaction diffusion systems. Thereby, the reactions do not have to produce the pattern, but only control the behavior of the phases that form spontaneously via phase separation.

1.4 Outline of thesis

In this thesis, we investigate how chemical reactions can control biomolecular condensates in cells. There are studies modeling biomolecular condensates with chemical reactions, for example stress granules[71, 103], centrosome[67, 68] and general frameworks[60, 104]. But all of them use the mass action kinetics framework, which assumes ideal, dilute solutions, which is not valid for phase separating mixtures. Work that overcomes this

¹⁷: The original reaction was an Activator-Inhibitor model, in which one of the two species speeds up the reaction rate (the activator), while the second species reduces the reaction rate (the inhibitor).

problem appeared only recently[105, 106]. Therefore, in this thesis, we develop a framework that combines phase separation and chemical reactions based on thermodynamic arguments and apply it to understand how chemical reactions can be used to control condensate size and formation.

We discuss the theoretical basis of phase separation and chemical reactions in Ch. 2. We first introduce the main quantities to describe multi-component reactive fluids, the volume fractions of all components, and their chemical potentials. Then, we introduce the framework of linear non-equilibrium thermodynamics to derive the dynamics of all species from thermodynamic quantities. Finally, we discuss the thermodynamics of binary and ternary phase separation.

In Ch. 3, we discuss the interplay of simple reactions and phase separation in a ternary fluid mixture. We discuss how chemical equilibrium is linked to phase separation and how it influences droplet formation. Then, we apply our theory to the RNA binding protein SAF-A and try to understand how RNA binding of SAF-A influences its phase separation behavior.

Afterward, we extend the model to include active reactions in Ch. 4. There, we discuss how external energy input can influence droplet formation and why fast and precise control of droplet formation requires a reaction cycle. Furthermore, we show how spatially inhomogeneous reaction rates can stabilize individual droplets at a fixed size and lead to states with multiple stable droplets. Finally, we discuss the results of this thesis in a broader context and give an outlook of what might be interesting further questions in Ch. 5

Theory of reactive fluid mixtures

2

This chapter introduces the formalism used in this thesis to study reactive, liquid mixtures with interacting particles that can phase separate. As discussed in Ch. 1 we use a mean-field description, where the state of the system is described by the local composition. We do not describe particles individually, instead, the local composition is described by volume fractions of all particle types and their evolution in time.

In the first step we introduce the thermodynamic basis of an incompressible, isothermal fluid with N different particle types, explain why we choose the volume fractions as the dynamical variables, and how reactive and diffusive fluxes determine their evolution in time. Then we show how these fluxes are linked to thermodynamics via the framework of linear non-equilibrium thermodynamics[107]. Afterward, we introduce the regular solution theory, which defines the free energy density f that is used throughout this thesis and explain how liquid-liquid phase separation is linked to f in a binary fluid. In the last step, we introduce a ternary free energy density and discuss phase separation for two specific choices of interactions in the ternary system.

2.1 Multicomponent fluid mixtures

We consider a fluid composed of N different species, where N_i is the particle number of species $i = 1, \dots, N$. Since we build our theory on thermodynamic arguments, we have to specify how the system interacts with its surrounding. The ensembles that match cell conditions the closest are the canonical (NVT) ensemble and the isothermal-isobaric (NpT) ensemble. In both cases, the temperature T is controlled by a heat bath, therefore, T is constant, but the total energy of the ensemble can change due to heat exchange with the surrounding. In addition, in both cases, no particles can enter or leave the system, so the system is closed. But in the NVT -ensemble the volume V_{sys} of the system is fixed and the equilibrium pressure follows from the derivative of the state function with respect to V_{sys} , while it is the other way around in a NpT -ensemble, where constant pressure is applied. As biological cells oftentimes adjust their volume, while the pressure inside remains (mostly) constant, the NpT -ensemble seems the better choice¹. We consider incompressible fluids only, so pressure differences equilibrate fast compared to diffusion and reaction and no center of mass velocity is present.

| | |
|--|----|
| 2.1 Multicomponent fluid mixtures | 15 |
| 2.2 Non-Equilibrium Thermodynamics | 18 |
| Diffusion | 21 |
| Reaction | 23 |
| 2.3 Multicomponent regular solution theory | 27 |
| Influence of protein size | 29 |
| Non-local interactions . | 29 |
| 2.4 Liquid-liquid phase separation | 30 |
| Binary Phase Separation | 31 |
| Maxwell construction . | 32 |
| Kinetics | 33 |
| Interface properties . . | 35 |
| Ternary Free Energy . . | 37 |
| 2.5 Simulations | 40 |
| 2.6 Summary | 41 |

¹: Neither matches cell conditions perfectly, in real systems the cell exchanges particles with the surroundings, and temperature can change as well. In addition important state variables like pH are not included in the model[108].

In addition, we are not interested in the effect of cell volume change in this study. The only dynamical processes we consider are diffusive dynamics that conserve the local density and reactions that conserve volume. In this case, the two ensembles are equivalent and we choose the notation of the canonical ensemble where the (Helmholtz) free energy $F(N_i, V, T)$ is the state function.

In summary, we assume systems with constant volume V_{sys} and temperature T . In addition, no particles are exchanged with the surrounding, but particle numbers N_i of each species i can still change due to chemical reactions. We neglect center of mass flows and assume the fluid to be incompressible with a mass density ρ_0 .

For a homogeneous mixture we introduce the species specific particle density $c_i = \frac{N_i}{V_{\text{sys}}}$, which is an intensive quantity and is thus independent of system size. Using c_i , we get the mass density $\rho_i = M_i c_i$, using the molecular mass M_i (the mass per i particle) and the **volume fraction** $\phi_i = v_i c_i$ using the molecular volume v_i (the volume per i particle). In incompressible systems v_i is a constant and for simplicity we assume the molecular mass density $m_i = M_i/v_i = m_0$ to be constant for all species. In this case volume fraction ϕ_i and mass density ρ_i are connected via $\rho_i = m_0 \phi_i$. If all species have the same molecular volume v_i as well, volume fraction, particle density and mass density are all connected via constant prefactors and we can use them interchangeably. But we will see later that different molecular volumes can have a big effect in polymer systems[109] and thus allow the molecular volumes to be different for now. In incompressible systems, it is convenient to describe the system in terms of volume fractions, because they always sum up to 1, $\sum_i \phi_i = 1$, which we will use in the following. Furthermore, we introduce an intensive **free energy density**²

$f(\Phi, T) = F(N_i, V_{\text{sys}}, T)/V_{\text{sys}}$, where $\Phi = (\phi_1, \dots, \phi_N)^T$ is the volume fraction vector. In this form $f(\Phi, T)$ is an intensive quantity which depends on intensive quantities only and we can choose V_{sys} arbitrarily.

From this description it is conceptually easy to go to an inhomogeneous mixture. In this case the volume fraction of each species $\phi_i(\mathbf{r}, t)$ becomes a field that depends on space \mathbf{r} and time t , while at each point in space $\sum_i \phi_i(\mathbf{r}, t) = 1$ has to be fulfilled due to incompressibility and constant mass density. Accordingly, the free energy density $f(\Phi(\mathbf{r}, t))$ depends on space and time as well³ which implies that the total free energy of the system is given by

$$F = \int_{V_{\text{sys}}} f(\Phi, \nabla\Phi) dV. \quad (2.1)$$

2: We use that F, N_i , and V_{sys} are extensive quantities and thus first order homogeneous functions in V_{sys} , so $V_{\text{sys}}^{-1}F(N_i, V_{\text{sys}}, T) = f\left(\frac{N_i}{V_{\text{sys}}}, \frac{V_{\text{sys}}}{V_{\text{sys}}}, T\right) = f\left(\frac{\phi_i}{v_i}, 1, T\right) = f(\Phi, T)$, where F indicates total free energies and f free energy densities.

3: We assume fast thermal conductivity so $T(\mathbf{r}, t) = T$ is constant in space and time and set by the thermal bath and thus drop the T dependence.

Here, we assume that the free energy density can not only depend on the local composition but also on composition gradients $\nabla\Phi$, where ∇ is the gradient operator.

Going from system-wide quantities to local fields that vary in space and time is based on the local equilibrium assumption[107], which assumes that thermodynamic quantities like a free energy density or entropy density can be defined locally. This assumption becomes problematic for small system sizes or if long-range interactions are present[110]. We assume short-range interactions only and therefore include non-local terms $f \propto \nabla\Phi$ where ∇ is the gradient operator. Because copy number of proteins in cells is usually low with total protein densities of roughly 10^6 Proteins/ μm^3 while cell volume can range from $1-10^6 \mu\text{m}^3$ [1], finite size effect can be important and the mean field and local equilibrium approximation would break down. Nevertheless, mean-field models are very successful in describing phase separation phenomena in cells[6, 16, 111] and we take the empirical success as a motivation to use them in our study. Furthermore, in active systems, the local equilibrium assumption can be violated by active processes, for example in active fluctuations that break detailed balance[112]. But it was shown, that the heat produced by active reactions does not violate the local equilibrium assumption on length and time scales relevant for cellular events[16, 113].

A consequence of a spatially varying free energy density is that the system is not in thermodynamic equilibrium and will relax towards the equilibrium state over time. As discussed above the only dynamical variables are the volume fraction fields $\phi_i(\mathbf{r}, t)$. The dynamics of the volume fractions follow generically from a continuity equation of the form⁴

$$\partial_t \phi_i(\mathbf{r}, t) = -\nabla \cdot \mathbf{j}_i(\mathbf{r}, t) + s_i(\mathbf{r}, t), \quad i = 1, \dots, N \quad (2.2)$$

where \mathbf{j}_i are the diffusive fluxes of species i , $\nabla \cdot \mathbf{j}_i$ is the divergence of \mathbf{j}_i , and s_i is the rate at which species i is created or destroyed due to chemical reactions. The continuity equation can be rationalized as follows, consider a small volume element v with boundaries O containing N particles. Then the number of particles in the volume element can change ($\partial_t N$) either via particle fluxes through the boundaries ($-\oint_O \mathbf{j}_i d\mathbf{O} = -\int_v \nabla \cdot \mathbf{j} dV$) or creation/destruction inside the volume due to reactions $\int_v s dV$. As this is true for arbitrary volumes we can write it in differential form, which results in Eq. 2.2, by applying the same logic to each species i and we use that $\phi_i(\mathbf{r}, t) = \frac{v_i}{v} N_i(\mathbf{r}, t)$ to convert particle numbers to volume fractions⁵.

As discussed before $\sum_i \phi_i(\mathbf{r}, t) = 1$ holds at every point in space at all times due to incompressibility. Therefore the sum over all N equations Eq. 2.2 has to vanish, $\sum_i \partial_t \phi_i = -\nabla \cdot$

4: We neglect center of mass flows for simplicity, but they can be included in the particle fluxes \mathbf{j}_i as well.

5: The factor v_i/v shows that v can in fact not be chosen arbitrarily, but has to be large compared to molecular volumes v_i , else quantities like volume fraction or concentration are not well defined.

$(\sum_i \mathbf{j}_i) + \sum_i s_i = 0$. As will be discussed in more detail the next section, we consider reactions that conserve mass only and, due to constant molecular mass density $m_0 = M_i/v_i$, this implies that reactions conserve volume as well. Therefore $\sum_i s_i = 0$ and we find that the sum over diffusive and reactive fluxes vanishes independently

$$\sum_i s_i(\mathbf{r}, t) = 0, \quad \text{and} \quad (2.3a)$$

$$\sum_i \mathbf{j}_i(\mathbf{r}, t) = 0. \quad (2.3b)$$

Eq. 2.3b underlines that the motion of particles is not independent of each other, because the total volume fraction is always 1. This can be used to eliminate one species from the description, which will be discussed in the next section.

2.2 Non-Equilibrium Thermodynamics

From Eq. 2.2 we see that the important quantities to calculate the dynamics of incompressible, multicomponent fluids are the diffusive fluxes \mathbf{j}_i and the reaction rates or reaction fluxes s_i . In this section, we discuss how both diffusion and reaction are linked to thermodynamics using the formalism of linear non-equilibrium thermodynamics[107]. The main idea is that the fluxes appearing in Eq. 2.2 are driven by thermodynamic forces⁶ in such a way, that the system ensures positive entropy production rate $\frac{dS}{dt} \geq 0$ and relaxes towards thermodynamic equilibrium, where the entropy production vanishes, $\frac{dS}{dt} = 0$.

It is instructive to calculate the **entropy production rate** for a reaction-diffusion process to see where the flux-force relation stems from. We use that the total free energy F and entropy S are related via $F = E - TS$, where E is the internal energy. For an isothermal system with constant volume and no particle exchange, E is constant so $T \frac{dS}{dt} = -\frac{dF}{dt}$ [60]. This and Eq. 2.1 leads to

$$T \frac{dS}{dt} = -\frac{dF}{dt} = -\int_{V_{\text{sys}}} \frac{df(\Phi, \nabla\Phi)}{dt} dV \geq 0. \quad (2.4)$$

In addition we can write a continuity equation for the free energy density, which can change due to a local free energy density change $\dot{f} = \partial_t f$ and free energy density fluxes \mathbf{j}_f

$$\frac{df}{dt} = \dot{f} - \nabla \cdot \mathbf{j}_f. \quad (2.5)$$

We can then expand df/dt in all variables Φ and $\nabla\Phi$ and try to

6: Those can be, for example, Temperature differences, chemical potential differences, or pressure differences.

connect the results to the local production \dot{f} and the flux \mathbf{j}_f

$$\frac{df}{dt} = \sum_i [(\partial_{\phi_i} f)(\partial_t \phi_i) + (\partial_{\nabla \phi_i} f) \cdot (\nabla(\partial_t \phi_i))] \quad (2.6)$$

where $\partial_{\phi_i} = \frac{\partial}{\partial \phi_i}$ and $\partial_{\nabla \phi_i} = \frac{\partial}{\partial \nabla \phi_i}$ are derivatives with respect to volume fraction and its gradient respectively. The calculation is done in the Appendix A, but using Eq. 2.2 and the product rule $\nabla(a(\mathbf{r})b(\mathbf{r})) = (\nabla a(\mathbf{r}))b(\mathbf{r}) + a(\mathbf{r})(\nabla b(\mathbf{r}))$, we end up with

$$\begin{aligned} \frac{df}{dt} = \sum_i \{ & \nabla \cdot [(\partial_{\phi_i} f)\mathbf{j}_i + (\partial_{\nabla \phi_i} f)(\nabla \cdot \mathbf{j}_i) - (\nabla \cdot \partial_{\nabla \phi_i} f)\mathbf{j}_i + (\partial_{\nabla \phi_i} f)s_i] + \\ & \nabla \cdot [(\partial_{\phi_i} f) - \nabla \cdot (\partial_{\nabla \phi_i} f)]\mathbf{j}_i + [(\partial_{\phi_i} f) - \nabla \cdot (\partial_{\nabla \phi_i} f)]s_i \} \end{aligned} \quad (2.7)$$

the terms in the first row are divergences of a flux and we identify them with the free energy density flux \mathbf{j}_f and the terms in the second row are scalar quantities which we identify as the local free energy production \dot{f} . Distinguishing these two is important because we assume no fluxes of particles through the boundaries. Together with the divergence theorem, this implies that the divergence of the free energy flux in Eq. 2.4 vanishes, $\int_{V_{\text{sys}}} \nabla \cdot \mathbf{j}_f dV = 0$ and only the local free energy density production $-\int_{V_{\text{sys}}} \dot{f} dV \geq 0$ remains.

Note that $(\partial_{\phi_i} f) - \nabla \cdot (\partial_{\nabla \phi_i} f)$ is the functional derivative of F with respect to ϕ_i , which signifies the free energy change of the system when the volume fraction of species i is changed and is directly related to the **chemical potential** μ_i of species i . The chemical potential μ_i is defined as the free energy change when an i particle is added to the system at constant particle number of all other species $N_{j \neq i}$, total volume V_{sys} and temperature T ⁷

$$\mu_i = \left. \frac{\delta F}{\delta N_i} \right|_{N_{j \neq i}, V_{\text{sys}}, T} = v_i [\partial_{\phi_i} f - \nabla \cdot (\partial_{\nabla \phi_i} f)]|_{N_{j \neq i}, V_{\text{sys}}, T}. \quad (2.8)$$

Replacing $\partial_i f$ in Eq. 2.4 with Eq. 2.7 and using μ_i we end up with

$$\frac{dS}{dt} = - \int_{V_{\text{sys}}} \sum_i [(\nabla \mu_i) \cdot \mathbf{j}_i + \mu_i s_i] dV \geq 0. \quad (2.9)$$

Here $\nabla \mu_i$ and μ_i are the thermodynamic forces corresponding to the fluxes \mathbf{j}_i and s_i respectively. The term thermodynamic forces stems from the following consideration: If $\mu_i < 0$ the total free energy F can be lowered by adding i particles to the system, while for $\mu_i > 0$, F can be lowered by removing i par-

7: As particle numbers can only vary in integer steps one has to write $\mu_i = F(N_i + 1, N_{j \neq i}, V_{\text{sys}}, T) - F(N_i, N_{j \neq i}, V_{\text{sys}}, T)$, but for large N_i the differential form is a good approximation.

ticles. Because the total free energy is minimized in a closed system μ_i determines if the reactions add ($s_i > 0$) or remove ($s_i < 0$) i particles. In the same way, $\nabla\mu_i$ indicates in which directions particles have to move in space via diffusive fluxes \mathbf{j}_i to lower F . Thus μ_i and $\nabla\mu_i$ ‘force’ the reactive fluxes s_i and diffusive fluxes \mathbf{j}_i in the direction of lower free energy. In addition, if the thermodynamic forces vanish, there is no energetically preferred direction for diffusive and reactive fluxes, so they have to vanish as well, which means $\mathbf{j}_i = 0$ if $\nabla\mu_i = 0$ and $s_i = 0$ if $\mu_i = 0$.

While these considerations constrain the fluxes, the functional relation between fluxes and forces is not generally known. Linear non-equilibrium thermodynamics now assumes that close to equilibrium, where the thermodynamic forces are small compared to thermal energy $\mu_i < k_B T$ and $l\nabla\mu_i < k_B T$, where l is a length scale large compared to intermolecular distances, but small compared to system size, we can expand the fluxes up to linear order in the forces

$$\mathbf{j}_i \approx - \sum_j L_{ij} \nabla\mu_j, \quad \text{and} \quad (2.10a)$$

$$s_i \approx - \sum_j k_{ij} \mu_j. \quad (2.10b)$$

8: Using a length L , time τ and energy $k_B T$ scale, $\partial_t \phi_i$ has units $1/\tau$, $\nabla \mathbf{j}_i$ has units L^2/τ and $\nabla \mu_i$ has units $k_B T/L$, so L_{ij} has units $L^2/(\tau k_B T)$ and k_{ij} $1/(\tau k_B T)$

9: If we write the relation for each particle type, we will see below, that cross-reactions leads to coupling of different species that participate in the same reaction. For example, a reaction $A \rightleftharpoons B$ leads to a reactive flux $s_A = -k(\mu_A - \mu_B)$. Cross-diffusion implies that the chemical potential gradient of species $j \neq i$ influence the diffusion of species i . This is important in incompressible systems as we will see below.

Here L_{ij} and k_{ij} are the diffusive and reactive mobilities⁸ and the corresponding matrices are symmetric and positive (semi-)definite due to the Onsager principle[107]. Which includes cross-diffusion[65, 114] and cross-reaction terms⁹. In general, all the thermodynamic fluxes can depend on all thermodynamic forces. But, in the case of an isotropic fluid, vectorial quantities ($\nabla\mu_i, \mathbf{j}_i$) do not couple to scalar quantities (μ_i, s_i)[107]. Therefore, the reactive fluxes are driven by chemical potentials and the diffusive fluxes are driven by gradients in chemical potentials. In this form Eq. 2.10 ensures that

1. The entropy production is always non negative

$$- \sum_i [(\nabla\mu_i) \mathbf{j}_i + \mu_i s_i] \leq 0 \quad (2.11)$$

2. Vanishes in equilibrium

$$\frac{dS}{dt} = 0 \iff \nabla\mu_i = 0 \ \& \ \mu_i = 0 \quad \forall i \quad (2.12)$$

3. A steady state is reached in equilibrium

$$\mathbf{j}_i = 0 \ \& \ s_i = 0 \quad \text{if} \quad \nabla\mu_i = 0 \ \& \ \mu_i = 0 \quad \forall i. \quad (2.13)$$

But the diffusive fluxes in this form do not fulfill incompressibility and it is oftentimes useful to write the reactive flux differently because for most reactions the condition $\mu_i < k_B T$ is not fulfilled. Therefore we have a closer look at the diffusive and reactive flux in the next sections.

Diffusion

The main problem in Eq. 2.10a is that the fluxes do not conserve volume fraction locally. Generally, this is not a problem, fluxes can lead to density differences that lead to pressures that induce fluxes to equilibrate the density differences. But for simplicity, we do not want to describe pressures and center of mass fluxes explicitly. Instead, we focus on the strictly incompressible case, where conservation of local volume fraction is built into the diffusive fluxes. As discussed above and in Eq. 2.3b this implies that a local flux of i particles has to be balanced by a flux of all other particle types.

One way to enforce incompressible diffusive dynamics is to include the constraint in the free energy using the method of Lagrange multipliers

$$\bar{f} = f + \lambda \left(1 - \sum_i \phi_i \right), \quad (2.14)$$

where λ is the Lagrange multiplier. Accordingly, the new chemical potentials and diffusive fluxes read

$$\bar{\mu}_i = \mu_i - \lambda, \quad (2.15)$$

$$\bar{\mathbf{j}}_i = - \sum_j L_{ij} (\nabla \mu_j + \nabla \lambda). \quad (2.16)$$

The condition $\sum_i \bar{\mathbf{j}}_i = 0$ is then fulfilled for

$$\nabla \lambda = \frac{\sum_{i,j} L_{ij} \nabla \mu_j}{\sum_{i,j} L_{ij}}, \quad (2.17)$$

which we use to rewrite the fluxes $\bar{\mathbf{j}}_i$ with modified mobilities in a form that conserves the local volume fraction

$$\bar{\mathbf{j}}_i = - \sum_j \Lambda_{ij} \nabla \mu_j, \quad (2.18)$$

$$\Lambda_{ij} = L_{ij} - \frac{\sum_{k,l} L_{ik} L_{jl}}{\sum_{k,l} L_{kl}}. \quad (2.19)$$

Note that both the original mobilities L_{ij} and the rescaled mobilities Λ_{ij} can, in general, depend on local volume fraction, temperature, and other thermodynamic variables, as long as the mobil-

10: This means as well that ‘anti-diffusion’ $\Lambda_{ij} < 0$ is possible for some i, j .

ity matrices are symmetric and positive (semi-)definite to ensure a positive entropy production rate¹⁰.

To make this more clear, we discuss a two commonly used examples of the mobility matrix \mathbf{L} .

1. The simplest case is a diagonal \mathbf{L} with constant mobility L for all species $L_{ij} = L\delta_{ij}$, where the Kronecker delta is $\delta_{ij} = 1$ if $i = j$ and $\delta_{ij} = 0$ if $i \neq j$. Then $\Lambda_{ij} = L[\delta_{ij} - \frac{1}{N}]$ and $\mathbf{j}_i = -L \sum_j [\delta_{ij} - \frac{1}{N}] \nabla \mu_j$. Thus due to incompressibility, a diagonal mobility matrix can lead to fluxes that are driven by the non-diagonal terms ($i \neq j$, cross-diffusion). For a binary system with species A and B one can rewrite this into a center of mass flux that vanishes by construction $\mathbf{j}_A + \mathbf{j}_B = 0$ and a exchange flux between A and B $\mathbf{j}_A - \mathbf{j}_B = -L \nabla(\mu_A - \mu_B)$. The exchange flux describes how much B is replaced by A , while density is conserved and it is driven by the **exchange chemical potential** $\mu_A - \mu_B$, which is the energy change when a B particle ($-\mu_B$) is replaced by an A particle ($+\mu_A$). The condition $\sum_i \mathbf{j}_i = 0$ can generally be used to eliminate one species from the description, not only in the binary case. While any species can be eliminated, we will introduce a solvent species which is meant to represent the cytosol and eliminate the solvent from the effective description.
2. Another important special case is $L_{ij} = L\phi_i\delta_{ij}$, because in the ideal, dilute limit, where $\mu_i = \text{const.} + k_B T \ln(\phi_i)$ and $\nabla \mu_i = k_B T \phi_i^{-1} \nabla \phi_i$ plugging this mobility in Eq. 2.10a results in $\mathbf{j}_i = -L k_B T \nabla \phi_i$. Introducing the diffusivity D to rewrite the mobility as $L = D/k_B T$ we recover Fick’s law of diffusion $\mathbf{j}_i = -D \nabla \phi_i$.

In the incompressible case, plugging $L_{ij} = L\phi_i\delta_{ij}$ into Eq. 2.19 results in $\Lambda_{ij} = L(\phi_i\delta_{ij} - \phi_i\phi_j)$, which is also known as Kramer’s model of inter-diffusion[65, 114].

To complete the picture, diffusive fluxes $\mathbf{j}_i(\mathbf{r}, t)$ are generally subject to thermal fluctuations described by a vector field $\boldsymbol{\xi}_i(\mathbf{r}, t)$ [115]. In isotropic fluids, these fluctuations are well described by a stochastic process that is uncorrelated in space and time and has zero mean. The standard deviation is related to the mobility coefficients Λ_{ij} via the fluctuation dissipation theorem[115]. Taken together we can write the correlation of $\boldsymbol{\xi}_i$ as

$$\langle \boldsymbol{\xi}_i(\mathbf{r}, t) \boldsymbol{\xi}_j(\mathbf{r}', t') \rangle = 2k_B T \Lambda_{ij} \mathbf{1} \delta(\mathbf{r} - \mathbf{r}') \delta(t - t'), \quad (2.20)$$

here $\mathbf{1}$ is the identity matrix that ensures that spatial components of $\boldsymbol{\xi}_i$ are uncorrelated. Note that due to cross-diffusion the fluxes of different components are in general correlated. Importantly

ξ_i conserves mass, because it is added to the flux j_i .

Reaction

Calculating the reactive flux s_i for each species i is more complicated than Eq. 2.10b suggests for two reasons. First, the flux force relation $s_i\mu_i$ suggests that i particles can be created/destroyed until $\mu_i = 0$, but in chemistry, particles can not be created or destroyed arbitrarily. Instead, species can be converted into each other in specific ratios, the stoichiometries. Therefore each reaction has to obey a conservation law dictated by those stoichiometries¹¹. In addition, there can be multiple reactions and it is more appropriate to establish a flux force relation for each reaction individually. And second, the free energy change in a reaction ΔF is usually larger than $k_B T$, such that the linear relation between flux and force is not well-founded.

In a first step, we discuss the kinetics of K different reactions of the form $\nu_{i,k}^f A_i \rightleftharpoons \nu_{i,k}^b A_i$, where $i = 1, \dots, N$ runs over all species and $k = 1, \dots, K$ runs over all reactions. We call the reaction on the left side the forward reaction and on the right side the backward reaction¹². Then $\nu_{i,k}^{f/b}$ are the forward (f) and backward (b) stoichiometric coefficient of species i in reaction k . In addition, we call the species on the left hand side reactants and on the right hand side products. Furthermore, we introduce catalysts or **enzymes** which are not consumed or produced in a reaction ($\nu_{i,k}^f = \nu_{i,k}^b$), but are still necessary for the reaction to proceed¹³ ($\nu_{i,k}^f > 0$). Next, we define the reaction flux of the k -th reaction s_k as the difference between forward s_k^f and backward s_k^b rate, $s_k = s_k^f - s_k^b$. Here $s_k^{f/b}$ describe how often the forward/backward reaction happens per time. Chemical reactions conserve mass as long as no nuclear reactions take place at the same time. Because we assume constant mass density $m_0 = M_i/v_i = \text{const.}$ this conservation law can be written as volume conservation of each reaction

$$\sum_i v_i \nu_{i,k} = 0, \quad (2.21)$$

here $\nu_{i,k} = \nu_{i,k}^b - \nu_{i,k}^f$ is the stoichiometric coefficient for species i in reaction k and $v_i \nu_{i,k}$ is the volume change of species i if reaction k proceeds once in forward direction. This is important, because when all reactions conserve total volume they obey incompressibility as well.

Next we connect the rate of individual reactions s_k with the total change of volume of species i , s_i in Eq. 2.2 using the stoichiometric coefficient $\nu_{i,k}$ and the molecular volume v_i . The total amount of i particles produced or destroyed is simply the

11: For example a reaction $A + A \rightleftharpoons B$ can only convert two A 's into one B and vice versa, so the sum $N_A + 2N_B$ is conserved.

12: This is done solely for notation reasons. Because we discuss reversible reactions only, there is no 'preferred' direction and we could as well call the forward direction the backward direction and vice versa

13: Enzymes are particularly important in biochemical reactions, where they speed up reactions by several orders of magnitude[1].

sum over all reactions times the number of particles produced in a reaction and thus

$$s_i = v_i \sum_k \nu_{i,k} s_k, \quad (2.22)$$

where v_i takes care of the conversion from particles to volume fraction.

We have decomposed the reaction rate for each species i into a sum over individual reactions k , but we do not know how to connect the rates s_k with thermodynamic arguments yet. For this, we focus on the free energy change ΔF_k in the k -th reaction. It is defined as the change of energy when the reaction runs in the backward direction once¹⁴

14: We could define it for a forward direction as well because the reaction has no preferred direction.

$$\Delta F_k = - \sum_i \nu_{i,k} \mu_i. \quad (2.23)$$

The chemical potential μ_i describes the energy per i particle and $-\nu_{i,k}$ describes how many i particles are created/destroyed in a single backward reaction k . Thus the free energy change for particle type i is $-\nu_{i,k} \mu_i$ and the total free energy change is given by $-\sum_i \nu_{i,k} \mu_i$.

Similar to Eq. 2.10b the reaction will proceed towards lower free energy. This implies that the reaction runs in the forward direction ($s_k^f > s_k^b$) if $\Delta F_k > 0$ and the reaction runs in the backward direction ($s_k^f < s_k^b$) if $\Delta F_k < 0$. And if the reaction is in equilibrium ($\Delta F_k = 0$) the net reaction flux vanishes ($s_k^f = s_k^b$). This is automatically fulfilled for reactions that obey detailed balance[115], where the ratio of forward and backward rate is related to the free energy change according to

$$\frac{s_k^f}{s_k^b} = \exp\left(\frac{\Delta F_k}{k_B T}\right). \quad (2.24)$$

For small $\Delta F_k \ll k_B T$, we can rewrite the reaction flux s_k and expand the exponential function to end up with

$$s_k = s_k^b \left(\exp\left(\frac{\Delta F_k}{k_B T}\right) - 1 \right) \approx s_k^b \frac{\Delta F_k}{k_B T}. \quad (2.25)$$

In this case, s_k^b corresponds to the reactive mobility and Eq. 2.25 is equivalent to the linear non-equilibrium thermodynamics result, but now on the level of individual reactions instead of particle types.

As stated before, usually $\Delta F_k > k_B T$ and the linear approximation is inaccurate, while the detailed balance condition Eq. 2.24 holds more generally for systems in local thermodynamic equilibrium. To connect the reaction kinetics and ther-

modynamic arguments we need a different approach. Carati et al.[116] derive a condition for the rates based on Eq. 2.24 and the assumption that the forward rate depends on the ‘forward’ chemical potential $\mu_k^f = \sum_i \nu_{i,k}^f \mu_i$ only, $s_k^f(\sum_i \nu_{i,k}^f \mu_i)$ (and analogous for the backward rate). Although it is intuitive to assume that the forward rate is determined by the state (chemical potential) of the particles involved in the forward reaction, this is not necessarily true and the forward rate might as well be influenced by the ‘backward’ chemical potential $\mu_k^b = \sum_i \nu_{i,k}^b \mu_i$ (and vice versa). But if we take this as an assumption, it follows that the system is in equilibrium $s_k^f(\mu_k^{\text{eq}}) = s_k^b(\mu_k^{\text{eq}})$ and this is independent from the equilibrium value μ_k^{eq} , so the functional dependence of $s_k^f(\mu)$ and $s_k^b(\mu)$ on μ is the same. In addition ΔF_k and $s_k = s_k^f - s_k^b$ have the same sign to ensure positive entropy production, so $s_k^{f/b}(\mu)$ has to be a monotonically increasing function[116]. Note that this does not prescribe a functional form, but limits the possible forms to those that are in line with non-equilibrium thermodynamics and the linear form Eq. 2.25 is a limiting case for small ΔF_k .

Specifically, we will use **Transition State Theory (TST)**[117, 118] to derive the forward and backward fluxes as functions of the chemical potentials. Transition state theory is used to find transition rates between two metastable states when the transition happens due to thermal fluctuations. The two metastable states are local minima in a high dimensional free energy landscape, in our case, these are μ_k^f and μ_k^b , that are connected via a saddle point μ_k^\ddagger , the transition state; see fig. 2.1 for a schematic representation. If the energy barrier $\Delta_k^{f/b} = \mu_k^\ddagger - \mu_k^{f/b}$ between the two states is large compared to $k_B T$, the probability to reach the saddle point is proportional to the Boltzmann weight of the barrier $\exp(-\Delta_k^{f/b}/k_B T)$. The rate at which a molecule switches from one state to another is then given by the probability to reach the saddle point times a kinetic prefactor connected to thermal vibrations of the molecules p [117]

$$s_k^f = p_k e^{-\mu_k^\ddagger/k_B T} \exp\left(\frac{\mu_k^f}{k_B T}\right) = k \exp\left(\frac{\mu_k^f}{k_B T}\right), \quad \text{and} \quad (2.26a)$$

$$s_k^b = p_k e^{-\mu_k^\ddagger/k_B T} \exp\left(\frac{\mu_k^b}{k_B T}\right) = k \exp\left(\frac{\mu_k^b}{k_B T}\right), \quad (2.26b)$$

where we include the transition state $\exp(-\mu_k^\ddagger/k_B T)$ and the rate factor p in one reaction rate k . In general k can depend on various parameters, e.g. temperature, pressure or local composition, via both μ_k^\ddagger and p [118]. For our study only the composition dependence is important and while k can depend on all concentra-

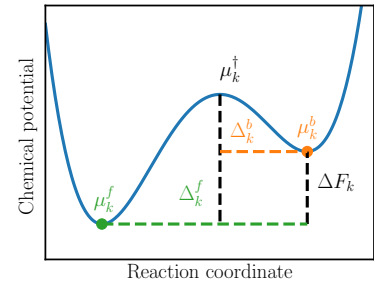


Figure 2.1: Schematic 1D representation of the chemical potential landscape in a reaction. The two stable states μ_k^f (green) and μ_k^b (orange) are connected along a one-dimensional minimum energy path via a saddle point μ_k^\ddagger (black). To jump from one state to another, thermal fluctuations have to overcome the energy barrier $\Delta_k^{f/b}$, which is proportional to the boltzmann factor $\exp(\Delta_k^{f/b}/k_B T)$ for high barriers $\Delta_k^{f/b} \gg k_B T$. In equilibrium the free energy difference between the states ΔF_k determines the probability ratio between product and reactant state via $\exp(\Delta F_k/k_B T)$.

tions, we will discuss only two special cases, either k is constant or it depends on the concentration of some catalyst or enzyme K , $k(\phi_K)$.

While the argument presented in [116] and TST are qualitatively different, the result is similar, Eq. 2.26 fulfills detailed balance by definition and is proportional to $\exp(\mu_f/b)$ as [116] proposed. Finally, we can write the total reaction flux of the k -th reaction as

$$s_k = k \exp\left(\frac{\mu_k^b}{k_B T}\right) \left[\exp\left(\frac{\Delta F_k}{k_B T}\right) - 1 \right]. \quad (2.27)$$

For ideal, dilute systems, where $\mu_i = \mu_{i,0} + \ln \phi_i$, Eq. 2.27 reduces to mass action reaction kinetics, where the forward and backward rate are proportional to the concentrations of products and reactants respectively

$$s_k = k_f \prod_i \phi_i^{\nu_{i,k}^f} - k_b \prod_i \phi_i^{\nu_{i,k}^b}. \quad (2.28)$$

Similar to diffusion, we recover the simple, well-known mass action kinetics for ideal, dilute solutions¹⁵. But we investigate interacting systems and in that case, diffusive fluxes have to be derived from chemical potential gradients and reaction rates from chemical potential differences.

Taking everything together the dynamics of incompressible, multicomponent, non-ideal, reactive mixtures are determined by a set of coupled partial differential equations of the form

$$\partial_t \phi_i = -\nabla \cdot \mathbf{j}_i + v_i \sum_k \nu_{i,k} s_k, \quad (2.29a)$$

$$\mathbf{j}_i = -\sum_{ij} \Lambda_{ij} \nabla \mu_j + \boldsymbol{\xi}_i, \quad \text{and} \quad (2.29b)$$

$$s_k = k \exp\left(\frac{\mu_k^b}{k_B T}\right) \left[\exp\left(\frac{\Delta F_k}{k_B T}\right) - 1 \right]. \quad (2.29c)$$

Here both dynamical processes, reaction, and diffusion, are driven by chemical potential differences. Reactions by differences between the left and right side of the reaction Eq. 2.23 and diffusion by chemical potential gradients. We will only consider simple conversion reactions of the form $A \rightleftharpoons B$, where $v_A = v_B = v$ and $|\nu_{i,k}| = 1$. Therefore, we absorb the volume v in s_k , such that in the following s_k is given in volume fraction change per time instead of particle number change per time.

15: The concentration dependence results directly from the chemical potential for constant rates k_f and k_b . Hence, unlike for diffusion, we do not need concentration dependent mobilities (rates) to arrive at the law of mass action.

2.3 Multicomponent regular solution theory

In Sec. 2.2 we have shown that the chemical potential μ_i is the driving force for reaction and diffusion processes. Therefore, to calculate μ_i , we need to specify the free energy F as a function of volume fraction ϕ_i . During most of this thesis we will use the multi-component form of the regular solution[109](Ch.2) and Flory-Huggins free energy[21–23], originally derived for a polymer-solvent mixture. It is based on a lattice model where each monomer and each solvent molecule occupy one lattice site and each particle interacts with the nearest neighbors, for a derivation see Appendix B. For the N -component case the free energy density and chemical potential are given by

$$\frac{v_0 f(\Phi)}{k_B T} = \sum_{i=1}^N \frac{\phi_i}{n_i} \ln(\phi_i) + h(\Phi), \quad (2.30)$$

$$\frac{\mu_i}{k_B T} = 1 + \ln(\phi_i) + h_i(\Phi), \quad (2.31)$$

where we write the free energy density in units of thermal energy $k_B T$ per lattice site volume v_0 and $\Phi = (\phi_1, \dots, \phi_N)^T$ is the volume fraction vector. The first term of f describes the **entropy density of mixing** N polymer species, where n_i is the number of i monomers in each polymer and we assume that all monomers occupy one lattice site¹⁶. The second term $h(\Phi)$ describes the **enthalpy density** containing the nearest neighbor interactions and internal energies. As described in Eq. 2.8 the chemical potential is the free energy change when adding an i polymer¹⁷ and $h_i(\Phi) = n_i \partial_{\phi_i} h(\Phi)$ is the energy per i polymer.

We use this free energy density because it has shown to be useful in the description of biomolecular condensates[6, 18] and it is one of the simplest free energy densities that shows phase separation[60]. In addition, all parameters have a clear physical meaning, e.g. interaction energies and polymer length[119] and allow to make qualitative predictions for experiments. Furthermore, unlike polynomial expansions, e.g. Ginzburg Landau type free energies[120], this form can be extended to multi-component mixtures in a straightforward manner[65] and to more complex systems, e.g. including electrostatic interactions[81]. Finally, it is used widely in soft matter physics[109] and polymer physics[119], so its properties and parameters are well known which makes it a good starting point. Of course, it is too simple to describe protein systems quantitatively, for example, it does not describe protein sequence and is based on a lattice model instead of continuous space. But, considering the simplifications, the model is surprisingly successful in describing the qualitative

¹⁶: Here the molecular volume introduced above is given by $v_i = n_i v_0$.

¹⁷: One could write the chemical potential per monomer as well, but as we keep the polymer length n_i fixed, the description in terms of polymers is more convenient.

behavior of biomolecular condensates[18, 60].

To use Eq. 2.30 we need to specify the enthalpy density $h(\Phi)$. If we include only energies per particle and two body nearest-neighbor interactions in the lattice model, the total energy is given by

$$h(\Phi) = \sum_{i=1}^N e_i \phi_i + \frac{1}{2} \sum_{i,j=1}^N e_{ij} \phi_i \phi_j \quad (2.32)$$

here the first term contains the internal energy of each particle type¹⁸ e_i and the second term describes interactions between i and j with (reciprocal) interaction strength $e_{ij} = e_{ji}$. A different path to derive the same result is to expand $h(\Phi)$ in Φ up to second order.

18: The internal energy itself contains both entropic $-Ts_i$ and enthalpic \bar{e}_i contributions, so $e_i = \bar{e}_i - Ts_i$. This can become important when discussing the temperature dependence of long polymers.

To discuss phase separation it is instructive to rewrite this in terms of relative pairwise interactions $\chi_{ij} = (2e_{ij} - e_{ii} - e_{jj})/2$, which describe how strong i and j interact compared to the self interactions of i and j and thus the propensity of i and j to mix ($\chi_{ij} < 0$) or demix ($\chi_{ij} > 0$). Using $\phi_i = 1 - \sum_{j \neq i} \phi_j$, we rewrite the pair interaction in Eq. 2.32 as

$$\begin{aligned} \sum_{i,j} \frac{e_{ij}}{2} \phi_i \phi_j &= \sum_{i,j \neq i} \frac{e_{ij}}{2} \phi_i \phi_j + \sum_i \left[\frac{e_{ii}}{2} \phi_i \left(1 - \sum_{j \neq i} \phi_j \right) \right] \\ &= \sum_i \frac{e_{ii}}{2} \phi_i + \sum_{i,j > i} \frac{2e_{ij} - e_{ii} - e_{jj}}{2} \phi_i \phi_j = \sum_i \frac{e_{ii}}{2} \phi_i + \sum_{i,j > i} \bar{\chi}_{ij} \phi_j \phi_i. \end{aligned} \quad (2.33)$$

Here $\bar{\chi}_{ii} = 0$ and $\bar{\chi}_{ij} = \bar{\chi}_{ji}$. In addition we can use incompressibility to eliminate one species from the effective description, as an example we replace the N -th species by using $\phi_N = 1 - \sum_{i=1}^{N-1} \phi_i$. For this we split the N -th species in Eq. 2.32 and assume that all sums over i and j run from 1 to $N-1$. Thus, Eq. 2.33 becomes

$$\frac{e_{NN}}{2} + \sum_i \frac{e_{ii} - e_{NN} + 2\bar{\chi}_{iN}}{2} \phi_i + \sum_{i,j} \frac{\bar{\chi}_{ij} - \bar{\chi}_{iN} - \bar{\chi}_{jN}}{2} \phi_j \phi_i \quad (2.34)$$

we can drop the term $e_{NN}/2$ because all processes are driven by derivatives of the free energy with respect to volume fractions. Taken together we can write the enthalpy in Eq. 2.32 which includes incompressibility and relative interactions up to second-order as

$$h(\Phi) = \sum_{i=1}^{N-1} w_i \phi_i + \frac{1}{2} \sum_{i,j=1}^{N-1} \frac{\chi_{ij}}{2} \phi_i \phi_j, \quad (2.35)$$

where now $w_i = e_i + \frac{e_{ii} - e_{NN} + 2\bar{\chi}_{iN}}{2}$ and $\chi_{ij} = \bar{\chi}_{ij} - \bar{\chi}_{iN} - \bar{\chi}_{jN}$, note that still $\chi_{ij} = \chi_{ji}$, but $\chi_{ii} = 0$ is **not** necessary.

Influence of protein size

While we will assume equal molecular volume of all species during this thesis, we kept the molecular volume till now because it is an important future direction of research in biomolecular condensates. The reason is, that proteins and RNA, which are the drivers of most condensates, can be very long biopolymers[1]. For example, in Ref.[16] a temperature dependent molecular volume is necessary to correctly describe their experiments.

In the Flory-Huggins free energy, (2.30), the role of protein length can be seen by comparing the enthalpic contribution, Eq. 2.35, to the entropic contribution, first term in Eq. 2.30. The enthalpic contribution is independent of protein size because the individual monomers all interact in the same way¹⁹. Thus, it does not matter how the monomers are arranged in a mean field model. Conversely, the entropic contribution depends inversely on the length of the protein. The reason is, that a protein consisting of n_i monomers occupies n_i adjacent lattice sites. Thus, the number of possible arrangements, and thereby the entropy of mixing, is reduced significantly. As a result, increasing the size of proteins will decrease the magnitude of the entropy, while it leaves the enthalpy unaltered. In the limit of large biopolymers, e.g. some DNA and RNA, the entropic contribution vanishes, and the interactions between molecules fully determine the free energy.

Although including molecule sizes will become an important extension in the future, in this thesis we discuss the simple case of equal molecular volumes only, $v_i = v_0$ for all i , where v_0 is the volume of a lattice site.

¹⁹: This is different for proteins, which are not made of a single monomer. Instead, proteins are made of different amino acids and are described by the sequence of these amino acids. A polymer model developed in Refs.[121, 122] allows individual monomers of a polymer/protein to interact differently. This concept has been applied to protein phase separation successfully, for example in Ref.[56].

Non-local interactions

In Eq. 2.1 we introduced the free energy density $f(\Phi, \nabla\Phi)$ that can depend on local volume fraction and its gradients, but so far we have only discussed the local term. Here we want to introduce the dependence of the free energy density on $\nabla\Phi$. One way to include non-local terms is to expand f in terms of gradients of Φ [123] around a homogeneous composition. In this case the linear term vanishes, because $\nabla\phi_i$ is a vectorial quantity, but f is a scalar. Thus, we get, including terms up to $\mathcal{O}((\nabla\Phi)^2)$

$$f(\Phi, \nabla\Phi) \approx f_0(\Phi) + \frac{1}{2} \sum_i \frac{\partial f}{\partial(\nabla^2\phi_i)} \nabla^2\phi_i + \frac{1}{2} \sum_{i,j} \frac{\partial^2 f}{\partial(\nabla\phi_i)\partial(\nabla\phi_j)} (\nabla\phi_i)(\nabla\phi_j) + \mathcal{O}(\nabla^4\phi), \quad (2.36)$$

where $f_0(\Phi)$ is the local free energy density discussed above and in the gradient expansion assumes that the composition varies on length scales large compared to inter-molecular distances[123], which is necessary for the mean-field approximation discussed above as well. Using the divergence theorem, we rewrite the $\nabla^2\phi_i$ term in terms of $(\nabla\phi_i)^2$ and a boundary term that vanishes for no-flux boundary conditions. In addition we call the expansion coefficient $\kappa_{ij} = \frac{\partial^2 f}{\partial(\nabla\phi_i)\partial(\nabla\phi_j)} - \delta_{ij} \frac{\partial^2 f}{\partial\phi_i\partial(\nabla^2\phi_i)}$ and end up with

$$f(\Phi, \nabla\Phi) \approx f_0(\Phi) + \frac{1}{2} \sum_{i,j} \kappa_{ij} (\nabla\phi_i)(\nabla\phi_j). \quad (2.37)$$

For a binary regular solution Cahn and Hilliard[123] found $\kappa = \chi v_0^{2/d}$, here v_0 is the volume per lattice site in a d dimensional cubic lattice and thus $v_0^{1/d}$ is the nearest neighbor distance. As one might expect the gradient term is determined by a combination of the relevant interaction energy χ and the relevant length scale $v_0^{1/d}$ and strong composition gradients increase the total free energy²⁰. An extension to multicomponent systems[65] with a constant lattice volume v_0 results in $\kappa_{ij} = -v_0^{2/d} \chi_{ij}$, which is the form we use in our simulations. From Eq. 2.37 we calculate the non-local contribution to the chemical potential defined by Eq. 2.8

$$\mu_i = v_i [\partial_{\phi_i} f_0 + \sum_j \kappa_{ij} \nabla^2 \phi_j], \quad (2.38)$$

where we assume κ_{ij} is constant, which is the case for our choice $\kappa_{ij} = -v_0^{2/d} \chi_{ij}$, but κ can, in general, be a function of composition, temperature, etc.²¹.

While studying the effect of the gradient term is an interesting topic on its own, e.g. to understand the ordering of multiple phases[66], wetting[125, 126] or late-stage coarsening in an emulsion of droplets[60], in our model the gradient term is necessary to introduce a surface tension γ , stabilize the interface between the two phases, and introduce a specific interface width w . We are mainly interested in the effect of chemical reactions in the bulk phases with low concentration fluctuations and by definition, the gradient term is non-zero only for spatially varying volume fractions. So it vanishes in the bulk phases and only contributes close to the interface region as we will see below.

2.4 Liquid-liquid phase separation

In the last section, we introduced the multi-component free energy we will use in this study. Here we discuss the simplest case, a binary system, and an extension to three components and

20: For a binary polymer blend of large polymers ($n \gg 1$) one gets an extra entropic contribution $\kappa = a^2/(36\phi(1-\phi))$ where na^2 is the mean square polymer chain length[19, 124].

21: To describe more realistic (bio-)polymers details about the polymer structure and the role of fluctuations descriptions beyond mean-field are necessary[124].

see under which conditions a purely diffusive system will phase separate and why.

Binary Phase Separation

The minimum example showing liquid-liquid phase separation is a binary system, in our case a protein B and a solvent C ; see fig. 2.2 for a schematic. We write $\phi = \phi_B$ for simplicity and incompressibility requires $\phi_C = 1 - \phi$. In addition we write $\chi_{BC} = \chi$ and $\kappa_{BC} = \kappa = v_0^{2/d} \chi$ so we obtain for the free energy density Eq. 2.30 and chemical potential Eq. 2.31

$$\frac{v_0 f(\phi)}{k_B T} = \phi \ln(\phi) + (1 - \phi) \ln(1 - \phi) + \chi \phi(1 - \phi) + \frac{\kappa}{2} (\nabla \phi)^2, \quad (2.39)$$

$$\frac{\mu}{k_B T} = \ln \frac{\phi}{1 - \phi} + \chi(1 - 2\phi) - \kappa \nabla^2 \phi, \quad (2.40)$$

we set the internal energy to zero as well, $w = 0$, as terms linear in ϕ become relevant when reactions are present only. We used incompressibility to replace ϕ_C already and thus Eq. 2.40 is the exchange chemical potential introduced in the discussion about diffusive fluxes above. The free energy in Eq. 2.39 contains an entropic, an enthalpic, and a non-local contribution. The entropic contribution $-v_0 s(\phi)/k_B = \phi \ln(\phi) + (1 - \phi) \ln(1 - \phi)$ attains its minimum value at $\phi = 0.5$ where $-v_0 s(0.5)/k_B \approx 0.5 \ln(0.25)$ independent of parameters and thus favors mixing in all cases; see fig. 2.3. The enthalpic part $v_0 h(\phi) = k_B T \chi \phi(1 - \phi)$ forms a parabola with an extremum at $\phi = 0.5$, where $v_0 h(0.5) = 0.25 k_B T \chi$, which is a minimum for $\chi < 0$ and a maximum for $\chi > 0$; see fig. 2.3. This means it favors demixing only for $\chi > 0$ and mixing for $\chi < 0$. Thus for phase separation $\chi > 0$ is necessary and we will discuss this case only. For now we assume that the volume fraction fluctuations in the bulk phases are small, in addition the bulk phases are assumed large compared to the interface region, so the non-local term is negligible here, but it will become important later.

Phase separation can only happen if the total free energy $F = \int_V f dV$ is lower in the phase-separated state than in the homogeneous mixture. For an average volume fraction $\bar{\phi} = \int_{V_{\text{sys}}} \phi dV$ the homogeneous free energy is $F_h = V_{\text{sys}} f(\bar{\phi})$. A simple graphical analysis of fig. 2.3 suggests that in the two-phase state with compositions (ϕ_1, ϕ_2) given by the free energy minima (blue dots) where $f(\phi_1) = f(\phi_2) = f_{\text{min}}$, the free energy density is lower by $\Delta f = f(\bar{\phi}) - f_{\text{min}}$ (black dashed line) compared to the homogeneous mixture. Thus, the total free energy is lower by $\Delta F = V_{\text{sys}} \Delta f$. For this specific example, this

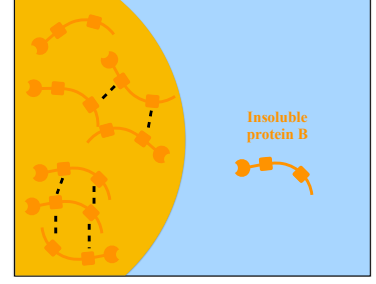


Figure 2.2: Schematic representation of a protein forming droplets due to enthalpic interactions. In this example, a Protein B (orange particles) interacts attractively with itself (black dashed lines) and forms protein-rich droplets (orange area) inside the solvent C (blue area). Attractive interactions are not necessary for phase separation, repulsion between protein and solvent works as well. But in most biomolecular condensates, attractive multivalent interactions lead to phase separation[56]

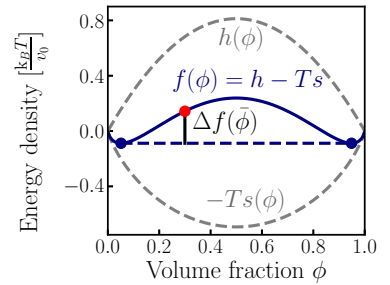


Figure 2.3: Free energy density of an interacting binary mixture. The free energy density $f(\phi)$ (blue line; Eq. 2.39) has an entropic contribution $-T s = \phi \ln(\phi) + (1 - \phi) \ln(1 - \phi)$ (lower grey dashed line) that always favors mixing and an enthalpic contribution $h = \chi \phi(1 - \phi)$ (upper grey dashed line) that favors demixing for $\chi > 0$ (here $\chi = 3.25$). Due to the competition between these two effects, f shows two local minima (blue dots) for high enough $\chi > \chi_c$, where χ_c is the critical interaction strength. In this case the free energy of the phase separated state is lower than the mixed state by $V \Delta f$ (black line) for a given average fraction $\bar{\phi}$ (red dot).

simple equilibrium analysis works qualitatively, although we neglected interface tension. For general free energies, the analysis is more complicated and the above analysis is misleading because the free energy minima are **not** the equilibrium volume fractions of the phases in general. Instead one generally minimizes the full free energy with respect to all independent variables, which we will do next.

Maxwell construction

For constant temperature and total volume, Gibbs's phase rule allows only two phases or one. Therefore, we can describe the phase-separated state in terms of the volume fractions ϕ_1, ϕ_2 and total volumes V_1, V_2 of each phase and write the total free energy as²² $F = V_1 f(\phi_1) + V_2 f(\phi_2)$. In addition, constant system volume $V_1 + V_2 = V_{\text{sys}}$ and mass conservation $V_1 \phi_1 + V_2 \phi_2 = V_{\text{sys}} \bar{\phi}$ restrict the free parameters from 4 to 2[60]. To find the equilibrium state we minimize F with respect to ϕ_1 and V_1 , which results in the two conditions

$$\frac{\partial F}{\partial \phi_1} = V_1(\mu(\phi_1) - \mu(\phi_2)) = 0, \quad \text{and} \quad (2.41a)$$

$$\frac{\partial F}{\partial V_1} = f(\phi_1) - f(\phi_2) + \phi_2 \mu(\phi_2) - \phi_1 \mu(\phi_1) = 0. \quad (2.41b)$$

The conditions above are always fulfilled for the homogeneous mixture ($\phi_1 = \phi_2$)²³. For interacting systems, it is possible to find two phases with different compositions ($\phi_1 \neq \phi_2$) that fulfill the conditions²⁴. In this case, the first condition, equal chemical potential in both phases, ensures that the free energy can not be reduced by moving particles between phases. The second condition is related to the osmotic pressure $\Pi = -(\partial F / \partial V_{\text{sys}})_{N_i}$ and makes sure there is no pressure difference between the two phases, $\Pi_1 - \Pi_2 = 0$ [60]. Since the total volume V_{sys} is constant, the volume of one phase can only be increased ($+f(\phi_1)$) at the expense of the other ($-f(\phi_2)$). At the same time mass conservation implies that particles from the expanding phase ($-\phi_1 \mu(\phi_1)$) have to be moved to the shrinking phase $\phi_2 \mu(\phi_2)$, which changes the composition in both phases. Equilibrium is reached when this process can not decrease the total free energy anymore.

In general, the solution of Eq. 2.41 has to be determined numerically, but for the simple binary regular solution free energy Eq. 2.39 we can use that the symmetry around $\phi = 0.5$, so $f(\phi) = f(1 - \phi)$ and $\mu(\phi) = -\mu(1 - \phi)$ to find a solution. As a result, the solution of Eq. 2.41 is given by $\phi_1 = 1 - \phi_2$ and $\mu(\phi_1) = 0$ and we obtain the **equilibrium volume fractions** (ϕ_1, ϕ_2) by finding the minima of $f(\phi)$ ²⁵. In binary systems there is a simple graphical interpretation of Eq. 2.41. The first

22: For now we assume that the volumes V_1 and V_2 are large so the interface energy is negligible compared to the bulk[60].

23: For ideal systems this is the only solution because μ increases monotonically with increasing ϕ and the first condition can not be fulfilled for $\phi_1 \neq \phi_2$.

24: Neither condition is influenced by linear terms in ϕ , which shows again that the diffusive equilibrium is independent of w_i terms in Eq. 2.35

25: It is important to keep in mind that this is not a general property of phase separation, which can be seen by adding a term $w\phi$ to f , this does change the positions of the minima, but it leaves the equilibrium construction unaltered.

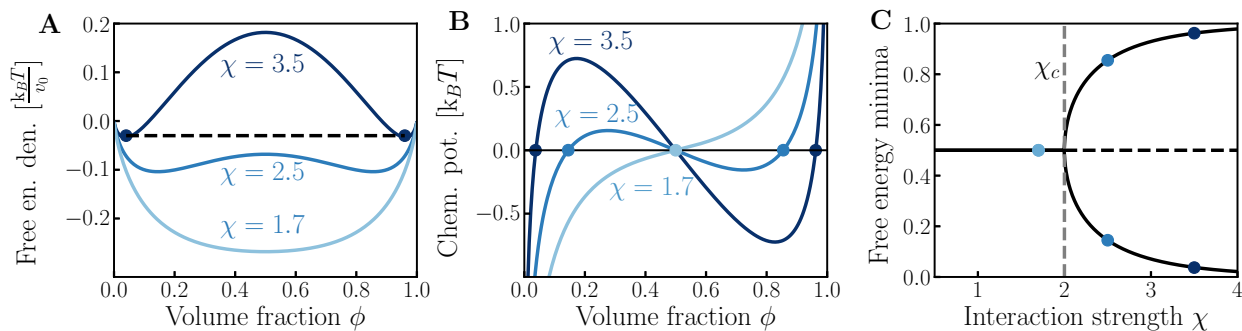


Figure 2.4: Phase separation behavior for binary mixtures. (A) Free energy density f Eq. 2.39 for different interaction strength χ . For low χ (light blue line) f has only one minimum at $\phi = 0.5$ and the homogeneous mixed state is always stable. For stronger χ two minima emerge and phase separation becomes energetically favorable (dark blue lines). The composition of the two phases is given by the free energy minima, which are connected by a common tangent (black dashed line). (B) Corresponding chemical potential; Eq. 2.40. In the region where phase separation is possible, the slope of the chemical potential changes sign, and for the free energy density in Eq. 2.39, the equilibrium compositions correspond to $\mu = 0$. (C) The free energy minima (stable, full lines) and maxima (unstable, dashed line) are fixed points of the system. At $\chi_c = 2$ the system undergoes a supercritical pitchfork bifurcation and two minima emerge in (A). For $\chi > \chi_c$ it is energetically favorable to phase separate into two phases and the composition of these phases is given by the free energy minima. That the free energy minima correspond to the equilibrium fractions in the phase separated state is a specific property for this free energy; see discussion in the text.

condition corresponds to equal slope of f in both phases and the second condition implies that a linear function with slope $\mu(\phi_1)$ starting at $f(\phi_1)$ intersects $f(\phi_2)$ as well; see dashed line in fig. 2.3. This construction works if Eq. 2.39 shows an inflection point and $\partial_\phi^2 f < 0$, which depends on the interaction parameter χ . As discussed before, for $\chi < 0$ the interaction favors mixing and no phase separation is possible. But fig. 2.4(A) shows that even for $\chi > 0$ the free energy does not necessarily favor phase separation. Instead, only above a critical interaction strength χ_c , two minima emerge and phase separation becomes energetically favorable over the homogeneous state. In fig. 2.4(B) the corresponding chemical potential is shown and the condition Eq. 2.41a can be fulfilled for $\chi > \chi_c$ only. fig. 2.4(C) shows how the two minima appear in a pitchfork bifurcation at $\chi = \chi_c$ and how the equilibrium fractions (ϕ_1, ϕ_2) move asymptotically towards $(0, 1)$ as $\chi \rightarrow \infty$. This limit corresponds to very strong enthalpic interactions (or very long polymers) so entropy is negligible[127].

In this study we will use the strong interaction regime, $\chi \gg \chi_c$, to avoid critical phenomena close to the critical point, e.g. strong concentration fluctuations and divergences of thermodynamic quantities[35].

Kinetics

Above we used an equilibrium construction to see that phase separation is energetically favorable for interaction strength $\chi > \chi_c$.

In this subsection, we discuss how the system reaches this equilibrium state dynamically using the evolution equation derived in sec. 2.2. For simplicity we assume constant diffusive mobility Λ . Then the dynamics are given by

$$\partial_t \phi = \Lambda \nabla^2 \mu. \quad (2.42)$$

Obviously all spatially constant chemical potentials $\mu(\mathbf{r}) = \text{const.}$ are steady states and thus the homogeneous concentration $\phi(\mathbf{r}) = \bar{\phi}$ is always a steady state, although the phase separated state is favorable for $\bar{\phi} \in [\phi_1, \phi_2]$. For non-zero temperature, thermal noise ξ is present in the diffusive flux, which induces spatial inhomogeneities. To determine whether small fluctuations can move the system from the homogeneous mixture to the phase separated state, we perform a linear stability analysis. The idea is to consider the system without noise $\xi = 0$ and introduce a perturbation $\delta\phi$ using plane waves in space²⁶ and an exponential growth rate in time, $\delta\phi = \epsilon \exp(\omega t + i\mathbf{k}\mathbf{r})$, where the amplitude is small, $\epsilon \ll 1$. We write the perturbed state for each wave vector k as $\phi(\mathbf{r}, t) = \bar{\phi} + \delta\phi$, where $\delta\phi = \epsilon \exp(\omega t + i\mathbf{k}\mathbf{r})$, and check whether the perturbation grows ($\omega > 0$) or shrinks ($\omega < 0$) in time. Since the amplitudes ϵ are small, we can expand μ around the homogeneous state $\mu(\phi) \approx \mu(\bar{\phi}) + (\partial_\phi \mu)|_{\bar{\phi}} \delta\phi + k^2 \kappa \delta\phi$. Writing $\delta\mu(\bar{\phi}) = (\partial_\phi \mu)|_{\bar{\phi}}$ the resulting equation for the growth rate $\omega(k)$ is²⁷

$$w = -\Lambda k^2 [\delta\mu(\bar{\phi}) + k^2 \kappa] = -w_0 v_0^{2/d} k^2 \left[\frac{\delta\mu(\bar{\phi})}{\chi} + v_0^{2/d} k^2 \right], \quad (2.43)$$

where $w_0 = \Lambda \chi v_0^{d/2}$ is the inverse characteristic time to diffuse one lattice length $v_0^{1/d}$ for a regular solution model (Eq. 2.40). As $k^2, \kappa > 0$ (for $\chi > 0$) to get positive growth rates the factor $\delta\mu$, which corresponds to the slope of μ or the curvature of f , has to be negative. In addition, even for negative $\delta\mu$ the κ term stabilizes all perturbations on length scales smaller than $\sqrt{-\kappa/\delta\mu}$, because $w < 0$ for $k^2 > -\delta\mu/\kappa$. As $w(k=0) = 0$, for $\delta\mu < 0$ a band of unstable modes $k \in]0, \sqrt{-\delta\mu/\kappa}[$ exists and the wavevector $k_{\text{max}} = \sqrt{-\delta\mu/(2\kappa)}$ has the fastest growth rate, so we expect to see a length scale $1/k_{\text{max}}$ for early times.

The necessary condition for linear instability of the homogeneous state is $\delta\mu(\bar{\phi}) < 0$. Comparing this to fig. 2.4(B) clearly all perturbations are stable if there is only one minimum in the free energy ($\chi < \chi_c$) as $\delta\mu(\bar{\phi}) > 0 \forall \bar{\phi}$, but even for $\chi > \chi_c$ the growth rate is not positive for all $\bar{\phi} \in [\phi_1, \phi_2]$, but only for a small subset $\bar{\phi} \in [\phi_s, 1 - \phi_s]$, enclosed by the **spinodal** volume fraction ϕ_s ; see fig. 2.5. These are defined by $\partial_\phi \mu = 0$,

26: Plane waves are used, because the differential operator becomes a simple factor $i\mathbf{k}$, $\nabla \delta\phi = i\mathbf{k} \delta\phi$, which simplifies the calculations significantly. The cost is that every wavevector \mathbf{k} has to be discussed separately in general.

27: Because only even derivatives appear, only the absolute value of the wavevector matters $k = |\mathbf{k}|$. This is expected for isotropic systems, as there is no preferred direction.

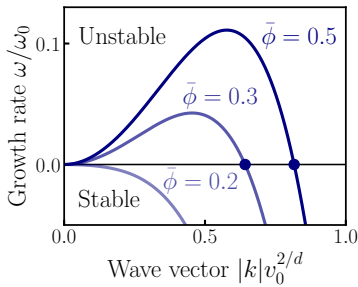


Figure 2.5: Perturbation growth rate for different average protein fraction. Perturbation growth rate ω as a function of wave vector $|k|$. For the free energy in Eq. 2.39. The homogeneous state $\bar{\phi}$ is unstable ($\omega > 0$) only for $\bar{\phi} > 0.25$. In this case a band of wave vectors limited by $k_{\text{min}} = 0$ and $k_{\text{max}} = \sqrt{-\delta\mu/\kappa}$ (blue dots) is unstable. This range is maximal for $\bar{\phi} > \phi_b$ (Eq. 2.44), where $\delta\mu = 4 - 2\chi$. So $\chi > \chi_c = 2$ (here $\chi = 3$) is necessary for the existence of unstable modes.

which for the simple free energy above results in the dashed line in fig. 2.6 and analytically

$$\phi_s = \frac{1}{2} \left(1 - \sqrt{1 - \frac{2}{\chi}} \right). \quad (2.44)$$

As a result, for average volume fractions $\bar{\phi} \in [\phi_1, \phi_s] \cup [1 - \phi_s, 1 - \phi_1]$ the homogeneous state is linearly stable, but phase separation is still energetically favorable compared to the homogeneous state. In this case, there is an energy barrier ΔE_{nuc} between the homogeneous and phase separated state that has to be crossed. The energy barrier vanishes as the average concentration approaches ϕ_s (or $1 - \phi_s$) and phase separation happens spontaneously. If $\bar{\phi}$ is close to the equilibrium volume fraction ϕ_1 or ϕ_2 , the energy barrier is large and the nucleation time τ_{nuc} can be approximated by the boltzmann factor of the nucleation barrier $\tau_{\text{nuc}} \propto \exp(\Delta E_{\text{nuc}}/(k_B T))$ according to classical nucleation theory[128].

A thorough investigation of the role of chemical reactions on nucleation is beyond the scope of this work, albeit it is an interesting topic on its own. We will therefore start with initial conditions where a small droplet of the dense phase is already present and thus circumvent the nucleation problem artificially. Alternatively, we will simulate systems in the spinodal region ($1 - \phi_s > \phi > \phi_s$), where small numerical errors grow exponentially and lead to phase separation.

Interface properties

We have shown that phase separation is energetically favorable for high enough interaction strength (fig. 2.4) and that the homogeneous state can be unstable or stable against small perturbations depending on the interaction and total amount of protein (fig. 2.5), but we have not discussed the interface between the two phases in a steady-state yet. This has been done for general forms of the free energy density as well as the regular solution as an example in the paper by Cahn and Hilliard already[123]. In the interface region the non-local κ term becomes dominant and penalizes strong concentration variations, because $\frac{\kappa}{2}(\nabla\phi)^2 \geq 0$. This effect counteracts the tendency of the local free energy density to form an infinitely thin interface and introduces a specific interface width w and an interface tension γ that depend on κ and χ .

Again we introduce the general idea to calculate w and γ and then give the specific results for the regular solution theory. Assume a one dimensional system with an interface at position $x = 0$ where $\phi(x \rightarrow -\infty) = \phi_1$ and $\phi(x \rightarrow \infty) = \phi_2$.

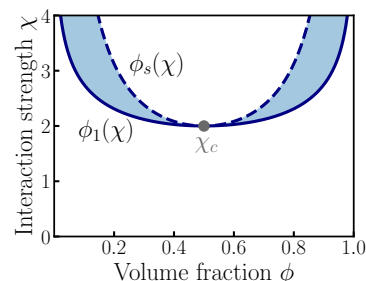


Figure 2.6: Phase separation happens spontaneously for intermediate average volume fractions only. Phase diagram as a function of interaction strength χ . Above the critical interaction χ_c phase separation into a phase with composition ϕ_1 and $1 - \phi_1$ (blue full line) is energetically favorable. But the homogeneous state is unstable against perturbations only in the dark blue region, where $\bar{\phi} \in [\phi_s, 1 - \phi_s]$ (dashed blue line) determined by Eq. 2.44. In the light blue region a nucleation barrier has to be overcome to induce phase separation.

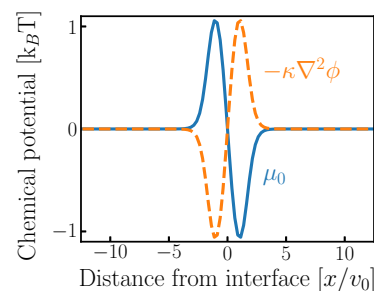


Figure 2.7: One dimensional chemical potential profile for a phase-separated state with interface at $x = 0$. The local (blue line) and nonlocal (dashed orange line) contributions to the chemical potential both vanish in the bulk phases ($|x| > 5$). In the interface region, they are both non-zero, but they cancel each other in equilibrium. Here a regular solution model for $\chi = 4$ is used.

Then, in thermodynamic equilibrium, the exchange chemical potential has to be uniform in space $\mu(x) = \mu_0(\phi_1) = \mu_0(\phi_2)$, where we write the chemical potential up to $\nabla^2\phi$ terms as $\mu = \mu_0(\phi) - \kappa\nabla^2\phi = \mu_0(\phi_1)$ (see Eq. 2.38) with the purely local part $\mu_0(\phi) = \partial_\phi f_0$. We thus have to solve the differential equation

$$\mu(\phi(x)) - \mu_0(\phi_1) = \kappa\nabla^2\phi(x), \quad (2.45)$$

with $\phi(x \rightarrow -\infty) = \phi_1$ and $\phi(x \rightarrow \infty) = \phi_2$ as boundary conditions. fig. 2.7 shows how the contribution of μ_0 and $\nabla^2\phi$ cancel everywhere and allow a homogeneous chemical potential even in the interface region. Analytically, the solution for generic symmetric double-well type free energies is well described by

$$\phi(x) = \frac{1}{2} \left[(\phi_2 + \phi_1) + (\phi_2 - \phi_1) \tanh \frac{x}{w} \right], \quad (2.46)$$

where the **interface width** w can be approximated for the regular solution theory by $w \approx v_0^{1/d} \sqrt{\frac{\chi}{\chi-2}}$ [60]. In the strong interaction limit ($\chi \gg \chi_c$) w coincides with the lattice volume²⁸; see fig. 2.8 for a comparison between simulation and Eq. 2.46 for the regular solution.

The interface energy $A\gamma$, with surface area A and **surface tension** γ , is defined as the energy difference between the total free energy derived from an equilibrium field $\phi(\mathbf{r})$, $F_I = \int_{V_{\text{sys}}} f(\phi) dV$ and a hypothetical perfectly phase-separated system without an interface $F_0 = V_1 f(\phi_1) + V_2 f(\phi_2)$, $A\gamma = F_I - F_0$. As an example consider a two dimensional flat interface of area A perpendicular to the x direction at $x = 0$, where the dilute phase is on the $x < 0$ side and the dense phase on the $x > 0$ side. Then the interface energy is given by

$$A\gamma = \int_{-\infty}^0 f(\phi(x)) - f(\phi_1) dx + \int_0^{\infty} f(\phi(x)) - f(\phi_2) dx. \quad (2.47)$$

The interface energy has two contributions, first the integral over the gradient term, $\int_{V_{\text{sys}}} \frac{\kappa}{2} (\nabla\phi)^2 dV$ and second a contribution from the deviation of the local free energy density from the equilibrium values $\Delta f_1 = f(\phi) - f(\phi_1)$ and $\Delta f_2 = f(\phi) - f(\phi_2)$ (this corresponds to Δf in fig. 2.2). This integral can be evaluated numerically or by expanding the free energy density around the critical point [123]. For the strong interaction limit (or far away from the critical point) Cahn and Hilliard [123] find (in our notation) $\gamma \approx \frac{\pi}{2\sqrt{2}} v_0^{-2/d} \chi k_B T$ using numerical techniques to solve the integral, similarly Mao et. al. [65] find $\gamma \approx \frac{\pi}{4} v_0^{-2/d} \chi k_B T$ for multiple phases, if each phase is dominated by one component.

28: As one would expect the interface can not be smaller than the smallest length scale in our theory

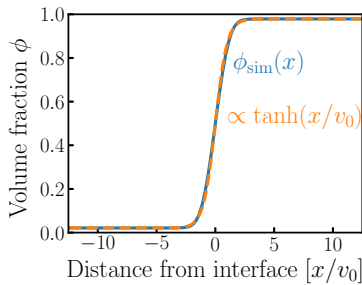


Figure 2.8: One dimensional interface in the phase separated state for a binary regular solution. The steady state profile $\phi(x)$ (blue) in a simulation of Eq. 2.42 is well described by a $\tanh(x/v_0)$ function (orange dashed line, in 1D systems v_0 is a length) in the strong interaction limit, here $\chi = 4$.

To summarize, the gradient term introduces a stable interface width $w \approx v_0^{1/d}$, which corresponds approximately to the lattice length scale for strong interactions. We, therefore, use $w = v_0^{1/d}$ as the length scale for all further problems. This is a convenient choice for simulations as well because a spatial resolution $dx \lesssim w$ is necessary and sufficient for numerical stability. A result of the stable interface is an extra interface energy $A\gamma$ determined by the interface tension γ and the geometry of the interface A . $A\gamma$, as defined in Eq. 2.47, has two contributions, one from the gradient term and one from the local free energy change across the interface. Notably for spherical interfaces with radius R the curvature introduces a Laplace pressure $p_L \propto \gamma/R$, which changes the equilibrium concentrations in droplet and solvent phase[60] and leads to coarsening of multiple droplets via Ostwald ripening[87]. While chemical reactions at interfaces are an important topic[129], we are mostly interested in bulk reactions here and the contribution of the interface region to reactions is negligible in our study.

Ternary Free Energy

If we want to discuss thermodynamically consistent reactions (Eq. 2.27) the binary description introduced above is insufficient, because reactions convert particles and thus break conservation of average volume fraction²⁹. As a result the system relaxes into a homogeneous state, where the average volume fraction corresponds to the free energy minimum. The dynamics correspond to a combination of Allen-Cahn and Cahn-Hilliard or model A and model B dynamics in the classification of Hohenberg and Halperin[35]. Thus to discuss equilibrium phase separation with reactions we need at least three species. We therefore introduce a second protein species A and extend the binary free energy Eq. 2.39 to the ternary case (using $\phi_C = 1 - \phi_A - \phi_B$)

29: If reactions are present, the two species are not independent of each other and the system has one degree of freedom less, so Gibbs phase rule permits only one phase for binary systems with reactions between the two species.

$$\begin{aligned} \frac{v_0 f}{k_B T} = & \phi_A \ln(\phi_A) + \phi_B \ln(\phi_B) + (1 - \phi_A - \phi_B) \ln(1 - \phi_A - \phi_B) \\ & + w_A \phi_A + w_B \phi_B + \chi_{AB} \phi_A \phi_B + \chi_{AC} \phi_A \phi_C + \chi_{BC} \phi_B \phi_C \\ & - v_0^{2/d} (\chi_{AB} \nabla \phi_A \nabla \phi_B + \chi_{AC} \nabla \phi_A \nabla \phi_C + \chi_{BC} \nabla \phi_B \nabla \phi_C), \end{aligned} \quad (2.48)$$

where χ_{ij} is the interaction strength between species i and j . We omitted the internal energy of the solvent because it does not react in our model. In addition, we now get two chemical potentials, one for A and one for B , but both chemical potentials are exchange chemical potentials with respect to C , i.e. $\mu_A = \delta F / \delta N_A - \delta F / \delta N_C$. The chemical potentials are given

by

$$\frac{\mu_A}{k_B T} = \ln \frac{\phi_A}{1 - \phi_A - \phi_B} + w_A + \chi_{AB}\phi_B + \chi_{AC}(1 - 2\phi_A - \phi_B) + \bar{\chi}\nabla^2\phi_B - \chi_{AC}\nabla^2\phi_A, \quad \text{and} \quad (2.49a)$$

$$\frac{\mu_B}{k_B T} = \ln \frac{\phi_B}{1 - \phi_A - \phi_B} + w_B + \chi_{AB}\phi_A + \chi_{BC}(1 - \phi_A - 2\phi_B) + \bar{\chi}\nabla^2\phi_A - \chi_{BC}\nabla^2\phi_B. \quad (2.49b)$$

where $\bar{\chi} = \chi_{AB} - \chi_{BC} - \chi_{AC}$. Due to multiple interaction parameters χ_{ij} a ternary solution allows more complex behaviour, e.g. multiple phases[65, 66] and composition dependent equilibrium concentrations[18]. But the conditions for phase separation presented for the binary case still hold. We get one more condition, mass conservation of species A , and one more parameter $\phi_{A,1}$, to minimize F . But also Gibbs phase rule now allows up to three phases³⁰, which results in $\mu_A(\phi_{A,1}, \phi_{B,1}) = \mu_A(\phi_{A,2}, \phi_{B,2}) = \mu_A(\phi_{A,3}, \phi_{B,3})$.

In this study, we want to investigate the specific case where B phase separates from C , while the transition between A and B can control phase separation. Therefore we restrict the interactions in the following way:

1. Phase separation happens mainly due to B interactions with C ; $\chi = \chi_{BC} > \chi_c$
2. The total amount of proteins is low compared to the solvent; $1 > \bar{\phi}_C \gg \bar{\phi}_A + \bar{\phi}_B$
3. A does not phase separate from the solvent on its own; $\chi_{AC} \ll \chi_c$.

While this still leaves considerable freedom, for example, whether A predominantly partitions into the solvent phase ($\chi_{BC} > \chi_{AC}$) or droplet phase ($\chi_{AC} > \chi_{BC}$) phase, we will discuss two example cases that simplify the calculations while the results are qualitatively the same for other choices as long as the above conditions are fulfilled. In the first case A does not interact at all; $\chi_{AC} = \chi_{BC} = 0$, while in the second case A interacts the same way as C ; $\chi_{AB} = \chi_{BC} = \chi$ and $\chi_{AC} = 0$, thus

$$h(\phi_B, \phi_A) = \chi\phi_B(1 - \phi_B - \phi_A), \quad \text{and} \quad (2.50a)$$

$$h(\phi_B) = \chi\phi_B(1 - \phi_B). \quad (2.50b)$$

The advantage of these two cases³¹ can be seen from fig.2.9, if A does not interact with C or B , A is approximately homogeneously distributed, given by $\bar{\phi}_A = \int_{V_{\text{sys}}} \phi_A dV$ and it just rescales the incompressibility condition³² $\phi_C = 1 - \phi_B - \bar{\phi}_A$; see the horizontal tie lines in fig.2.9A. Importantly no phase separa-

30: This is true for the N component case as well, where F has to be minimized with respect to $N - 1$ species and N phase volumes in the incompressible case. Although this reduces again if chemical reactions are present, because reactions introduce new conservation laws and the species are not independent of each other anymore.

31: In both cases a term linear in ϕ_B appears, which can be included in the w_B term as well. It appears when incompressibility is used for $\chi\phi_B\phi_C$ and does not influence phase separation. But we keep it because it is the familiar form of a regular solution theory.

32: Due to reactions $\bar{\phi}_A(t)$ is a function of time though.

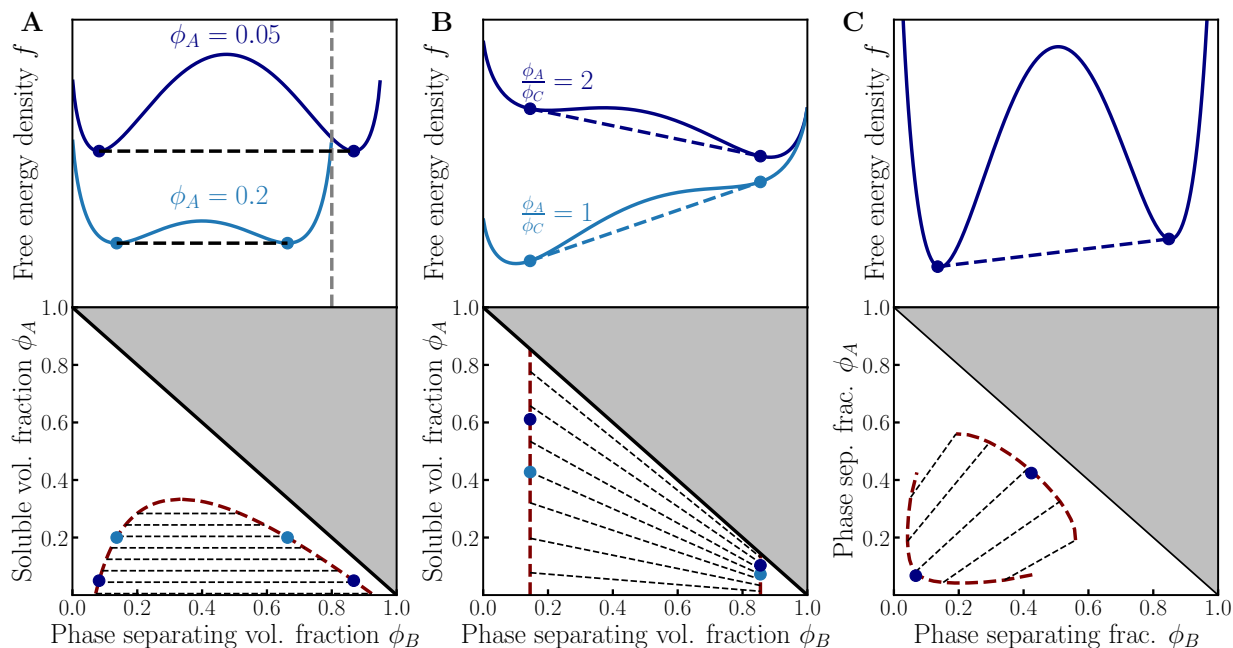


Figure 2.9: Ternary phase diagram for different interactions of A . The top row shows three examples of effective free energies as a function of ϕ_B while the bottom panels show the regions where phase separation is favorable (enclosed by maroon dashed lines) in the $\phi_A - \phi_B$ phase space. In the grey area $\phi_A + \phi_B > 1$, which violates incompressibility. **A** A does not interact with B or C and thus distributes homogeneously in both phases (horizontal tie lines in the lower panel); Eq. 2.50a. Above a critical amount of A phase separation is suppressed, because the remaining B - C interaction is too weak. Here, $\chi = 2.5$. **B** If A interacts like C , Eq. 2.50b, we can write an effective free energy where the ratio ϕ_A/ϕ_C is constant (top panel). In this case, the ternary system effectively behaves like the binary one and the equilibrium volume fractions of the phase-separated state become independent of the total amount of A (bottom panel). Here, $\chi = 3$. **C** A and B interact attractively while C is neutral (does not interact). In this case, phase separation is favorable only if enough A and B are present. The tie lines have positive slope, which indicates attractive interactions. Here, $\chi = -10$ and the free energy density has been modified by a linear term $6.5\phi_+$ to show the double well form of the free energy. This has no effect on the phase separation behavior.

tion happens above a certain amount of A , because it takes up too much space. So this scenario is most useful for small amounts of A . The disadvantage of this choice is that A accumulates at the interface between droplet and solvent phase because it acts as a buffer to reduce the unfavorable B - C contacts. In addition, A gradients are not penalized with the purely enthalpic choice for $\kappa_{ij} = v_0^{2/d} \chi_{ij}$ and we have an extra parameter κ_{AA} to stabilize the interface.

If A interacts like C , it gets excluded from the B rich phase in the same way as C ; see fig.2.9B. In this case the chemical potential of A reduces to $\mu_A = k_B T (\ln(\phi_A/\phi_C) + w_A)$ and in equilibrium the ratio of A to C , ϕ_A/ϕ_C , has to be constant everywhere. Under this condition, the free energy reduces to the binary case as shown in fig. 2.9(B). We find that in this case the equilibrium volume fractions of B in solvent rich and B rich phase are independent of the total amount of A and are given by the same values as in the binary system with the same interaction χ . This makes the theoretical treatment easier because the

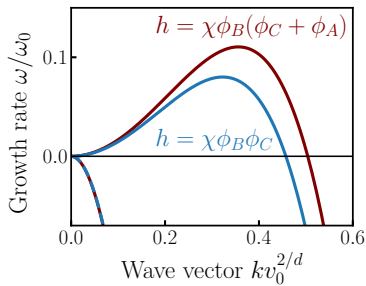


Figure 2.10: Linear stability analysis for a ternary system. Perturbation growth rate ω as a function of wave vector $|k|$. The growth rates for A interacting like C , Eq. 2.50b, and not interacting, Eq. 2.50a, are shown in maroon and blue respectively. In both cases there is one stable mode (dashed line) and one unstable model (solid line). While the magnitude and range of the unstable modes differ, the behavior is qualitatively the same as in the binary case; see fig. 2.5. Parameters used are $\chi = 3.5$, $\bar{\phi}_A = 0.15$ and $\bar{\phi}_B = 0.4$.

33: As for the binary system, unstable modes only exist for $\bar{\phi}_B > \phi_b$ and ϕ_b can depend on $\bar{\phi}_A$.

equilibrium volume fractions do not depend on time and can be treated as constants. Here the disadvantage is that the A volume fraction in the droplet phase becomes very small, which can lead to numerical instabilities if diffusive noise is included in the simulations.

Finally, fig. 2.9C shows the special case that A and B interact attractively, while C is neutral, i.e. does not interact at all. In this case, the enthalpy is given by $h = \chi\phi_A\phi_B$ and $\chi \ll 0$. We do not discuss this case in detail but want to mention it because it is important for some biomolecular condensates and complex coacervates[84]. It is supposed to showcase the complex behavior that is possible in ternary systems, but not in binary systems. Note how the slope of the tie lines change sign from fig. 2.9B to C, indicating that A and B repel in fig. 2.9B and attract each other in fig. 2.9C; see as well Ref.[111] for a discussion about the information content in tie lines.

If not otherwise noted, we will from now on use the enthalpy in Eq. 2.50b, $h = \chi\phi_B(1 - \phi_B)$, i.e. A interacts like C , in all calculations and simulations.

In addition to the more complex interactions, in the ternary system we have to describe the dynamics of two species and the diffusive dynamics are given by two, in general coupled, partial differential equations

$$\partial_t \phi_A = \nabla \left(\sum_{j=A,B} \Lambda_{Aj}(\Phi) \nabla \mu_j \right), \quad \text{and} \quad (2.51a)$$

$$\partial_t \phi_B = \nabla \left(\sum_{j=A,B} \Lambda_{Bj}(\Phi) \nabla \mu_j \right). \quad (2.51b)$$

The linear stability of Eq. 2.51a for the two above mentioned cases, Eq. 2.50b and Eq. 2.50a, is shown in fig. 2.10 for the simple case of equal, constant diffusivities $\Lambda_A = \Lambda_B = \Lambda$ and neglecting cross diffusion $\Lambda_{AB} = 0$. For the calculations see App.C. In both cases, one eigenvalue, or growth rate, contains a band of unstable modes (solid lines)³³, while the other eigenvalue is always stable. If A interacts like C , the band of unstable modes is longer and shorter wavevectors are unstable. The reason for this is that the total interaction energy is higher and thus the tendency to form sharp interfaces is stronger.

2.5 Simulations

All numerical simulations in this thesis were done with the python package py-pde[130] and extensions developed in the Zwicker group. The package uses finite difference methods to solve partial differential equations, in our case of the form Eq. 2.2. Thereby,

we use the explicit Euler method for time evolution. Because of the 4th order derivatives, both the volume fraction as well as the chemical potential need to be supplied with boundary conditions, where we applied either no flux or periodic boundary conditions as indicated in the figures. The py-pde package allows for grids with unequal spacing and special symmetries, for example spherically symmetric and cylindrical grids. In this case, the Laplace operator in spherical or cylindrical coordinates is used[130]. Stochastic simulations are done by solving the stochastic differential equation in the Itô representation[131].

2.6 Summary

In this chapter, we have introduced the theoretical basis of this thesis. We will mostly stay in the ternary description, although an extension to more components is conceptually straightforward using Eq. 2.30. In addition we will discuss the strong interaction limit ($\chi \gg \chi_c$) with interactions described by either Eq. 2.50a or Eq. 2.50b. Using the framework of non-equilibrium thermodynamics introduced in sec.2.2, neglecting cross diffusion and assuming constant diffusivity for simplicity, the general dynamics are determined by³⁴

$$\partial_t \phi_A = \Lambda_A \nabla^2 \mu_A + \sum_k \nu_{A,k} s_k, \quad \text{and} \quad (2.52a)$$

$$\partial_t \phi_B = \Lambda_B \nabla^2 \mu_B + \sum_k \nu_{B,k} s_k. \quad (2.52b)$$

The forward and backward reaction rates $s_k = s_k^f - s_k^b$ are connected to the free energy change of reaction ΔF_k via a detailed balance condition

$$\frac{s_k^f}{s_k^b} = \exp\left(\frac{\Delta F_k}{k_B T}\right). \quad (2.53)$$

In addition, the actual rates are determined by Eq. 2.27. Starting from this we will next introduce the simple switch reaction between A and B in a closed system and discuss its implication on thermodynamic equilibrium.

³⁴: We assume the molecular volumes of A and B are equal (this is necessary for conversion reactions to conserve volume) and given by the lattice volume $v_A = v_B = v_0$ (this is an assumption to simplify calculations).

Using the theory introduced in Ch. 2 we here discuss the influence of passive chemical reactions on phase separation in a closed system that relaxes to equilibrium. We start with the simplest toy model, a ternary system with solvent C and a protein that can exist in two forms, a soluble form A and a phase separating form B . A chemical reaction $A \rightleftharpoons B$ can switch between the soluble and phase separating form; see fig. 3.1. The theoretical description is based on the ternary free energy in Eq. 2.48 and the chemical potentials of A and B in Eq. 2.49. In the first step, we introduce the chemical equilibrium for this system and demonstrate that the equilibrium ratio of A and B depends on the local composition due to the same enthalpic interactions that drive phase separation.

Parts of this chapter are based on results from Kirschbaum and Zwicker; ‘Controlling biomolecular condensates via chemical reactions’, J. R. Soc. Interface (2021) **18**, Ref.[105]. In particular, Sec.3.1 and Sec.3.2 contain more detailed discussions about the model used in Ref.[105]

3.1 Chemical Equilibrium

The chemical reaction $A \rightleftharpoons B$ is in equilibrium if the chemical potentials of A and B are equal $\mu_A = \mu_B$. In this case, the thermodynamic force discussed in Section 2.2, $\mu_A - \mu_B$ vanishes. Thus, there is no energetically preferred direction for the reaction. Using Eq. 2.49 we can write the chemical equilibrium condition as

$$\frac{\mu_B - \mu_A}{k_B T} = \ln \frac{\phi_B}{\phi_A} + w_B - w_A + h_B - h_A = 0, \quad (3.1)$$

where $h_i = (k_B T)^{-1} \partial_{\phi_i} h$ is the interaction enthalpy per i particle. Therefore, we can define the equilibrium ratio K as

$$K = \left. \frac{\phi_B}{\phi_A} \right|_{\text{eq}} = \exp(\Delta w + \Delta h(\phi_A, \phi_B)). \quad (3.2)$$

Here $\Delta w = w_A - w_B$ is the internal energy difference between A and B and $\Delta h = h_A - h_B$ is the interaction energy or enthalpy difference between A and B . In the chemistry literature the ratio between products (B) and reactants (A) in equilibrium is called

- 3.1 Chemical Equilibrium . 43**
 - Equilibrium ratio in an homogeneous mixture 44**
- 3.2 Phase separation and chemical reactions 47**
 - Equilibrium dynamics . 50**
 - Chemical Reactions control droplets 54**
- 3.3 SAF-A Phase separation 56**
 - Modified free energy . . 57**
 - Strong binding approximation 59**
 - Localized binding sites can nucleate droplets 61**
 - FRAP simulation 64**
 - Model predictions 65**
- 3.4 Droplets control chemical reactions 68**
 - Chemical equilibrium in droplets 68**
 - Kinetics of an association reaction 70**
- 3.5 Summary 71**

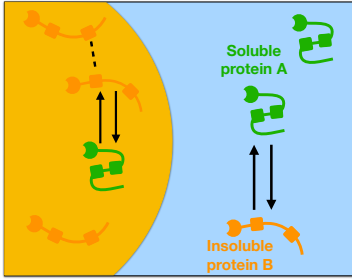


Figure 3.1: Schematic of a phase separating system with chemical reactions. A protein can exist in two forms, the phase separating form B (orange particles) forms droplet (orange background), while form A (green particles) is soluble in the solvent C (blue background). In both phases, droplet and solvent phase, the reversible chemical reaction can switch between states A and B (black arrows).

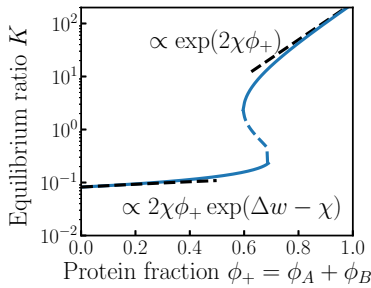


Figure 3.2: The equilibrium ratio is strongly influenced by the total protein fraction. Equilibrium ratio K (Eq. 3.5) as a function of total protein fraction ϕ_+ (blue line). For small ϕ_+ the protein state A is dominant ($K \ll 1$) and K scales only weakly with ϕ_+ (lower dashed black line). For high ϕ_+ state B becomes favorable ($K \gg 1$) due to enthalpic interactions and K increases exponentially with ϕ_+ (upper black line). In between, there is a bi-stable crossover region where either A or B is favored depending on the initial conditions. Here $\chi = 4$ and $\Delta w = 1.5$.

1: For a analytical solution for general pairwise interactions see Appendix.E.

the equilibrium constant or equilibrium ratio K [132]. Eq. 3.2 shows that the ratio is not constant, but depends on local composition due to interactions, we, therefore, call it equilibrium ratio K rather than equilibrium constant in the following.

Equilibrium ratio in an homogeneous mixture

In a homogeneously mixed system of A , B , and C the volume fractions $\phi_i(\mathbf{r}, t) = \bar{\phi}_i(t)$ are constant in space. In addition, the total amount of protein $\phi_+ = \phi_A(t) + \phi_B(t)$ and solvent ϕ_C are conserved and thus constant in time as well. Therefore, the state of the system is fully determined by the ratio $\phi_B(t)/\phi_A(t)$ which relaxes towards the equilibrium ratio given in Eq. 3.2. In equilibrium, the volume fractions of A and B are thus given by

$$\phi_A^{\text{eq}} = \frac{1}{1+K}\phi_+, \quad \text{and} \quad (3.3a)$$

$$\phi_B^{\text{eq}} = \frac{K}{1+K}\phi_+. \quad (3.3b)$$

Thus all proteins are in state B for $K \gg 1$ ($\phi_B^{\text{eq}} = \bar{\phi}_+$) and all proteins are in state A for $K \ll 1$ ($\phi_A^{\text{eq}} = \bar{\phi}_+$).

In an ideal, dilute solution we would expect K to be constant and $\phi_{A,B}^{\text{eq}}$ to scale linearly with ϕ_+ . But in general, ϕ_+ is an important control parameter for the ratio of the two protein states because $\Delta h(\phi_A, \phi_B)$ in Eq. 3.2, and thus K , depends on ϕ_+ . To see this, we can calculate the equilibrium ratio in Eq. 3.2 as a function of the total amount of protein $\phi_+ = \phi_A + \phi_B$ for the special case that A does not interact with C , but repels from B in the same way as C does (Eq. 2.50b)

$$\Delta h(\phi_B) = -\chi(1 - 2\phi_B). \quad (3.4)$$

In this case Δh depends on ϕ_B only and we get a simple expression for $K(\phi_B)$ in chemical equilibrium¹ using Eq. 3.2

$$K = \exp(\Delta w - \chi(1 - 2\phi_B)) = \exp(\Delta w - \chi + 2\chi\phi_B). \quad (3.5)$$

In fig. 3.2, K is plotted as a function of ϕ_+ for $\chi = 4$ and $\Delta w = 1.5$. While $K(\phi_B)$ is a simple exponential function of ϕ_B its dependence on $\phi_+ = \phi_A + \phi_B$ is more complicated because $\phi_A = \phi_B K(\phi_B)$ can have multiple solutions for a fixed ϕ_+ ; see fig. 3.2. From fig. 3.2 it is clear that K is strongly influenced by the total amount of protein and varies by ca. three orders of magnitude when going from a system without protein to pure protein.

Furthermore, we can distinguish two regimes: for low total

protein fractions, $\phi_+ \ll 1$, the non-ideal contribution is small. $\chi\phi_B \ll 1$. Thus, the equilibrium ratio scales linearly with protein amount $K \propto \chi\phi_+$; lower black line in fig. 3.2. For high amounts of protein and $\chi > \Delta w$, the non-ideal contribution becomes dominant. As a result, K scales exponentially with ϕ_+ , $K \propto \exp(2\chi\phi_B)$; upper black dashed line in fig. 3.2. Notably, the crossover is not smooth but happens via two saddle-node bifurcations, and varying ϕ_+ dynamically would even show hysteresis. The reason for this is best illustrated by plotting the chemical equilibrium concentrations in the $\phi_B - \phi_A$ plane instead of the $K - \phi_+$ plane. Due to the simple form of Eq. 3.5, we find an analytic expression $\phi_A^{\text{eq}}(\phi_B)$ as well

$$\phi_A^{\text{eq}}(\phi_B) = \phi_B \exp(-\Delta w + \chi(1 - 2\phi_B)), \quad (3.6)$$

which is plotted in a ϕ_B vs ϕ_A phase space in fig. 3.3. For a given ϕ_+ , the intersection of $\phi_A + \phi_B = \phi_+$ (black dashed line in fig. 3.3) and chemical equilibrium (blue line) gives the equilibrium volume ratio K (purple dot). Varying ϕ_+ and finding the corresponding K results in fig. 3.2. For low protein fraction, the chemical equilibrium line is approximately linear and corresponds to the lower black dashed line in fig. 3.2. In the crossover region three equilibrium ratios exist, two stable and one unstable, while for large protein fractions only the exponential branch, where virtually all proteins are in-state B , is stable.

For the simple choice of Δh in Eq. 3.4 the model has two parameters², the interaction strength χ and the internal energy difference Δw . It is instructive to discuss the limiting cases of these parameters as shown in the $\phi_A - \phi_B$ phase space in fig. 3.4. For large $|\Delta w| \gg \chi > 0$, one of the two species is strongly favored, A for $\Delta w < 0$ and B for $\Delta w > 0$, and the effect of interactions becomes negligible in the discussion of chemical equilibrium; see fig. 3.4A. For $|\Delta w| \gg \chi > 0$ and $\Delta w < 0$, the equilibrium ratio becomes

$$K \approx e^{\Delta w - \chi}(1 + 2\chi\phi_B), \quad (3.7)$$

which is in a good approximation constant for all total protein fractions because $\phi_B \ll 1$; see light blue line in fig. 3.4A. If B is favored, $\Delta w \gg \chi > 0$ and $\Delta w > 0$, the interaction is negligible only for very large $\Delta w \gg \chi$ because for low total protein fractions the factor $\exp(\Delta w - \chi)$ contains a $-\chi$ term that favors A ; see dark blue line in fig. 3.4A. To sum up, the two limits $|\Delta w| \gg 0$ correspond to the binary mixtures of A and C ($\Delta w < 0$) and B and C ($\Delta w > 0$) respectively. The internal energy differences are so large that one of the two protein forms is strongly favorable.

The χ dependence, for a fixed value of $\Delta w - \chi$, shown in

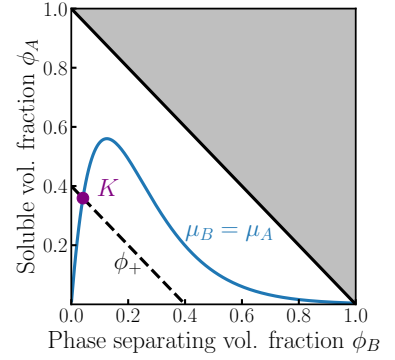


Figure 3.3: Phase space diagram of a homogeneous ternary mixture with chemical reactions. In chemical equilibrium ($\mu_A = \mu_B$) the volume fractions of A and B are constrained by Eq. 3.2 (blue line) on the one hand and by the total protein volume fraction $\phi_+ = \phi_A + \phi_B$ (black dashed line) on the other hand. The intersection of these two constraints (purple dot) defines the volume fractions ($\phi_A^{\text{eq}}, \phi_B^{\text{eq}}$) in a homogeneous mixture in equilibrium. In the gray area $\phi_A + \phi_B > 1$, which is forbidden due to incompressibility. Here $\chi = 4$ and $\Delta w = 1.5$.

²: The temperature is an important control parameter for both $\chi(T)$ and $\Delta w(T)$. Since they can scale differently with T it is, in general, possible to switch between an interaction dominated and internal energy dominated behavior by changing T . But we assume isothermal systems so we will not discuss the role of temperature in detail.

Figure 3.4: Parameter dependence of chemical equilibrium in $\phi_B - \phi_A$ phase space. Blue lines indicate the condition $\mu_A = \mu_B$ in $\phi_A - \phi_B$ space. **A** Increasing Δw for fixed χ favors the phase separating state B over the soluble state A (dark blue line), in the limit $\Delta w \rightarrow \infty$ no A is present. For low or negative Δw the interactions χ are negligible and the equilibrium ratio K is almost constant (light blue line) and given by $K = \exp(\Delta w - \chi)$. **B** In non-interacting systems ($\chi = 0$, light blue line) the equilibrium ratio becomes a constant $K = \exp(\Delta w)$, while for increasing χ the interactions favor the phase separating state (dark blue lines).

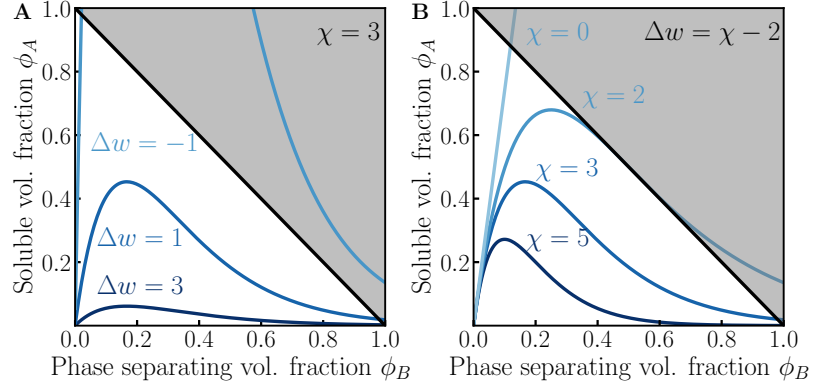


fig. 3.4, is straightforward. If the interaction vanishes, $\chi \rightarrow 0$, K becomes a constant $K = \exp(\Delta w)$ and chemical equilibrium becomes a straight line in fig. 3.4B (light blue line). For high χ , the high B fractions branch shown in fig. 3.2 becomes stable (e.g. for $\chi = 3$). Increasing χ shifts the crossover between low B fraction branch to high B fraction branch towards lower total protein fraction, which can be seen from the shift of the blue curves maxima for higher χ in fig. 3.4B.

To see non-monotonic behavior of the equilibrium ratio K , it is necessary to switch between the high B fraction and low B fraction branch in fig. 3.2 depending on the total fraction of proteins ϕ_+ . This is possible if the argument of the exponential factor $\exp(\Delta w - \chi + 2\chi\phi_B)$ can change sign as a function of ϕ_B . As a result, the factor $\Delta w - \chi$ should be smaller than zero, but $\Delta w + \chi$ should be larger than zero. This restricts the internal energy difference to the same order of magnitude as the interactions driving phase separation. This is a strong restriction for biological systems as it requires parameter tuning, but can be circumvented by driving the reaction out of equilibrium which we will discuss later.

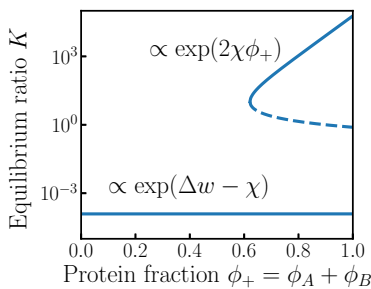


Figure 3.5: Equilibrium ratio K for strong interactions $\chi = 10$ and weak internal energy difference $\Delta w = 1$. In this limit the lower branch of K is always stable and independent of ϕ_+ , while the upper branch appears for high total protein fraction only, where interactions become more relevant. For high total protein, the difference between the branches is $\exp(2\chi)$ and thus in each branch, only one type of protein species is present.

Before discussing the kinetics of these homogeneous, reactive mixtures a short last note on the strong interactions limit χ for weak internal energy differences $0 < \Delta w \ll \chi$, which is shown in fig. 3.5. In this limit, the low B fraction branch is always stable, while the high B fraction branch appears for high total protein fractions and the difference between high K and low K is approximately $\exp(2\chi)$, which becomes large for high χ . Thus, a dense mixture of a protein that can exist in two states that interact strongly repulsive, but are close in internal energy, shows bistability with almost perfect separation (only A in the

lower branch and only B in the higher branch).

So far we have only discussed the equilibrium state of the system. In this part, we will shortly discuss the kinetics using the framework introduced in Sec.2.2. Since we assume an homogeneous mixture, the dynamics are given by the reaction only. As discussed in Ch. 2, the reaction has to obey detailed balance, so the forward s^f and backward s^b rate are related by

$$\frac{s^f}{s^b} = \exp \frac{\mu_A - \mu_B}{k_B T}, \quad (3.8)$$

while the total reaction flux s is given by $s = s^f - s^b$. This ensures that the reaction relaxes to equilibrium, i.e. $s = 0$ for $\mu_A = \mu_B$. But, a priori we do not know the functional form of s^f/s^b and here we use transition state theory Eq. 2.27 to model the reaction flux³. In this case the dynamics are described by

$$\partial_t \phi_A = -k e^{\frac{\mu_A}{k_B T}} \left(1 - e^{\frac{\mu_B - \mu_A}{k_B T}}\right), \quad \text{and} \quad (3.9a)$$

$$\partial_t \phi_B = k e^{\frac{\mu_A}{k_B T}} \left(1 - e^{\frac{\mu_B - \mu_A}{k_B T}}\right). \quad (3.9b)$$

For the simple reaction $A \rightleftharpoons B$ with equal molecular volumes of A and B the reaction rate obeys $s_A = -s_B$ and because $\phi_+ = \text{const}$, we can rewrite the dynamics in terms of the ratio of ϕ_B/ϕ_A as

$$\partial_t \left(\frac{\phi_B}{\phi_A} \right) = k e^{w_B + \chi(1-2\phi_B)} \left(1 + \frac{\phi_B}{\phi_A}\right) \left(K - \frac{\phi_B}{\phi_A}\right). \quad (3.10)$$

This shows that the ratio relaxes exponentially to $\frac{\phi_B}{\phi_A} = K$ with an effective rate $\bar{k}(t) = k e^{w_B + \chi(1-2\phi_B)} (1 + \phi_B/\phi_A)$ that depends on time via $\phi_{A/B}(t)$.

3.2 Phase separation and chemical reactions

We discussed the basics of ternary phase separation in Sec.2.4 and the equilibrium of a simple conversion reaction in Sec.3.1. In this section, we discuss the combination of both processes. The system behavior is then dominated by the two equilibrium conditions discussed above, chemical equilibrium $\mu_A = \mu_B$ and equilibrium in both phases. Here, we call the B -rich phase, the droplet phase, and the B -poor phase, the solvent phase. Thereby, ϕ_i^{in} and ϕ_i^{out} describe the volume fraction inside and outside the droplet respectively. The phase equilibrium condition then becomes $\mu_i^{\text{in}} = \mu_i^{\text{out}}$ and $\Pi^{\text{in}} = \Pi^{\text{out}}$. Graphically, chemical and

3: While the quantitative dynamics differ using TST, this still behaves like the Allen-Cahn equation or model A[35] in the limit of $\phi_+ \rightarrow 1$, which can show transient phase separation on its own in in-homogeneous systems, while it relaxes to the equilibrium state $\mu_A - \mu_B = 0$.

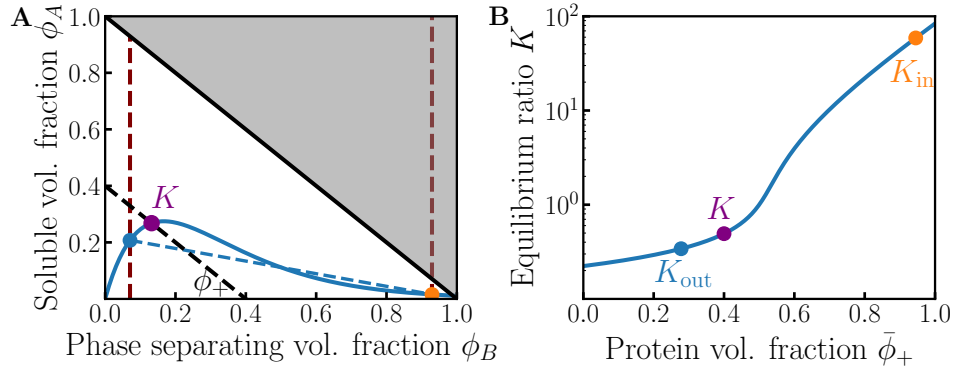


Figure 3.6: Combined equilibrium for reactions and phase separation. **A** Chemical equilibrium (blue line) in ϕ_A vs ϕ_B space. Chemical equilibrium is a necessary condition for the equilibrium state. But if the homogeneous state (purple dot) lies in the binodal region (maroon dashed lines) the phase separated state (blue and orange dot) is energetically favorable and droplets can form. **B** Equilibrium ratio K as a function of total protein fraction. Unlike the homogeneous case, there are now three important equilibrium fractions, the homogeneous one for a given ϕ_+ (purple) and the two ratios in droplet K_{in} (orange dot) and solvent K_{out} (blue dot) phase. For $K < K_{out}$ the homogeneous state is always stable, but for $K > K_{out}$ droplets can form and the equilibrium ratio in droplet (K_{in}) and solvent (K_{out}) phase is different. Parameters are $\bar{\phi}_+ = 0.4$ (only A), $\chi = 3$ and $\Delta w = 1.5$.

phase equilibrium can be combined as shown in fig. 3.6A. The most important point is that phase separation is compatible with chemical equilibrium because the chemical equilibrium curve (blue line) intersects the phase equilibria (maroon dashed line) such that the two intersections (blue and orange dots) lay on a tie line (blue dashed line)[106].

As a result, the equilibrium conditions for the chemical potential $\mu_A = \mu_B$, $\mu_A^{in} = \mu_A^{out}$ and $\mu_B^{in} = \mu_B^{out}$ can be fulfilled at the same time, while mechanical equilibrium, $\Pi^{in} = \Pi^{out}$, is not directly influenced by the chemical equilibrium condition. The main difference to ternary phase separation without reactions is that the mass conservation constraint for A and B gets replaced by the chemical equilibrium condition that determines the ratio of the two species, while the total amount of protein is still conserved[105, 133]. Thus the system is fully determined for a given total protein fraction $\bar{\phi}_+$.

The phase separated state can be characterized analogous to chemical equilibrium using the partition coefficient for each species Γ_i which is the ratio of volume fraction between droplet and solvent phase in equilibrium[133, 134] and can be calculated from $\mu_i^{in} = \mu_i^{out}$

$$\Gamma_i = \frac{\phi_i^{in}}{\phi_i^{out}} = \frac{\phi_C^{out}}{\phi_C^{in}} \exp(h_i^{out} - h_i^{in}) \quad (3.11)$$

for $i = A, B$. If $\Gamma_i > 1$ species i is enriched in the droplet phase, while for $\Gamma_i < 1$ species i is enriched in the solvent phase. In the phase separated state, the equilibrium ratio K is different in solvent and droplet phase; see fig. 3.6B. The two equilibrium

ratios are given by

$$K_{\text{in}} = \frac{\phi_B^{\text{in}}}{\phi_A^{\text{in}}} = \exp(\Delta w + \Delta h_{\text{in}}), \quad (3.12a)$$

$$K_{\text{out}} = \frac{\phi_B^{\text{out}}}{\phi_A^{\text{out}}} = \exp(\Delta w + \Delta h_{\text{out}}). \quad (3.12b)$$

Comparing Eq. 3.12 and Eq. 3.11, we get an interesting relation between partition coefficients, describing phase equilibrium, and equilibrium ratios, describing chemical equilibrium

$$\frac{K_{\text{in}}}{K_{\text{out}}} = \exp(h_A^{\text{in}} - h_A^{\text{out}} - h_B^{\text{in}} + h_B^{\text{out}}) = \frac{\Gamma_A}{\Gamma_B}. \quad (3.13)$$

This relation is obvious from the definition of equilibrium ratios and partition coefficients, but the fact that phase separation influences equilibrium ratios has only started to be acknowledged recently[135]. This relation can be generalized to more complex reactions and multiple phases[133] and shows that both processes, phase separation and equilibrium reactions, are intimately linked via the chemical potential.

For a ternary system without reactions, phase separation is energetically favorable if $\bar{\phi}_B > \phi_B^{\text{out}}$. This condition remains true, but now $\bar{\phi}_B$ is not conserved anymore. Instead it is determined by chemical equilibrium Eq. 3.3b; purple dot in fig. 3.6. So the question of whether phase separation is energetically favorable depends on $\bar{\phi}_+$ and K . For general forms of enthalpic interactions, the problem becomes very complicated. Therefore, we again return to the simple example where A interacts like C , $h = \chi\phi_B(1 - \phi_B)$ discussed above already. In addition, we focus on the two new parameters, the internal energy difference Δw and the total protein fraction $\bar{\phi}_+$ for a fixed interaction strength χ . In addition, we assume χ to be high enough to show phase separation for $\bar{\phi}_B > \phi_B^{\text{out}}$. Clearly, the minimum amount of protein fraction necessary for phase separation tends to ϕ_B^{out} for $\Delta w \rightarrow \infty^4$, while no phase separation is possible at all for $\Delta w \rightarrow -\infty$; see fig. 3.7. According to Eq. 3.3b the separation between regions where phase separated droplets are stable and unstable is given by

$$\frac{K}{1 + K} \bar{\phi}_+ = \phi_B^{\text{out}}, \quad (3.14)$$

which corresponds to the black line in fig. 3.7. Note that this result is specific for this choice of enthalpic interaction, but it holds more generally under the constraint that A interacts weakly as introduced in Ch. 2. In this case, the reaction always reduces the propensity to phase separate compared to the case where all proteins are in state B .

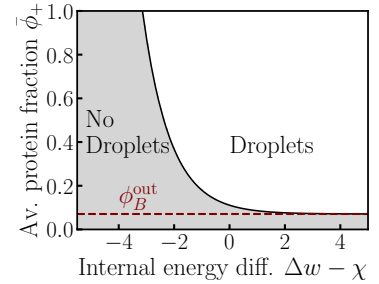


Figure 3.7: Phase diagram of droplet stability. The black line separates region of stable droplets (white area) from regions without droplets (grey area). For fixed interaction strength, here $\chi = 4$, the minimum total protein fraction necessary for droplets to be stable is ϕ_B^{out} (maroon line) and increases for decreasing internal energy difference up to the point where no phase separation is possible even for $\bar{\phi}_+ = 1$.

4: In this limit all proteins are in state B and we are back in an effective binary system.

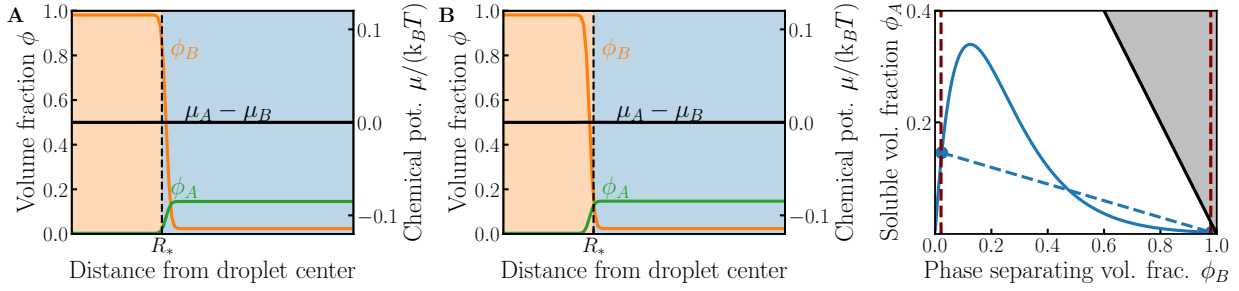


Figure 3.8: Simulation of a phase separated droplet for different mobilities. In panels A and B the volume fraction (left y-axis) of A (green line) and B (orange line) and chemical potential difference (right y-axis black solid line) are plotted along a radial cut through the droplet in the steady state. The blue and orange regions correspond to solvent and droplet phase respectively. The stable radius R_* is indicated by the black dashed line. In both panels $\chi = 4$, $\Delta w = 2$, and $\bar{\phi} = 0.2$ and simulations were done for spherically symmetric radial grids and no flux boundary conditions. **A** uses constant, diagonal mobilities $\Lambda_{AA} = \Lambda_{BB} = \Lambda$, $\Lambda_{AB} = 0$ and LNEQ reactions $s = k(\mu_A - \mu_B)$. **B** uses Kramer mobilities [114] $\Lambda_{ij} = \Lambda(\phi_i \delta_{ij} - \phi_i \phi_j)$ and TST reactions $s = \lambda(\exp(\mu_A/k_B T) - \exp(\mu_B/k_B T))$. **C** Shows the corresponding ϕ_A vs ϕ_B phase space. The equilibrium fractions in droplet and solvent phase are expected to coincide with the intersection of the binodal (maroon dashed lines) and chemical equilibrium (blue line). The blue dots are taken from the simulations in **A** and match very well with theoretical predictions.

Equilibrium dynamics

In its general form, the dynamics of the system discussed above are given by [136]

$$\partial_t \phi_i = \nabla \left[\sum_{i,j} \Lambda_{ij}(\Phi) \nabla \mu_j \right] + \nu_i s \quad i, j = A, B, \quad (3.15)$$

where, according to Sec.2.2, the reaction flux is either described by linear non-equilibrium thermodynamics (LNEQ) (Eq. 2.25) $s = k(\mu_A - \mu_B)$ or TST (Eq. 2.26) $s = \lambda(e^{\mu_A/k_B T} - e^{\mu_B/k_B T})$. This again emphasizes that the system is a combination of Allen-Cahn/model A [137] (reaction, non-conserved order parameter) and Cahn-Hilliard/model B [123] (diffusion, conserved order parameter) dynamics. The dynamics, for example the scaling of domain growth [35], behavior around the critical point [102] and combination of both models [120] have been and still are widely discussed. But we are mostly interested in how the cell can use reactions to switch between a state where droplets are stable or not. Therefore, we focus on the steady state of the system rather than on the quantitative dynamics, i.e. how fast the state is reached. In addition, to circumvent the nucleation problem, we start with an initial state of a droplet larger than the critical radius. Fig. 3.8 shows the steady state, which corresponds to the equilibrium state, for two different choices of mobilities and reaction rates. Thereby, fig. 3.8A uses the most simple model, diagonal, constant mobilities $\Lambda_{ij} = \Lambda \delta_{ij}$ and LNEQ reactions $s = k(\mu_A - \mu_B)$, while **B** uses the more complex scaled mobilities [65, 114] $\Lambda_{ij} = \Lambda(\phi_i \delta_{ij} - \phi_i \phi_j)$ and transition state theory reaction rates $s = \lambda(e^{\mu_A/k_B T} - e^{\mu_B/k_B T})$. Notably, the steady

states are very similar, although there is a small but significant difference between the steady state radii that we attribute to the fact that the simulations are not fully relaxed. It is not surprising that both simulations give the same result because the equilibrium state is independent of kinetics and should not depend on our choice of mobilities or rate models as long as they are thermodynamically consistent.

The steady state simulation in fig. 3.8 illustrates the findings of fig. 3.6 discussed above. Although the ratio of B to A volume fraction in droplet and solvent phase is significantly different, the chemical potential difference $\mu_A - \mu_B$ vanishes everywhere. This is reminiscent of phase separation, where a strong concentration gradient is present although the chemical potential is constant in space. In addition, fig. 3.8C shows that the simulated ratio of B to A in droplet and solvent phase fits very well to the predictions from analyzing the equilibrium state for both simulations, simple and more complex kinetics; fig. 3.8A/B.

While we do not discuss the passive dynamics in detail, we want to analyze the steady state for the mobilities and reaction rate used in fig. 3.8A as an example case. The dynamical equations are then given by

$$\partial_t \phi_A = \Lambda \nabla^2 \mu_A - k(\mu_A - \mu_B), \quad \text{and} \quad (3.16a)$$

$$\partial_t \phi_B = \Lambda \nabla^2 \mu_A + k(\mu_A - \mu_B). \quad (3.16b)$$

We can add and subtract Eq. 3.16 and describe the system in terms of total protein fraction $\phi_+ = \phi_A + \phi_B$ and difference between state A and B $\phi_- = \phi_A - \phi_B$ and the corresponding chemical potentials $\mu_+ = \mu_A + \mu_B$ and $\mu_- = \mu_A - \mu_B$ which results in⁵

$$\partial_t \phi_+ = \Lambda \nabla^2 \mu_+, \quad \text{and} \quad (3.17a)$$

$$\partial_t \phi_- = \Lambda \nabla^2 \mu_- + 2k\mu_-. \quad (3.17b)$$

If we want to solve for the steady state we need boundary conditions on the boundary Ω . For closed systems it is natural to assume no flux conditions on the boundary, $\mathbf{n} \nabla \mu_A|_{\Omega} = \mathbf{n} \nabla \mu_B|_{\Omega} = 0$, where \mathbf{n} is an outward pointing normal vector on the boundary⁶. In this case, the two equations are decoupled and we see that $\mu_+ = \text{const.}$ is the only steady state solution for Eq. 3.17a. In addition, clearly $\mu_- = 0$ is a solution of Eq. 3.17b, but is it the only possible solution? To see that it is, let us assume there are two solutions μ_1 and μ_2 . Since Eq. 3.17b is linear $f = \mu_1 - \mu_2$ is a solution as well. To show that this leads to a contradiction, we start from

$$\nabla(f \nabla f) = (\nabla f)^2 + f \nabla^2 f = (\nabla f)^2 + 2k f^2, \quad (3.18)$$

5: Because μ_A and μ_B are exchange chemical potentials with respect to C , μ_+ corresponds to replacing two C particles with one A and one B , while μ_- is the exchange chemical potential between A and B because the C contribution vanishes.

6: In the chemical potential picture boundary conditions for μ_A and μ_B are enough to define the system, but for the simulations we need boundary conditions for ϕ_i and we use no-flux conditions as well, which physically corresponds A and B not interacting with the boundaries.

where we applied $\nabla^2 \mu_- - 2k\mu_- = 0$ in the last step. Now we integrate this over the whole volume V_{sys} and get

$$\int_{V_{\text{sys}}} \nabla(f\nabla f) dV = \int_{V_{\text{sys}}} (\nabla f)^2 + 2kf^2 dV. \quad (3.19)$$

Applying Gauß integral theorem to the left hand site, where \mathbf{S} is the outward pointing boundary surface element, we obtain

$$\oint_{\Omega} f\nabla f d\mathbf{S} = \int_{V_{\text{sys}}} (\nabla f)^2 + 2kf^2 dV. \quad (3.20)$$

Now ∇f vanishes on the boundary due to no-flux conditions, but both $(\nabla f)^2$ and $2kf^2$ are non-negative (negative reaction rates $k < 0$ are nonphysical). As a result f and ∇f have to vanish everywhere and thus $\mu_1 = \mu_2 (= 0)$ is the only solution; \square .

This still holds if we use transition state theory reaction rates because we can rewrite

$$\lambda \left[\exp\left(\frac{\mu_A}{k_B T}\right) - \exp\left(\frac{\mu_B}{k_B T}\right) \right] = 2\lambda \exp\left(\frac{\mu_+}{2k_B T}\right) \sinh\frac{\mu_-}{2k_B T}. \quad (3.21)$$

Since μ_+ has to be a constant in the steady state independent of reaction flux, the prefactor $2k \exp(\mu_+/(2k_B T))$ is constant. In this case the analysis above still works and we arrive at

$$\oint_{\Omega} f\nabla f d\mathbf{S} = \int_{V_{\text{sys}}} (\nabla f)^2 + 4\lambda f^2 \sinh\frac{f}{2k_B T} dV. \quad (3.22)$$

Now f and $\sinh(f)$ have the same sign so $f \sinh(f) \geq 0$ therefore, again the only solution is $f = 0$ and thus $\mu_1 = \mu_2$. One has to keep in mind, that this simple analysis holds for general $k, \lambda > 0$, but only for constant diffusivities Λ . This is a sanity check to see that the only steady state solution of these equations is the local equilibrium solution, so gradients in the chemical potential vanish and the reaction is in equilibrium.

One important information we can get from the dynamical equations not included in the discussion about thermodynamic equilibrium is the stability of the homogeneous state, given by the purple dot in fig. 3.6. To see if chemical reactions stabilize or destabilize the homogeneous state. In order to analyze this we perform a linear stability analysis similar to the discussion in Ch. 2 and Eq. 2.43. We start with the simple form Eq. 3.16, which is sufficient to see the generic effect of reactions. To simplify the calculations even further, we write Eq. 3.16 in non-dimensional form, where we introduce a time scale $\bar{t} = t/\tau$, the energy scale $k_B T$ and the molecular length scale $\bar{\nabla} = v_0^{-1/d} \nabla$. The time $\tau = v_0^{2/d} k_B T \Lambda^{-1}$ is defined as the average time to diffuse one molecular length scale. With this the equations become

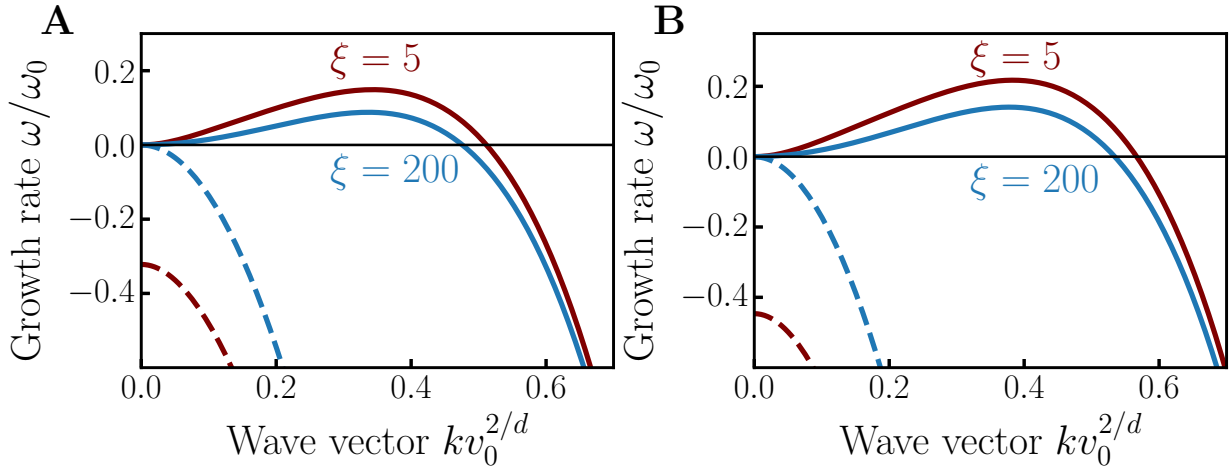


Figure 3.9: Linear stability of a reacting mixture for different reaction diffusion lengths. Perturbation growth rates as functions of the wave vector. The larger and smaller growth rates are shown as solid and dashed lines respectively. **A** Growth rates around the homogeneous state where $\phi_B(t=0) = 0.35$ and $\phi_A(t=0) = 0.15$, so the reaction is not in equilibrium. **B** Growth rates around the homogeneous state in chemical equilibrium. In both panels, the growth rates are identical to the case without reactions for slow reactions (blue lines, $\ell = 200 v_0^{1/d}$). But for fast reactions (maroon line, $\ell = 5 v_0^{1/d}$) the $k = 0$ mode of the negative eigenvalue does not vanish, which implies that the mass is not conserved. Parameters are $\chi = 3.5$, $\bar{\phi}_+ = 0.5$, $\Delta w = 2$ and $\Lambda = 1 v_0^{2/d}/(\tau k_B T)$, $\omega_0 = v_0^{-2/d} \Lambda k_B T$.

$$\partial_{\bar{t}} \phi_A = \bar{\nabla}^2 \bar{\mu}_A - \ell^2 (\bar{\mu}_A - \bar{\mu}_B), \quad \text{and} \quad (3.23a)$$

$$\partial_{\bar{t}} \phi_B = \bar{\nabla}^2 \bar{\mu}_B + \ell^2 (\bar{\mu}_A - \bar{\mu}_B), \quad (3.23b)$$

where $\bar{\mu}_i = \mu_i/(k_B T)$ and $\ell^2 = \bar{\Lambda}/\bar{k}$ is the squared reaction diffusion length scale⁷. The reaction diffusion length compares the characteristic reaction time k to the diffusive mobility Λ , so for $\ell \ll 1$, the reaction is fast and this regime is often called diffusion limited and for $\ell \gg 1$, diffusion is fast which is called reaction limited[106]. We performed linear stability analysis⁸ on Eq. 3.23 and the results are shown in fig. 3.9 for the case where the average B fraction is above the spinodal fraction, Eq. 2.44, so the system is unstable without reactions. The two cases in A and B are performed away from the chemical equilibrium state (A) and at the chemical equilibrium state (B). For fast diffusion (blue lines) the result is identical to the ternary case without reactions; see fig. 2.10. For fast reaction (maroon lines) the stable eigenvalue does not vanish for $k \rightarrow 0$ this means that mass conservation is broken, which comes from the k independent reaction. In addition, the band of unstable modes becomes wider and the most unstable growth rate is higher. This means that, if the homogeneous equilibrium state is such that $\bar{\phi}_B > \phi_s$, reactions can not suppress droplet formation. Instead, reactions can only stabilize the homogeneous mixture by keeping the average B fraction low.

7: In non-dimensional form this corresponds to the (inverse) Damköhler number as well, which compares reactive to diffusive time scales. Here the diffusive time scale would be the time to diffuse one interface width.

8: For the linear stability calculations see App.C.

Chemical Reactions control droplets

In this section, we discuss the framework introduced above in the context of biomolecular condensates. Can the cell use simple passive conversion reactions to control the formation and dissolution of droplets and, if so, under what conditions? What is new in this framework compared to the case without reactions, are the different control parameters. Those are the total protein fraction $\bar{\phi}_+$, the internal energy difference Δw , and the interaction strength χ . For binary phase separation, the important control parameters are the total amount of phase separating material $\bar{\phi}_B$ and interaction strength χ . Thus, with reactions $\bar{\phi}_B$ is a variable instead of a control parameter, and in addition, internal energy differences, constants in the chemical potential, can influence the system behavior because individual particle counts are not conserved anymore.

To be useful as a control mechanism of biomolecular condensates the cell has to be able to adjust the parameters. The total amount of protein can be controlled by protein production and degradation, but this process is slow[1], so we can regard $\bar{\phi}_+$ as a constant that can be varied on time scales long compared to the reaction-diffusion dynamics. The internal energy difference Δw can, in general, be tuned on evolutionary timescales[138] and it depends on external parameters, similar to χ , e.g. temperature, pressure, or pH. Changes in external parameters are responsible for the formation of biomolecular condensates, for example, in stress granules[37, 139]. But they are not very precise because they influence all processes in cells. Therefore, for fast and precise control neither $\bar{\phi}_+$ nor Δw are suitable control parameters. We come back to this when discussing active reactions which can overcome this limitation.

The mechanism by which a reaction $A \rightleftharpoons B$ can control phase separation is simple, phase separation without reactions depends on the total amount of phase separating material, $\bar{\phi}_B$, and phase separation is favorable if the total amount of B is higher than the binodal, or solvent phase, fraction $\bar{\phi}_B > \phi_B^{\text{out}}$. With reactions the total amount of B is not conserved anymore, but depends on the equilibrium ratio K . As discussed above, the adjusted condition for phase separation is that the total amount of protein is higher than the binodal limit $\bar{\phi}_+ > \phi_+^{\text{out}}$; see fig. 3.7. The total protein fractions in droplet and solvent phase are thereby determined by the respective equilibrium ratios

$$\phi_+^{\text{in}} = (1 + K_{\text{in}}^{-1})\phi_B^{\text{in}}, \quad \text{and} \quad (3.24a)$$

$$\phi_+^{\text{out}} = (1 + K_{\text{out}}^{-1})\phi_B^{\text{out}}. \quad (3.24b)$$

For $\bar{\phi}_+ < \phi_+^{\text{out}}$ no phase separation is present and the equi-

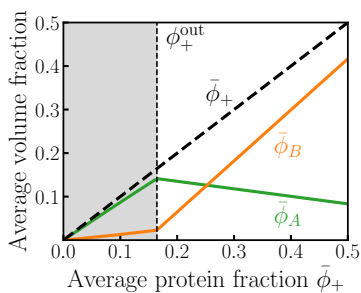


Figure 3.10: Droplets can invert the ratio of protein states. Volume fraction of A (green line) and B (orange line) as a function of average protein fraction (black dashed line). Without droplets most of the proteins are in state A (grey area), but as soon as droplets form this trend reverses and state B becomes dominant (white area) since the enthalpic interactions become dominant. Parameters are $\chi = 4$ and $\Delta w = 2$. The image is taken from [105] under the Creative Commons CC-BY-4.0 license.

librium ratio K determines $\phi_A^{\text{eq}}, \phi_B^{\text{eq}}$, but for $\bar{\phi}_+ > \phi_+^{\text{out}}$ droplets form with the respective equilibrium ratios. The effect of this is shown in a plot of the average A and B volume fractions as a function of average protein fractions, fig. 3.10. In the homogeneous state (grey area), state A is favored ($K \ll 1$). But as soon as droplets form, the trend reverses, and the ratio shifts in favor of B . In fact, the maximum total amount of A is reached for $\bar{\phi}_+ = \phi_+^{\text{out}}$ and decreases for higher total protein fractions. Taken together, the total protein fraction $\bar{\phi}_+$ is a control parameter for the ratio of state A and B . While the ratio inversion is not very sensitive to $\bar{\phi}_+$, it could still be a useful mechanism to control the amount of B and A in a non-trivial way. The general behavior is qualitatively similar to the active (B) and inactive (A) states of enzymes[140], where the protein is in the inactive state (homogeneous mixture) when it is not needed and gets activated (here via phase separation) by external cues (here changing $\bar{\phi}_+$).

Since the protein fractions in droplet and solvent phase, determined by Eq. 3.24a, are constants for given parameters⁹ χ , $\bar{\phi}_+$ and Δw , the final droplet volume is simply given by the conservation of total protein material

$$V_D = \frac{\bar{\phi}_+ - \phi_+^{\text{out}}}{\phi_+^{\text{in}} - \phi_+^{\text{out}}} V_{\text{sys}}, \quad (3.25)$$

analogous to phase separation without reactions. As a result, the droplet volume scales with system size V_{sys} and individual droplet sizes can not be controlled by these passive reactions. Conversely, Ostwald ripening[87] and coalescence[60] will minimize the surface area such that only one droplet remains. As expected the droplet volume scales linearly with the total amount of protein, just like standard phase separation.

The corresponding dependence of droplet volume on the internal energy difference is shown in fig. 3.11. For $\Delta w \ll \chi$, all proteins are in state A such that no droplets form. For $\Delta w \gg \chi$, all proteins are in state B , and the system behaves like a binary phase separating mixture. In this case, the droplet size is maximal (black dashed line). In between, there is a sharp transition, where slight changes in Δw can have a big impact on droplet volume, i.e. the droplet size is very sensitive to changes in Δw . On the one hand, the strong response to slight changes in Δw could be useful for the cell to respond to external cues, for example in stress granules[103]. But on the other hand, to use this effect cells need to finetune the internal energy differences. On long timescales, this is possible, since evolution does tune protein interactions[138]. Later we will show that active reactions can overcome this problem by tuning chemical equilibrium.

So far, we developed a general framework based on thermo-

9: In fact ϕ_B^{in} and ϕ_B^{out} are independent of $\bar{\phi}_+$ and Δw as shown in Ch. 2

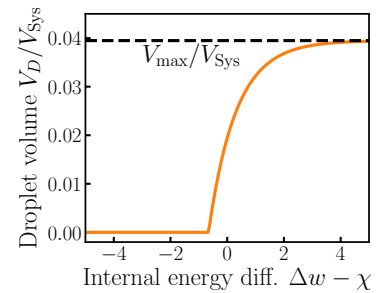


Figure 3.11: Internal energy controls steady state droplet size. Steady state droplet volume for different internal energy differences. Droplet volume V is given relative to system size V_{sys} because, like in the non-reactive case, the droplet volume scales with system size. If state A is favored ($\Delta w < \chi$) no droplets form. For large $\Delta w > \chi$ droplet size approaches the binary phase separation limit $V_{\text{max}}/V_{\text{sys}}$ because all proteins are in state B . In between there is a sharp transition where droplet size is very sensitive to changes in Δw . Parameters used are $\chi = 4$ and $\bar{\phi}_+ = 0.06$. The image is slightly modified from [105, 141] under the Creative Commons CC-BY-4.0 license.



Figure 3.12: Schematic representation of the SAF-A protein. SAF-A has a length of 806 amino acids and contains a prion like domain (RGG in red) known to be a driver of phase separation[143, 144]. In addition the RGG domain can bind to RNA as well. Image modified from [142] under the Creative Commons license.

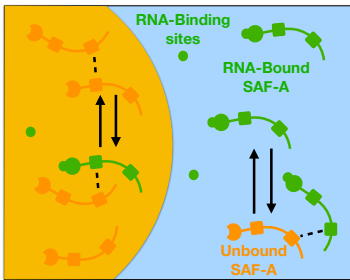


Figure 3.13: Schematic representation of the SAF-A model. The SAF-A proteins can exist in two states: either they diffuse freely (orange particle) or bind to RNA (green circles) and thereby become immobile (green particles). Due to attractive interactions in the RGG domain (black dashed lines), SAF-A can form condensates (orange area) inside the cytosol (blue area). The binding-unbinding process can be described as a chemical reaction (black arrows).

dynamics to incorporate simple conversion reactions into a liquid mixture that shows phase separation. Next, we will discuss how this framework can be useful in understanding the phase separation behavior of a specific protein, SAF-A, an RNA binding protein[142].

3.3 SAF-A Phase separation

Together with collaborators in Edinburgh, we used our model to help understand the phase separation behavior of the RNA binding protein SAF-A. SAF-A is involved in regulating the structure of chromatin in human and other mammalian cells[142, 145]. Fig. 3.12 shows a schematic of the SAF-A protein and its functional domains. For our discussion, the RGG domain (red) is important because it contains parts responsible for binding to RNA as well as prion-like domains that are recognized as important drivers of phase separation in cells due to multiple weak interactions [143].

In the first step, we want to build a simple model based on the information we have about SAF-A phase separation. First, the RGG domain of SAF-A phase separates *in vitro* due to associative enthalpic interactions[142]. At the same time, SAF-A proteins can bind to chromatin-associated RNA[142], which we simply call RNA from here on. For high RNA concentration, the SAF-A RNA complex can form a hydrogel like structure with low diffusivity. We translate these properties into a model as shown in fig. 3.13, the SAF-A molecules can exist in two states, either freely diffusing or bound to RNA. In the RNA bound state, their mobility is drastically reduced, which we capture by setting the diffusivity low compared to the free form. We model the switch between the RNA bound and the unbound state as a chemical reaction, where binding to RNA lowers the free energy by a factor of $-\epsilon$, $\epsilon > 0$. In addition, we introduce a new parameter, the number of binding sites N_R that limits the maximum number of SAF-A that can be in the bound state. We do not model the RNA explicitly, but just assume that a certain number of lattice sites in the lattice fluid model are binding sites for SAF-A. The total number of SAF-A proteins in the model is conserved and we assume that the lattice sites not occupied by SAF-A are filled with solvent or cytosol molecules. Lastly, we model the weak attractive interaction of SAF-A using a Flory parameter χ as discussed above. It is not clear if RNA bound SAF-A still interacts weakly or not, which makes a big difference in the model as we will see. Because the number of binding sites is limited and we distinguish between bound and unbound SAF-A, the entropy of mixing is different from a normal ternary system, which we will discuss next.

Modified free energy

We start by deriving the entropy of mixing from a lattice model similar to the regular solution and Flory-Huggins entropy of mixing. We consider M total lattice sites with $N_P = N_B + N_U$ SAF-A proteins, of which N_B are bound and N_U are unbound. The other lattice sites are filled with $N_C = M - N_P$ solvent molecules. In addition, we assume that only N_R lattice sites are binding sites for SAF-A¹⁰, so we first distribute N_B bound SAF-A proteins on N_R binding sites and afterward the remaining $N_U + N_C$ molecules on the $M - N_B$ lattice sites. Thus the number of microstates is given by

$$\Omega = \binom{N_R}{N_B} \binom{M - N_B}{N_U}. \quad (3.26)$$

From the number of microstates we can calculate the entropy of mixing[60] according to

$$\frac{S}{k_B} = \ln \Omega, \quad (3.27)$$

applying Stirling's formula $\ln N! \approx N \ln(N) - N$ for large N we get

$$\ln \binom{N_R}{N_B} \approx N_R \ln N_R - N_B \ln N_B - (N_R - N_B) \ln(N_R - N_B), \quad (3.28)$$

$$\ln \binom{M - N_B}{N_U} \approx (M - N_B) \ln(M - N_B) - N_U \ln N_U - N_C \ln N_C. \quad (3.29)$$

Here, the factor $-N_R$ cancels with $N_B + (N_R - N_B)$ and the factor $-(M - N_B)$ cancels with $N_U + N_C$ since all lattice sites are filled. Assuming equal molecular volume v_0 of all species for simplicity¹¹, we can replace particle numbers by volume fractions and get for the total entropy of mixing, using $\psi_M = N_R/M$

$$\begin{aligned} \frac{S}{k_B} = & N_R \ln \frac{\psi_M}{\psi_M - \phi_B} - N_B \ln \frac{\phi_B}{\psi_M - \phi_B} \\ & + (M - N_B) \ln \frac{1 - \phi_B}{1 - \phi_U - \phi_B} - N_U \ln \frac{\phi_U}{1 - \phi_U - \phi_B} \end{aligned} \quad (3.30)$$

and, finally, for the local entropy density in the local equilibrium approximation $s = S/(Mv_0)$ (we drop a term $\psi_M \ln \psi_M$ because it is constant and constants in the free energy density do

¹⁰: This does not necessarily mean that only N_R RNAs are present, oftentimes specific motifs on the RNA are necessary for the protein to bind[146].

¹¹: Mixtures of multiple proteins, like the cytosol, have a wide size distribution[1]. We thus assume that all proteins have average protein size and neglect chain correlations in the entropy.

not influence the equilibrium properties of the system)

$$\begin{aligned}
 -\frac{sv_0}{k_B} &= (\psi_M - \phi_B) \ln(\psi_M - \phi_B) + \phi_B \ln \phi_B \\
 &\quad - (1 - \phi_B - \phi_U) \ln \frac{1 - \phi_B}{1 - \phi_U - \phi_B} + \phi_U \ln \phi_U,
 \end{aligned}
 \tag{3.31}$$

where we introduce the minus sign because the entropy densities enters the free energy density as $-Ts$. While this form of the entropy density of mixing looks similar to the regular solution in Eq. 2.48, the introduction of limiting binding sites has a significant effect, namely ϕ_B is bound by $[0, \psi_M]$ due to $\ln(\psi_M - \phi_B)$. In addition, the bound particles limit the available space for the unbound SAF-A and cytosol particles to $1 - \phi_B$, which leads to a term $\ln(1 - \phi_B)$ that vanishes if all species are distributed evenly. In general ψ_M can depend on space and time, for example if RNA is inhomogeneously distributed or gets produced/degraded. For now we assume homogeneously distributed binding sites and thus $\psi_M = \text{const}$ and discuss the more complex case later.

The enthalpic part has three contributions, first, an energy gain of $-\epsilon\phi_B$ for the bound SAF-A. Second, the contribution of weak interactions, similar to the regular solution. Thereby, it is not clear whether bound ϕ_B and unbound ϕ_U interact with each other or not, so we propose two enthalpic interactions. Either the bound form does interact, and thus the interaction is described via $\chi(\phi_U + \phi_B)(1 - \phi_U - \phi_B)$ or the bound form does not interact, which leads to $\chi\phi_U(1 - \phi_U - \phi_B)$. These are similar to the forms introduced in Eq. 2.50a and Eq. 2.50b but here the bound form does not interact like the solvent, but like the phase separating protein. And lastly, from the χ parameter we get an interface term¹² with $\kappa_{ij} = -v_0^{2/d}\chi_{ij}$. For now we assume that the bound form of SAF-A does interact and thus the total enthalpy is given by

12: This is the same form of κ we used in Eq. 2.48

$$\begin{aligned}
 \frac{hv_0}{k_B T} &= -\epsilon\phi_B + \chi(\phi_U + \phi_B)(1 - \phi_U - \phi_B) \\
 &\quad + \frac{v_0^{2/d}\chi}{2} [(\nabla\phi_U)^2 + 2(\nabla\phi_U)(\nabla\phi_B) + (\nabla\phi_B)^2].
 \end{aligned}
 \tag{3.32}$$

The corresponding free energy density f is then given by $f = h - Ts$. Using f , we can again calculate the chemical potentials of the bound and unbound forms of SAF-A, which are given by

(neglecting the non-local parts)

$$\frac{\mu_U}{k_B T} = \ln \frac{\phi_U}{1 - \phi_U - \phi_B} + \chi(1 - 2\phi_U - \phi_B), \quad \text{and} \quad (3.33a)$$

$$\frac{\mu_B}{k_B T} = \ln \frac{1 - \phi_B}{1 - \phi_U - \phi_B} + \ln \frac{\phi_B}{\psi_M - \phi_B} + \chi(1 - \phi_U - 2\phi_B) - \epsilon. \quad (3.33b)$$

Thus, the binding strength ϵ corresponds to the internal energy difference Δw for the generic case discussed above. The entropic factor $\ln(\phi_B/(\psi_M - \phi_B))$ ensures that $\phi_B < \psi_M$ so the number of bound SAF-A is limited by the number of binding sites. The chemical potential for the unbound form looks almost identical to Eq. 2.49 with the exception that the bound and unbound forms attract each other unlike forms A and B that we discussed earlier.

As mentioned above, we model the binding-unbinding kinetics as a chemical reaction $U \rightleftharpoons B$ and the ratio of binding to unbinding rate is given by a detailed balance condition Eq. 2.24

$$\frac{s_f}{s_b} = \exp \frac{\mu_U - \mu_B}{k_B T}, \quad (3.34)$$

where the total rate is $s = s_f - s_b$. For the diffusive dynamics we assume that the bound form of SAF-A is immobile compared to the free form $\Lambda_B \ll \Lambda_U = \Lambda$. For example, Ref.[147] found a diffusivity $D \approx 25 \mu\text{m}^2\text{s}^{-1}$ for the free form, while the RNA bound complex had a much lower diffusivity $D \approx 0.04 \mu\text{m}^2\text{s}^{-1}$, so almost three orders of magnitude lower. In this case, the dynamics are given by¹³

$$\partial_t \phi_U = \Lambda \nabla^2 \mu_U - s, \quad \text{and} \quad (3.35a)$$

$$\partial_t \phi_B = \Lambda_B \nabla^2 \mu_B + s. \quad (3.35b)$$

The simulation results shown below were obtained by solving the coupled partial differential equations in Eq. 3.35. But to gain further insight into the system we next introduce a strong binding approximation that simplifies the analytics.

Strong binding approximation

While the weak interactions driving phase separation are on the order $\sim 1k_B T$ [7], the binding strength of RNA binding proteins to RNA is often on the order of $\sim 10k_B T$ [148]. Therefore, we assume that the binding strength ϵ is much larger than the interaction strength χ , $k_B T \epsilon \gg k_B T \chi > k_B T$. Using Eq. 3.33 and Eq. 3.34 we can write the condition for binding equilibrium as

¹³: In the simulations we use a small, but finite Λ_B and neglect it only in the analytical calculations.

$$\mu_B - \mu_U = \ln \frac{\phi_U}{\phi_B} \ln \frac{\psi_M - \phi_B}{1 - \phi_B} + \chi(\phi_B - \phi_U) + \epsilon = 0. \quad (3.36)$$

Using $\epsilon \gg \chi$, $\phi_U + \phi_B = \phi_P$ and $\phi_B \ll 1$, this can be approximated as

$$(\phi_P - \phi_B)(\psi_M - \phi_B) = \phi_B e^{-\epsilon}. \quad (3.37)$$

The factor $\phi_B e^{-\epsilon} \ll 1$ is much smaller than one and for very strong binding it is approximately 0. Thus, the bound fraction can be approximated by $\phi_B = \min(\phi_P, \psi_M)$. Thus, either all proteins are bound or all binding sites are saturated, if the binding reaction is in equilibrium. This depends on the local protein fraction ϕ_P . Since no phase separation is possible for $\psi_M > \bar{\phi}$, we cap $\psi_M \in [0, \bar{\phi}]$ and do not discuss the behavior for $\psi_M > \bar{\phi}$ in detail. For $\psi_M > \bar{\phi}$, the dynamics is determined by the slowest time scale, the unbinding rate s_b , which is a limit we are not interested in at the moment.

In addition, we assume that binding is fast, in Ref.[146] association rates of $\sim 5 \mu\text{M}^{-1}\text{s}^{-1}$ were measured, although for DAZL proteins instead of SAF-A. Thus, for $1 \mu\text{M}$ of RNA binding sites a protein diffuses $\approx 4 \mu\text{m}$ before a binding event happens on average, which is quite far considering nucleus sizes of $\approx 6 \mu\text{m}$ [3]. But due to the strong binding and Eq. 3.34, once proteins are bound the unbinding rate is very low and all binding sites get saturated quickly. A simulation of Eq. 3.35 shown in fig. 3.14 shows that the strong binding approximation works well already for rather low binding strength $\epsilon = 4 \approx \chi$. Thus, we will use $\phi_B \approx \psi_M$ in the following analytical calculation.

Using this result, we eliminate ϕ_B from the free energy replacing it with the binding site density ψ_M . The reduced free energy, and the chemical potential of the unbound SAF-A, in the strong binding approximation are given by

$$\frac{v_0 f_{\text{SB}}}{k_B T} = \phi_U \ln \phi_U + (1 - \phi_U - \psi_M) \ln(1 - \phi_U - \psi_M) + \chi(\phi_U + \psi_M)(1 - \phi_U - \psi_M), \quad (3.38)$$

$$\mu = \ln \frac{\phi_U}{1 - \phi_U - \psi_M} + \chi(1 - 2(\phi_U + \psi_M)). \quad (3.39)$$

In this form, the free energy is almost identical to binary phase separation of total protein $\phi = \phi_U + \psi_M$ from the cytosol. The only difference is that the entropic part contains only the unbound fraction $\phi_U \ln \phi_U$, which is a result of all binding sites being occupied, so the entropy of bound SAF-A is constant. Rewrit-

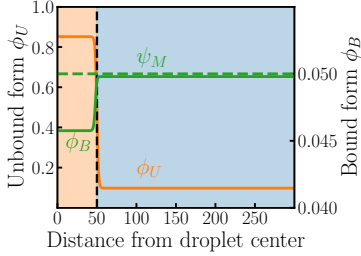


Figure 3.14: Unbound SAF-A forms droplets. Unbound (left axis, orange line) and Bound (right axis, green line) SAF-A volume fractions along the radial cut through a droplet in the steady state. The dashed green line shows the binding site density ψ_M . Even for driving on the order of $k_B T$ (here $\epsilon = 4$), almost all binding sites are saturated. Simulation were done in a spherical symmetric box. Parameters are $\psi_M = 0.05$, $\chi = 3.5$, $\epsilon = 4$ and $\bar{\phi}_P = 0.15$.

ing f and μ in terms of total protein fraction we get

$$\frac{v_0 f_{\text{SB}}}{k_{\text{B}}T} = (\phi - \psi_M) \ln(\phi - \psi_M) + (1 - \phi) \ln(1 - \phi) + \chi\phi(1 - \phi), \quad (3.40)$$

$$\mu = \ln \frac{\phi - \psi_M}{1 - \phi} + \chi(1 - 2\phi). \quad (3.41)$$

In the strong binding approximation, the total fraction of proteins is bound from below by ψ_M because we assume $\bar{\phi} > \psi_M$ and thus $\phi \in [\psi_M, 1]$, while $\phi_U \in [0, 1 - \psi_M]$. The corresponding free energy density for different binding site densities is shown in fig. 3.15. Varying ψ_M from 0 to $\bar{\phi}$ (light to dark blue) for fixed $\bar{\phi}$ shifts the SAF-A fraction in the dilute phase ϕ^{out} to higher values because the bound SAF-A is homogeneously distributed; see fig. 3.14 as well. Thus, high binding site densities suppress phase separation, and above a critical binding site density no droplets form. To calculate the equilibrium SAF-A fractions in droplet and solvent phase the Maxwell construction is still valid and for small $\bar{\phi}$ and ψ_M we assume that the solvent phase increase is linear in ψ_M , $\phi^{\text{out}}(\psi_M) \approx \phi_0^{\text{out}} + \psi_M$. In this case, the predicted steady state droplet volume is

$$\frac{V_D}{V_{\text{sys}}} = \frac{\bar{\phi} - \phi_0^{\text{out}} - \psi_M}{\phi^{\text{in}} - \phi_0^{\text{out}} - \psi_M}. \quad (3.42)$$

ϕ^{in} and ϕ_0^{out} are derived from a Maxwell construction to the binary free energy for $\psi_M = 0$. The behavior is reminiscent of phase separation with conversion reactions (discussed in Sec. 3.2). Here, the binding site densities limit the amount of free SAF-A and thus inhibit phase separation, while there the internal energy difference Δw controls the total amount of phase separating material. In both cases, Ostwald ripening and coalescence lead to a single droplet and more sophisticated processes are necessary to control droplet size and number.

The dependence of total droplet volume on binding site density is shown in fig. 3.16 for numerical simulations as well as predictions from Eq. 3.42. The linear approximation $\phi^{\text{out}}(\psi_M) \approx \phi_0^{\text{out}} + \psi_M$ fits well to the numerical results. In addition, we find that total droplet volume decreases linearly with binding site density and vanishes above a critical binding site density as expected from fig. 3.15.

Localized binding sites can nucleate droplets

So far we only discussed homogeneous and time independent distributions of binding sites. But RNA and RNA binding motifs

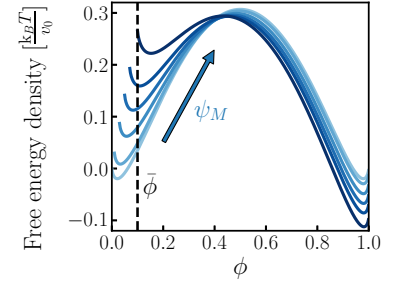


Figure 3.15: Effective free energy density for the strong binding approximation. Reduced free energy density, Eq. 3.40, as a function of total SAF-A fraction for different binding site densities. Here ψ_M is varied between 0 and $\bar{\phi}$ and darker color signifies higher ψ_M . More binding sites imply that less free SAF-A can move to form droplets. Therefore, higher ψ_M shifts the effective ϕ^{out} and thus reduces the propensity to phase separate. Parameters are $\chi = 4$ and $\bar{\phi} = 0.1$

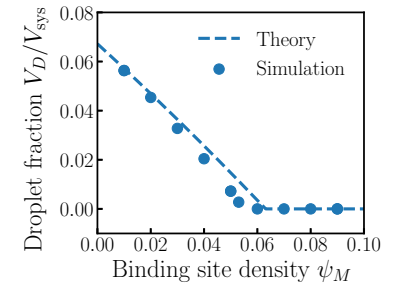
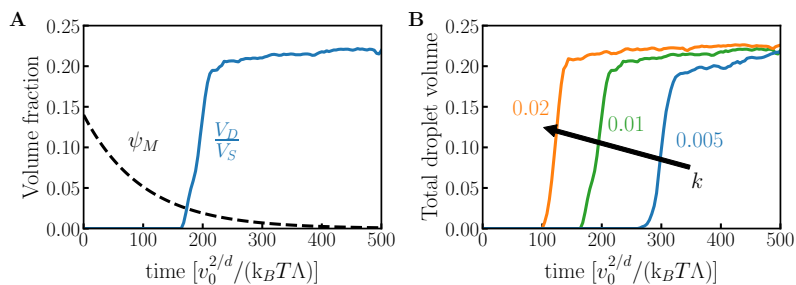


Figure 3.16: RNA saturation density controls droplet size. Steady state droplet size as a function of binding site density. Blue dots are simulations and the dashed lines are predictions from Eq. 3.42. For low binding site densities ψ_M the total droplet size decreases linearly with ψ_M , while droplets fully dissolve for high binding site densities. Parameters used are $\chi = 3.5$, $\epsilon = 4$ and $\bar{\phi} = 0.1$.

Figure 3.17: Degradation of RNA leads to droplet formation. Total droplet volume (solid lines) as a function of time. **A** Shows the decay of RNA binding site density (black dashed line) for $k = 0.01$. For low enough ψ droplets can form (blue line). **B** Droplet volume for different decay rates k . Faster decay corresponds to earlier droplet formation. Parameters used are $\chi = 4$, $\bar{\phi} = 0.25$ and $\psi(0) = 0.15$.



can be degraded or created and thus $\psi_M(t)$ can change over time. In addition, RNA is not homogeneously distributed and neither are the binding sites so $\psi_M(\mathbf{x})$ can depend on space as well. We start by discussing homogeneously distributed binding sites that get degraded over time with a degradation rate k . In this case, $\psi_M(t)$ is given by

$$\psi_M(t) = \psi_M(0) \exp(-kt). \quad (3.43)$$

The dynamics for this case are shown in fig. 3.17. The effect of RNA degradation is straightforward: For high ψ_M no droplets can form, as discussed above but, once the binding site density is low enough, droplets start to form; see fig. 3.17A. Increasing the degradation rate shifts the droplet nucleation to earlier times; see fig. 3.17B. The effective control of free SAF-A via ψ_M allows crossing the phase boundary between a homogeneous and a phase separating state. Because the RNA levels are cell cycle dependent[69] this is a possible mechanism to time droplet formation and dissolution and to couple it to other cellular processes.

The effect of spatially inhomogeneous binding site distribution $\psi(x)$ is less obvious and depends on whether bound SAF-A still interacts weakly, and thus contributes to the enthalpic gain of droplets, or not. If it does not interact, so $h = \chi\phi_U(1 - \phi_U - \phi_B)$, areas of high $\psi(x)$ should repel droplets or have no influence on droplet formation. But if bound SAF-A does still interact, so $h = \chi(\phi_U + \phi_B)(1 - \phi_U - \phi_B)$, we would expect that areas of high binding site density act as nucleation centers. The reason is, that local enrichment of bound SAF-A will lead to an accumulation of free SAF-A around the area of bound SAF-A and thus nucleate droplets¹⁴. To test this we simulate a 2-dimensional system where the RNA is centered in a circle around the center. Inside the circle, the binding site density is much higher than outside. We then compare the results to homogeneously distributed binding sites with the same total amount of binding sites. For an average concentration $\bar{\phi}$ in the nucleation and growth regime, so

¹⁴: If the total SAF-A fraction is chosen such that the system is in the nucleation and growth regime, i.e. $\bar{\phi}$ is below the spinodal volume fraction.

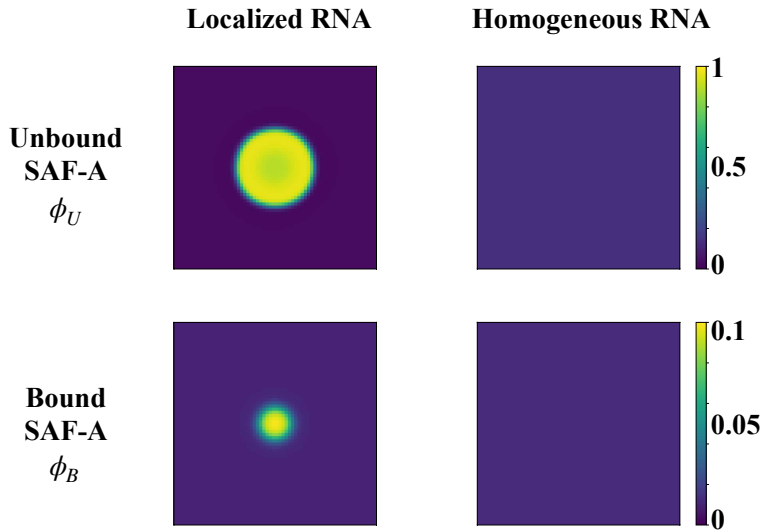
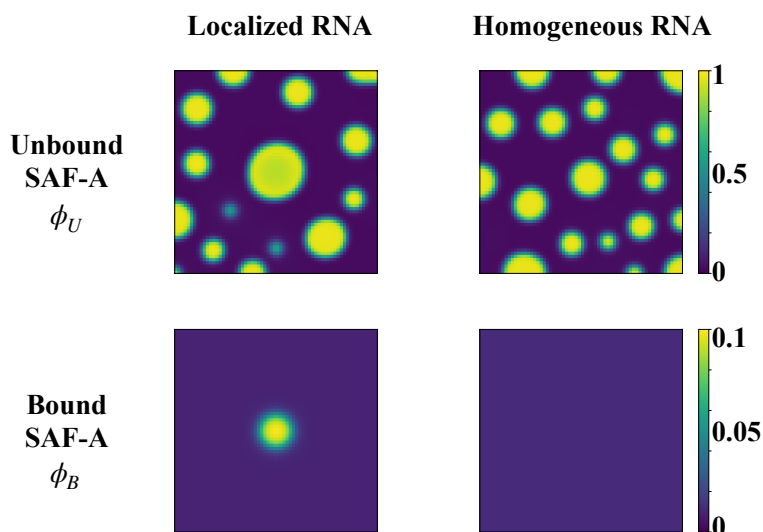


Figure 3.18: Localized binding sites can nucleate SAF-A droplets. Shown are simulations of unbound (top) and bound (bottom) SAF-A for binding sites localized in the center (left) and homogeneously distributed (right). The localized binding sites are initialized with a tanh function where the inside is $\psi_M = 0.1$ and the outside is $\psi_M = 0.01$ because $\psi_M = 0$ leads to problems with the numerics. $\bar{\phi} = 0.15$ is chosen such that the system is in the nucleation and growth regime. Parameters used are $\chi = 4$, $\epsilon = 4$, $\bar{\phi} = 0.15$, $\bar{\psi}_M = 0.011$.

$\bar{\phi}$ is smaller than the spinodal fraction, we see a co-localization of the droplet and binding sites, see fig. 3.18 left panels, while for homogeneously distributed binding sites, no droplets form, see fig. 3.18 right panels. This effect is only observed if the sum of unbound and bound SAF-A in the localization center exceeds the spinodal fraction. In other cases, noise would be necessary to nucleate droplets. It would be interesting to test whether localized binding sites together with noise lead to controlled nucleation sites. On the other hand, if the average fraction lies above the spinodal fraction, as shown in fig. 3.19, droplets form everywhere both with localized and homogeneously distributed binding sites. However, for localized binding sites the first droplet forms reliably at the high binding site area and is significantly larger than the other droplets; see fig. 3.19 top left panel. This effect could be a reliable way for the cell to accumulate SAF-A around RNA even without having enough binding sites for each protein.

In conclusion, localized binding sites can have the opposite effect of homogeneous binding sites. While the former can facilitate phase separation, locally push the system over the spinodal, and control where droplets nucleate, the latter generally suppresses phase separation. In addition, a time dependent binding density can switch between states where droplets form and dissolve over time. The nucleation induced by localized RNA corresponds to the ‘Scaffolded Condensate Model’ introduced by us in Ref.[73] as a possible mechanism of size control of droplets in sub saturated solutions.

Figure 3.19: SAF-A phase spinodal decomposition for localized RNA binding sites. Shown are simulations of unbound (top) and bound (bottom) SAF-A for binding sites localized in the center (left) and homogeneously distributed (right). The localized binding sites are initialized with a hyperbolic tangent function $\tanh(r - r_0)$ function where the inside is $\psi_M = 0.1$ and the outside is $\psi_M = 0.01$ because $\psi_M = 0$ leads to problems with the numerics. $\bar{\phi} = 0.25$ is chosen such that the system is in the spinodal decomposition regime. Parameters used are $\chi = 4$, $\epsilon = 4$, $\bar{\phi} = 0.25$, $\bar{\psi}_M = 0.011$.



FRAP simulation

An important method to quantify the liquid like properties of biomolecular condensates is **Fluorescence Recovery After Photobleaching** (FRAP)[34], which quantifies the dynamical exchange of particles between condensates and cytosol. To perform FRAP molecules that are enriched in the droplet are marked with a fluorescent marker. After droplet formation, the droplet is visible under a light microscope due to the fluorescent markers; see fig. 3.20A. In the next step, a high intensity light source illuminates a small probe area to induce stimulated emission which increases the emission rate of the fluorescent marker. The high emission rate depletes the marker because it emits only a limited number of photons and thus it turns dark upon the illumination, this is the bleaching step in fig. 3.20A. Over time depleted markers leave the droplet and new molecules enter because of the fast exchange of particles with the surrounding. As a result, the fluorescence signal recovers over time; see fig. 3.20A and B. The time it takes to recover to the original signal strength can be used to get information on the diffusion rates of molecules[149]. Oftentimes the signal does not recover to the base level before bleaching. In the case of SAF-A, this is attributed to the bound SAF-A being immobile and thus the difference between the initial signal and recovered signal can be used to get an estimate on ψ_M [142].

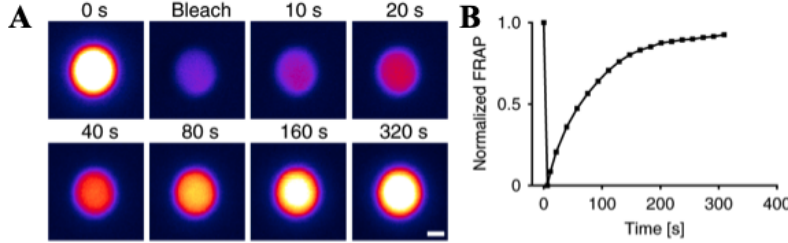


Figure 3.20: Experimental example of Tau-GFP FRAP. **A** Microscopy image of a Tau protein droplet with a fluorescent marker GFP. After bleaching (second top panel) the fluorescent signal decreases significantly and slowly recovers over 320 seconds because of particle exchange with the surrounding. **B** Time course of the fluorescence signal after bleaching at $t \approx 0$. The time it takes to recover the initial fluorescence signal can be used to calculate the particles diffusivity[149]. Image modified from [150] under the Creative Commons license.

We can simulate FRAP using our model by introducing two extra species, bleached versions of the bound and unbound SAF-A; see fig. 3.22. The simulation procedure is the following: We start with a single droplet in a two dimensional box and let it equilibrate. Afterward, at $t = 0$, we relabel a fixed fraction of bound and unbound SAF-A as bleached and consider them as individual species that behave exactly like their unbleached counterparts. Then, we let the system evolve further and due to diffusion, the bleached and unbleached species start to mix. A qualitative simulation of the process is shown in fig. 3.22, where the effect of the immobile bleached fraction can be seen as a bright spot of the bleached SAF-A (darker spot in the unbleached SAF-A) in the bleached region even after recovery time (right panels). We can then monitor the unbleached SAF-A fraction in the droplet center to get the recovery rate as shown in fig. 3.21 for two different binding site densities. Notably, the fraction that does not recover is exactly the binding site density¹⁵. This analysis suggests that the immobile fraction found in FRAP experiments could be a good indicator of the binding site density. In addition, the long timescales, unbinding rates, and SAF-A-RNA complex diffusion could in principle be measured if the FRAP experiment is long enough to see the recovery of the immobile fraction. However, these timescales might exceed fluorescence lifetimes.

Model predictions

Our qualitative model leads to a set of predictions on SAF-A phase separation that are testable experimentally. First, for homogeneous distribution of RNA, phase separation is suppressed for high RNA levels (high binding site density ψ_M), while it is favored for low RNA levels. Second, increasing the interac-

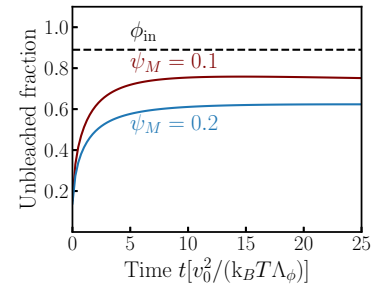


Figure 3.21: Numerical simulation of FRAP for different binding site densities. Fraction of unbleached proteins in the droplet center as a function of time after bleaching. The signal does not recover to the equilibrium fraction ϕ_{in} (black dashed line), because the bound form is immobile and does not recover on this time scale. ψ_M can be inferred from the difference between the recovered signal and the initial signal. Parameters used are $\chi = 3.5$, $\epsilon = 4$, $\Lambda_B = 0.001\Lambda$ and $\psi = 0.1$

¹⁵: Because of finite size effects the recovery in fig. 3.22 is even lower, but for fig. 3.21 we used spherical symmetric simulation boxes to simulate bigger systems and avoid this effect.

tion strength, e.g. by changing the sequence, should increase the threshold of binding site density for which phase separation is suppressed. Furthermore, we expect the binding ϵ to be strong, on the order of $10k_B T$ [148], so the strong binding approximation is fulfilled. Only very strong disruptions in the RNA binding domain should have an impact on the phase separation properties of SAF-A. At the moment it is not clear if RNA bound SAF-A can still interact with itself, i.e. if the enthalpic interaction is better described by $h = \chi(\phi + \psi)(1 - \phi - \psi)$ or $h = \chi\phi(1 - \phi - \psi)$. This can be tested in several ways, first, the suppression of phase separation is stronger if bound SAF-A does not contribute to the enthalpy, similar to the ternary case discussed above. Second, if the bound SAF-A does interact, we expect that localized RNA acts as a nucleation center, so high local RNA concentrations should coincide with droplet formation. And third, we expect that SAF-A phase separation is coupled to cell cycle or transcription state [69] because the number of binding sites varies with RNA transcription activity.

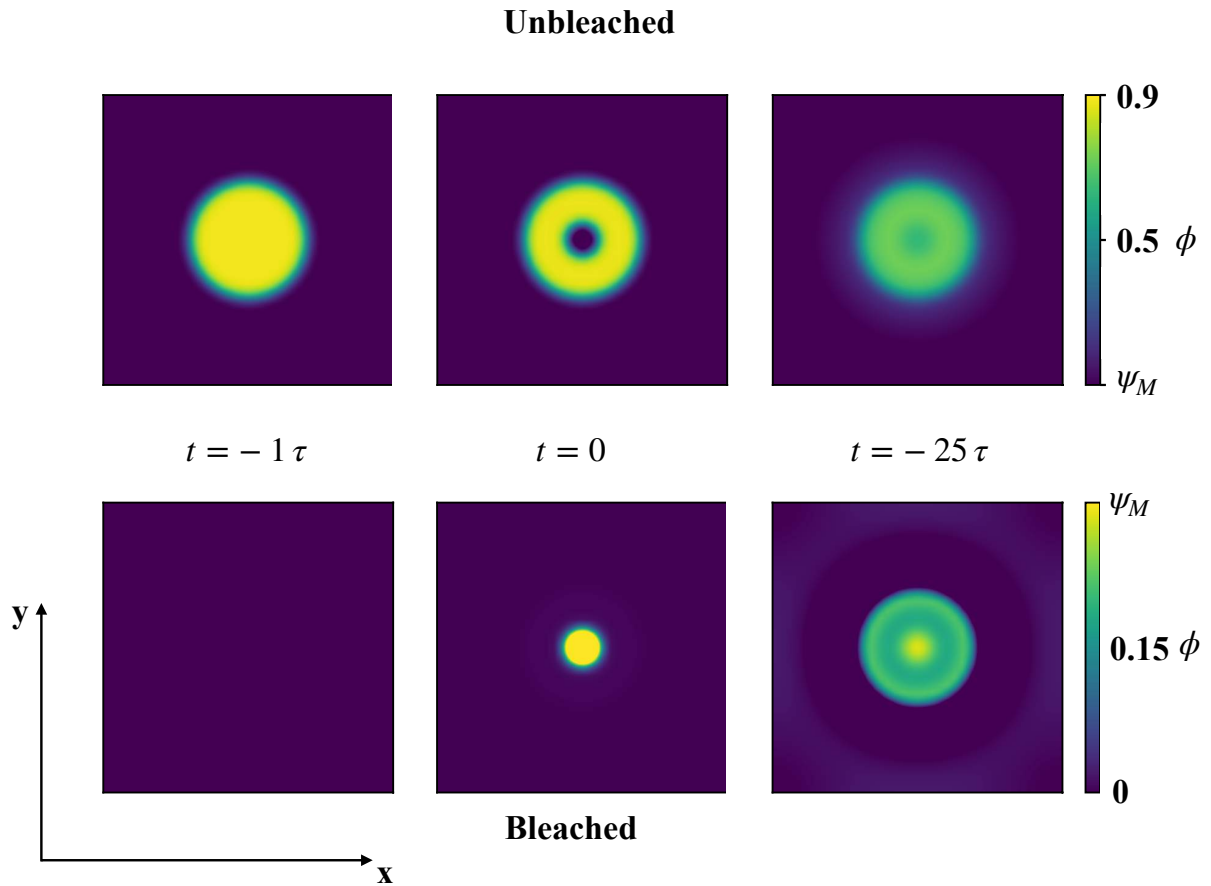


Figure 3.22: 2-dimensional Numerical Simulation of FRAP. Before the bleaching process, for $t < 0$, a single SAF-A droplet forms (top-left panel) and no bleached SAF-A is present (bottom-left panel). At $t = 0$, the center of the droplet gets bleached in an area smaller than the droplet size. Now the proteins in the center of the droplets are relabeled as bleached SAF-A (bottom-center panel). As a result, there appears to be a hole in the unbleached protein field (top-center panel). Over time the two species mix, the bleached SAF-A smears out (bottom-right panel) and the hole gets filled with unbleached proteins again (top-right panel). Parameters are $\chi = 3.5$, $\epsilon = 4$, $\psi_M = 0.2$, and $\bar{\phi} = 0.4$.

3.4 Droplets control chemical reactions

So far we discussed how passive chemical reactions can be used to control if droplets form as well as their size. Here, we discuss the opposite case, namely how the properties of a reaction are influenced by the presence of a phase-separated fluid mixture. For the case of amyloid fibers, this has been investigated in Refs.[134, 151] and they found that the droplet state can have an impact on fiber formation and length distribution under the condition that the diffusivities decrease for longer fibers, as the Stokes-Einstein relation predicts. Here, we want to focus on the effect of a two phase system on the equilibrium ratio and dynamics of a reaction, in the case that the reactants and products have certain affinities for one of the phases as described by the partition coefficient; see Eq. 3.11. We assume both phases are dominated by one species, B or C , oftentimes called scaffolds[5, 152] while the other species, often called clients, do not influence phase equilibrium and distribute into the two phases according to their affinity.

Chemical equilibrium in droplets

16: We assume that R and P have the same molecular volume, so the reaction conserves volume.

The first step is to check whether chemical equilibrium of a simple conversion reaction $R \rightleftharpoons P$ is influenced by phase separation, where R is called reactant and P is the product. As discussed in Ch. 2, the force driving the reaction is the chemical potential difference between the reactant chemical potential, μ_R , and product chemical potential, μ_P , which is given by¹⁶

$$\frac{\mu_R - \mu_P}{k_B T} = \ln \frac{\phi_R}{\phi_P} + \Delta w + \Delta h, \quad (3.44)$$

where $\Delta w = w_R - w_P$ is the internal energy difference and $\Delta h = h_R - h_P$ is the interaction energy difference between R and P . In the analytical model, we describe the two phases by their volumes V_1 and V_2 and for a given system volume V_{sys} the ratio of the two phases, V_1/V_2 , is an important parameter. We assume that each phase predominantly consists of one scaffold species, either 1 or 2 and the clients P and R do not influence phase separation. But we assume that they are influenced by phase separation because the scaffolds interact specifically with reactant R through $h_{R,1/2}$, and product P through $h_{P,1/2}$. From the interactions, we can define equilibrium partition coefficients¹⁷

17: See Appendix.D for a calculation of the partition coefficient of dilute species.

for R and P

$$\Gamma_R = \frac{\phi_{R,1}}{\phi_{R,2}} = \exp(h_{R,2} - h_{R,1}), \quad \text{and} \quad (3.45a)$$

$$\Gamma_P = \frac{\phi_{P,1}}{\phi_{P,2}} = \exp(h_{P,2} - h_{P,1}), \quad (3.45b)$$

the partition coefficient describes the enrichment ($\Gamma_i > 1$) or depletion ($\Gamma_i < 1$) of species i in phase 1 compared to phase 2. In addition, we can calculate an equilibrium ratio by setting Eq. 3.44 to 0 in each phase

$$K_1 = \frac{\phi_{R,1}}{\phi_{P,1}} = \exp(-\Delta w - \Delta h_1), \quad \text{and} \quad (3.46a)$$

$$K_2 = \frac{\phi_{R,2}}{\phi_{P,2}} = \exp(-\Delta w - \Delta h_2), \quad (3.46b)$$

where $\Delta h_i = h_{R,i} - h_{P,i}$ for $i = 1, 2$. To see the influence of phase separation on reactive equilibrium, we plot the fraction of reactants and products for different phase volumes ψ in fig. 3.23. We see that if reactants enrich in phase 1 and products in phase 2, by increasing the volume of phase 1 the amount of products decreases and the amount of reactants increases. As a result the relative phase volume determines which site of the reaction, reactants or products, is more stable.

To compare the behavior to a homogeneous mixture and see whether phase separation influences the dynamics and equilibrium of the reaction discussed above, we simulate a homogeneous mixture with the same average composition of scaffolds as the two phase system, i.e. a fixed value V_1/V_2 . The simulation is done for an incompressible, four component regular solution, where the total fraction of scaffold 1 and 2 is identical and the fraction of reactants and products is low. The dynamical equations become

$$\partial_t \phi_1 = \Lambda \nabla^2 \mu_1, \quad (3.47a)$$

$$\partial_t \phi_R = \Lambda \nabla^2 \mu_R - k(\exp(\mu_R/k_B T) - \exp(\mu_P/k_B T)), \quad \text{and} \quad (3.47b)$$

$$\partial_t \phi_P = \Lambda \nabla^2 \mu_P + k(\exp(\mu_R/k_B T) - \exp(\mu_P/k_B T)), \quad (3.47c)$$

where incompressibility was used to remove scaffold species 2, all diffusive mobilities were chosen identical and transition state theory was used to describe the reaction. We start with a two-phase initial condition and first let R and P partition into the phases without reactions present. After equilibration, we turn on the reactions and monitor the relaxation to equilibrium as shown in fig. 3.24 (blue and maroon lines). We then simulate a homo-

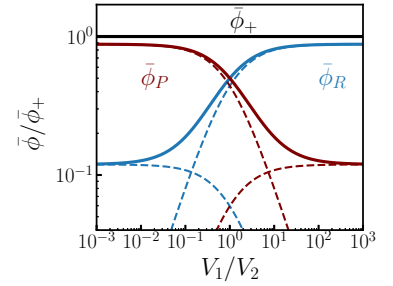


Figure 3.23: Chemical equilibrium is determined by phase separation. Average volume fractions of reactants (blue) and products (maroon) as a function of relative phase volume V_1/V_2 . The dashed lines correspond to the contributions from each phase. Parameters used are $\Delta w = 0$, $\Delta h_1 = -2$, $\Delta h_2 = 2$ and $\bar{\phi}_P + \bar{\phi}_R = 0.02$.

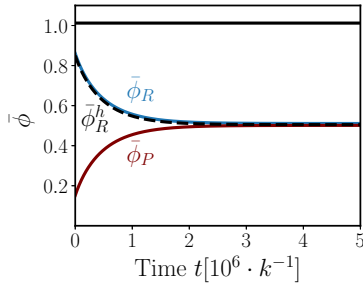


Figure 3.24: Comparison of the dynamics for a homogeneous and phase separated system. The relaxation of the conversion reaction for a phase separated (solid lines) and homogeneous (dashed black line) are shown. In the phase separated system both product (maroon) and reactant (blue) are shown. The relaxation behavior is the same with and without phase separation. The black line is the total amount of P and R . Parameters used are $\chi = 3$, $\Delta w = 0$, $\Delta h_1 = -2$, $\Delta h_2 = 2$, $k = 0.0001 \Lambda v_0^{2/d}$ and $\bar{\phi}_P + \bar{\phi}_R = 0.02$.

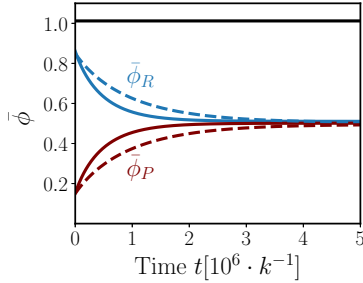


Figure 3.25: Dynamics in a phase separated system for different rates. The relaxation of the conversion reaction in a phase separated system for homogeneous (solid lines) and phase dependent (dashed lines) reaction rates. The product (maroon) and reactant (blue) are shown. The relaxation behavior is influenced by phase separation for spatially dependent reaction rates (here $k\phi_1$). The black line is the total amount of P and R . Parameters used are $\chi = 3$, $\Delta w = 0$, $\Delta h_1 = -2$, $\Delta h_2 = 2$, $k = 0.0001 \Lambda v_0^{2/d}$ and $\bar{\phi}_P + \bar{\phi}_R = 0.02$.

18: Here we assume $v_R = v_0$ and $v_P = 2v_0$ to conserve volume.

geneous mixture with the same initial composition as shown as a black dashed line in fig. 3.24. We find that although parameters are chosen such that reactants enrich in phase 1 while products enrich in phase 2, the relaxation is identical to the homogeneous mixture. This picture would change if the reaction rate is different in the two phases as shown in fig. 3.25. In general, there is no a priori way to see that the reaction rate is different or the same in both phases, but the rate can be controlled by enzymes that can partition into one phase and thus make the rate depend on phase.

We here choose a constant reaction rate because we want to understand how chemical equilibrium is influenced by phase separation. And in modeling, we are able to disentangle kinetics from equilibrium by varying them independently of each other. The result is that chemical equilibrium is not influenced by phase separation if the composition of the homogeneous mixture is the same as the phase separated state. The reason is, that the reaction is driven by chemical potential differences instead of local concentration and the interactions are additive. So it is irrelevant if the interactions are strongly localized or homogeneously spread, as long as the average interaction in the system is the same. This in turn would change if we include higher order terms in the interaction, for example, three body interactions because they are not additive anymore.

Kinetics of an association reaction

Lastly, we discuss an association reaction $R + R \rightleftharpoons P$ and how phase separation influences the dynamics under the assumption of constant reaction rate. This is an interesting problem because mass action kinetics predicts a forward rate $k_f \phi_R^2$ and a backward rate $k_b \phi_P$ and thus for inhomogeneous mixture a total rate of

$$S_h = V_{\text{sys}} k_f \phi_R^2 \quad (3.48)$$

while in a perfect enrichment of R into phase 1, $\phi_{R,1} = \phi_R \frac{V_{\text{sys}}}{V_1}$ the rate becomes

$$S_1 = V_1 k_f N_R^2 \frac{V_{\text{sys}}^2}{V_1^2} = V_{\text{sys}} k_f N_R^2 \frac{V_{\text{sys}}}{V_1}, \quad (3.49)$$

which results in a speedup of $\frac{V_{\text{sys}}}{V_1}$ because the probability for particles to meet is increased. But is this still the case if we include the influence of interactions on the reaction? To answer this question, we repeat the simulation for the simple conversion reaction with the association reaction $R + R \rightleftharpoons P$ ¹⁸. The result is shown in fig. 3.26 and it shows that the equilibrium position is influenced by the presence of phase separation. We suspect the

reason is, that the driving force is now $2\mu_R - \mu_P$, together with the entropy of mixing depending on particle size as discussed in Eq. 2.30[22]. But we only started investigating this effect and further research is necessary.

3.5 Summary

In this chapter, we extended a standard model for phase separation, the binary regular solution model, to a ternary system, where the phase separating protein B can exist in a second state A that does not phase separate. The two states are connected via a simple conversion reaction $A \rightleftharpoons B$. Using detailed balance of the rates and transition state theory, we show that there is a thermodynamic connection between reactions and phase separation because the non-ideal interactions that drive phase separation enter the free energy change of reaction. The reason for this is that the chemical potential is the driver of both processes, reaction, and diffusion. As a result in non-ideal mixtures the equilibrium ratio K , which describes the equilibrium state of a reaction, depends on the local concentration of particles; see fig. 3.2 and fig. 3.3. In addition, we showed that phase separation and chemical equilibrium are compatible, unlike in a binary mixture; see fig. 3.6. We identify the internal energy difference $\Delta w = w_A - w_B$ as an important control parameter of the system, see fig. 3.4, besides the interaction strength χ and the total protein fraction ϕ_+ . Since the internal energy difference is a constant in the chemical potential, it can not influence standard phase separation due to particle conservation and becomes important only when particle numbers or type can change, for example in a reaction.

The internal energy difference controls how much of the total protein is present in state A or B and by controlling the amount of B it can ultimately control phase separation. However, we find that precise control of droplet size is only possible in a very narrow range of Δw and restricted to $\Delta w \approx \chi$; see fig. 3.11. We showed that a simple conversion reaction can control phase separation via Δw , independent of interaction strength χ , temperature T or total protein fraction ϕ_+ . For a biological system, this control can only be achieved either on evolutionary timescales or via global parameters. For example, Δw can depend on temperature, pressure, or pH. But the change of global parameters is in general not well suited for droplet control because it affects all kinds of cellular processes. Though there are examples of biomolecular condensates that form as a response to changes in global parameters, such as stress granules[139]. As a result, passive reactions can play a role in the control of droplet formation and dissolution but are insufficient for precise and fast

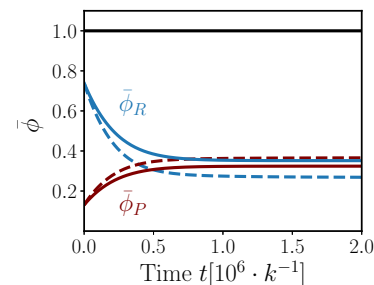


Figure 3.26: Dynamics in a phase separated system for an association reaction. The relaxation of the association reaction in a phase separated system for homogeneous (solid lines) and phase dependent (dashed lines) reaction rates. The product (maroon) and reactant (blue) are shown. The equilibrium position is influenced by phase separation and increases the equilibrium fraction of products. The black line is the total amount of P and R . Parameters used are $\chi = 3$, $\Delta w = 2.5$, $\Delta h_1 = -2$, $\Delta h_2 = 2$, $k = 0.001 \Lambda v_0^{2/d}$ and $\bar{\phi}_P + \bar{\phi}_R = 0.02$.

control of droplets. Such reactions can neither control droplet number nor individual droplet size. The underlying cause is that passive systems relax to thermodynamic equilibrium and it is difficult to change equilibrium properties (internal energies, interaction energies). Quantities that are easier to control, e.g. reaction rates via enzymes, do not influence the equilibrium state. Therefore, to gain fast and precise control it is necessary to go beyond passive reactions, which we will do in the next chapter.

We applied the framework to an example in cells, the phase separation behavior of SAF-A and its interaction with RNA. It is known from experiments[142, 145] that SAF-A contains a low complexity RGG domain that can both, bind to RNA[142] and phase separate in vitro. In its RNA bound form, SAF-A diffuses significantly slower than in the free form[3]. As a minimal model incorporating this information, we build a ternary liquid model, where SAF-A can exist in two forms, an immobile, RNA bound form and an unbound form; see fig. 3.13. In addition, we introduce a new parameter, the binding site density ψ_M which limits the number of bound SAF-A, either due to low RNA levels or the low number of binding motifs necessary for bond formation. Because RNA binding is usually much stronger than the weak interaction driving phase separation, we assume all bounds are saturated. We find a simple equilibrium model that shows that the number of binding sites decreases the phase separation propensity by limiting the number of SAF-A molecules that can move together to form droplets; see fig. 3.15. Furthermore, time dependent binding site density, for example, due to transcription dependent RNA levels, can control droplet formation by releasing the SAF-A and lifting the concentration above the phase separation threshold; see fig. 3.17. Counterintuitively, under the condition that bound SAF-A still interacts weakly with other SAF-A, localized binding sites can act as nucleation centers instead of suppressing phase separation as shown in fig. 3.18. And lastly, we showed how our model can be used to simulate FRAP experiments and get information about SAF-A mobility as well as an estimate for the binding site density in experiments.

In the last part, we started discussing the effect of phase separation on reactions if reactants and products have a certain affinity for either of the phases. We found that the equilibrium ratio of a simple conversion reaction $R \rightleftharpoons P$ depends on the relative phase volumes; see fig. 3.23. In addition, for a fixed amount of scaffold proteins 1 and 2, the relaxation to equilibrium of the reaction is not influenced by phase separation if the reaction rate is the same in both phases. The reason is that the chemical potential drives phase separation and we consider only second order interactions which are additive, so the total interaction is the same in the homogeneous and phase separated mixture;

see fig. 3.24 and fig. 3.25. Lastly, the chemical equilibrium of more complex reactions, for example, association reactions, is influenced by phase separation. But the mechanism is different than the one predicted from mass action kinetics because of the non-ideal chemical potentials; see fig. 3.26. However, this is only a proof of principle and this part needs more research to understand which effect is responsible for the shift in equilibrium ratio and speed up of relaxation to equilibrium.

Active Reactions

4

So far we have discussed equilibrium processes only. But inside cells, many processes are driven out of equilibrium mostly by the constant supply of chemical energy[153]. This chemical energy is usually supplied via hydrolysis of nucleoside triphosphates (NTPs) that are converted into nucleoside diphosphates (NDPs) (or nucleoside monophosphates (NMPs)) and a phosphate group. Examples include GTP, CTP, or UTP, but the most prominent one is ATP[154], which is the one we use as an example. Chemical energy can be used to drive reactions that would otherwise be energetically unfavorable, like phosphorylation of proteins[153], and thereby control which reactions occur. But chemical energy can also be converted into movement, for example, the movement of molecular motors[155, 156] hydrolyses one ATP per motor step. In this example, the motors (myosin, kinesins, and dyneins) 'walk' on polar filaments (actin or microtubules), and the ATP driven reaction breaks the left-right symmetry of motor steps, which leads to simultaneous directed motion (ATP driven) and random motion (thermally driven) on a line. The main ingredients are broken detailed balance, leading to left-right symmetry breaking, and non-equilibrium thermodynamics, which couple chemical reactions and force-generating processes[115].

In cells the ATP hydrolysis reaction $\text{ATP} + \text{H}_2\text{O} \rightleftharpoons \text{ADP} + \text{P}_i$, where $\text{P}_i = \text{PO}_3$ is an inorganic phosphate group, is kept away from equilibrium via ATP production by the ATPase enzymes[157]. Since the ATP consumption rate in cells is high, it has to be replenished quickly to keep the reaction out of equilibrium[158]¹. Under physiological conditions the free energy of reaction is $\Delta F = \mu_{\text{ATP}} + \mu_{\text{H}_2\text{O}} - \mu_{\text{ADP}} - \mu_{\text{P}_i} \approx 15 - 30 k_{\text{B}}T$ [1]. The energy is dissipated as heat if the reaction proceeds alone, but the energy is also used² to drive other reactions. The stereotypical reactions we have in mind are post-translational modifications, which are known to play an important role in formation of biomolecular condensates[73, 159]. As an example, we introduce a phosphorylation-dephosphorylation reaction cycle, in which a protein can be either phosphorylated, state A , or not, state B . Oftentimes, these two reactions are driven by enzymes, where kinases K are specific enzymes for the phosphorylation reactions and phosphatases P are enzymes that catalyze the dephosphorylation reaction[3]. Taken together, the reaction cycle is given by the phosphorylation and dephosphorylation reactions

| | |
|---|-----|
| 4.1 Non-equilibrium reaction | 77 |
| Driven reaction cycle | 79 |
| Non-equilibrium steady state | 81 |
| Energy cost to control droplets | 84 |
| 4.2 Enzymatic reactions | 87 |
| Enrichment in droplets | 87 |
| Active droplets | 89 |
| 4.3 Binary active droplets | 91 |
| Collective dynamics | 93 |
| Single droplet growth | 94 |
| Linearization | 101 |
| 4.4 Multicomponent active droplets | 103 |
| Droplet size in cells | 107 |
| 4.5 Reactions as a switch for Droplet | 109 |
| 4.6 Summary | 111 |

1: For example, in a bacterial cell of $1 \mu\text{m}^3$ volume, 10^{10-11} ATPs molecules are consumed/produced per hour[1]

2: The energy released by ATP hydrolysis is not converted perfectly into usable energy for other processes. Instead, parts of the energy are dissipated as heat. The efficiency depends on the process, just like any thermodynamic process involving energy conversion.



So one of the three phosphoryl groups of ATP is taken up by the protein in the phosphorylation reaction (Eq. 4.1a) and released as a free P_i in the dephosphorylation reaction (Eq. 4.1b). Since the enzymes appear on both sides of the reaction equation, they do not influence the free energy of reaction, but they are important for the reaction kinetics. The main point is, that the energy of ATP hydrolysis is used to create high energy states, here A , that would not be present in equilibrium. This chapter aims to investigate the effect of such a non-equilibrium reaction on phase separating proteins.

Phase separation and chemical activity are linked in another context, motility induced phase separation (MIPS)[160]. Here active, Brownian, or self-propelled particles phase-separate due to concentration-dependent mobilities[161]. The particle-based dynamics can be mapped to a field theory that is similar to model B[161]. But the activity leads to two extra terms that are forbidden by symmetry in passive systems: One of them can be included in the free energy[162] and one has to be added to the diffusive fluxes directly[163]. In this context, the combination of model A and model B in ternary systems has been discussed in detail as well[120]. The derived field theories show a variety of new phenomena, for example travelling waves[120], multiphase systems[163] or reversed Ostwald ripening[163]. In all these systems, activity leads to the directed motion of particles, a hallmark of active matter[164], which in turn leads to collective phenomena[160]. This is different from activity in our models, where driven chemical reactions drive transition between protein states and those states have different properties³.

3: In our case, different internal energies, interaction properties, or mobilities.

In this chapter, we extend the model discussed in Ch. 3 to include active reactions that drive the system away from equilibrium. We start by introducing fuel F and waste W molecules that supply the external energy and couple them to the conversion reaction between protein state A and B discussed in Ch. 3. Afterward, we introduce a non-equilibrium reaction cycle and discuss the effect of reaction kinetics on the non-equilibrium steady state of droplets. In particular, we discuss how enzymes, which catalyze the driven reaction, can control droplet formation and dissolution. Finally, we show how enzymes that distribute inhomogeneously and partition into droplets can control individual droplet size.

Parts of this chapter are based on results from Kirschbaum,

Zwicker, ‘Controlling biomolecular condensates via chemical reactions’, *J. R. Soc. Interface* (2021)**18**[105]. In particular, Sec.4.1, Sec.4.2, and Sec.4.4 contain more detailed discussions about the model used in Ref.[105]

4.1 Non-equilibrium reaction

In the first step, we use the same reaction discussed in Ch. 3, a protein that exists in a soluble state A and a phase separating state B . But now fuel F molecules are converted into waste W molecules in the conversion process between the protein states; see fig. 4.1. If the external driving biases the reaction towards state A , the reaction becomes $A + W \rightleftharpoons B + F$, where F and W correspond to ATP and ADP in Eq. 4.1a respectively⁴. The free energy of reaction is then given by

$$\Delta F_a = \mu_A + \mu_W - \mu_B - \mu_F, \quad (4.2)$$

where μ_i is the chemical potential of species i . We make three important assumptions regarding the treatment of fuel and waste. First, motivated by the fast recovery rate of ATP by ATPases[158], we assume that the chemical potentials of fuel and waste are controlled from the outside by coupling them to a chemostat[165]. Second, ATP and ADP diffuse fast $\sim 10^{3-4} \mu\text{m}^2/\text{s}$ [166, 167] because they are small molecules⁵, so we assume that the chemical potential of fuel and waste equilibrates fast via diffusion and is constant everywhere. And third, we assume the volume fractions of fuel and waste to be negligible compared to A , B , and C , so we do not model them as individual species. Instead, fuel and waste only appear in the free energy of reaction, Eq. 4.2, as a constant driving $\Delta\mu = \mu_F - \mu_W > 0$ that influences the reaction equilibrium. Under these assumptions, the introduction of fuel and waste does not influence the phase separation behavior directly, but it is a constant, indefinite energy supply that is injected locally into the system, which is a key property of active matter in general[164]. As a consequence, $\Delta\mu$ is a new control parameter in our model.

One advantage of introducing activity in this way is that the reaction still obeys a detailed balance condition

$$\frac{s_a^f}{s_a^b} = \exp \frac{\mu_A - \mu_B - \Delta\mu}{k_B T}, \quad (4.3)$$

where s_a^f and s_a^b are the driven forward and backward reaction rates and $s_a = s_a^f - s_a^b$ is the total active reaction rate. Unlike other non-equilibrium reaction-diffusion models, where the driving is not modelled explicitly[70, 71, 168], in this model we

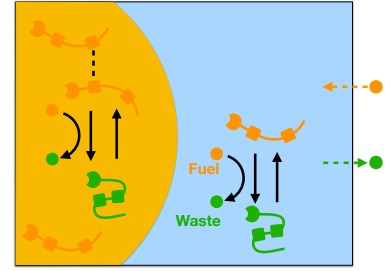


Figure 4.1: Schematic of a phase separating system with active chemical reactions. The chemical reaction between phase separating (orange particles) and soluble state (green particle) is driven by fuel (orange circle) and waste (green circle). The chemical potential of fuel and waste is held constant via particle exchange with the surroundings (green and orange dashed arrows). The figure is slightly adjusted from Ref.[105] under the Creative Commons CC-BY-4.0 license.

4: By swapping the role of fuel and waste, the reaction can be driven towards state B as well. In addition, we name the new species fuel and waste because fuel has a higher chemical potential, so $\mu_F - \mu_W > 0$, but this is only a convention.

5: The faster values from Ref.[166] were obtained in water, the slower ones in Ref.[167] in mice cells.

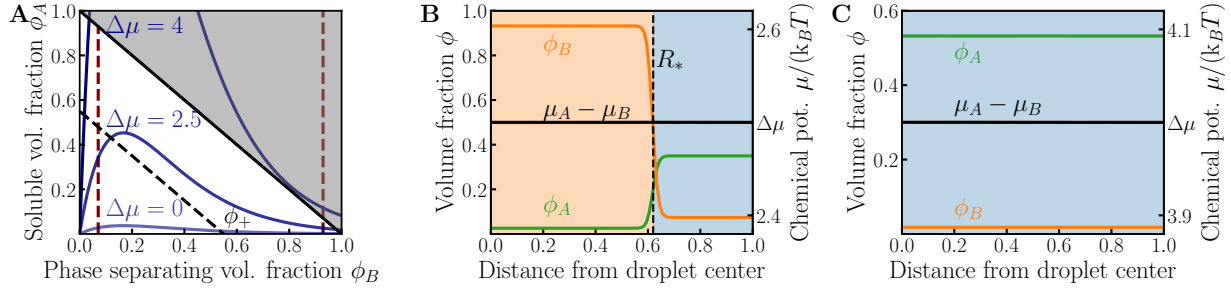


Figure 4.2: External driving can control phase separation. **A** By influencing the internal energy difference, the external driving $\Delta\mu$ can control the equilibrium ratio between A and B , where higher driving (darker blue) moves the equilibrium to lower K . **B/C** Steady state profile of volume fractions (left axis) and chemical potential (right axis) along a radial cut through the system. **B** For medium driving (here $\Delta\mu = 2.5 k_B T$), B droplets can form and in the steady state $\mu_A - \mu_B = \Delta\mu$ everywhere, so the reaction flux vanishes. **C** For strong driving ($\Delta\mu = 4 k_B T$) droplets are unstable because the equilibrium B fraction is lower than the binodal (see maroon line in **A**). Still, the reaction flux vanishes everywhere because $\mu_A - \mu_B = \Delta\mu$. Parameters used are $\chi = 3$, $\Delta w = 3.5$ and $\phi_+ = 0.55$. Simulations in **B/C** were done in spherically symmetric boxes.

know how much energy is injected into the system ($\Delta\mu$ per reaction) and how it is injected (by influencing the free energy of reaction). It is thus possible to investigate how a reaction has to be driven to show certain behavior[73].

In a first step, we consider the same system as in Sec. 3.2, but instead of Eq. 3.1, the free energy of reaction is given by Eq. 4.2. Then, the reaction flux vanishes for

$$\mu_A - \mu_B = \Delta\mu. \quad (4.4)$$

This can be thought of as chemical equilibrium under the condition that the chemical potential difference between fuel and waste is fixed. For $\Delta\mu = \text{const}$, we can map this to an equilibrium system by including $\Delta\mu$ in an effective internal energy difference $\Delta w \rightarrow \Delta w - \Delta\mu/k_B T$. So mathematically this system is identical to the passive reaction with a re-scaled internal energy difference.

The effect of $\Delta\mu$ on the ratio of B and A is shown in fig. 4.2A. As the driving strength increases, the equilibrium ratio⁶ shifts to lower B fraction and, for high enough total protein fraction, from a state where droplets are stable to a state where droplets are unstable; see fig. 4.2A. The steady-state of medium and strong driving are shown in fig. 4.2B and C respectively. In both cases, the reaction flux vanishes because $\mu_A - \mu_B = \Delta\mu$, but for medium driving, droplets are stable while for high driving droplets dissolve and almost all proteins are in state A . But, independent of driving strength, the reaction flux vanishes everywhere, $s_a = 0$, and as a result, the reaction does not burn energy in the steady-state because no net ATP consumption takes place⁷.

Unlike molecular motors, introducing a reaction that keeps the system out of equilibrium can not change the phase separa-

6: We keep the term equilibrium ratio for the ratio of B to A at which the reaction flux vanishes, i.e. $\mu_A - \mu_B = \Delta\mu$, although the system is not in thermodynamic equilibrium.

7: The individual forward and backward flux do not vanish, but in the steady state the amount of ATP converted to ADP is equal to the amount of ADP converted to ATP.

tion behavior directly, only indirectly by shifting the equilibrium ratio. For polar filaments, non-equilibrium thermodynamics allows a direct, kinetic coupling between chemical energy and directed motion of motors[115, 156] $v \propto \zeta \Delta\mu$ via an Onsager coefficient ζ . But direct coupling between chemical reactions and diffusion is not allowed in isotropic systems[107, 115] and reactions can influence phase separation only indirectly in this framework.

In the context of biomolecular condensates, external driving can be controlled easier and faster than the internal energy difference, for example by changing the concentrations of ATP and/or ADP in in-vitro experiments. But since the energy from ATP is the driver of all kinds of processes in cells and lots of energy is spent on keeping it constant [1], the driving strength is not suitable for precise control of condensates. Indeed, misregulation of ATP levels is related to diseases like cancer[169]. So changing the driving strength has the same downsides as changing global parameters like temperature or pH as discussed before.

Driven reaction cycle

As discussed in the introduction to this chapter, post-translational modifications like phosphorylation can have different pathways for the phosphorylation and dephosphorylation reaction (Eq. 4.1). The phosphorylation reaction, Eq. 4.1a, is driven by ATP consumption, while the dephosphorylation reaction, Eq. 4.1b, proceeds without external energy input. In this section, we discuss a simplified version of the reaction cycle to see how a reaction cycle is different from individual reactions, driven or passive. Neglecting the enzymes and the phosphate group⁸, we reduce Eq. 4.1 to the minimum and write the reaction cycle as



We call the first reaction the passive reaction s_p because it does not need supply of fuel, while the second is called active reaction s_a . For each reaction we write a detailed balance condition (Eq. 3.8 and Eq. 4.3)

$$\frac{s_p^f}{s_p^b} = \exp \frac{\mu_A - \mu_B}{k_B T}, \quad \text{and} \quad (4.6a)$$

$$\frac{s_a^f}{s_a^b} = \exp \frac{\mu_A - \mu_B - \Delta\mu}{k_B T}. \quad (4.6b)$$

8: This implies that fuel and waste have identical molecular volume, so the volume of reaction is conserved. Because ATP has a molecular weight of ~ 500 Da[1] and a median protein of ~ 300 amino acids has a molecular weight of ~ 30 kDa[1], it is reasonable to neglect the volume of ATP and ADP.

9: See Appendix.F for the calculation.

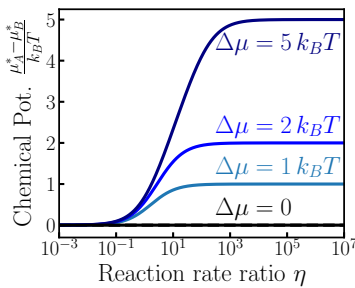


Figure 4.3: Steady state chemical potential for different reaction rates. The steady state chemical potential as a function of reaction rate ratio η for different driving strength $\Delta\mu$. For very low $\eta \ll 1$, the passive reaction dominates. In the intermediate regime the steady state chemical potential increases homogeneously until it reaches the limit set by the external driving for high $\eta \gg 1$. The figure is reprinted from Ref.[105] with minor adjustments under the Creative Commons CC-BY-4.0 license.

10: This is a result of fuel reacting together with B to form waste and A . If we swap the role of fuel and waste, i.e. $\Delta\mu < 0$, the active reaction will increase the amount of B and thus increase the propensity to phase separate.

As a result, for $\Delta\mu \neq 0$, the two reactions can not vanish simultaneously because $\mu_A - \mu_B = 0$ and $\mu_A - \mu_B = \Delta\mu$ can not be fulfilled at the same time. But the total reaction flux $s = s_p + s_a$ can vanish everywhere. To solve $s_p + s_a = 0$, equilibrium considerations are insufficient. Instead, the reaction kinetics are important as well. Using Eq. 4.6, we write the kinetics for both reactions in terms of the backward rates only

$$s_p = s_p^b (e^{(\mu_A - \mu_B)/(k_B T)} - 1), \quad \text{and} \quad (4.7a)$$

$$s_a = s_a^b (e^{(\mu_A - \mu_B - \Delta\mu)/(k_B T)} - 1). \quad (4.7b)$$

Solving this for the steady state⁹, $s_p + s_a = 0$, results in a condition for $\mu_A^* - \mu_B^*$ in terms of the ratio of backward rates $\eta = s_a^b/s_p^b$ and driving strength $\Delta\mu$

$$\mu_A^* - \mu_B^* = \Delta\mu - k_B T \ln \frac{e^{\Delta\mu/(k_B T)} + \eta}{1 + \eta}, \quad (4.8)$$

where the μ_i^* denotes the value of μ_i if the total reaction flux vanishes. This result holds generally for reactions that obey detailed balance, though the form of η is not known in general. For transition state theory kinetics (Eq. 2.27), the backward fluxes are given by $s_p^b = \lambda_p e^{\mu_B/(k_B T)}$ and $s_a^b = \lambda_a e^{(\mu_B + \mu_F)/(k_B T)}$ and thus $\eta = \lambda_a \lambda_p^{-1} e^{\mu_F/(k_B T)}$ is a constant. The steady state chemical potential is shown in fig. 4.3 as a function of the rate ratio η for different driving strengths. In the trivial case of zero driving, $\Delta\mu = 0$, the chemical potential difference is independent of η because the two reactions both vanish for $\mu_A - \mu_B = 0$. In that case the two reactions can be considered as the same reaction. In the limiting cases of fast active reaction, $\eta \gg 1$, the steady state chemical potential becomes $\mu_A^* - \mu_B^* = \Delta\mu$, while for fast passive reactions, $\eta \ll 1$ the system reduces back to the equilibrium case and $\mu_A^* - \mu_B^* = 0$. Thus, in the limit where one reaction is much faster, the system behaves as if only the fast reaction was present. But for intermediate η , the steady state chemical potential can take any value between 0 and $\Delta\mu$. Consequently, the driving strength sets the range of possible chemical potential differences $\mu_A - \mu_B$ that can be reached, while the ratio η determines the actual steady state value.

The active reaction in the reaction cycle, Eq. 4.5, always lowers the total amount of B in the system and thus always decreases the propensity to phase separate¹⁰. As a result, the active reaction cycle will not show phase separation if the passive does not. To discuss the influence of active reactions on phase separation we will thus discuss the case where droplets form in the passive case and see how active reactions influence those droplets. Note that the reaction cycle could be set up the other way around, the active reaction could produce droplet material, and, starting

from a system without droplets, active reactions could move the system above the binodal so droplets can form. A priori it is not clear if the driven reaction, for example, phosphorylation, induces or suppresses phase separation. One can find biological examples for both cases[73]. Here, we only discuss the reaction cycle in Eq. 4.5 for phase separating B . The reverse case follows directly if A is the phase separating state and B is soluble. In that case, the passive system would not show phase separation and the activity induces phase separation.

Non-equilibrium steady state

In the next step, we discuss the kinetics of the reaction cycle in Eq. 4.5. For simplicity, we focus on the special case of constant mobility for both species and neglect cross diffusion. Following the passive case in Eq. 3.17, the dynamics are given by

$$\partial_t \phi_+ = \Lambda \nabla^2 \mu_+, \quad \text{and} \quad (4.9a)$$

$$\partial_t \phi_- = \Lambda \nabla^2 \mu_- - 2s, \quad (4.9b)$$

where $\mu_+ = \mu_A + \mu_B$ and $\mu_- = \mu_A - \mu_B$. The total reaction flux is given by $s = s_a + s_p$, where we have to specify the kinetics of s_a and s_p . We consider two example kinetics, linear non-equilibrium thermodynamics (LNEQ) and transition state theory (TST). The reaction kinetics for these two cases are given by (see Eq. 2.25 and Eq. 2.27)

$$s_{p,L} = k_p(\mu_A - \mu_B) \quad \& \quad s_{a,L} = k_a(\mu_A - \mu_B - \Delta\mu), \quad \text{and} \quad (4.10a)$$

$$s_{p,TST} = \lambda_p \left(e^{\mu_A/(k_B T)} - e^{\mu_B/(k_B T)} \right) \quad \& \quad s_{a,TST} = \lambda_a e^{\mu_F/(k_B T)} \left(e^{(\mu_A - \Delta\mu)/(k_B T)} - e^{\mu_B/(k_B T)} \right). \quad (4.10b)$$

The total reaction flux in both cases can be written as (see Appendix.F for the TST derivation)

$$s_L = (k_p + k_a) \left(\mu_- - \frac{\eta_L}{1 + \eta_L} \Delta\mu \right), \quad \text{and} \quad (4.11a)$$

$$s_{TST} = \bar{\lambda} \exp \frac{\mu_+}{2k_B T} \sinh \left[\frac{\mu_- - \mu_-^*}{2k_B T} \right], \quad (4.11b)$$

where $\eta_L = k_a/k_p$ and the effective rate for transition state theory is given by

$$\bar{\lambda} = 2\lambda_p \sqrt{(e^{\Delta\mu/(k_B T)} + \eta_{TST})(1 + \eta_{TST})} e^{-\Delta\mu/(2k_B T)}, \quad (4.12)$$

with $\eta_{TST} = \lambda_a e^{\mu_F/(k_B T)} / \lambda_p$. The steady state chemical potential difference for linear non-equilibrium thermodynamic fluxes

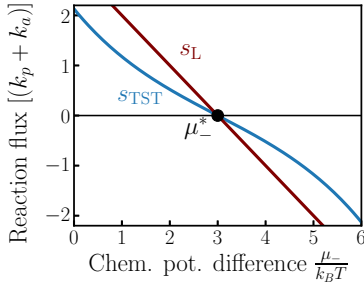


Figure 4.4: Total reaction flux has a unique steady state. The total reaction flux $s = s_a + s_p$ as a function of chemical potential for linear non-equilibrium thermodynamics (maroon) and TST kinetics (blue). In both cases, the steady state chemical potential, μ_-^* , is a unique stable fixpoint of the reaction and the rate increases homogeneously with distance from μ_-^* . Parameters used are $k_p + k_a = \bar{\lambda}e^{\mu_+/(2k_B T)} = 1$ (used as a timescale) and $\mu_-^* = \mu_{-,L}^* = 3k_B T$.

11: Note that, although the volume fractions differ significantly between phases, the chemical potentials are constant in space. So no diffusive fluxes are present and the reactions are homogeneous in space. This comes back to the idea that both reaction and diffusion are linked to the chemical potential.

is given by $s_L = 0$. The result does not correspond to Eq. 4.8, instead, $\mu_{-,L}^* = \eta_L/(\eta_L + 1)\Delta\mu$ because Eq. 4.10a is a linear expansion of Eq. 4.6 for $\mu_- \ll k_B T$ and $\mu_- - \Delta\mu \ll k_B T$.

The reaction rates vanish if and only if $\mu_- = \mu_-^*$ (or $\mu_- = \mu_{-,L}^*$), which can be seen from fig. 4.4. The figure illustrates the functional form of Eq. 4.11 for both types of kinetics. The steady state chemical potential μ_-^* is a stable fixpoint of the reaction and the rate increases homogeneously with distance from the steady state. This means that for constant rates $k_p + k_a$ and $\bar{\lambda}e^{\mu_+/(2k_B T)}$ we expect the same qualitative behavior for linear non-equilibrium and transition state reaction kinetics. Furthermore, we can again map the reaction to an effective equilibrium reaction, just like for the driven reaction alone. In this case, $\Delta w \rightarrow \Delta w - \mu_-^*/k_B T$ and the steady state chemical potential μ_-^* takes the role of $\Delta\mu$ in fig. 4.2.

As already discussed in Sec. 3.2, the only steady state solution of Eq. 4.9 for reaction rates of the form Eq. 4.11 is $\mu_+(\mathbf{r}) = \text{const}$ and $\mu_-(\mathbf{r}) = \mu_-^*$. For passive reactions, this result is not surprising, but it holds more generally for reaction fluxes $s(\mu_-)$ that vanish for μ_-^* and obey $\text{sgn}(s(\mu_-)) = \text{sgn}(\mu_-)$ (see Sec. 3.2), even if they are driven. The dynamics are quantitatively different, especially for the TST kinetics because the rate depends on μ_+ . But the steady-state is the same as the passive reaction with a rescaled internal energy difference. Consequently, the steady state shown in fig. 4.5A for LNEQ kinetics looks very similar to fig. 4.2B, with the exception that the steady state chemical potential $\mu_A^* - \mu_B^*$ is given by Eq. 4.11a instead of $\Delta\mu$.

The difference between the two systems, reaction cycle and only one reaction, can be seen from fig. 4.5B, the individual chemical potential differences driving the passive ($\mu_A - \mu_B$) and active ($\mu_A - \mu_B - \Delta\mu$) reaction do not vanish. Instead, the passive reaction is constantly producing B , while A is produced by the active reaction¹¹ as can be seen from fig. 4.5B and C. The two contributions cancel locally ($s_a = -s_p$) and the total reaction flux vanishes everywhere; see fig. 4.5C. As a result, the main difference compared to the passive case is that the reaction cycle requires energy input to maintain the steady state. If the energy supply is removed ($\Delta\mu = 0$), the system relaxes to the equilibrium state. For this reason, such states are called **Non-Equilibrium Steady State (NESS)**[170, 171].

To see that the NESS shows the same qualitative behavior as the passive case, i.e. Ostwald ripening and coalescence, we show a simulation of multiple droplets coarsening over time in fig. 4.6 (upper panels). The number of droplets decreases over time and the merging of droplets is visible in fig. 4.6B. In addition, the total reaction flux is relaxing to the steady state over

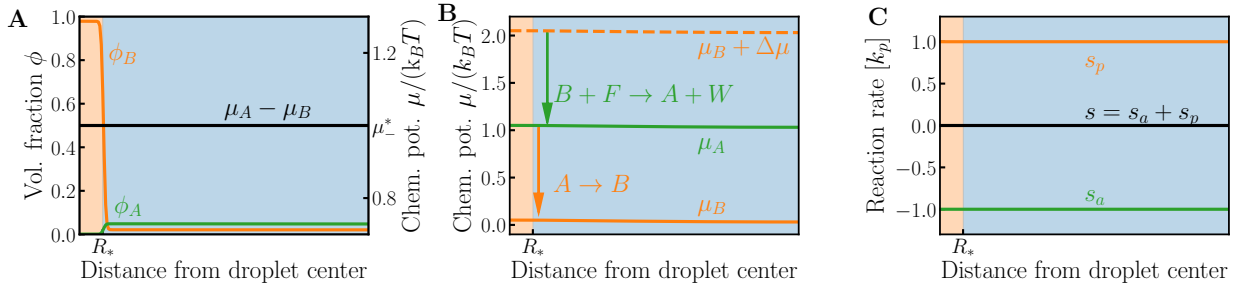


Figure 4.5: Steady state simulation of phase separation with a linear non-equilibrium reaction cycle. All panels show the steady state simulation of Eq. 4.9 for linear non-equilibrium reaction kinetics, Eq. 4.10a. **A** Volume fraction (left axis) of A (green line) and B (orange line) and chemical potential difference $\mu_A - \mu_B$ (black line, right axis) along the system length. A stable B rich phase forms, where the chemical potential difference is determined by $\mu^* = \Delta\mu\eta/(\eta + 1)$ (Eq. 4.11a) **B** Individual chemical potentials of A (green line), B (orange line) and $B + \Delta\mu$ (orange dashed line). Both chemical potentials are constant in space, so no diffusive fluxes are present. But the reactive fluxes do not vanish because $\mu_A > \mu_B$ and $\mu_B + \Delta\mu > \mu_A$. Thus, according to Eq. 4.10a the passive reaction converts A to B (orange arrow) while the active reaction converts B to A (green arrow). **C** Active (green), passive (orange) and total (black) reaction rates along the system length. The active reaction produces A ($s_a < 0$), while the passive reaction produces B ($s_p > 0$) constantly, although the total reaction flux vanishes everywhere because $s_a = -s_b$. Parameters used are $\Lambda = 1 v_0^2 \tau^{-1}$, $k_b = k_a = 0.01 \tau^{-1}$, $\chi = 4$, $\Delta w = 4$, $\Delta\mu = 2 k_B T$ and $\bar{\phi}_+ = 0.14$. Simulation was performed in a one dimensional box with no flux boundary conditions.

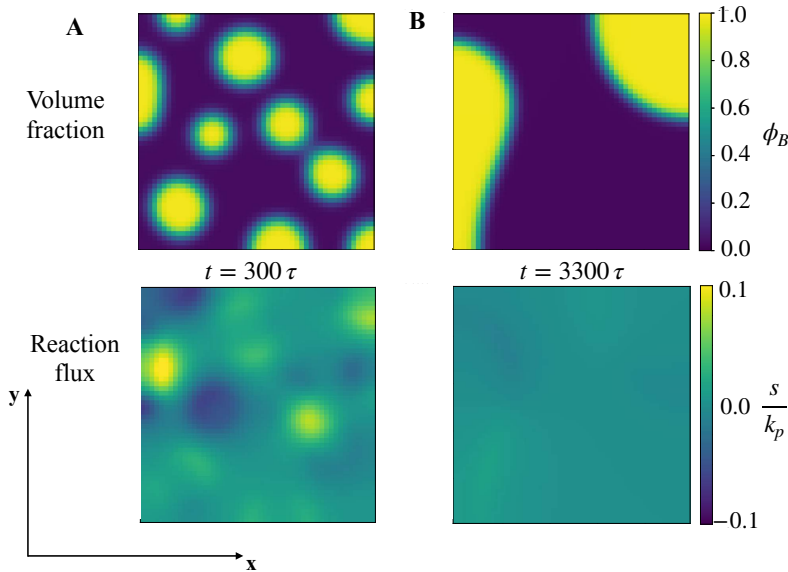


Figure 4.6: Time evolution of multiple droplets shows Ostwald ripening and coalescence. Two dimensional simulation of Eq. 4.9 with LNEQ reaction kinetics. Shown are the B volume fraction (upper panels) and total reaction fluxes s (lower panels) at early (**A**) and late (**B**) times. In the beginning multiple droplets form (**A**, top) which coarsen over time via coalescence and Ostwald ripening into few large droplets (**B**, top). Simultaneously, the reactions (bottom row) relax to the steady state, where the total reaction flux vanishes everywhere (**B**, bottom). Parameters used are $\Lambda = 1 v_0 \tau^{-1}$, $k_b = k_a = 0.01 \tau^{-1}$, $\chi = 4$, $\Delta w = 4$, $\Delta\mu = 2$, and $\bar{\phi}_+ = 0.35$. Simulation was performed in a two dimensional box with no flux boundary conditions and box size of $50 \times 50 \sqrt{v_0}$.

time and vanishes everywhere for late time; see fig. 4.6B lower panel. But the reaction is already close to equilibrium for early times as can be seen from the scale of the total reaction flux $\leq 0.1 k_p$ in fig. 4.6A lower panel. The simulation was done for a reaction-diffusion length of $\xi = 10 \sqrt{v_0}$, so the dynamics are diffusion-limited and the reaction relaxes fast compared to coarsening. This shows that the two dynamical processes, diffusion mediated phase separation and reactions, proceed independently of each other. That can be seen from Eq. 4.9 for $\mu_A - \mu_B = \mu_-^*$, $\partial_t \phi_- = 0$, but $\partial_t \phi_+$ does not vanish necessarily. So for diffusion-limited systems, ϕ_- relaxes fast and the system reduces to the dynamics of ϕ_+ under the condition that $\mu_A - \mu_B = \mu_-^*$ everywhere.

To summarize, for constant reaction rates, we find that we can reduce the non-equilibrium reaction cycle to an effective single reaction, the total reaction flux $s = s_a + s_p$. The total reaction flux can vanish everywhere for a fixed chemical potential difference; see fig. 4.5. The main differences between driven reaction only and reaction cycle are, first, the NESS depends on a kinetic parameter, namely the reaction rate ratio η . And second, the NESS converts fuel to waste constantly, i.e. burns energy constantly. We discuss the consequences of the energy consumption and the kinetic dependence for control of droplet formation and dissolution next.

Energy cost to control droplets

The non-equilibrium steady state (NESS) discussed above is constantly converting fuel to waste because $s_a < 0$. Since the energy in the system is constant in a steady-state, the energy input from the fuel has to be dissipated. This dissipation can be quantified by a steady-state entropy production rate σ_* . As shown in Appendix.A, the local entropy production rate for the reaction-diffusion system discussed here is

$$T\sigma = \sum_i \mathbf{j}_i \nabla \mu_i + s_a(\mu_A - \mu_B - \Delta\mu) + s_p(\mu_A - \mu_B). \quad (4.13)$$

This holds for both, linear non-equilibrium and transition state kinetics. As shown in fig. 4.5B, the steady state chemical potential gradients vanish ($\nabla \mu_i = 0$), so the diffusive entropy production vanishes. In addition the total reaction flux vanishes, i.e. $s_a = -s_p$, and thus the remaining entropy production rate is

$$T\sigma_* = -s_a^* \Delta\mu > 0. \quad (4.14)$$

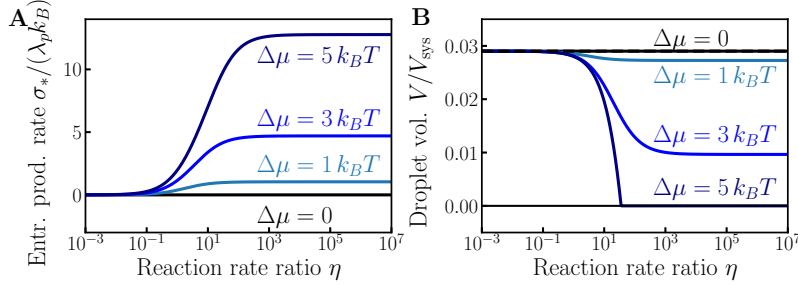


Figure 4.7: Driven reaction cycles can control droplet size. **A** Steady state entropy production rate as a function of reaction rate ratio η for different driving strength $\Delta\mu$. **B** Steady state droplet volume as a function of η for different $\Delta\mu$. The relation is analogous to varying Δw in the passive case; see fig. 3.11. In both cases TST kinetics were used. Parameters used are $\lambda_p = 1$ (used as a timescale), $\chi = 4$, $\bar{\phi}_+ = 0.05$ and $\Delta w = 3$. Figure was taken from Ref.[105] with minor adjustments under the Creative Commons CC-BY-4.0 license.

For the two kinetic schemes, LNEQ and TST, the active reaction flux in the stationary state, s_a^* , is given by

$$\frac{s_{a,L}^*}{k_p} = -\frac{\eta}{1+\eta} \Delta\mu, \quad \text{and} \quad (4.15a)$$

$$\frac{s_{a,TST}^*}{\lambda_p} \approx -\eta e^{(\mu_+^* + \Delta\mu)/(2k_B T)} \left(\frac{e^{\Delta\mu/(k_B T)}}{\sqrt{(1+\eta)(e^{\Delta\mu/(k_B T)} + \eta)}} \right), \quad (4.15b)$$

in the TST expression the approximation $e^{\Delta\mu/(k_B T)} \gg 1$ is used. The entropy production as a function of reaction rate ratio η is shown in fig. 4.7A for different driving strengths. In both cases the energy cost σ_* scales superlinear with $\Delta\mu$ for a fixed η because the steady state reaction flux increases with driving and the cost per reaction is always $\Delta\mu$. For a fixed driving strength, varying η interpolates between regimes where the passive ($\eta \ll 1$) or active ($\eta \gg 1$) reaction is dominant (similar to fig. 4.3). For $\eta \ll 1$, the entropy production vanishes because the driven reaction is very slow compared to the passive one. For $\eta \gg 1$, the steady state chemical potential difference approaches $\Delta\mu$ (see fig. 4.3) and accordingly the entropy production becomes $\sigma_* = k_p \Delta\mu^2$ for LNEQ and $\sigma_* \propto \lambda_p \sinh(\Delta\mu/(2k_B T)) \Delta\mu$ for TST. In the latter case ($\eta \gg 1$) the slow passive reaction is balanced by the fast active reaction. While the passive reaction does not influence the dynamics significantly, it still leads to a considerable entropy production rate¹² as seen from fig. 4.7A.

Since the steady state can be mapped to a passive reaction, the influence of reaction rate ratio on steady state droplet volume shown in fig. 4.7B, is very similar to the effect of internal energy difference shown in fig. 3.11. For low $\eta \ll 1$, the system behaves like the passive case and for the parameters used in fig. 4.7B, this corresponds to stable droplets. Increasing η for a

¹²: The entropy production rate is given in terms of λ_p however. We assume that the passive rate is fixed and the active rate λ_a is varied to vary η .

fixed $\Delta\mu$ reduces the number of proteins in state B in the system and thus the total droplet volume. For weak driving, droplet volume can only be reduced slightly, but for strong enough driving, droplets can be dissolved completely.

Therefore, the reaction cycle offers two ways to dissolve droplets, one is to increase the driving for fixed, but high η . This is similar and has the same downsides as the active reaction discussed in Sec. 4.1. The other is increasing η for a fixed $\Delta\mu$. In this case, $\Delta\mu$ sets the limits of control achievable, for low driving, droplets can be dissolved partially, but for strong driving full dissolution is possible. Increasing driving above the point where dissolution is possible increases the sharpness of the transition between formation and dissolution of droplets, see fig. 4.7B, i.e. the sensitivity to changes in η . But higher driving comes at the cost of higher entropy production to keep droplets dissolved, see fig. 4.7A, so there is an optimal $\Delta\mu$ that fully dissolves droplets, but keeps the entropy production low.

To summarize this part about Non-equilibrium reactions, both active reactions (Eq. 4.4) as well as driven reaction cycles (Eq. 4.5) can be described in the framework of passive reactions by rescaling the internal energy difference as long as the reaction rates, $k_{a/p}$ or $\lambda_{a/p}$, are constant in space. In these cases, phase separation is only influenced by changing the total amount of B available; see fig. 4.2A. The external driving does not influence the diffusion dynamics directly. The reason for this is, that reactions and diffusion do not couple directly in isotropic systems. In addition, the dynamics are fully determined by the chemical potential so the reactions do not distinguish between the droplet and solvent phase because the chemical potential is the same in both phases. One qualitative difference between reaction cycles and passive reactions is the constant consumption of energy in a NESS; see fig. 4.7A. This behavior is reminiscent of futile cycles found in biology[172], for example in metabolic pathways. A futile cycle is a reaction cycle that constantly burns energy by ATP hydrolysis without an apparent benefit for the cell. But it has been hypothesized that those cycles can control the steady-state of reactions[172] and even drive oscillations in fluctuating systems[173]. In our system the energy is used to reduce the number of proteins in state B and thus suppress phase separation, which would occur in passive systems; see fig. 4.7B. We showed in Eq. 4.8 that the steady state chemical potential, and thus the total amount of B , is influenced by the driving strength $\Delta\mu$ and the reaction rate ratio η . This is another difference compared to the passive case, a NESS with a reaction cycle depends on the reaction kinetics as well as the free energy of reaction[174]. This has an important effect on the control of biomolecular condensates because varying the driving strength

influences other processes and has the same downsides as varying global parameters like temperature. But varying η is possible, for example by enzymes that speed up the reaction without changing the free energy of reaction, as shown in Eq. 4.1 for a phosphorylation-dephosphorylation cycle. Changing reaction rates via enzymes to control droplet formation and dissolution is specific, reasonably fast, and precise. Specific because kinases and phosphatases oftentimes act on specific proteins or protein families[175]. Reasonably fast because enzymes in cells can be activated and deactivated by chemical modifications and do not have to be produced[36]. And precise because the rate constants in enzymatic reactions depend on the amount of enzyme¹³, so the rate ratio η can in theory be fine-tuned by the number of enzymes. But this still allows no precise control over the phase separation process, for example, size and count of droplets. The reaction cycle only shifts the equilibrium ratio to values of lower B fraction, see fig. 4.2A, and thereby switches between a state where droplets are stable or not. In the next section, we show how enzymes that break the symmetry between the droplet and solvent phase can lead to a NESS where the chemical energy is converted into diffusive fluxes.

4.2 Enzymatic reactions

At the end of the last section, we discussed enzymes as possible mechanisms to control the ratio of A to B and thus switch between a state where droplets are stable ($\bar{\phi}_B > \phi_B^{\text{out}}$) and unstable ($\bar{\phi}_B < \phi_B^{\text{out}}$). In this section, we introduce enzymes as extra species that can be enriched or depleted in droplets. First, we introduce the enzyme species E explicitly and then show how we can model it implicitly because the enzyme fraction can be derived directly from the B fraction under certain approximations. Afterward, we show how enzymes localizing in droplets (see fig. 4.8) can break the symmetry between the droplet and solvent phase and induce diffusive fluxes between the phases in a non-equilibrium steady state (NESS).

Enrichment in droplets

There are several cases of enzymes co-localizing with their substrate¹⁴ in biomolecular condensates[73]. As an example, we show a confocal microscopy image of stress granules in fig. 4.9. Stress granules form as a response to external stresses, for example, temperature or pH changes, hence the name. In fig. 4.9, stress granule formation is triggered by arsenite treatment[36]. The kinase DYRK3 localizes to stress granules in its active state, fig. 4.9 (center of small panels) and phosphorylates proteins that

¹³: For example in Michaelis-Menten kinetics[176].

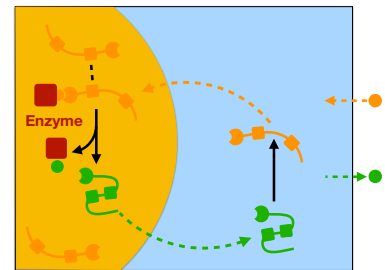


Figure 4.8: Enzymes in droplets drive diffusive fluxes between the phases. The system is the same as in fig. 4.1, but with enzymes (maroon particles) enriching in droplets and catalyzing the active reactions in droplets. As a result, the active reaction happens predominantly in the droplet and the passive reaction in the solvent phase.

¹⁴: The proteins that are post-translationally modified with the help of an enzyme are called substrate and the modified version is called product.

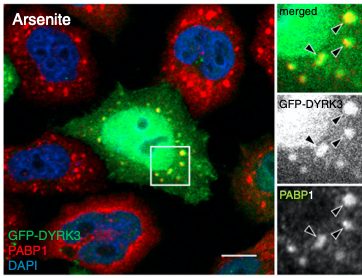


Figure 4.9: Enzyme DYRK3 co-localizes with stress granules. Confocal image stack of HeLa cells shows that DYRK3 colocalizes with stress granules (indicated by PABP1). DYRK3 phosphorylates PRAS40, which leads to downstream effects that dissolve stress granules[36]. Reprinted from Wippich, et al., "Dual Specificity Kinase DYRK3 Couples Stress Granule Condensation/Dissolution to mTORC1 Signaling", *Cell*, Vol.152, P791-805[36], fig.2C, with permission from the publisher Elsevier under the License number 5264830529640.

15: We use a simplified version of the enzyme kinetics, $A + W + E \rightleftharpoons B + F + E$. Standard Michaelis Menten kinetics involves an intermediate state $B + E \rightleftharpoons BE \rightarrow A + E$, where the last step is considered irreversible[176].

are important for stress granule formation, which leads to the dissolution of stress granules[78].

To model this effect, we include the enzyme E as an extra species in our model. In general, both reactions of the phosphorylation dephosphorylation cycle, Eq. 4.1, can be influenced by enzymes. For simplicity, we treat only one of them, here the kinase, explicitly. This means, that the phosphatase is either distributed homogeneously and its activity is not influenced by phase separation, or that the dephosphorylation reaction proceeds without the help of an enzyme. As discussed before, enzymes do not influence the free energy change of reaction, but increase the reaction rate. We assume that, for low enzyme concentrations, the rate increases linearly with the amount of enzymes, $s_a \propto \phi_E$, similar to Michaelis Menten enzyme kinetics¹⁵. Since the enzyme is not used up in the reaction, the total amount of enzymes in the system is conserved, $\bar{\phi}_E = V_{\text{sys}}^{-1} \int V_{\text{sys}} \phi_E dV = \text{const}$. We thus write the active reaction rate with explicit dependence on enzyme concentration as

$$\frac{s_{a,L}}{k_p} = \eta \frac{\phi_E}{\bar{\phi}_E} (\mu_A - \mu_B - \Delta\mu), \quad \text{and} \quad (4.16a)$$

$$\frac{s_{a,TST}}{\lambda_p} = \eta \frac{\phi_E}{\bar{\phi}_E} \left[\exp\left(\frac{\mu_A - \Delta\mu}{k_B T}\right) - \exp\left(\frac{\mu_B}{k_B T}\right) \right]. \quad (4.16b)$$

Where we normalized with respect to $\bar{\phi}_E$ so Eq. 4.16 reduces to Eq. 4.10 for homogeneously distributed enzymes. But, the important point is that enzymes do not distribute homogeneously in a multiphase system. Instead, due to enthalpic interactions, they get enriched in one phase. Under the assumption that the average enzyme fraction is low, $\bar{\phi}_E \ll 1$, and that the enzyme interactions χ_{Ej} are on the order of $k_B T$, we can approximate the enzyme partition coefficient Γ_E as (see Appendix.D and Ref.[134] for the derivation)

$$\Gamma_E = \frac{\phi_E^{\text{in}}}{\phi_E^{\text{out}}} \approx e^{\chi_E(\phi_B^{\text{in}} - \phi_B^{\text{out}})}, \quad (4.17)$$

where $\chi_E = \chi_{EC} - \chi_{EB}$ is the affinity for the B rich droplet phase compared to the solvent phase[105]. For $\chi_E > 0$, the enzyme fraction is enriched in the droplet and for $\chi_E < 0$ in the solvent phase. Here, we discuss the case $\chi_E > 0$ only and thus enzymes behave like clients partitioning into droplets formed by the scaffold B [5, 152]. The total droplet volume in cells is usually low[6], thus, we consider systems where the total droplet volume is small compared to system volume, so $\psi = V/V_{\text{sys}} \ll 1$, where V is the total droplet volume. In this case, the fraction of enzymes in droplet and solvent phase can be approximated by

$$\phi_E^{\text{in}} \approx \Gamma_E \bar{\phi}_E, \quad \text{and} \quad (4.18a)$$

$$\phi_E^{\text{out}} \approx \bar{\phi}_E. \quad (4.18b)$$

Thus, for small droplets, $\psi \ll 1$, Eq. 4.17 together with Eq. 4.18 imply that the local enzyme fraction follows directly from the B volume fraction¹⁶. To illustrate this, we simulate a four component system without reactions, a protein B that phase separates together with an enzyme E from the solvent C and another protein A . In addition, the average volume fractions of all species, except the solvent, are very low. A steady state of this system is shown in fig. 4.10. We find the numerical partition coefficients, $\Gamma_E \approx 6.2$ and $\Gamma_A \approx 0.024$, to be in good agreement with the analytical prediction from Eq. 4.17: $\Gamma_E \approx 6.4$ and $\Gamma_A \approx 0.021$ ¹⁷

In addition, the approximation for small droplet volume in Eq. 4.18 is valid, which can be seen from $\phi_E^{\text{out}} = \bar{\phi}_E$ in fig. 4.10. Finally, the enzyme is enriched at the droplet-solvent interface because $\chi > \chi_E$, so the enzyme acts as a surfactant to reduce the number of B - C contacts. This is not a numerical artifact, but a physical effect to lower the surface energy[177]. For reactions, this effect is negligible because the interface region is small compared to system volume.

Thus, to simplify the numerical simulations, we assume that the enzyme fraction in droplet and solvent phase is a constant, and for $\bar{\phi}_E < \phi_E^{\text{in}} \ll 1$, the effect of the enzyme on conserved volume fraction, $\sum_i \phi = 1$, is negligible. So, instead of describing the enzyme explicitly, we assume it is enriched in the droplet, which leads to an increase of the active reaction rate by a factor of Γ_E compared to the solvent phase according to Eq. 4.16.

Active droplets

Enzymes enriching in droplets influence the reaction rate according to Eq. 4.16 and thus the steady state chemical potential (Eq. 4.8). While it remains the same in the solvent phase¹⁸, the steady state chemical potential in the droplet phase becomes

$$\mu_{-,L}^{*,\text{in}} = \frac{\Gamma_E \eta}{\Gamma_E \eta + 1} \Delta\mu, \quad \text{and} \quad (4.19a)$$

$$\mu_{-,TST}^{*,\text{in}} = \Delta\mu - k_B T \ln \frac{e^{\Delta\mu/(k_B T)} + \Gamma_E \eta}{1 + \Gamma_E \eta}. \quad (4.19b)$$

All effects we will discuss below rely heavily on this asymmetry of the steady-state chemical potential difference between droplet and solvent phase, $\Delta\mu_-^* = \mu_-^{*,\text{in}} - \mu_-^*$. Therefore, we discuss

16: As long as E does not diffuse very slow compared to B .

17: The deviations for Γ_A probably result from the very low $\phi_A^{\text{in}} \approx 0.0006$.

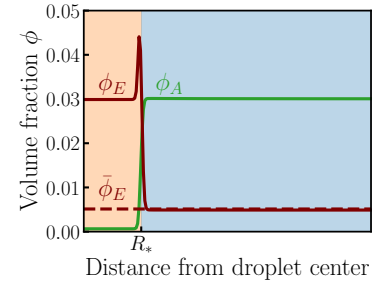


Figure 4.10: Distribution of enzyme and protein A without reactions. Volume fraction of the enzyme (solid maroon line) and protein state A (green line) as a function of distance from droplet center. The B rich droplet (orange area) inside the solvent phase (blue area) is small compared to the total system volume $\psi \approx 0.01$. ϕ_E is enriched in the droplet by a factor Γ_E , while it is approximately the average enzyme fraction (dashed maroon line) in the solvent phase. Parameters are $\Lambda_{ij} = \delta_{ij} v_0^{2/3} \tau^{-1}$, $\chi = 4$, $\chi_E = 2$, $\bar{\phi}_A = 0.03$, $\bar{\phi}_B = 0.03$ and $\bar{\phi}_E = 0.005$. Simulation was done in a spherically symmetric box with no flux boundary conditions.

18: Under the assumption that $\psi \ll 1$, so $\phi_E^{\text{out}} = \bar{\phi}_E$ and Eq. 4.17 are valid.

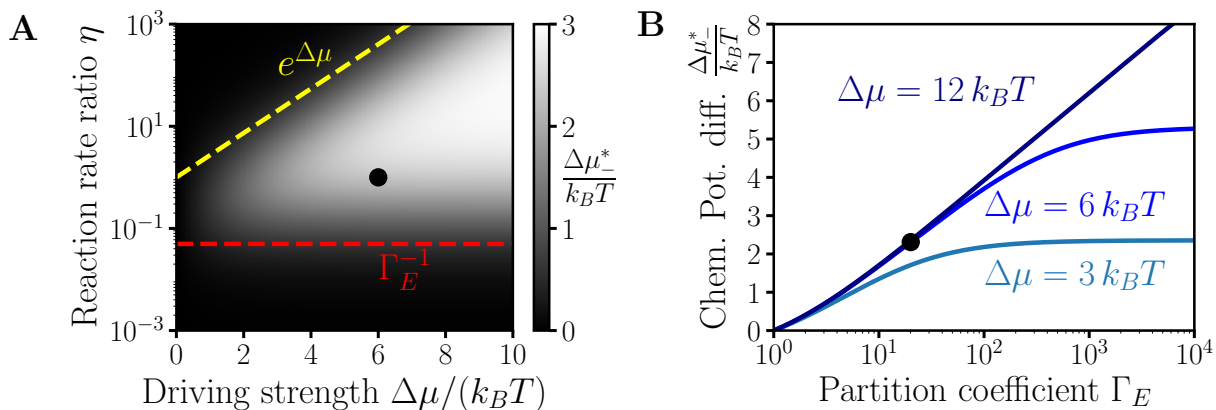


Figure 4.11: Strong driving and high reaction rate ratios induce significant chemical potential differences. **A** Difference between the steady state chemical potential in droplet and solvent phase as a function of driving ($\Delta\mu$) and reaction rate ratio (η). The red dashed line indicates $\eta = \Gamma_E^{-1}$ and the yellow dashed line $\eta = \exp(\Delta\mu/(k_B T))$. **B** The same chemical potential difference as a function of $\Gamma_E \approx \exp(\chi_E)$ for different driving strengths. The black dot indicates the same conditions in both plots. Parameters are $\chi_E = 3$ (in A) and $\eta = 1$ (in B).

19: The qualitative results are similar for LNEQ.

when this difference is significant for TST next¹⁹ :

1. In the solvent phase, μ_-^* (Eq. 4.8), has to be such that the B fraction outside is higher than the binodal, $\bar{\phi}_B > \phi_B^{\text{out}}$. Otherwise droplets are not stable to begin with, as discussed before.
2. If the reaction rate ratio η is small, such that $\eta\Gamma_E \ll 1$, the absolute value of the potential difference is small as can be seen from fig. 4.11A. We assume that $\chi_E \sim \mathcal{O}(1)$, so $\Gamma_E \lesssim 10^4$. The red dashed line in fig. 4.11A indicates $\eta = \Gamma_E^{-1}$ and below that line the chemical potential difference is below $1 k_B T$. At the same time, for very high $\eta > e^{\Delta\mu/(k_B T)} \gg 1$ (see the yellow line in fig. 4.11A), the active reaction is dominant in the solvent phase as well. As a result, the enzyme can not induce a chemical potential difference between the droplet and solvent phase. Therefore, η should be larger than Γ_E^{-1} but smaller than $e^{\Delta\mu/(k_B T)}$ to achieve a strong effect on $\Delta\mu_-^*$, $\Gamma_E^{-1} < \eta < e^{\Delta\mu/(k_B T)}$.
3. The maximum difference is $\Delta\mu_-^* = \Delta\mu$, which is achieved for $\mu_-^{*,\text{out}} = 0$ and $\mu_-^{*,\text{in}} = \Delta\mu$. Thus, for low driving $\Delta\mu$, the chemical potential difference is always low. At the same time, higher driving increases the range of η values as discussed before. Fig. 4.11B shows that the chemical potential difference scales almost linearly with χ_E independent of driving strength until a plateau with the value $\Delta\mu - \mu_-^{*,\text{out}}$ is reached. The crossover to the plateau in fig. 4.11B happens approximately when driving and enzyme interaction are equal $\Delta\mu \approx k_B T \chi_E \approx k_B T \ln(\Gamma_E)$. Thus, for strong driving, the partition coefficient becomes the limiting factor for the chemical potential difference. In this regime, even stronger driving leads to the same

chemical potential difference and increases the dissipation without any effect. To summarize, the driving should be strong enough to have an effect $\Delta\mu \gtrsim k_B T$, there is no a priori upper bound, but strong driving ($\Delta\mu \gg k_B T \chi_E$) leads to higher dissipation without affecting the chemical potential difference.

4. Finally, the chemical potential difference scales linearly with $\chi_E = \ln(\Gamma_E)$ for $\eta\Gamma_E \lesssim e^{\Delta\mu}$ and reaches a plateau for $\eta\Gamma_E \gg e^{\Delta\mu}$. The plateau value is given by $\mu_-^{*,\text{in}} = \Delta\mu$; see fig. 4.11B. Thus, by varying the enzyme segregation between 1 and ∞ , the chemical potential difference can be tuned between 0 and $\Delta\mu - \mu_-^{*,\text{out}}$.

As a result, we have a restricted parameter range of η , $\Delta\mu$ and Γ_E for which we can expect significantly different ($> 1 k_B T$) steady-state chemical potentials in the droplet and solvent phase.

In the next section, we discuss the effect of the steady state chemical potential difference between droplet and solvent phase. Thereby, we call systems with enrichment of enzymes in droplet phases **active droplets** because the active reaction is happening predominantly in the droplet phase. In the next sections, we show that those active droplets show new effects compared to the systems with homogeneous reaction rates discussed so far.

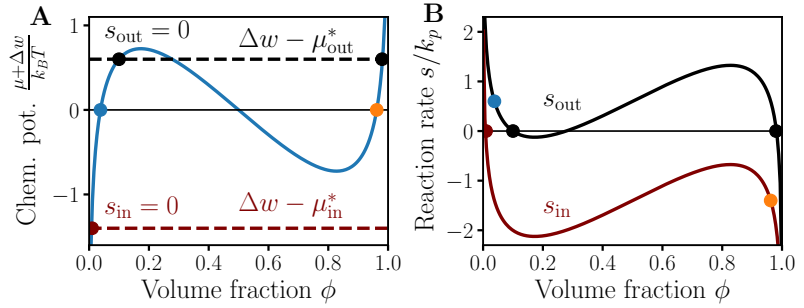
4.3 Binary active droplets

In Ch. 3 we argued, that binary reaction-diffusion systems inevitably end up in a homogeneous steady state because the reaction relaxes to the absolute minimum of the free energy density at every point in space. In driven systems, this is not necessarily the case anymore as the external driving keeps the system away from thermodynamic equilibrium[51] and allows for more complex behavior even in a binary system. This is similar to other work, for example, [60, 71], where binary phase separating systems with reactions are discussed. However, in those studies activity was included implicitly, by using mass-action kinetics, which breaks detailed balance in non-ideal solutions.

We start with the most simple case, a binary system consisting of two protein states A and B . A corresponding binary regular solution free energy (Eq. 2.39) and chemical potential (Eq. 2.40) determine the dynamics. The binary free energy has several advantages for the analytical discussion. First, in the phase separated state, the chemical potential is simply $\mu(\phi_1) = \mu(\phi_2) = -k_B T \Delta w$, where ϕ_1 and ϕ_2 are the equilibrium volume fractions in droplet and solvent phase respectively. Here, $\Delta w = w_A - w_B$ is the internal energy difference discussed in Ch. 2. Second, we have to discuss only one volume fraction

Figure 4.12: Active reactions reverse the reaction rate in droplets.

A Rescaled chemical potential $\mu + k_B T \Delta w$ (blue solid line) as a function of volume fraction. The rescaled, binary chemical potential vanishes at the phase coexistence points (blue and orange dot), while the chemical reaction vanishes for $\mu = \mu_{\text{in}}^*$ (maroon dot) in the droplet and $\mu = \mu_{\text{out}}^*$ (black dot) in the solvent phase. **B** Chemical reaction as a function of volume fraction inside (maroon) and outside (black dots) the droplet. Parameters are $\Delta w = 0.6$, $\mu_{\text{out}}^* = 0$, $\mu_{\text{in}}^* = 2k_B T$, $\chi_E = 3.5$, $k_p = k_a = 1$.



20: For this choice of variables, the chemical potential is proportional to the negative internal energy difference: $\mu \propto -k_B T \Delta w$.

($\phi = \phi_B$) and one chemical potential²⁰ ($\mu = \mu_B - \mu_A$) and solve only one dynamical equation ($\partial_t \phi$). Furthermore, we discuss the case of linear non-equilibrium reactions first, so the total reaction flux in the droplet and solvent phase is given by

$$\frac{s_{\text{in}}}{k_p} = -(1 + \Gamma_E \eta) \left(\mu + \frac{\Gamma_E \eta}{1 + \Gamma_E \eta} \Delta \mu \right), \quad \text{and} \quad (4.20a)$$

$$\frac{s_{\text{out}}}{k_p} = -(1 + \eta) \left(\mu + \frac{\eta}{1 + \eta} \Delta \mu \right), \quad (4.20b)$$

where $\partial_t \phi_{\text{in/out}} \propto s_{\text{in/out}}$ and the enzyme is enriched in the droplet by a factor Γ_E . The effect of different steady state chemical potentials in droplet and solvent phase is shown in fig. 4.12. The phase coexistence fractions are given by ϕ_{in} in droplet and ϕ_{out} in solvent phase (orange and blue dots in fig. 4.12A). Unlike in the ternary case with passive reactions, phase coexistence and steady state of the reaction (black and maroon lines) are incompatible both in droplet and solvent phase for $\Delta w \neq 0$. Thus a steady state where both diffusion and reaction vanish everywhere is impossible. If the enzyme was homogeneously distributed, the black dashed line in fig. 4.12 indicates the steady state for the reaction everywhere because $\mu + \mu_{\text{out}}^* = 0$. As a result, at the phase coexistence fractions (orange and blue dots), the reaction flux would be positive, and the dense phase will grow because new material is produced in both phases. This is what happens in model A or Allen-Cahn dynamics for $\Delta w \neq 0$ and the final state is a homogeneous volume fraction given by one of the black dots²¹ in fig. 4.12A. But, if the enzyme is enriched in the droplet phase, it can lead to a sign change of the reaction in the droplet (maroon line in fig. 4.12B) for high μ_{in}^* . This leads to the production of droplet material in the solvent and degradation in the droplet phase, see orange and blue dots in

21: The initial condition determines in which state the system will end up. With noise, it will always be the one with lower free energy, in fig. 4.12A that is the higher volume fraction.

fig. 4.12B, as discussed in Refs.[70, 71, 104] for mass action kinetics. However, there are two parameter restrictions to achieve this scenario in our system²² :

1. The volume fraction for which the reaction flux vanishes in the solvent phase $s_{\text{out}} = 0$ (indicated by the intersection of the black dashed line with the rescaled chemical potential in fig. 4.12A) has to be higher than the equilibrium volume fraction ϕ^{out} . In this case, the mixture is supersaturated and droplets form in the first place. This corresponds to $k_{\text{B}}T\Delta w > \mu_{\text{out}}^*$. At the same time, the volume fraction defined by $s_{\text{out}} = 0$ has to be below the chemical potential maximum, else the reaction in the solvent phase vanishes for very high protein fractions. In that case, the solvent phase would predominantly consist of protein, which makes no sense. So $\mu_{\text{out}}^* < k_{\text{B}}T\Delta w < \mu(\phi_s)$.
2. The enzyme enrichment in the droplet, described by Γ_E , has to be chosen such that $\mu_{\text{in}}^* > k_{\text{B}}T\Delta w$ so that the reaction flux in the droplet phase is negative.

So far we only discussed the phase space and reactions in the droplet and solvent phase qualitatively. In systems with mass action kinetics[70, 71, 104], the competition between production in the solvent and degradation in the droplet can lead to stable droplet size and states with multiple stable droplets. To see if this is possible for non-equilibrium reaction cycles with segregating enzymes, we investigate the dynamics of this simple binary example, simulate a system of multiple droplets, and discuss how a single droplet grows or shrinks in time next.

Collective dynamics

To test whether thermodynamically consistent reaction cycles with segregating enzymes can show similar effects as mass action kinetics, we simulate the dynamics given by

$$\partial_t \phi = \nabla^2 \mu - \ell^{-2}(\phi_E) \left(\mu + \frac{\eta(\phi_E)}{1 + \eta(\phi_E)} \Delta \mu \right), \quad (4.21)$$

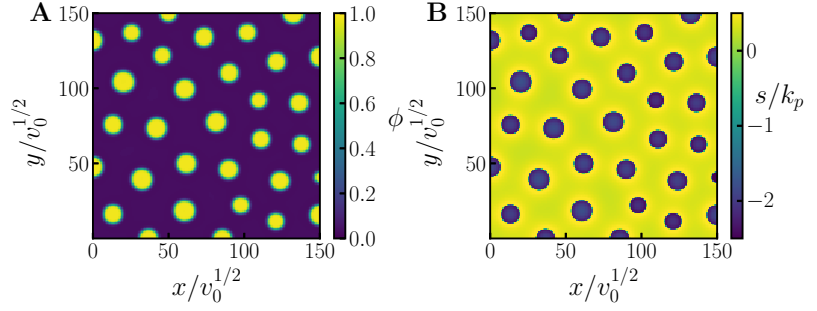
where $\ell = \sqrt{\Lambda/[k_p(1 + \eta(\phi_E))]}$ is the reaction diffusion length scale. For simplicity, we discuss linear non-equilibrium reactions because the analytical results are easier to interpret²³ while the qualitative results are the same for TST kinetics. We account for the enzyme segregation in the simulation by interpolating between k_a in the solvent and $k_a \Gamma_E$ in the droplet phase using a hyperbolic tangent function. So, the reaction rate is calculated using $k_a(\phi) = 0.5k_a((1 + \Gamma_E) + (\Gamma_E - 1) \tanh(\phi - 0.5))$. An example simulation of multiple droplets is shown in fig. 4.13A. Close to the steady state²⁴, multiple droplets of similar size are

22: The restrictions for the multi-component case are less strict because it has more degrees of freedom.

23: Analytical results for transition state theory are given in Appendix.G and the numerical results indicate which kinetics were used.

24: The average volume fraction change was $< 5 \cdot 10^{-7}$ per lattice side per time step $dt = 10^{-3}\tau$.

Figure 4.13: Enzyme enrichment in droplets can lead to stable collective droplet states. **A** Two dimensional simulation of Eq. 4.21 shows multiple stable droplets of similar sizes. **B** The reaction flux s (Eq. 4.20) shows that phase separating proteins are degraded in the droplet ($s < 0$) and produced in the solvent ($s > 0$) phase. Parameters are $\Delta w = 1$, $\Delta\mu = 3 k_B T$, $\ell_{\text{out}} = 9.5 v_0^{1/2}$, $\eta = 0.1$ and $\Gamma_E = 15$. Simulations were done for LNEQ kinetics up to $t = 5000 v_0/\Lambda$.



stable. At the same time, the reaction flux shown in fig. 4.13B, does not vanish everywhere. Instead, inside the droplets, droplet material gets degraded ($s < 0$), while it gets produced in the solvent phase ($s > 0$), similar to the mass action results in Refs.[70, 71]. To understand this effect in more detail, we next analyze the growth dynamics of a single droplet in a large system.

Single droplet growth

To discuss the dynamics of a single droplet analytically, we start with an initial droplet of radius R and discuss the dynamics in droplet and solvent phase separately in what we call an ‘effective droplet model’[60]. Therefore, we indicate the phase of a quantity by subscripts ‘in’ and ‘out’, for example, ϕ_{in} . The dynamics are then given by²⁵

$$\partial_t \phi_{\text{in}} = \Lambda \nabla^2 \mu_{\text{in}} - (k_p + \Gamma_E k_a) \left(\mu_{\text{in}} + \frac{\Gamma_E \eta}{1 + \Gamma_E \eta} \Delta\mu \right), \quad r \leq R, \quad \text{and} \quad (4.22a)$$

$$\partial_t \phi_{\text{out}} = \Lambda \nabla^2 \mu_{\text{out}} - (k_p + k_a) \left(\mu_{\text{out}} + \frac{\eta}{1 + \eta} \Delta\mu \right), \quad r > R, \quad (4.22b)$$

where, due to inhomogeneous distribution of enzymes, the reaction kinetics in droplet and solvent phase are different. As a result, the reaction diffusion length scales are different in droplet $\ell_{\text{in}} = \sqrt{\Lambda/(k_p + \Gamma_E k_a)}$ and solvent $\ell_{\text{out}} = \sqrt{\Lambda/(k_p + k_a)}$ phase as well²⁶. The boundary conditions at the system boundaries $r = 0$ and $r = L$ are no flux conditions $\mathbf{j}(r = 0, L) = 0$ and at the droplet-solvent interface, the chemical potential has to be equal $\mu_{\text{in}}(R) = \mu_{\text{out}}(R) = \mu_R$ to ensure a continuous chemical potential across the interface. In addition, at the interface the phase coexistence condition has to be fulfilled[60] and thus $\mu_R = -k_B T \Delta w$.

The effective droplet model assumes a thin interface region compared to droplet size, which is the case for high interaction

²⁵: Assuming the same diffusivity Λ in both phases.

²⁶: Because $\Gamma_E > 1$, $\ell_{\text{out}} > \ell_{\text{in}}$, so the reaction-diffusion length is always higher in the solvent than the droplet.

strength, as discussed in Ch. 2. Furthermore, it assumes that the radius R varies slowly, so the reaction diffusion equation in each phase is close to the steady state, $\partial_t \phi_{\text{in/out}} \approx 0$. In this case, the dynamics happen predominantly by moving the interface and thus changing the droplet radius, which in turn is driven by fluxes at the boundary between the two phases²⁷. Assuming a spherically symmetric system, the flux from the solvent into the droplet is given by $J_{\text{out}} = 4\pi R^2 \Lambda \mathbf{e}_r \nabla \mu_{\text{out}}|_{r=R}$, while the flux from the droplet into the solvent is given by $J_{\text{in}} = -4\pi R^2 \Lambda \mathbf{e}_r \nabla \mu_{\text{in}}|_{r=R}$, where \mathbf{e}_r is the outward pointing radial normal vector. The change of droplet volume $V = 4\pi R^3/3$ is then given by the difference between these fluxes[60]

$$\partial_t V = \frac{J_{\text{out}} - J_{\text{in}}}{\phi_{\text{in}} - \phi_{\text{out}}}, \quad (4.23)$$

where the factor $\phi_{\text{in}} - \phi_{\text{out}}$ takes care of converting a volume element of solvent phase, ϕ_{out} , to droplet phase, ϕ_{in} . $J_{\text{in}} - J_{\text{out}}$ is the net influx into the droplet. Therefore, if $J_{\text{in}} = J_{\text{out}}$, the volume change vanishes, $\partial_t V = 0$, i.e. the droplet is in a stationary state when the two fluxes balance each other. Due to the no flux boundary conditions at $r = 0, L$ and the steady state condition $\partial_t \phi_{\text{in}} = 0$, the (negative) integrated reactive flux, $-S_{\text{in}}$, inside the droplet is equal to the diffusive outflux, J_{in} , out of the droplet:

$$\Lambda \int_V \nabla^2 \mu = \Lambda \oint_{A_R} \mathbf{e}_r \nabla \mu dA = J_{\text{in}} = -4\pi \int_0^R s_{\text{in}} r^2 dV = -S_{\text{in}}, \quad (4.24)$$

where A_R is the surface of the droplet. And analogously $J_{\text{out}} = S_{\text{out}}$ ²⁸. We thus need to calculate the fluxes $J_{\text{in/out}}$ or $S_{\text{in/out}}$ to calculate the droplet dynamics, Eq. 4.23.

To calculate the fluxes, we first determine the steady state chemical potential as a function of r in both phases. We assume a spherically symmetric system where the system size L is large compared to the reaction diffusion length in the solvent, $L \gg \ell_{\text{out}}$. Then, solving Eq. 4.22 for the steady state²⁹, we end up with

$$\mu_{\text{in}}(r) = -\mu_{\text{in}}^* + (\mu_{\text{in}}^* - k_B T \Delta w) \frac{R \sinh(r/\ell_{\text{in}})}{r \sinh(R/\ell_{\text{in}})} \quad r \leq R, \quad \text{and} \quad (4.25a)$$

$$\mu_{\text{out}}(r) = -\mu_{\text{out}}^* + (\mu_{\text{out}}^* - k_B T \Delta w) \frac{R}{r} \exp\left(-\frac{r-R}{\ell_{\text{out}}}\right), \quad r > R, \quad (4.25b)$$

for droplet and solvent phase respectively. Here, $\mu_{\text{in}}^* = \Gamma_E \eta / (1 + \Gamma_E \eta) \Delta \mu$ and $\mu_{\text{out}} = \eta / (1 + \eta) \Delta \mu$. Eqs. 4.25 are shown in

27: Because we assume a steady state in each phase, only fluxes between the phases can change the radius.

28: There is no minus sign here because J_{out} flows into the droplet and thus $J_{\text{out}} = \oint_{A_R} (-\mathbf{e}_r) \nabla \mu dA = S_{\text{out}}$.

29: See Appendix.G for a derivation.

Figure 4.14: Influence of the reaction diffusion length on the steady state chemical potential profile.

A Chemical potential inside the droplet as a function of distance from the droplet center. **B** Chemical potential outside the droplet as a function of distance from the droplet center. Parameters are $w = -0.5$, $\mu_*^{\text{out}} = 0.15 k_B T$, $\mu_*^{\text{in}} = 2 k_B T$, $\ell_{\text{in}} = 158 - 0.0158 R$ and $\ell_{\text{out}} = 158 - 0.158 R$ (dark to light grey).

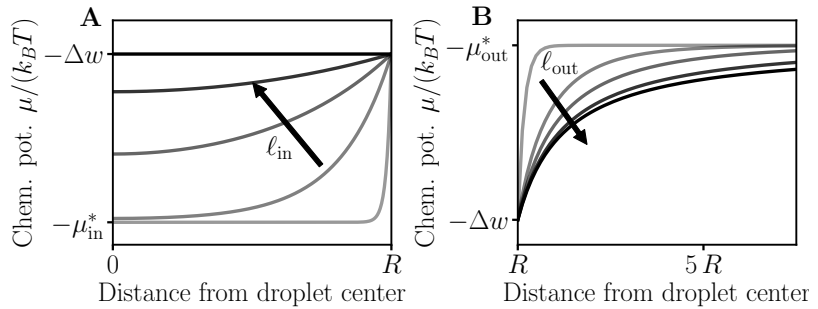


fig. 4.14A and B for the droplet and solvent phase respectively. Both take the phase coexistence value at the interface, $\mu(R) = -k_B T \Delta w$, and then homogeneously relax to $\mu_{\text{in}} = -\mu_{\text{in}}^*$ and $\mu_{\text{out}} = -\mu_{\text{out}}^*$, over a length that is determined by the reaction diffusion length. Thus, for system size (R in the droplet and L in the solvent) large compared to the reaction diffusion length, the reaction only contributes close to the interface and vanishes everywhere else (light gray lines in fig. 4.14). As a result, the reaction can drive diffusive fluxes only close to the interface because the chemical potential is flat everywhere else. For system sizes small compared to the reaction diffusion length, diffusion is fast and thus the chemical potential is flat and fixed by the interface value almost everywhere (dark gray/black line in fig. 4.14A). In this case, the reaction is only a small perturbation to the fast diffusive dynamics.

As the system size is always large compared to the reaction diffusion length, the chemical potential far away from the droplet is determined by the condition that the reaction vanishes³⁰ ($\mu_{\text{out}}(r \gg R) = \mu_{\text{out}}^*$). In the droplet, the situation is less clear, as droplets are small compared to the solvent phase, the individual droplets can be small compared to the reaction diffusion length in the droplet. In fact, fig. 4.12B shows that, for high μ_{in}^* , the steady state is reached for very low volume fractions in the droplet phase. As a result, the droplet dissolves itself for large droplet radii. This can be circumvented by restricting the steady state chemical potential in the droplet, such that it is larger than the chemical potential at the binodal fraction: $0 > k_B T \Delta w - \mu_{\text{in}}^* > k_B T \Delta w + \mu(1 - \phi_b)$. A similar condition is necessary for the solvent phase, as discussed above. This ensures that the volume fraction in the droplet/solvent phase does not get too low/high. But, this is not necessary if $R < \ell_{\text{in}}$ because the chemical potential and volume fraction never reach those values.

A simulation of Eq. 4.22 is shown in fig. 4.15. Unlike in passive phase separation, the volume fraction in droplet and sol-

³⁰: This is why $k_B T \Delta w - \mu_{\text{out}}^* < k_B T \Delta w + \mu(\phi_s)$, else the volume fraction far away from the droplet would be very high; see fig. 4.12A.

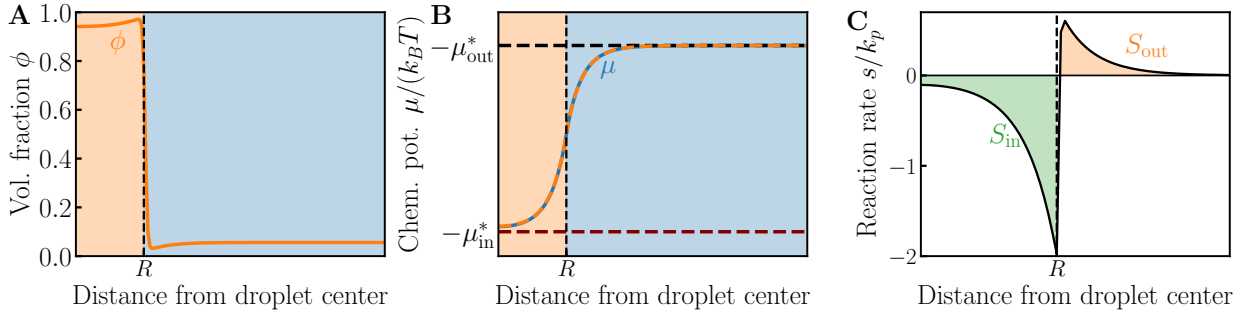


Figure 4.15: NESS of a single droplet in a large solvent phase. **A** Volume fraction as a function of distance from droplet center. In the steady state, gradients in ϕ are present inside each phase, which is not the case in passive phase separation. **B** Corresponding chemical potential from the simulation (blue line) and the analytical prediction Eq. 4.25 (orange dashed line). The reaction flux vanishes for $\mu = -\mu_{\text{out}}^*$ (black dashed line) in the solvent and $\mu = -\mu_{\text{in}}^*$ (maroon dashed line) in the droplet phase. At the interface, the phase coexistence condition requires $\mu = -\Delta w$. **C** Reaction flux calculated from the chemical potential using Eq. 4.20. Inside the droplet (green shaded area) droplet material gets degraded and outside (orange shaded area) it gets produced. The integrated reaction flux in droplet and solvent phase is equal in the steady state ($S_{\text{in}} = S_{\text{out}}$). Parameters are $\Delta w = 1$, $\Delta\mu = 3 k_{\text{B}}T$, $\ell_{\text{out}} = 9.5 v_0^{1/3}$, $\eta = 0.1$ and $\Gamma_E = 15$. Simulations were done for LNEQ kinetics in a spherically symmetric box of length $L = 500 v_0^{1/3}$.

vent phase is not constant, but shows small variations because of the chemical reactions in both phases; see fig. 4.15A. This implies the presence of diffusive fluxes in the individual phases, even in the steady state. In the solvent phase far away from the interface, the volume fraction becomes flat and both diffusion and reaction vanish. The chemical potential in fig. 4.15B behaves as predicted from Eq. 4.25 and the numerical result (blue line) and analytical prediction from the effective droplet model (dashed orange line) match very well³¹. The maroon and black dashed lines indicate the values for which the reaction vanishes in the droplet and solvent phase respectively. Thus, the distance of the chemical potential from those lines is proportional to the local reaction flux; compare fig. 4.15B and C. Finally, the total reaction flux is shown in fig. 4.15C for the droplet (blue shaded area) and solvent (orange shaded area). Again, it shows that droplet material is degraded in the droplet and produced outside and in a steady-state, the fluxes sum up to zero, $S_{\text{out}} = -S_{\text{in}}$.

Now that we know the steady state chemical potential from Eq. 4.25 and saw that it matches well with simulations, fig. 4.15, we can calculate the droplet growth rate and predict the stable radius. The droplet growth depends on the difference between influx into the droplet and degradation of droplet material due to reactions. The total reaction flux in the droplet is given by

$$\begin{aligned} \frac{S_{\text{in}}}{k_p} &= 4\pi \int_0^R \frac{s_{\text{in}}}{k_p} r^2 dr \\ &= -4\pi(1 + \eta\Gamma_E)(\mu_{\text{in}}^* - k_{\text{B}}T\Delta w)\ell_{\text{in}}^2 R \left(\frac{R}{\ell_{\text{in}}} \coth \left[\frac{R}{\ell_{\text{in}}} \right] - 1 \right) \end{aligned} \quad (4.26)$$

³¹: A chemical potential gradient between droplet and solvent is present even in the steady state. This is reminiscent of electrochemical gradients across membranes, which control the partitioning of charged molecules on both sides of the membrane[178].

the total reaction flux in the solvent in turn is given by (assuming $L \gg \ell_{\text{out}}$, i.e. $L \rightarrow \infty$ in the integration)

$$\begin{aligned} \frac{S_{\text{out}}}{k_p} &= 4\pi \int_R^\infty \frac{s_{\text{out}}}{k_p} r^2 dr \\ &= -4\pi(1 + \eta)(\mu_{\text{out}}^* - k_B T \Delta w) \ell_{\text{out}}^2 R \left(1 + \frac{R}{\ell_{\text{out}}}\right). \end{aligned} \quad (4.27)$$

As already discussed, for $S_{\text{out}} > 0$ and $S_{\text{in}} < 0$, it is necessary that $\mu_{\text{in}}^* > k_B T \Delta w > \mu_{\text{out}}^*$ (see fig. 4.12B). This is the only case we discuss in detail because it follows from Eq. 2.43 that the droplet disappears or grows indefinitely if both fluxes have the same sign. In addition, $\coth(x) \geq 1$ and all other factors are positive as well, so the factor $\mu_{\text{in/out}}^* - k_B T \Delta w$ determines the sign of the rate, independent of the radius R . The scaling of the rates with radius, which is important for droplet growth, is determined by the ratio of reaction diffusion length and radius R . We discuss the four limiting cases, large and small reaction-diffusion length in droplet and solvent phase, and discuss the scaling with $\ell_{\text{in/out}}$ and R only:

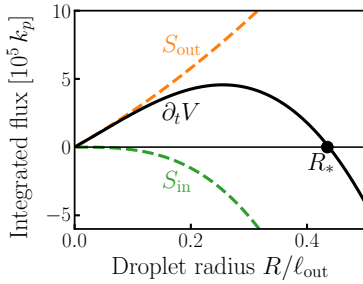


Figure 4.16: The competition between reactions in droplet and solvent phase introduce a stable droplet size. Droplet growth rate (black line) as a function of droplet size. The droplet growth is given by the difference between degradation of droplet material in the droplet (green dashed line) and production in the solvent phase (orange dashed line). Because these fluxes have different signs and scale differently with droplet size (see Eq. 4.27 and Eq. 4.27), a steady state droplet size R_* , independent of system volume, emerges (black dot). Parameters are $k_p = 0.001 \Lambda v_0^{-2/3}$, $\eta = 0.1$, $\Gamma_E = 60$, $\chi = 4$, $\Delta w = 1$ and $\Delta\mu = 4 k_B T$.

- ▶ $R/\ell_{\text{in}} = x \ll 1$: In this case, we approximate $x \coth(x) - 1 \approx x^2/3$ and thus $S_{\text{in}} \propto -\frac{4\pi R^3}{3} = -V$. If the reaction is slow compared to diffusion, the chemical potential in the droplet is flat, see fig. 4.14, and thus the reaction is proportional to the droplet volume.
- ▶ $R/\ell_{\text{in}} = x \gg 1$: In this case, we approximate $x \coth(x) - 1 \approx x$ and thus $S_{\text{in}} \propto -4\pi R^2 \ell_{\text{in}} = -A_R \ell_{\text{in}}$. This case is only possible if $0 > k_B T \Delta w - \mu_{\text{in}}^* > k_B T \Delta w + \mu(1 - \phi_s)$, else the droplet dissolves itself. As can be seen from fig. 4.14, only a small area around the interface contributes to the integral and thus, the flux scales with droplet surface area.
- ▶ $R/\ell_{\text{out}} \ll 1$: $S_{\text{out}} \propto 4\pi \ell_{\text{out}}^2 R$, from purely diffusive dynamics we expect an influx of $4\pi \Lambda R$ [60], which is what we get here as well.
- ▶ $R/\ell_{\text{out}} \gg 1$: $S_{\text{out}} \propto 4\pi \ell_{\text{out}} R^2$, for strong reactions, the influx scales with droplet surface instead of droplet radius. The reason is the same as in the droplet phase.

Since $\ell_{\text{out}} > \ell_{\text{in}}$ for $\Gamma_E > 1$, the case $\ell_{\text{in}} \gg R \gg \ell_{\text{out}}$ is impossible, but the other three combinations are possible. Plugging Eq. 4.26 and Eq. 4.27 into Eq. 4.23, we can calculate the steady state droplet radius, defined by $\partial_t V = 0$. An example shown in fig. 4.16 illustrates how the different scalings of S_{in} and S_{out} with droplet radius introduce a steady state radius R_* for which the growth rate vanishes. For small droplets, the influx from the

solvent dominates the growth (blue dashed line in fig. 4.16, but for large enough droplets the degradation inside the droplet becomes too strong because $S_{\text{in}} \propto R^3$. As a result, the degradation of droplet material in the droplet itself limits the droplet growth. In addition, the figure shows that the steady state radius is stable because the droplet grows for $R < R_*$ ($\partial_t V > 0$) and shrinks for $R > R_*$ ($\partial_t V < 0$).

Because of the hyperbolic cotangent function, we can not solve for the steady state radius analytically, but we can calculate the limiting cases $\ell_{\text{in}} \gg R$ and $\ell_{\text{in}} \ll R$ by setting Eq. 4.23 to 0³². For $\ell_{\text{in}} \ll R$, the steady state radius becomes

$$R_* = \frac{(1 + \eta)(k_{\text{B}}T\Delta w - \mu_{\text{out}}^*)\ell_{\text{out}}}{(1 + \eta\Gamma_E)(\mu_{\text{in}}^* - k_{\text{B}}T\Delta w)\ell_{\text{in}} - (1 + \eta)(k_{\text{B}}T\Delta w - \mu_{\text{out}}^*)\ell_{\text{out}}}. \quad (4.28)$$

32: We assume strong phase separation and thus $\phi_{\text{in}} - \phi_{\text{out}} \approx 1$.

As said before, this limit is only valid for restricted μ_{in}^* . But, in this regime, for $\ell_{\text{out}} \ll R$, both reaction fluxes scale with R^2 , so the difference between the pre-factors determines the droplet size. Since it is not clear which pre-factor is higher, the stable radius can become negative, which is nonphysical and corresponds to the case where droplets dissolve. As a result, in this regime, strong fine-tuning of parameters is necessary to gain control over droplet size.

This is different for $\ell_{\text{in}} \gg R$, because the reaction flux in the droplet scales with droplet volume, while the flux in the solvent scales with droplet radius. In this case, the steady state radius becomes

$$\begin{aligned} R_* &= \left(\frac{3\Lambda}{k_p(1 + \eta\Gamma_E)} \frac{k_{\text{B}}T\Delta w - \mu_{\text{out}}^*}{\mu_{\text{in}}^* - k_{\text{B}}T\Delta w} \right)^{1/2} \\ &= \ell_{\text{in}} \left(3 \frac{k_{\text{B}}T\Delta w - \mu_{\text{out}}^*}{\mu_{\text{in}}^* - k_{\text{B}}T\Delta w} \right)^{1/2}. \end{aligned} \quad (4.29)$$

Here, the first factor is the reaction-diffusion length in the droplet and as a result, the second factor has to be small, to ensure $\ell_{\text{in}} \gg R_*$. This is the case for strong driving $\Delta\mu \gg k_{\text{B}}T$ and fast active reaction in the droplet $\Gamma_E\eta \gg 1$. Unlike in all other cases discussed so far, Eq. 4.29 is independent of system size V_{sys} . This effect, found already for active droplets with mass action kinetics[70, 71], allows multiple droplets to be stable, see fig. 4.13, and precise control over the droplet size. Since the chemical reaction in the droplet does not attain a steady state, there is no restriction on $\mu_{\text{in}}^* - k_{\text{B}}T\Delta w$ (except that it is positive). Therefore, the range of parameters for which droplet size control is achieved is larger than for $\ell_{\text{in}} \ll R$ and the mechanism of size control is more robust. In addition, $\ell_{\text{in}} \gg R$ implies slow reactions compared to diffusion. This means, that the reactions are only a small perturbation to the diffusive dynamics, but still have

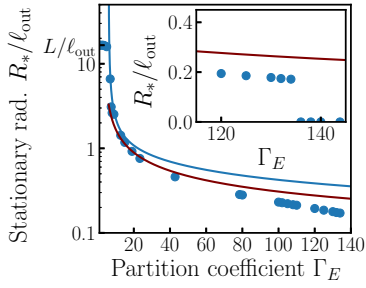


Figure 4.17: Higher enzyme partitioning decreases droplet size. Stationary droplet radius as a function of enzyme partition coefficient. For weak partitioning, droplets are large and eventually reach full system size. For strong partitioning, droplets shrink and eventually dissolve fully (see inset). Simulation results (blue dots) show the same trend as analytical predictions Eq. 4.29 (maroon line) and Eq. 4.28 (blue line). The deviation for small droplets are due to surface tension effects for small droplets[60] not included in the analytics. Parameters are $k_p = 0.001 \Lambda v_0^{-2/3}$, $\eta = 0.1$, $\chi = 4$, $\Delta w = 1$ and $\Delta\mu = 4 k_B T$. Simulations were done in a spherically symmetric box of length $L = 500 v_0^{1/3}$ with no flux boundary conditions.

33: Except the parameter regime around the full dissolution, which allows a switch like control; see the inset in fig. 4.17.

a strong impact on the final state. This makes it a suitable control mechanism for droplet size in cells.

To see whether $\ell_{\text{in}} \gg R$ is a reasonable approximation for biomolecular condensates, we now try to estimate the reaction diffusion length based on diffusion coefficients D and enzymatic reaction rates k_{cat} . The corresponding reaction diffusion length is $\ell = \sqrt{(D/k_{\text{cat}})}$. The diffusivity of proteins is approximately $D \sim 0.1 - 10 \mu\text{m}^2\text{s}^{-1}$ [179] and depends on protein size and confirmation. Typical enzymatic reaction rates are on the order of $k_{\text{cat}} \sim 10^{-2} - 10^2 \text{s}^{-1}$ [1]. Plugging this into the equation for the reaction diffusion length, we get $\ell \sim 30 - 0.03 \mu\text{m}$. Condensates range from small condensates in the nucleus with radii $R \sim 10 \text{nm}$ [14] medium sized stress granules $R \sim 2 - 0.1 \mu\text{m}$ [180] to large condensates in *Xenopus laevis* oocytes with $R \sim 400 \mu\text{m}$ [15]. This shows, that $\ell_{\text{in}} \gg R$ is a good approximation for small condensates and for medium sized condensates $R \sim \mathcal{O}(\mu\text{m})$, if the reactions are not too fast, i.e. $k_{\text{cat}} \sim 10^{-2} - 1 \text{s}^{-1}$.

Ultimately, we want to understand how enzyme segregation can control droplet size. Thus, we are particularly interested in the behavior of R_* as a function of enzyme segregation $\Gamma_E \approx e^{\chi E}$. We restrict the analytical discussion to the case $\ell_{\text{in}} \gg R$ in Eq. 4.29. There, Γ_E appears twice, first, in the reaction-diffusion length scale as a factor $(\eta\Gamma_E)^{-1/2}$ and, second, in the steady state chemical potential $\mu_{\text{in}}^* = \eta\Gamma_E/(1 + \eta\Gamma_E)\Delta\mu$. Therefore, for $\eta\Gamma_E \ll 1$, the stable radius scales with Γ_E^{-1} and for $\eta\Gamma_E \gg 1$ it scales with $\Gamma_E^{-1/2}$. The comparison between numerical and analytical results is shown in fig. 4.17. Thereby, the blue line corresponds to Eq. 4.28 and the maroon line to Eq. 4.29. For low partitioning, the system goes back to the homogeneous reaction rate discussed earlier in this chapter. In this case, the droplet takes over the whole system and the droplet radius approaches system size $R_* \rightarrow L$, see fig. 4.17. For strong segregation, the droplet size gets smaller, as predicted by Eq. 4.29. But, for low radii, the numerical results deviate from the analytical results because we neglect the effect of the Laplace pressure[181] in the analytical calculations, which becomes important for small droplets[60]. The inset of fig. 4.17 shows that droplets can be fully dissolved for strong enough segregation. In fact, the crossover to full dissolution is discontinuous because of the Laplace pressure as well[60]. The scaling $\Gamma_E^{-1/2}$ seems suboptimal for a control parameter because of the low sensitivity³³. But, one has to keep in mind that the actual control parameter is χE and thus, the radius scales with $R_* \propto \exp(-\chi E/2)$, so it is very sensitive to changes in χE .

Linearization

So far, we have deliberately described the system in terms of the chemical potential(s) instead of volume fractions to highlight the importance of the chemical potential in describing non-ideal reaction diffusion processes. In the existing literature about reactions in biomolecular condensates, descriptions in terms for volume fractions or concentrations were used, see Refs.[70, 71]. Can we write the active droplet model developed above in terms of volume fractions? And if so, do we recover the same model used in Refs.[60, 70, 71]? In this section, we show that it is possible to write the active droplet dynamics in Eq. 4.21 in terms of volume fractions. Therefore, we linearize the chemical potential in droplet and solvent phase around the equilibrium volume fractions and get

$$\mu_{\text{in/out}} \approx -k_{\text{B}}T\Delta w + (\partial_{\phi}\mu_{\text{in/out}})|_{\phi_{1,2}}(\phi - \phi_{1,2}) - \kappa\nabla^2(\phi - \phi_{1,2}). \quad (4.30)$$

Here, we used that $\mu(\phi_1) = \mu(\phi_2) = -k_{\text{B}}T\Delta w$. The derivative of the chemical potential is given by

$$(k_{\text{B}}T)^{-1}\partial_{\phi}\mu = \frac{1}{\phi(1-\phi)} - 2\chi, \quad (4.31)$$

which is identical for the special case of a regular solution free energy because $\phi_1 = 1 - \phi_2$. With the linearized chemical potential, we can rewrite the diffusive fluxes as

$$\mathbf{j}_{\text{in/out}} = -D_{\text{in/out}} \left[\nabla\phi_{\text{in/out}} - \frac{\kappa}{\delta_{\text{in/out}}}\nabla^3\phi_{\text{in/out}} \right], \quad (4.32)$$

where $\delta_{\text{in/out}} = \partial_{\phi}\mu_{\text{in/out}}|_{\phi_{1,2}}$ and $D_{\text{in/out}} = \Lambda\delta_{\text{in/out}}$. Thus, the diffusive flux takes the form of Fick's law of diffusion with an extra $\nabla^3\phi$ term. From the simulation in fig. 4.15A, we see that the volume fraction in the individual phases are small and $\kappa/\delta_{\text{in/out}} \sim \mathcal{O}(v_0^{2/d})$ for our choice of $\kappa \propto \chi$. Therefore, the third order gradient term is small compared to the gradient term and we neglect it in the following discussion.

We can plug the linearized chemical potential in the reaction flux as well and end up with

$$s_{\text{in}} = -(k_a\Gamma_E + k_p) \left(\delta_{\text{in}}(\phi_{\text{in}} - \phi_1) + \frac{\Gamma_E\eta}{1 + \Gamma_E\eta}\Delta\mu - k_{\text{B}}T\Delta w \right), \quad \text{and} \quad (4.33)$$

$$s_{\text{out}} = -(k_a + k_p) \left(\delta_{\text{out}}(\phi_{\text{out}} - \phi_2) + \frac{\eta}{1 + \eta}\Delta\mu - k_{\text{B}}T\Delta w \right). \quad (4.34)$$

Using effective rates $\bar{k}_{\text{in}} = (k_a\Gamma_E + k_p)\delta_{\text{in}}$ and $\bar{k}_{\text{out}} = (k_a + k_p)\delta_{\text{out}}$ and effective steady state fractions $\phi_0^{\text{in}}\delta_{\text{in}} = -k_{\text{B}}T\phi_1 +$

$\Gamma_E \eta / (1 + \Gamma_E \eta) \Delta \mu - k_B T \Delta w$ and $\phi_0^{\text{out}} \delta_{\text{out}} = -k_B T \phi_2 + \eta / (1 + \eta) \Delta \mu - k_B T \Delta w$, we end up with the reaction flux that resembles familiar mass action kinetics

$$s_{\text{in}} = -\bar{k}_{\text{in}}(\phi_{\text{in}} - \phi_0^{\text{in}}), \quad \text{and} \quad (4.35)$$

$$s_{\text{out}} = -\bar{k}_{\text{out}}(\phi_{\text{out}} - \phi_0^{\text{out}}). \quad (4.36)$$

Taking Eq. 4.32 and Eq. 4.35, we end up with the linearized dynamics for the droplet and solvent phase

$$\partial_t \phi_{\text{in}} = D_{\text{in}} \nabla^2 \phi_{\text{in}} - \bar{k}_{\text{in}} (\phi_{\text{in}} - \phi_0^{\text{in}}), \quad r \leq R, \quad \text{and} \quad (4.37\text{a})$$

$$\partial_t \phi_{\text{out}} = D_{\text{out}} \nabla^2 \phi_{\text{out}} - \bar{k}_{\text{out}} (\phi_{\text{out}} - \phi_0^{\text{out}}), \quad r > R. \quad (4.37\text{b})$$

Now the conditions for droplet size control are the same as those discussed for the chemical potential, we can pretty much repeat the section above and replace the word chemical potential with volume fraction. The only difference is, that the boundary condition at the interface now reads $\phi_{\text{in}}(R) = \phi_1$ and $\phi_{\text{out}}(R) = \phi_2$. While we do not repeat all arguments from above, we can use Eq. 4.37 to calculate the steady state radius in terms of the reaction diffusion lengths $\ell_{\text{in/out}} = \sqrt{D_{\text{in/out}} / \bar{k}_{\text{in/out}}}$ and the volume fraction differences. The calculations are analogous to the discussion above and we give the result for $\ell_{\text{in}} \gg R_*$ only and end up with

$$R_* = \ell_{\text{in}} \left(3 \frac{\phi_0^{\text{out}} - \phi_2}{\phi_1 - \phi_0^{\text{in}}} \right)^{1/2}. \quad (4.38)$$

Note the strong similarity to Eq. 4.29. Since the system size is large compared to the reaction diffusion lengths, the volume fraction far from the droplet always reaches ϕ_0^{out} . Therefore, $\phi_0^{\text{out}} - \phi_2$ is the supersaturation far away from the droplet[60]. In addition, we call $\phi_1 - \phi_0^{\text{in}}$ the reaction force as it describes how far the reaction is from the steady state in the droplet. Thus, the stable radius increases with supersaturation and decreases with reaction force. In experiments, concentrations (volume fraction), diffusion coefficients, and reaction rates are measured instead of chemical potentials, diffusive and reactive mobilities³⁴. Therefore, this form of the stable radius is more useful to compare with experimental values.

The important conclusion from this short part is, that we recover the results from Refs.[70, 71] by linearizing the chemical potential. Therefore, we map our thermodynamic system to an effective droplet model, where the diffusive and reactive fluxes in each phase can be described by Ficks's law of diffusion and mass action kinetics. The advantage of our model is, that we can predict the precise form of the reaction cycle and the necessity

34: We have used reaction rates as a name for the rate factor all the time so far. This is correct for TST kinetics, but for linear non-equilibrium thermodynamic reactions, the Onsager coefficient contains an energy scale and is strictly a rate per $k_B T$.

to have different reaction rates in droplet and solvent phase to achieve size control and eventually splitting of droplets as predicted by Ref.[104] for a similar dynamical system.

4.4 Multicomponent active droplets

So far we have discussed the binary system only since the discussion is easier with fewer variables. In this section, we present results for the four-component system with enzymes segregating into droplets. We show that the results obtained for the binary case are transferable to the four-component case and individual size control is still possible. In the four-component system, the dynamics are given by

$$\partial_t \phi_+ = \Lambda \nabla^2 \mu_+, \quad (4.39a)$$

$$\partial_t \phi_- = \Lambda \nabla^2 \mu_- - 2s, \quad \text{and} \quad (4.39b)$$

$$\partial_t \phi_E = \Lambda \nabla^2 \mu_E, \quad (4.39c)$$

where we assume equal diffusivity for all species for simplicity. In addition, we write the dynamics in terms of sum, $\phi_+ = \phi_A + \phi_B$, and difference, $\phi_- = \phi_A - \phi_B$, of A and B volume fractions because the dynamics for the sum is independent of the reaction and of model B type. Here, we apply transition state theory for the reaction kinetics and get for passive and active reaction fluxes ($s = s_p + s_a$):

$$s_p = \lambda_p \left[\exp\left(\frac{\mu_A}{k_B T}\right) - \exp\left(\frac{\mu_B}{k_B T}\right) \right], \quad \text{and} \quad (4.40a)$$

$$s_a = \lambda_a e^{\mu_F/k_B T} \frac{\phi_E}{\phi_E} \left[\exp\left(\frac{\mu_A - \Delta\mu}{k_B T}\right) - \exp\left(\frac{\mu_B}{k_B T}\right) \right]. \quad (4.40b)$$

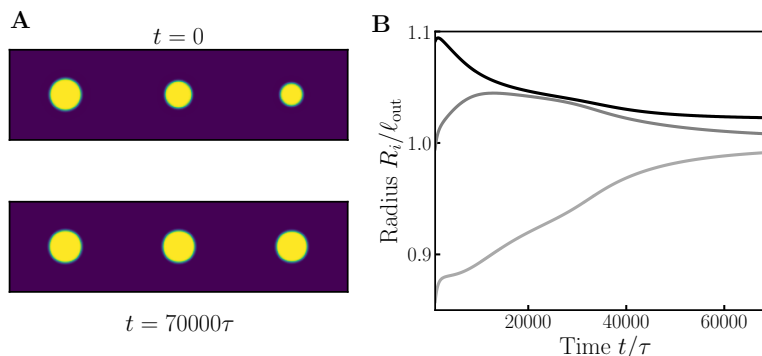
As a result, the reaction diffusion length depends on the local enzyme fraction, $\ell = \sqrt{\Lambda/(\lambda_p(1 + \eta\phi_E/\phi_E))}$.

First, we simulate three droplets with different initial sizes in a cylindrical box³⁵; see fig. 4.18A. We find, that over time the droplets all attain roughly the same size, fig. 4.18B, similar to the binary case; see fig. 4.13. This indicates, that the behavior leading to collective states with multiple stable droplets in the binary system, is transferable to the more complex four-component case, at least qualitatively.

Next, we investigate a single droplet in a large solvent phase, to see whether droplet size control is possible and is caused by the same effect as in the binary system. The resulting volume fraction profiles for a simulation of Eq. 4.39 in a NESS are shown in fig. 4.19A. As expected, the enzyme segregates into the droplet (maroon line) while the soluble protein A gets expelled (green

³⁵: A cylindrical box allows effective three dimensional simulations of multiple droplets. While droplets can only interact via the z -direction, it shows the main features, i.e. suppressed coarsening and takes less computation time than full three dimensional simulations.

Figure 4.18: Multiple droplets of the same size are stable in a four component system. **A** Snapshots of a simulation with three droplets of different initial radii (upper panel) and after $t = 7000 \tau$. All droplets attain roughly the same size. **B** Corresponding time course of the droplet radii. Parameters are $\chi = \chi_E = 4$, $\Delta w = 2$, $\Delta \mu = 10 k_B T$, $\Lambda_{ij} = \delta_{ij} k_B T v_0^{2/3} / \tau$, $\lambda_p = 10^{-3} \tau^{-1}$, $\eta = 3$ and $\bar{\phi}_+ = 0.25$. Simulations were done for TST kinetics in a cylindrical simulation box of length $L_z = 300 v_0^{1/3}$ and $R_{\max} = 50 v_0^{1/3}$. The figure is taken from [105] with minor adjustments.



line). As already seen in fig. 4.10, the enzyme is enriched at the droplet interface if $\chi_E < \chi$ to reduce the surface energy. But, in the NESS with reactions, the enzyme volume fraction in the droplet is not constant, but varies slightly and increases towards the droplet center. This variation inside the droplet phase is small compared to the partitioning $\Gamma_E \approx \exp(\chi_E)$. Thus the assumption we made earlier, replacing ϕ_E with Γ_E , is not strictly valid for the NESS, but still a reasonable approximation³⁶. The corresponding chemical potential profile for the chemical potential difference $\mu_- = \mu_B - \mu_A$ (solid blue line in fig. 4.19B) is qualitatively the same as in the binary system. The steady state chemical potential in droplet (maroon dashed line) and solvent (black dashed horizontal line) are calculated for $\phi_E^{\text{in}} = \exp(\chi_E) \bar{\phi}_E$ and $\phi_E^{\text{out}} = \bar{\phi}_E$ and match reasonably well with the numerical results. The purely diffusive dynamics of the total protein fraction (blue dashed line) and enzyme (not shown) lead to flat chemical potentials μ_+ and μ_E in the steady state. So, they are independent of the reaction-diffusion dynamics that lead to droplet size control.

From the chemical potential, we can calculate the reaction fluxes shown in fig. 4.19C. Just like in the binary case, B is degraded in the droplet (green shaded area) and produced in the solvent phase (orange shaded area). The actual rate is slightly different because TST is used in the former and LNEQ in the latter, but the effect is the same. Furthermore, the analytical prediction for the binary system (orange dashed line in fig. 4.19B), Eq. 4.25, fits the numerical results remarkably well. The only difference is, that the boundary condition at the interface is not given by the internal energy difference, Δw . Instead, it follows from the value of μ_+ in the steady state, which has to be constant everywhere and depends on the internal energy difference, but

36: This result can help modeling scaffold client systems[5, 152] in a mean-field model, by describing clients only indirectly through the partition coefficient. The simulation shows, that this is a valid approximation even in non-equilibrium conditions.

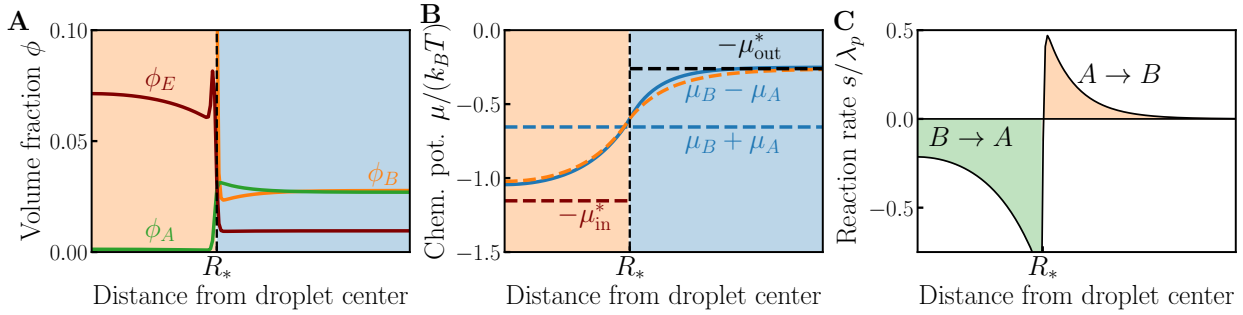


Figure 4.19: Droplet size can be controlled by enzyme partitioning into the droplet. **A** Steady state volume fractions of A (green), B (orange) and the enzyme E (maroon) along a cut through the droplet. **B** Steady state chemical potential corresponding to A for the difference, $\mu_B - \mu_A$ (blue solid line), and sum, $\mu_B + \mu_A$ (blue dashed line), of the protein chemical potentials. As expected, $\mu_B + \mu_A$ is flat in the steady state. But, $\mu_B - \mu_A$ shows a gradient between the phases because of the different steady state chemical potential in droplet (maroon dashed line) and solvent (black dashed line) phase. The orange dashed line is an analytical prediction using Eq. 4.25. **C** Reaction rate in droplet (green shaded area) and solvent (orange shaded area) phase. Similar to the binary case, droplet material B is degraded in the droplet and produced in the solvent. Parameters are $\chi_E = 2$, $\chi = 4$, $\Delta w = 4$, $\Delta\mu = 5 k_B T$, $\Lambda_{ij} = \delta_{ij} k_B T v_0^{2/3} / \tau$, $\lambda_p = 10^{-3} \tau^{-1}$, $\eta = 0.3$, $\bar{\phi}_+ = 0.06$ and $\bar{\phi}_E = 0.001$. Simulations were done for TST kinetics and in a spherical simulation box with $R_{\max} = 300 v_0^{1/3}$. Figure B is taken from [105] with minor adjustments.

on the total amount of protein and the interaction χ as well³⁷. The reason for the good fit, although different kinetics are used, is that the kinetics influence the values of $\mu_{-}^{*,\text{in}}$ and $\mu_{-}^{*,\text{out}}$ (Eq. 4.8). But they appear in the equation for $\mu_{-}(r)$ as a constant prefactor and do not influence the shape of μ_{-} as a function of r . In addition, all chemical potentials are on the order of $k_B T$, thus the difference between TST and LNEQ kinetics is small³⁸.

Fig. 4.19C shows that the reaction flux in droplet and solvent has the opposite sign. Thus, we expect that the steady state droplet radius R_* is determined by a flux balance similar to the binary case, see fig. 4.17. The integrated flux as a function of radius is shown in fig. 4.20 for a numerical simulation. The different scalings of S_{in} and S_{out} with R introduce a stable steady state radius R_* . We can predict a scaling of the reaction flux with droplet size, similar to Eq. 4.26 and Eq. 4.27, under a set of assumptions. First, for low total enzyme fraction, $\bar{\phi}_E \ll 1$, small droplet volume, $V \ll V_{\text{sys}}$, and strong phase separation, $\chi \gg 1$, we can approximate the enzyme fractions as $\phi_E^{\text{out}} \approx \bar{\phi}_E$ and $\phi_E^{\text{in}} \approx \Gamma_E \bar{\phi}_E \approx e^{-\chi_E} \bar{\phi}_E$; see Eq. 4.18 and fig. 4.10. Second, we assume that the reaction diffusion length inside the droplet is large compared to the droplet, $\ell_{\text{in}} \gg R$ and that the reaction is close to the steady state in the solvent phase. In that case, we can calculate analytical predictions for the scaling of the reaction, see Appendix.G. We find, that the integrated flux in the droplet phase scales with droplet volume V and the inverse of the enzyme partition coefficient, $S_{\text{in}} \propto \exp(-\chi_E) V$. The integrated flux outside the droplet scales with droplet area A_R for small reaction-diffusion length $\ell_{\text{out}} \ll R$, $S_{\text{out}} \propto A_R$, or with

³⁷: See Appendix.F for an analytical treatment of the NESS.

³⁸: In general, the driving strength is large compared to temperature, $\Delta\mu \gg k_B T$. But since the steady state chemical potential, i.e. μ_{in}^* , is the important quantity, all relevant chemical potentials can be on the order of $k_B T$.

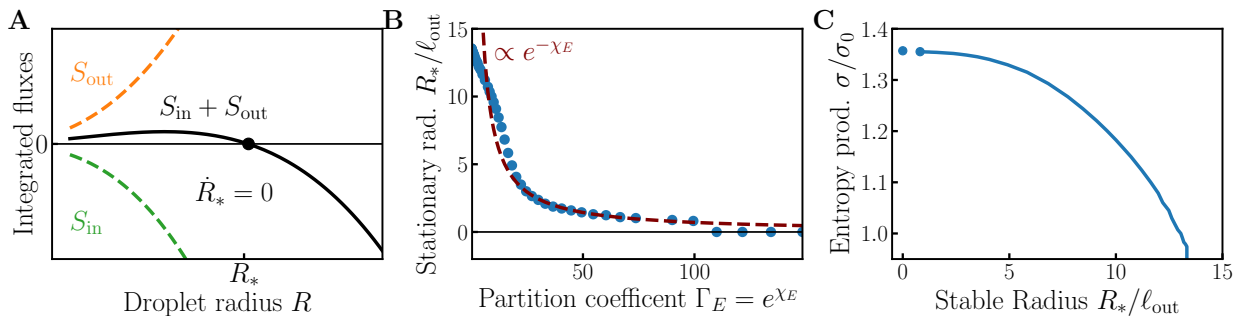


Figure 4.20: Stronger partitioning leads to smaller droplets, but higher energy cost. **A** Integrated reaction flux in droplet (green dashed line), solvent (orange dashed line) and their sum (black dashed line) as a function of droplet radius. Similar to the binary case in fig. 4.16, the competition between the two fluxes leads to a stable, steady state droplet radius R_* (black dot). Results are from a numerical simulation. **B** Stationary radius as a function of partition coefficient calculated from the enzyme interaction strength χ_E . The result is very similar to the binary case, see fig. 4.17. **C** Steady state entropy production as a function of stable droplet radius. Because of the sudden jump from a finite radius to full dissolution (see **B**), the entropy production has a discontinuity at small radii (blue dots). The entropy production is normalized with respect to the state with homogeneously distributed enzyme $\Gamma_E = 1$. Notably, smaller stable radii require more energy input. Parameters are $\Gamma_E = 25$ ($\chi_E = 3.2$) (in A), $\chi = 4$, $\Delta w = 4$, $\Delta\mu = 5 k_B T$, $\Lambda_{ij} = \delta_{ij} k_B T v_0^{2/3} / \tau$, $\lambda_p = 5 \cdot 10^{-4} \tau^{-1}$, $\eta = 0.2$, $\bar{\phi}_+ = 0.06$ and $\bar{\phi}_E = 0.001$. Simulations were done for TST kinetics and in a spherical simulation box with $R_{max} = 300 v_0^{1/3}$. The figures are taken from [105] with minor adjustments.

39: Note that we found the same scalings for the binary system, which is not surprising considering the similar results for the NESS in fig. 4.19 and fig. 4.15.

droplet radius for large reaction-diffusion length³⁹, $\ell_{out} \gg R$, $S_{out} \propto R$. Fig. 4.20B compares the numerical results (blue dots) and the predicted scaling for the enzyme partition coefficient (maroon dashed line). The scaling works well for intermediate partitioning but fails for low partitioning and strong partitioning. For low partitioning, the assumption of large reaction diffusion length compared to droplet size breaks down, which explains the mismatch. Furthermore, strong partitioning leads to full dissolution due to the Laplace pressure[60], which is not included in the analytical calculation, and thus the partitioning needed for dissolution is overestimated. Finally, fig. 4.20C shows the steady state entropy production rate calculated from Eq. 4.13 for the numerical results of fig. 4.20B. We find, that smaller droplets have a higher entropy production, indicating that keeping droplets small requires more energy. While it is intuitive that smaller droplets, i.e. more control compared to the passive case, require more energy, it is surprising as well because the active reaction happens predominantly in the droplet. Therefore, smaller droplets mean less concentrated active reactions. But, in our model, the active reaction happens in the solvent as well, and especially far away from the droplet lots of energy is burned in the steady state reaction cycle.

In fig. 4.7A, we showed that the steady-state entropy production scales super-linearly with the driving strength $\Delta\mu$. Furthermore, the driving strength indicates how far from equilibrium the reactions are. Thus, we investigate the influence of driving strength on the steady-state radius next. fig. 4.21 shows

the numerical results for the stable droplet radius as a function of enzyme interaction and driving strength⁴⁰. We find, that for very low driving, very high segregation of enzymes is necessary to reduce droplet size. But, above a threshold of $\Delta\mu \approx 4 k_B T$, the driving strength does not affect the stable droplet radius anymore. This can be explained via fig. 4.11B, which shows, that for a fixed $\eta\Gamma_E$, increasing $\Delta\mu$ above a threshold does not affect the steady state chemical potential $\mu_-^{*,in}$. And because $\mu_-^{*,in}$ appears in the equation for R_* , see Eq. 4.29, increasing the driving strength above that point leads to higher entropy production, but does not affect droplet size. Finally, the factor η has a similar effect on the droplet radius as varying Γ_E ; see Eq. 4.29.

In this section, we have shown that droplet size can be controlled by non-equilibrium reaction cycles, if the reaction rate is different in the droplet and solvent phases. In this case, the reaction can drive diffusive fluxes between the phases that stop droplet growth at a fixed size. This steady state droplet radius is independent of system size and instead determined by a combination of kinetic quantities, the reaction diffusion length, and thermodynamic quantities, the chemical potential differences. In our example⁴¹, the rate difference is caused by enzymes accumulating in the droplet due to weak enthalpic interactions. Thereby, stronger partitioning in the droplet phase reduces droplet size and can dissolve droplets. Furthermore, we show that the driving strength has little influence on droplet size above a certain threshold. In cells, η can be regulated by changing the total amount of enzymes, either via the production of enzymes or by activating them through upstream processes. The optimal case for size control would be a reaction cycle as described in Eq. 4.1, where the phosphatase partitions into the solvent phase, while the kinase partitions into the droplet phase. In this case, only the active reaction happens in the droplet and only the passive reaction happens in the solvent. Furthermore, $\mu_{in}^* = \Delta\mu$ and $\mu_{out}^* = 0$ because of the perfect separation of the reactions. This would circumvent the problem of a futile cycle, where energy is wasted because both reactions happen in both phases. Every A protein that gets produced in the droplet diffuses out of the droplet, gets converted into B by the passive reaction, and diffuses back into the droplet, where the cycle starts again. Thereby, each cycle is accompanied by one ATP hydrolysis reaction.

Droplet size in cells

In this part, we want to give an order of magnitude approximation for possible active droplet radii in cells. Therefore, we combine the analytical prediction for steady-state droplet radius,

40: Here, for negative χ_E the enzyme repels from the phase separating protein B and gets enriched in the solvent phase (similar to state A).

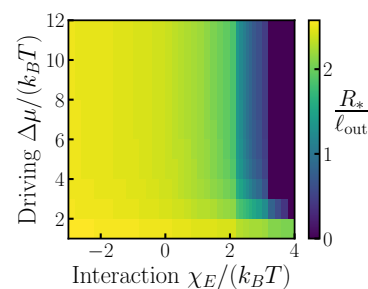


Figure 4.21: The stable radius depends only weakly on driving strength. Stationary radius (color code) as a function of enzyme interaction and driving strength. Above a minimum driving strength (here $\Delta\mu \approx 4 k_B T$), the driving has almost no impact on the result. This is reminiscent of fig. 4.11B. For a fixed $\eta\Gamma_E$, increasing $\Delta\mu$ above a threshold does not affect the steady state chemical potential $\mu_-^{*,in}$ and thus the dynamics. Parameters are the same as in fig. 4.20. Simulations were done for TST kinetics and in a spherical simulation box with $R_{max} = 300 v_0^{1/3}$.

41: In general, every asymmetry in the reaction rates can cause the same effect.

Eq. 4.29 and known literature values for protein diffusivity, enzymatic reaction rates, and protein concentrations. We estimate the diffusivity of proteins by $D \sim 0.1 - 10 \mu\text{m}^2\text{s}^{-1}$ depending mostly on protein size[179]. Estimating reaction rates and comparing them to our reactions is more difficult because usually mass action kinetics are used to describe reactions. In addition, enzymatic reactions are often described using Michaelis Menten kinetics. Assuming that the substrate (here the droplet material) is abundant, which is the case in the droplet phase, the rate of the enzymatic Michaelis Menten reaction can be approximated by a single rate $k_{\text{cat}} \sim 0.01 - 100 \text{s}^{-1}$ [1]. If the enzyme is strongly segregated and the active reaction dominates in the droplet phase, we can write the total reaction flux as

$$S_{\text{in}} \approx -k_{\text{cat}}\Gamma_E\bar{\phi}_E V, \quad (4.41)$$

where V is the droplet volume. To calculate the diffusive influx into the droplet, we assume the protein and enzyme are dilute in the solvent, so $\phi_C \approx 1$. We can then approximate the chemical potential in the solvent phase by $\mu_B \approx \mu_B(\phi_B^{\text{out}}) + k_B T(\phi_B - \phi_B^{\text{out}})/\phi_B^{\text{out}}$. Far away from the droplet interface, the B fraction is set by the equilibrium ratio of the reaction⁴², K , and the total protein fraction $\bar{\phi}_+$: $\phi_B(r \gg R) \approx K/(1 + K)\bar{\phi}_+$. The diffusive influx can then be approximated as

$$J \approx 4\pi R \frac{\Lambda k_B T}{\phi_B^{\text{out}}} \left(\frac{K}{1 + K} \bar{\phi}_+ - \phi_B^{\text{out}} \right). \quad (4.42)$$

With $D = \Lambda k_B T / \phi_B^{\text{out}}$, we can calculate the stable droplet radius by setting $J + S = 0$

$$4\pi R D \left(\frac{K}{1 + K} \bar{\phi}_+ - \phi_B^{\text{out}} \right) - \frac{4\pi R^3}{3} \Gamma_E \bar{\phi}_E k_{\text{cat}} = 0. \quad (4.43)$$

The stable droplet radius is then given by

$$R_*^2 = \frac{3D}{k_{\text{cat}}\Gamma_E} \frac{\Delta\phi_B}{\bar{\phi}_E}. \quad (4.44)$$

Assuming that enzyme and protein have the same molecular volume⁴³ this can be written in terms of particle concentration as well, $\Delta\phi_B/\bar{\phi}_E = \Delta c_B/\bar{c}_E$. Because the total amount of enzyme is low, we assume $\Gamma_E \bar{c}_E$ to be small, but at the same time, the protein variation of B in the solvent is small as well, $\Delta c_B \ll 1$. As a result, we estimate $\Delta c_B/(\Gamma_E \bar{c}_E) \sim 0.01 - 100$.

We present two scenarios, where we assume a typical diffusivity of $D \approx 1 \mu\text{m}^2\text{s}^{-1}$ for both[105]: First, we assume fast enzymatic reactions ($k_{\text{cat}} \approx 100 \text{s}^{-1}$) and strong enzyme segregation ($\Delta c_B/(\Gamma_E \bar{c}_E) \approx 0.01$), which results in an approximate sta-

42: Assuming the driven reaction is slow in the solvent phase.

43: Usually enzymes are large compared to the substrate[1], so we might expect the stable radius to be larger than estimated here.

ble droplet size $R_* \approx 1.7 \cdot 10^{-2} \mu\text{m}$. Second, for slow reactions ($k_{\text{cat}} \approx 0.1 \text{s}^{-1}$) and weak segregation ($\Delta c_B / (\Gamma_E \bar{c}_E) \approx 10$), we end up with a much larger droplet size, $R_* \approx 17 \mu\text{m}$. This shows, that with reasonable parameter assumptions, droplets on all relevant length scales for the cell, from $\sim 10 \text{nm}$ to tens of μm , can be realized.

4.5 Reactions as a switch for Droplet

We want to end by showing how timed active reactions can switch between a stable droplet state and a homogeneous mixture. The starting point is an equilibrium phase separating system as discussed in Sec. 3.2, i.e. a mixture of a solvent C and a protein that exists in a soluble state A and a phase separating state B and a conversion reaction $A \rightleftharpoons B$ switches between the two states. For the process to work best, chemical equilibrium, defined by the equilibrium ratio K and the total protein fraction $\bar{\phi}_+$, has to be such that the average B fraction is close to the binodal ϕ_1 and below spinodal ϕ_s , i.e. $\phi_1 < K/(1+K)\bar{\phi}_+ < \phi_s$; see blue dot in fig. 4.22. In this case, both the droplet and the homogeneous state are metastable, although the droplet state is the equilibrium state.

To form droplets, the system needs to cross an energy barrier, where the transition is driven by thermal noise. If the B fraction in the homogeneous mixture is close to the binodal, the nucleation is well described by classical nucleation theory[128], where the nucleation rate τ scales with the Arrhenius factor of the energy barrier ΔE , $\tau \propto e^{\Delta E/k_B T}$. For high energy barriers, the nucleation time can become very large⁴⁴ and thus it is difficult to predict when and where droplets form. Furthermore, once droplets form, they will not dissolve spontaneously in large systems because the total energy gain of the droplet state compared to the homogeneous state scales with system volume.

As a result, the nucleation in cells might be controlled by other (active) processes[182]. Here, we show that active reactions can in principle switch between the droplet and homogeneous state. Thereby, the active reaction happens only for a short amount of time, while both droplet and homogeneous state remain metastable if no active reaction is present. It is necessary that the driven reaction can drive the transition towards state B (green dot in fig. 4.22) and state A (red dot in fig. 4.22). This corresponds to two different reaction pathways, which we denote by $A + F \rightleftharpoons B + W$ and $A + W \rightleftharpoons B + F$ for simplicity. The first reaction can shift the equilibrium B fraction into the spinodal region while the second reaction can shift it out of the binodal region. Thereby, droplet formation happens spontaneously in the former, and droplets get dissolved in the latter

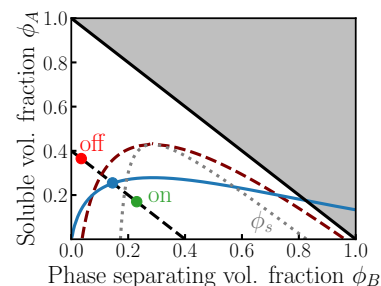


Figure 4.22: Active reaction can move the chemical equilibrium and control droplets in time. Chemical equilibrium (blue line) in the ϕ_A vs ϕ_B plane. Chemical equilibrium (blue dot) lies between the binodal (maroon dashed line) and the spinodal (grey dotted line). Activating a driven reaction can move the homogeneous mixture into the spinodal area (green dot) or outside the binodal (red dot) and thus turn droplets trigger droplet formation or dissolve existing droplets. Parameters are $\Delta w = 1.6$, $\chi = 3.5$, $\bar{\phi}_+ = 0.4$, $\Delta\mu_{\text{on}} = 3.5 k_B T$ and $\Delta\mu_{\text{off}} = -0.75 k_B T$. Here, A does not interact with B or C , i.e. the enthalpy is given by $h\nu_0/k_B T = \chi\phi_B(1 - \phi_B - \phi_A)$.

⁴⁴: For classical nucleation theory to be valid, the energy barrier needs to be high compared to thermal energy $k_B T$.

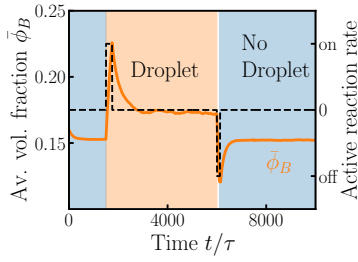


Figure 4.23: Active reactions can be used to switch droplets on and off. Average B volume fraction (left axis, orange line) and driven reaction rate (right axis, black dashed line) as a function of time. In the blue shaded area, the system is in a homogeneous state and in the orange shaded area a single droplet is present. The active reaction can switch the droplet on and off with short pulses (black dashed line). Parameters are the same as in fig. 4.22. In addition, the simulation was done in a two dimensional square box of size $32 \times 32 v_0^{1/2}$ and the kinetic parameters are $\Lambda_{ij} = \delta_{ij} v_0/\tau$, $k_p = 3 \cdot 10^{-3} \Lambda v_0^{-2}$, $\eta_{\text{off}} = 1$, $\eta_{\text{on}} = 7$ and $\langle \xi_i(\mathbf{r}, t) \xi_j(\mathbf{r}', t') \rangle = 0.05 \Lambda_{ij} k_B T$.

case. We call the first and second reactions the ‘on’ and ‘off’ switch respectively and the corresponding steady state chemical potential are $\Delta\mu_{\text{on}}$ and $\Delta\mu_{\text{off}}$.

To check this hypothesis, we perform numerical simulations with thermal noise as introduced in Eq. 2.20 in Sec. 2.2. To avoid numerical problems with the noise for small volume fractions, we perform simulations with high average protein fractions. For the same reason we use enthalpic interactions of the form $v_0 h/k_B T = \chi \phi_B (1 - \phi_B - \phi_A)$, i.e. A does not interact with the other species, to avoid that the A fraction in the droplet is very low. Finally, we do not use the thermodynamically correct noise amplitude of $2k_B T \Lambda_{ij}$, instead, we use a reduced amplitude of $0.05 k_B T \Lambda_{ij}$. The reason for this is that the free energy variations in the regular solution theory are small, for example for $\chi = 3.5$, the difference between free energy minima and maximum is $\sim 0.25 k_B T$. As a result, the noise amplitude is much larger than the free energy variations and the noise would dominate the dynamics. Although we expect noise to be important in cells, the noise strengths compared to interactions are overestimated in our model, therefore, we tune it down artificially.

We simulate the on and off switch using time dependent reaction rates. In the example below, we specifically use

$$k_a^{\text{on}}(t) = \frac{k_{\text{on}}}{2} \left[\tanh \frac{t - t_{\text{on},1}}{\sigma} - \tanh \frac{t - t_{\text{on},2}}{\sigma} \right], \quad (4.45a)$$

$$k_a^{\text{off}}(t) = \frac{k_{\text{off}}}{2} \left[\tanh \frac{t - t_{\text{off},1}}{\sigma} - \tanh \frac{t - t_{\text{off},2}}{\sigma} \right] \quad (4.45b)$$

where k_a^{on} and k_a^{off} are the on- and off-switch reaction rates respectively and $t_{i,1/2}$ control at which times the reaction is turned on ($t_{i,1}$) and off $t_{i,2}$. We call $\Delta t_{\text{on/off}} = t_{\text{on/off},1} - t_{\text{on/off},2}$ the pulse duration. In addition, we model the active reactions using linear non-equilibrium thermodynamics. In this case, the total reaction flux is given by $s^{\text{on/off}}(t) = (k_p + k_a^{\text{on/off}}(t))(\mu_A - \mu_B - \Delta\mu_{\text{on/off}})$.

The results of an example simulation are shown in fig. 4.23. For early times the system is a homogeneous mixture. Then, the ‘on’ reaction is present and leads to droplet formation. Afterwards, the droplet is stable and only dissolves once the ‘off’ reaction dissolves it. Here, the ‘on’ and ‘off’ pulses have a duration of $\Delta t_{\text{on}} = 50 \tau$ and $\Delta t_{\text{off}} = 25 \tau$ respectively, which is short compared to the simulation time of 10000τ . Thus, it is possible to control the formation and dissolution of stable droplets with short pulses of (active) chemical reactions. Corresponding simulation snapshots are shown in fig. 4.24 for the three stages, homogeneous mixture, droplet, and homogeneous mix-

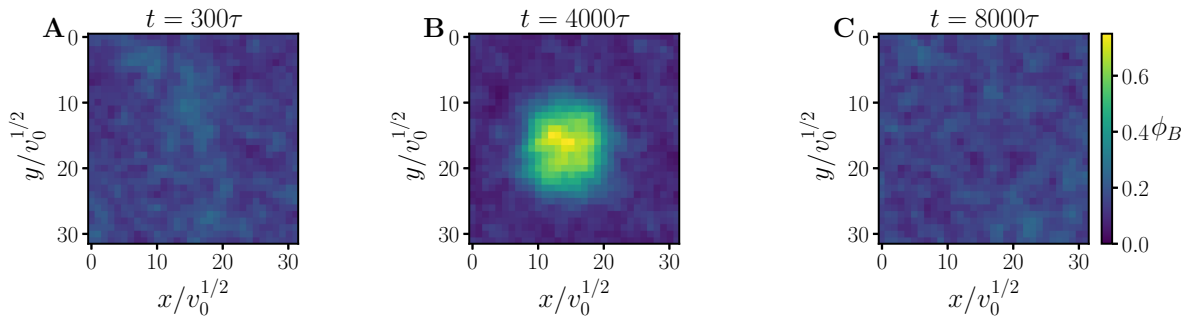


Figure 4.24: Simulation snapshots of driven droplet formation and dissolution. Simulation Snapshots of the B volume fraction from the simulation shown in fig. 4.23 for different times. The colorbar in C holds for all three plots. **A** For early times, a homogeneous mixture with thermal noise is present and droplets will only form for spontaneously on long time scales. **B** The ‘on’ reaction has triggered the formation of a single droplet. The thermal noise influences not only the volume fraction, but also deforms the droplet. **C** After active dissolution, the system is back to the homogeneous state. Parameters are the same as in fig. 4.23.

ture again. The snapshots show that the thermal noise is deforming the droplet shape and leads to fluctuating volume fraction fields.

This is only a proof of principle and further research is necessary to understand the details of this process, for example, the parameter dependencies. But, the preliminary results show, that short active reaction pulses can control formation and dissolution in a bistable system, where both the droplet and the homogeneous state are metastable. Unlike the active droplets discussed above, here the activity is only needed for short amounts of time as a switch. Thus, the control of formation and dissolution is efficient. Furthermore, by controlling the activity of enzymes, the active reaction can be turned on and off.

4.6 Summary

In this chapter, we extended the model of phase separation with passive conversion reactions to active reactions. Active reactions are driven out of equilibrium by external energy supply. In our model, this external energy is supplied by fuel molecules getting converted into waste molecules. The chemical potential difference between fuel and waste, $\Delta\mu$, is constant in the whole system, thus it can be used to fuel other processes. Here, it changes the free energy of reaction for the conversion between two protein states A and B (Eq. 4.4). We find that if we replace the passive reaction with the active reaction, the system can be mapped back to the passive case with a rescaled internal energy difference $\Delta w \rightarrow \Delta w - \Delta\mu/k_B T$; see fig. 4.2A. The diffusive dynamics remain unaltered by the activity because, in isotropic systems, reactions can not drive diffusive fluxes directly[107]. As a result, an active reaction can control phase separation only

by varying the driving strength. But, this has the same downside as changing other global quantities, for example, temperature and pH, as changing the driving influences many other processes as well. If there is only one reaction present, it will inevitably reach the steady state and behave like an equilibrium reaction under the constraint that $\Delta\mu = \text{const.}$

To keep the reaction away from its steady state, we introduce a reaction cycle in our model. This is inspired by post-translational modifications of proteins, for example phosphorylation dephosphorylation cycles[153]; see Eq. 4.1. In the example we introduce, the passive and active reactions are both present. In this case, there are two ways to switch between states A and B , directly, $A \rightleftharpoons B$ and with the help of external energy, $A + W \rightleftharpoons B + F$; see Eq. 4.5. We find that the total reaction flux can still vanish everywhere in space, $s = 0$; see fig. 4.5C. But, the individual reaction fluxes do not vanish. Instead, the two reaction cancel each other everywhere, $s_a = -s_p \neq 0$; see fig. 4.5C. The condition of vanishing reaction flux, $s_a = -s_p$, is fulfilled for a unique steady state chemical potential difference $\mu_A - \mu_B$; see Eq. 4.8 and fig. 4.3. The steady state chemical potential takes values between 0 and $\Delta\mu$, depending on the ratio of the reaction rates between active and passive reactions, η . Thus, if the rate of the passive reaction is fast ($\eta \ll 1$), the system behaves as if only the passive reaction was present and if the rate of the active reaction is fast ($\eta \gg 1$), the system behaves as if only the active reaction is present. In this way, the kinetic parameter η interpolates between the passive case (discussed in Sec. 3.1) and the active case (discussed in Sec. 4.1). As a result, the steady state chemical potential takes the role of $\Delta\mu$ in fig. 4.2A, thus it controls the amount of protein in state B and thereby, if droplets form or not⁴⁵; see fig. 4.7B.

45: As long as the total protein volume fraction exceeds the solvent phase volume fraction, $\bar{\phi}_+ > \phi_B^{\text{out}}$.

The steady state of a reaction cycle depends on the reaction kinetics, unlike the passive or active reactions alone, where the steady state is fully determined by the free energy of reaction. This is an important property of reaction cycles because reaction kinetics can be controlled more precisely, for example via enzymes that speed up biochemical reactions. Oftentimes, enzymes act on specific proteins[175] and their activity can be controlled by upstream processes reasonably fast[36]. Furthermore, the reaction rate scales with the amount of active enzymes[176], so the rates can in theory be tuned continuously⁴⁶. Thus, a reaction cycle, like a phosphorylation-dephosphorylation cycle[73], can be used as a specific, fast, and precise control mechanism for droplet formation and dissolution. However, this control comes at an energy cost, that can be quantified in this model via the entropy production rate; see fig. 4.7A. We find that dissolving droplets and keeping them dissolved costs energy, while droplet

46: The linear scaling of the rate with enzyme concentration is valid for low amounts of enzyme in Michaelis Menten kinetics[176].

formation is energetically favorable and does not require external energy; compare fig. 4.7A and B. This is similar to the results obtained in Ref.[71, 103], which models the phase separation of stress granules. There the authors argue, that this is a feature because the cell needs stress granules in critical situations. Thus, the constant energy consumption keeps stress granules dissolved under normal conditions, but the cell does not need to pay energy to form stress granules when they are needed. In addition, Ref.[71] finds that the individual size of droplets can be controlled as well. But we showed, while the reaction cycle can control the available B protein, it can not control the diffusive dynamics, which still shows coalescence and Ostwald ripening; see fig. 4.6. The reason is, that the reaction can vanish everywhere, in the droplet and the solvent phase; see fig. 4.5C. Thus, to control individual droplet size with reactions, it is necessary to convert reactive into diffusive fluxes between the phases. Those diffusive fluxes can counteract Ostwald ripening and coalescence. As mentioned before, direct conversion from reactive to diffusive fluxes is not possible[107]. In addition, for equal reaction rates in droplet and solvent, this is not possible for reactions driven by the chemical potential because the chemical potential does not distinguish between droplet and solvent phase.

In general, the reaction rates k and λ in Eq. 4.10 are not constant, but depend on external parameters, for example temperature, pH or composition. We assumed them constant because the composition is the only variable parameter in our model and there is no a priori way to know how the rate should depend on composition. Thus, we generally expect that the rates in droplet and solvent are different, but we do not know how strong the effect is. Instead, we introduce a mechanism that leads to different rates in droplet and solvent phase inspired by biological examples[73]. In many biological examples, enzymes and their substrate co-localize into droplets. Thus, we introduced an enzyme E that speeds up the driven reaction and partitions into the droplet; see fig. 4.8. We show, that the different reaction rates in droplet and solvent lead to different steady state chemical potentials in both phases; see fig. 4.11B. As a result, the reaction in droplet and solvent phase may have different signs, i.e. that protein state B gets degraded in the droplet and produced in the solvent; see fig. 4.12B. The degradation of droplet material in the droplet limits droplet growth and can introduce a stable droplet size independent of system size; see fig. 4.16. Furthermore, a collective state of multiple droplets of the same size is stable, similar to the results obtained with mass action kinetics in Refs.[70, 71], see fig. 4.13. We find, that the stable droplet radius can be controlled by the partitioning of the en-

zyme. Thereby, stronger partitioning reduces droplet size and can lead to full dissolution of droplets; see fig. 4.17. In addition, keeping droplets small requires more energy, as quantified by the entropy production; see fig. 4.20C. In the limit of weak partitioning, we are back to the reaction cycle with homogeneous rates discussed before. Furthermore, we showed that this qualitative picture can be extended to more complex systems with multiple species; see fig. 4.19 and fig. 4.20. In this case, the non-reactive species are not only indirectly influenced by the reactions, via the size of droplets; see fig. 4.19A and B. In addition, we find that the different reaction rates in droplet and solvent maintain a chemical potential gradient across the droplet solvent interface and thus drive diffusive fluxes; see fig. 4.15B. This gradient is determined by the reaction diffusion length, see fig. 4.14, which is an important parameter in all reaction-diffusion systems[183]. Finally, we estimated stable droplet radii using literature values for the diffusivity and reaction rate. We find that reasonable parameters can stabilize droplets on all relevant length scales for cells, from ~ 10 nm to ~ 10 μ m.

In this thesis, we developed a thermodynamic model that combines phase separation and chemical reactions. The important new idea compared to previous work is, that the reaction rates are derived from thermodynamic arguments instead of mass action kinetics. This is important because mass action kinetics assume ideal, dilute solutions, assumptions that are not fulfilled in phase separating solutions. In fact, phase separation is driven by weak interactions between molecules, which makes it inherently non-ideal. In addition, phase separation leads to the formation of phases with different compositions, so it can not be described as a dilute solution.

This thesis aimed to understand how simple biochemical reactions can control droplets formed via phase separation in the context of biomolecular condensates. Thereby, we identified the key ingredients for individual size control of droplets: **(i)** A molecule that exists in two states, one state is soluble in the solvent and one state phase separates and forms droplets. **(ii)** A non-equilibrium reaction cycle that is coupled to an external energy supply and switches between the two states. **(iii)** Different reaction rates in droplet and solvent phase. Under these conditions, it is possible to control individual droplet size, independent of system size, and stabilize multiple droplets[73]. The droplet size in this case depends on the reaction diffusion length scale of the system, in particular on the partition coefficient of the enzyme into the droplet.

5.1 Passive reactions

First, we discussed the interplay of phase separation and a conversion reaction $A \rightleftharpoons B$ in equilibrium. As expected, equilibrium systems allow only limited control on phase separation. Effectively, passive reactions influence the total amount of the phase separating material and thus whether droplets form or not. This is in contrast, to work in Refs.[70, 71], where the same reaction, described by mass action kinetics, leads to an arrested state of multiple droplets that can be controlled by reaction rates¹. Because chemical reactions and phase separation are both driven by chemical potential differences, the formation of equilibrium droplets and the partitioning of other species are intimately linked to the equilibrium ratio in droplets[133]. In addition, for constant reaction rates, the reaction does not distinguish between

5.1 Passive reactions . . . 115

5.2 Active reactions 117

¹: The authors in Refs.[70, 71] explicitly mention that they consider non-equilibrium reaction. But, it is not clear how non-equilibrium reactions lead to reaction fluxes that resemble mass action kinetics[60].

the two phases because the chemical potential in both phases is equal. We conclude that it is important to consider the thermodynamics of reactions when modeling biochemical reactions in biomolecular condensates[40].

Furthermore, the different compositions of the droplet and solvent phase influence the equilibrium ratio of reactions inside the droplet. This means that droplets are chemically distinct environments, different from the solvent phase. In non-equilibrium *in vitro* experiments, droplets can even have different pH than the surrounding[184]. Therefore, it is important to consider that droplets will not only influence reaction kinetics by concentrating molecules in space[40] but also influence the equilibrium of the reaction.

We showed that the framework of a chemical reaction switching between two states of a molecule does not necessarily mean that the chemical composition of the molecule changes. The two states *A* and *B* can be bound and unbound states of a protein, as discussed in Sec. 3.3, but also differently folded protein states[16]. Particular interesting examples would be (bio)polymers that undergo a coil to globule transition as a function of temperature or solvent condition[185, 186]. In a good solvent, the polymer is in an expanded state, the coil, while it is in a compact state, the globule, in a bad solvent due to positive self interactions². The control parameter for the transition can be temperature or solvent conditions. This type of transition has been shown in proteins[186] and the self-interactions inducing the coil to globule transition have been linked to phase separation in biomolecules[187]. Thus, it would be interesting to model coil to globule transition in our framework and try to link the internal energy differences, Δw , with the interaction strength, χ , because of the self interaction and the inter-molecule interactions have the same origin.

Biomolecular condensates are assumed to play an important role in organizing biochemical reactions in space by concentrating reactants[188, 189]. We showed that the thermodynamics of phase separation influence the equilibrium ratio of reactions. It would thus be interesting to investigate in more detail, how chemical reactions behave in a two phase system as compared to the homogeneous mixture. Our model can be used to investigate how relaxation to equilibrium of a reaction is influenced by droplets: **(i)** Under which conditions are reaction rates increased or decreased. **(ii)** Under which conditions is the reactive equilibrium influenced by droplets and how? **(iii)** Can droplets ‘choose’ reaction pathways by including some molecular, but excluding others? In addition, extending the model to more components and more reactions will be an important future direction for research. Purely diffusive multicomponent systems

2: This is the case for an upper critical solution transition. Entropy driven transitions associated with a lower critical solution temperature are possible as well, but those are not captured in the simple regular solution model with temperature independent interaction strength χ .

have been studied[49, 63, 65] recently. But, it is not clear how multiple reactions would influence how many phases form or which phases form. In particular, more components allow for more phases in theory, but the reactions introduce conservation laws that reduce the number of possible phases. Thus, opening up the possibility for interesting interactions between the two processes.

In a more general context, investigating different temperature dependencies of Δw and χ would be an interesting approach. For example, if Δw increases stronger with T than χ , it could lead to reaction induced lower critical solution temperature. Also, the scaling of the average radius with time $\langle R \rangle(t)$ as a function of reaction diffusion length would be interesting to analyze to see whether we recover model B type $\langle R \rangle \propto t^{1/3}$ or model A type $\langle R \rangle \propto t^{1/2}$ dynamics. Another direction would be to replace the simple regular solution model with more complex free energy densities. For example, it would be interesting to investigate the role of biopolymer size using the Flory Huggins free energy, or the role of electrostatic interactions using Voorn-Overbeek theory[81, 190].

5.2 Active reactions

In the second part of this thesis, we investigated how active reactions can influence phase separation. We find that driving the conversion reaction via fuel and waste molecules, $A + W \rightleftharpoons B + F$ has the same restrictions as the passive reaction. In fact, the system can be mapped to an effective equilibrium system with rescaled internal energy difference. The main reason is that in isotropic systems, reactions can not drive diffusive fluxes directly and vice versa, so the two processes are independent of each other. Furthermore, the system is fully determined by energetic properties and independent of reaction rates and diffusivities. This is different if both reactions, the passive and active reactions, are happening simultaneously. In this case, the non-equilibrium steady state depends on the reaction kinetics and not only the thermodynamics. For homogeneous reaction rates, the system can still be mapped to an effective equilibrium system, but the reaction kinetics can be controlled in a fast, precise, and specific way in biological cells, for example by enzymes. Thus, by controlling the activity of enzymes, the cell can control if droplets form or dissolve[36]. This is similar to the results obtained in Ref.[71, 103], which models the phase separation of stress granules. But Ref.[71] finds that the individual size of droplets can be controlled as well, which is not possible in our model for homogeneous reaction rates.

We find that the size control of individual droplets and a

3: But different diffusivities in droplet and solvent phase are not sufficient for size control because the diffusivity does not change the steady state chemical potential.

4: So droplets can not form spontaneously.

5: This effect is similar to but different from the case of localized RNA we discussed in Sec. 3.3. Similar because it induces nucleation locally, but different because it involves the constant turnover of droplet material via active processes.

NESS with multiple stable droplets requires the reaction rates to be different in droplet and solvent phase. Motivated by experimental findings, for example in stress granules[36], we explain the asymmetry in the rates with enzymes that enrich in the droplet phase and thus speed up the driven reaction in the droplet only. But, any effect that leads to different reaction rates in droplet and solvent phase leads to size control of droplets³. For example, autocatalytic reactions of the form $A + B + W \rightleftharpoons B + B + F$ would achieve the same effect. Furthermore, we expect that the reaction rates in droplet and solvent are different, even without the effect of enzymes because droplets form chemically distinct environments. But, it is hard to estimate a priori if the reactions are faster or slower in the droplet and by how much[40].

In our model, individual droplet size is determined by the reaction diffusion length, reminiscent of other processes in biology, for example in morphogenesis[72, 100, 101]. In addition, robust control requires that the reaction diffusion length is large compared to the droplet size, i.e. reactions need to be slow compared to diffusion on the scale of droplet radii. Slow reactions burn less energy, which makes this mechanism useful for efficient size control. In the opposite case, fast reactions, and small reaction diffusion length is sub-optimal for size control, but they can induce a steady state chemical potential gradient between droplet and solvent phase. While this requires constant burning of fuel, it could control the exchange of ions between the phases, similar to the electrochemical gradient across biological membranes[178].

Finally, we want to discuss some possible future directions of research. In Ref.[73], we suggest a second possible mechanism to control droplet size, which is discussed in Ref.[67] for mass action kinetics: If the driven reaction is localized, for example by an enzyme that is bound to a membrane, and the driven reaction produces droplet material in a sub saturated environment⁴, the local production of droplet material can induce droplet formation⁵. In this case, the droplet material gets produced in the droplet center and flows out of the droplet because of the sub saturated solvent phase and the balance of these processes leads to stable droplet size. Thus, the mechanism of size control is very similar to the case we discussed above, but with different signs (production in the droplet, degradation in the solvent). Another direction of research is the investigation of more complex and more realistic reactions. While there is work on non-equilibrium reaction networks in non-ideal systems[191], there has not been a thorough investigation of the effect of multiple phases on complex reaction networks. By including or excluding certain species, droplets could affect the dynamics of

reaction networks and the selection of reaction pathways. For example, the multiphase nucleus has been discussed as an ‘assembly line’[192] that controls how proteins are processed locally when moving from one phase to the next[193]. Another approach is to use more realistic reaction models, for example, the full Michaelis Menten model for enzymatic reactions instead of the simplified one we use here. Interestingly, co-localizing enzymes and substrates in droplets while expelling products would resemble the condition of in vitro reaction chambers. It would be interesting to see if condensates can be used as reaction chambers to speed up reactions or make them more efficient.

Appendix



Entropy production

The aim is to calculate the entropy production $\frac{dS}{dt}$, which is given by

$$T \frac{dS}{dt} = -\frac{dF}{dt} = -\int_{V_{\text{sys}}} \partial_t f(\Phi, \nabla\Phi) dV \geq 0, \quad (\text{A.1})$$

as $dF = -TdS$ due to constant temperature T and internal energy E in the systems under consideration. Because the free energy density f follows a continuity equation with local free energy density production \dot{f} and free energy density flux \mathbf{j}_f , we calculate $\partial_t f$ according to

$$\partial_t f = \dot{f} - \nabla \cdot \mathbf{j}_f. \quad (\text{A.2})$$

At the same time we can expand f in all ϕ_i and their derivatives $\nabla\phi_i$ and try to match the result with \dot{f} and \mathbf{j}_f

$$\begin{aligned} \partial_t f &= \sum_i [(\partial_{\phi_i} f)(\partial_t \phi_i) + (\partial_{\nabla\phi_i} f) \cdot (\nabla(\partial_t \phi_i))] \\ &= \sum_i [(\partial_{\phi_i} f)(s_i - \nabla \cdot \mathbf{j}_i) + (\partial_{\nabla\phi_i} f) \cdot \nabla(s_i - \nabla \cdot \mathbf{j}_i)]. \end{aligned} \quad (\text{A.3})$$

In a next step we make use of the product rule $\nabla(a(x)b(x)) = (\nabla a(x))b(x) + a(x)(\nabla b(x))$ to rewrite the equation as

$$\begin{aligned} \partial_t f &= \sum_i \{(\partial_{\phi_i} f)s_i - (\nabla \cdot (\partial_{\nabla\phi_i} f))s_i \\ &\quad + (\nabla(\partial_{\phi_i} f)) \cdot \mathbf{j}_i + (\nabla \cdot (\partial_{\nabla\phi_i} f))(\nabla \cdot \mathbf{j}_i) \\ &\quad - \nabla \cdot [(\partial_{\phi_i} f)\mathbf{j}_i + (\partial_{\nabla\phi_i} f)(\nabla \cdot \mathbf{j}_i) + (\partial_{\nabla\phi_i} f)s_i]\}. \end{aligned} \quad (\text{A.4})$$

Applying the product rule to the last term in the second row another time, we end up with

$$\begin{aligned} \partial_t f &= \sum_i \{[\partial_{\phi_i} f - \nabla \cdot (\partial_{\nabla\phi_i} f)]s_i \\ &\quad + [\nabla(\partial_{\phi_i} f - \nabla \cdot (\partial_{\nabla\phi_i} f))] \cdot \mathbf{j}_i \\ &\quad - \nabla \cdot [(\partial_{\phi_i} f - \nabla \cdot (\partial_{\nabla\phi_i} f))\mathbf{j}_i + (\partial_{\nabla\phi_i} f)(\nabla \cdot \mathbf{j}_i) + (\partial_{\nabla\phi_i} f)s_i]\}. \end{aligned} \quad (\text{A.5})$$

The first two lines are scalar quantities and we thus identify them as the free energy production \dot{f} , while the last line is the divergence of a flux, which we identify as \mathbf{j}_f

$$\dot{f} = \sum_i [\partial_{\phi_i} f - \nabla \cdot (\partial_{\nabla \phi_i} f)] s_i + [\nabla (\partial_{\phi_i} f - \nabla \cdot (\partial_{\nabla \phi_i} f))] \cdot \mathbf{j}_i, \quad (\text{A.6a})$$

$$\mathbf{j}_f = \sum_i (\partial_{\phi_i} f - \nabla \cdot (\partial_{\nabla \phi_i} f)) \mathbf{j}_i + (\partial_{\nabla \phi_i} f) (\nabla \cdot \mathbf{j}_i) + (\partial_{\nabla \phi_i} f) s_i \quad (\text{A.6b})$$

In our systems the flux \mathbf{j}_f does not contribute to the total entropy production $\frac{dS}{dt}$, as the flux vanishes on the boundaries. We can therefore restrict our discussion of the total entropy production to the free energy production rate f and write

$$T \frac{dS}{dt} = - \int_{V_{\text{sys}}} \sum_i \{ [\partial_{\phi_i} f - \nabla \cdot (\partial_{\nabla \phi_i} f)] s_i + [\nabla (\partial_{\phi_i} f - \nabla \cdot (\partial_{\nabla \phi_i} f))] \mathbf{j}_i \} \geq 0. \quad (\text{A.7})$$

Using the definition of the chemical potential, $\mu_i = \partial_{\phi_i} f - \nabla \cdot (\partial_{\nabla \phi_i} f)$, we end up with

$$T \frac{dS}{dt} = - \int_{V_{\text{sys}}} \sum_i \{ (\mu_i s_i + (\nabla \mu_i) \mathbf{j}_i) \} \geq 0. \quad (\text{A.8})$$

In the main text, we call the integrand the local entropy production rate σ (see Eq. 4.13). We will do this from here on as well get

$$T\sigma = - \sum_i [\mu_i s_i + (\nabla \mu_i) \mathbf{j}_i]. \quad (\text{A.9})$$

We can rewrite the reaction term in terms of individual reactions k instead of species i (see Sec. 2.2

$$\sum_i \mu_i s_i = \sum_{i,k} \nu_{i,k} \mu_i s_k, \quad (\text{A.10})$$

where we $\nu_{i,k} = v_i (\nu_{i,k}^b - \nu_{i,k}^f)$ is the stoichiometric coefficient of species i in reaction k and already includes the conversion from particle to molecular volume change. We then identify the free energy change of reactions $\sum_i \nu_{i,k} \mu_i = -\Delta F_k$ and end up with

$$T\sigma = \sum_k \Delta F_k s_k - \sum_i (\nabla \mu_i) \mathbf{j}_i. \quad (\text{A.11})$$

Where $\sigma \geq 0$ for linear non-equilibrium thermodynamics, i.e. $\mathbf{j}_i \propto -\nabla \mu_i$ and $s_k \propto \Delta F_k$. The reaction flux depends $+\Delta F_k$ and not $-\Delta F_k$ because of the way we defined forward and backward directions, by defining the stoichiometric coefficient the other way around, i.e. $\nu_{i,k} = \nu_{i,k}^f - \nu_{i,k}^b$, we would end up with $s_k \propto -\Delta F_k$.

Entropy production of a driven reaction cycle

We now calculate the entropy production of the specific reaction cycle with the two reaction $A \rightleftharpoons B$, and $A + +E \rightleftharpoons B + F + E$, where A and B are the two proteins species, F and W are fuel and waste molecules and E is the enzyme. The chemical potential difference between fuel and waste is fixed from the outside and given by the driving strength $\Delta\mu = \mu_F - \mu_W > 0$. Thus, the free energy of reaction for the first (passive) reaction is $\Delta F_p = \mu_B - \mu_A$ and the reaction flux

is s_p , while the free energy of reaction of the second (driven) reaction is $\Delta F_a = \mu_B - \mu_A + \Delta\mu$ and the reaction flux is s_a . As a result, the total entropy production rate becomes

$$-T\sigma = (\mu_A - \mu_B)s_p + (\mu_A - \mu_B - \Delta\mu)s_a + \sum_i \mathbf{j}_i(\nabla\mu_i). \quad (\text{A.12})$$

In the case of homogeneously distributed enzymes, the non-equilibrium steady state contains reaction terms only because $\nabla\mu_i = 0$ everywhere (see Sec. 4.1). In addition, the total reaction flux vanishes, thus $s_a = -s_p$. We can then write the entropy production rate as

$$-T\sigma = -\Delta\mu s_a. \quad (\text{A.13})$$

So it is just given by the energy input, i.e. the amount of fuel converted to waste times the energy per fuel conversion. In the context of droplet size control, it is interesting to measure how much of the energy input, $s_a\Delta\mu$, gets converted into diffusive fluxes that are necessary for size control, i.e. the ratio $r = \sum_i \mathbf{j}_i(\nabla\mu_i)/(s_a\Delta\mu)$.

B

Flory Huggins Free Energy

In this appendix we derive the Flory-Huggins free energy, following the original derivation of Flory[22, 23] and Huggins[21]. Starting from an Ising like lattice model, the aim is to derive a mean field free energy density that depends on the local concentration, or volume fraction, of polymers only. In the standard Ising model each particle occupies a single lattice site, while in the Flory Huggins theory a monomer occupies one lattice site. Therefore a polymer consisting of n monomers occupies n correlated lattice sites, which leads to a different entropy of mixing than in the standard Ising model.

In the Following we will introduce the Ising lattice model, then the Flory Huggins lattice model and free energy density and finally an extension to multiple species.

Lattice Model

Consider a d dimensional lattice with M lattice sites, where each lattice site is occupied by either a B or C particle. Here we use the nomenclature from the main text, but in other context B and C could be spin up and spin down or just $+1$ and -1 . In addition we assume an incompressible fluid, so the lattice contains no empty sites. Furthermore we assume that the interactions between particles are short ranged, such that the only relevant interaction are between nearest neighbors. In this case the total energy, or Hamiltonian, H of the lattice is given by the sum of energies per lattice site $H = \sum_{n=1}^M h_n$. The energy per lattice site h_n is in turn given by a sum over the nearest neighbor interactions and thus

$$H = \frac{1}{2} \sum_{n,i} \sigma_{n,i} \sum_{m \in \text{NN}} \sum_j \sigma_{m,j} e_{ij} + \sum_{n,i} e_i \sigma_{n,i}. \quad (\text{B.1})$$

Here $\sigma_{n,i} = 1$ if site n is occupied by a particle of type i and $\sigma_{n,i} = 0$ else. The sums over i and j run over all species, the sum over m runs over all nearest neighbors of n . $e_{ij} = e_{ji}$ is the (symmetric) interaction energy between species i and j and e_i is the internal energy of species i , which is irrelevant for diffusive processes, but becomes important when reactions are present. In the Ising model this corresponds to an external field usually called h . For now we take $i, j = B, C$ and one can map this to the original Ising model where $\sigma = \pm 1$. But the general form will become useful for the multicomponent case.

In the current form each particle is treated explicitly, the crucial mean field assumption is that we first replace the actual occupancy $\sigma_{m,j}$ with the probability $p_{m,j}$ of finding an j particle at site m . And second assume that lattice sites are uncorrelated, so the probability of finding a j particle is equal for all lattice sites, $p_{m,j} = \phi_j = \frac{N_j}{M} \forall m$, where N_j is the total number of j particles. ϕ_j is just the fraction of lattice sites occupied by j particles, which we call volume fraction later.

Taken together we use $\sigma_{m,j} \approx \phi_j$, which is independent of m and thus the sum over nearest

neighbors just gives a factor z , which is the number of neighbors of a lattice site, e.g. $z = 4$ for the 2D cubic lattice. With this assumption we can write Eq.B.1 as

$$H \approx \frac{z}{2} \sum_{i,j} \phi_j e_{ij} \sum_n \sigma_{n,i} + \sum_{i,n} \sigma_{n,i} e_i. \quad (\text{B.2})$$

As the interaction of each particle $\phi_j e_{ij}$ is independent of space or lattice site, we can carry out the sum over n and get

$$H \approx \sum_{i,j} \frac{z e_{ij}}{2} N_i \phi_j + \sum_i e_i N_i. \quad (\text{B.3})$$

In this form the energy depends only on the total amount of particles in the lattice, not their position, thus the name mean field. This is an important point, because we now calculate the partition function Z which, for a canonical ensemble (so the particle numbers N_i , the total volume V (here lattice sites M) and the temperature T are constant), is given by

$$Z = \sum_{\sigma} e^{-\beta H(\sigma)}. \quad (\text{B.4})$$

here σ characterizes a certain microstate, which corresponds to a certain particle arrangement on the lattice, and the sum runs over all possible microstates. In the sum each microstate is weighted with the associated energy relative to the thermal energy $\beta = (k_B T)^{-1}$. Here k_B is the Boltzmann constant and T is the temperature of the system. As we have seen in Eq.B.3 H is independent of the lattice arrangement, so each arrangement has the same weight and Z is given by

$$Z = \Omega \exp \left(- \sum_{i,j} \frac{z e_{ij}}{2 k_B T} N_i \phi_j - \sum_i \frac{e_i}{k_B T} N_i \right), \quad (\text{B.5})$$

where Ω is the total number of microstates. In our lattice description we can calculate Ω explicitly by counting the number of different ways one can distribute N_B B particles and N_C C particles on $M = N_B + N_C$ lattice sites, which is given by the binomial

$$\Omega = \binom{M}{N_B} = \frac{M!}{N_B! (M - N_B)!}. \quad (\text{B.6})$$

Using the partition function we get the free energy F according to

$$F = -k_B T \ln(Z), \quad (\text{B.7})$$

which is the most important quantity in our system as F is minimized in thermodynamic equilibrium and determines the dynamics towards equilibrium as well.

The logarithm of Ω can be approximated for large M and N_B using Stirlings formula $\ln(N!) \approx N \ln(N) - N$ and we get

$$\begin{aligned} - \ln \left(\frac{M!}{N_B! (M - N_B)!} \right) &\approx N_B \ln(N_B) + (M - N_B) \ln(M - N_B) - M \ln(M) \\ &= N_B \ln \frac{N_B}{M} + (M - N_B) \ln \frac{M - N_B}{M} \\ &= N_B \ln(\phi_B) + (M - N_B) \ln(1 - \phi_B). \end{aligned} \quad (\text{B.8})$$

Taken together we get for the total free energy F

$$\frac{F}{k_B T} = N_B \ln(\phi_B) + (M - N_B) \ln(1 - \phi_B) + \sum_{i,j=B,C} \frac{z e_{ij}}{2k_B T} N_i \phi_j + \sum_i \frac{e_i}{k_B T} N_i. \quad (\text{B.9})$$

To include space into our description, we assume that each lattice site occupies a volume v_0 , so the total volume is given by $V = M v_0$. With this we can define the free energy density $f = F/V$ and get (using $\phi_C = 1 - \phi_B$)

$$\frac{v_0 f(\phi_B)}{k_B T} = \phi_B \ln(\phi_B) + (1 - \phi_B) \ln(1 - \phi_B) + \chi \phi_B (1 - \phi_B) + w_B \phi_B. \quad (\text{B.10})$$

Where we introduced the factor $\chi = \frac{z}{2k_B T} (2e_{BC} + e_{BB} - e_{CC})$, which describes the relative interaction energy when mixing B and C ($2e_{BC}$) compared to the demixed state ($e_{BB} + e_{CC}$) and compares it to the thermal energy $k_B T$. In addition the effective internal energy difference between B and C becomes $w_B = \frac{1}{k_B T} (e_B - e_C + e_{BB} - e_{CC})$ and we skipped constants in the free energy density, because only derivatives of f are relevant for physical processes. In this form the free energy is a function of the volume fraction of B only.

Multicomponent regular solution

In this subsection, we extend the discussion from above to K species instead of two, now N_i for $i = 1, \dots, K$ is the number of i particles in the system and we assume all M lattice sites are occupied, so $\sum_i N_i = M$. In addition, for now each particle occupies one lattice site. The enthalpy is described by Eq. B.3, but the entropy of mixing is different of K species. In this case we have to arrange N_i particles of type i on M lattice sites, where $\sum_i N_i = M$. The number of arrangements Ω in this case is given by the multinomial coefficient

$$\Omega = \binom{M}{N_1, N_2, \dots, N_K} = \frac{M!}{\prod_{i=1}^K N_i!}. \quad (\text{B.11})$$

To calculate the free energy according to Eq. B.7, we have to calculate the logarithm of Ω . We apply stirlings formulat immediately and get

$$\begin{aligned} \ln(\Omega) &\approx M \ln M - M - \sum_{i=1}^K N_i \ln N_i - N_i \\ &= - \sum_{i=1}^K N_i \ln \frac{N_i}{M} = - \sum_{i=1}^K N_i \ln(\phi_i). \end{aligned} \quad (\text{B.12})$$

Taken together, the total free energy of the multicomponent system is given by

$$\frac{F}{k_B T} = \sum_{i=1}^K N_i \left[\ln(\phi_i) + \frac{e_i}{k_B T} + \sum_{j=1}^K \frac{z e_{ij}}{2k_B T} \phi_j \right]. \quad (\text{B.13})$$

And the corresponding free energy density becomes

$$\frac{v_0 f}{k_B T} = \sum_{i=1}^K \phi_i \left[\ln(\phi_i) + \frac{e_i}{k_B T} + \sum_{j=1}^K \frac{z e_{ij}}{2 k_B T} \phi_j \right]. \quad (\text{B.14})$$

In the main text we use a slightly different version because the form usually used in the literature uses parameters $\chi_{ij} = (z/(2k_B T))(2e_{ij} - e_{ii} - e_{jj})$ instead of the e_{ij} [65].

Flory-Huggins entropy of mixing

In this subsection, we discuss the extension to polymers that consist of multiple monomers and thus occupy multiple adjacent lattices sites, i.e. includes different particle sizes. We discuss the binary case, but it can be extended to multiple species in a straight forward manner. Thereby, we follow the calculation of the original paper by Flory closely, see Ref.[22]. The aim is to calculate the entropy of mixing from the number of lattice arrangements, similar to the case above. Assume two types of molecules, a solvent and a polymer. The solvent occupies one lattice site, while the polymer consists of x monomers and each monomer occupies one lattice site. Thus each polymer needs x adjacent lattice sites to fit in. Here, we assume that the polymerization, i.e. the number of monomers per polymer is constant. Again, we assume M total lattice sites, N polymer molecule, thus Nx monomers and $M - Nx$ solvent molecules.

We want to calculate the total number of arrangements of N polymers and $M - Nx$ solvents on M lattice sites. Therefore, we first arrange the N polymers and fill the remaining sites with solvents. In addition, we assume that the probability of a lattice site to be occupied by a monomer is given by the average probability, i.e. $\phi = Nx/M$. In an empty lattice, the first monomer of the first polymer can start anywhere, for a lattice with coordination number z , the second monomer can thus be on one of the z neighboring sites. For an empty lattice, the expected number of empty adjacent lattice sites is z . But, for the third monomer its only $z - 1$ because the first monomer sits on one of the z neighbors. For the fourth it is even less, but we assume it is $z - 1$ for every monomer after the first. This overestimates the number of real arrangements and we neglect that the polymer might have preferred conformations and assume each neighboring site is equally possible.

This discussion only holds for the first polymer, for the $n + 1$ th polymer, a total number of nx lattice sites is already filled. Thus, the probable number of empty lattice sites for the second monomer is $z(M - nx)/M$, while it is $\alpha = (z - 1)(M - nx)/M$ for the following monomers. So the possible number of arrangements for the $n + 1$ th polymer for a fixed position of the first monomer is

$$p_{n+1} = \frac{z}{z - 1} \alpha^{x-1} = (z - 1)^{x-1} \frac{(M - nx)^{x-1}}{M^{x-1}}. \quad (\text{B.15})$$

Here the factor $z/(z - 1)$ takes care of the second monomer having z instead of $z - 1$ possible neighboring sites and the exponent $x - 1$ takes care of the first monomer being fixed. Now, the first monomer can start on any of the $M - nx$ free sites, thus the total number of arrangements for the $n + 1$ th polymer is

$$\omega_{n+1} = \frac{1}{2}(M - nx)p_{n+1} \approx \frac{1}{2}(M - nx)^x M^{1-x} (z - 1)^{x-1}, \quad (\text{B.16})$$

where the factor $1/2$ corrects for the symmetry of the polymer, i.e. the start and end of the polymer can be exchanged, without changing the configuration. The approximation assumes

that $z(z-1)^{x-2} \approx (z-1)^{x-1}$. For three dimensional lattices, for example, the cubic lattice where $z = 9$, this is a good approximation, but even for two dimensions its only a factor of 2. Taking the result from Eq. B.16, we can add one polymer after the other and get the total number of confirmation for N polymers as

$$\Omega = \frac{1}{N!} \prod_{n=1}^N \omega_n = \frac{1}{N!2^N} \left(\frac{(z-1)}{M} \right)^{N(x-1)} \prod_{n=1}^N (M-xn)^x \quad (\text{B.17})$$

where the factor $N!$ corrects for exchange of indistinguishable polymers. The product series can be written as

$$\begin{aligned} \prod_{n=1}^N (M-xn)^x &= (M-x)(M-2x)\dots(M-Nx) \\ &= \left(\prod_{n=1}^N (M-xn) \right)^x \\ &= \left(x^N \prod_{n=1}^N (M/x-n) \right)^x \\ &= x^{xN} \left(\frac{(M/x)!}{(M/x-N)!} \right)^x. \end{aligned} \quad (\text{B.18})$$

and thus the total number of arrangements are

$$\Omega = \left(\frac{(z-1)}{M} \right)^{N(x-1)} \frac{x^{xN}}{2^N(N!)} \left(\frac{(M/x)!}{(M/x-N)!} \right)^x. \quad (\text{B.19})$$

From this, we get the entropy of mixing of N perfectly aligned polymers and $M - Nx$ solvents, using $\Delta S_0 = k_B \ln(\Omega)$ and the stirling approximation, $\ln(N!) \approx N \ln(N) - N$:

$$\Delta S_0 \approx -k_B \left[N \ln \frac{N}{M} + (M-xN) \ln \frac{M-xN}{M} \right] + k_B N [(x-1)(\ln(z-1)-1) - \ln 2]. \quad (\text{B.20})$$

This reduces to the entropy of mixing derived above for $x = 1$, except for the $\ln 2$ term, which stems from the symmetry of the polymer, i.e. that beginning and end are indistinguishable. This term does not arrive in the first place for molecules that occupy one lattice site.

From Eq. B.20, we can calculate the entropy of N polymers on a lattice in the absence of solvent, i.e. $M - xN = 0$, and get

$$\Delta S_P = k_B N [\ln x - \ln 2 + (x-1)(\ln(z-1)-1)]. \quad (\text{B.21})$$

This is the entropy of pure polymers. We need to consider it as the standard state of the pure polymer in the derivation of the total entropy of mixing. ΔS_0 is the entropy of arranging N polymers and $M - xN$ solvents, but the entropy of mixing is the difference between ΔS_0 and the standard state, i.e. the pure polymer and pure solvent state. Because of the correlation of lattice sites, Eq. B.21 has to be used as the standard state for the pure polymer system. Thus, the entropy of mixing N entangled polymers and $M - xN$ solvent molecules is given by the

difference between ΔS_0 and ΔS_P (using $\phi = Nx/M$)

$$\Delta S = \Delta S_0 - \Delta S_P = -k_B [N \ln \phi + (M - xN) \ln(1 - \phi)]. \quad (\text{B.22})$$

And the entropy density $\Delta s = \Delta S/(Mv_0)$, where v_0 is the lattice volume:

$$\frac{\Delta s v_0}{k_B} = - \left[\frac{\phi}{x} \ln \phi - (1 - \phi) \ln(1 - \phi) \right]. \quad (\text{B.23})$$

The generalization to K components results in

$$\frac{\Delta s v_0}{k_B} = - \left[\sum_{i=1}^K \frac{\phi_i}{n_i} \ln(\phi_i) \right], \quad (\text{B.24})$$

where n_i is the polymerization, i.e. the number of monomers, of species i and $v_i = n_i v_0$ is the corresponding molecular volume.

Finally, we want to discuss some limitations of the Flory-Huggins entropy of mixing: **(i)** In the derivation for p_{n+1} , we neglect that for high polymer fraction, it is possible that there is no way to fit another polymer into the system although more than x free lattice sites are available. Simply because the free lattice sites are not connected. Thus, for high polymer concentration, the number of configurations decreases faster than p_{n+1} suggests. **(ii)** We assume that each monomer can occupy every neighboring cell, i.e. that the polymer can bend perfectly. This is not the case for stiff, rod-like polymers for example. **(iii)** It assumes that all polymers have the same number of monomers, which is usually not the case, especially for long polymers, where a distribution of lengths is expected. **(iv)** It inherits all the limitations of the lattice model and mean field model already discussed above.

Linear Stability of a ternary mixture

In this appendix we calculate the linear stability of a ternary system with chemical potentials (here $\phi_C = 1 - \phi_A - \phi_B$)

$$\frac{\mu_A}{k_B T} = \ln \frac{\phi_A}{\phi_C} + \sum_{j=A,B,C} \chi_{Aj} (\phi_j - v_0^{2/d} \nabla^2 \phi_j), \quad (\text{C.1a})$$

$$\frac{\mu_B}{k_B T} = \ln \frac{\phi_B}{\phi_C} + \sum_{j=A,B,C} \chi_{Bj} (\phi_j - v_0^{2/d} \nabla^2 \phi_j), \quad (\text{C.1b})$$

where we used the regular solution model and $\kappa_{ij} = -\chi_{ij} v_0^{2/d}$. The time evolution via diffusion is given by the continuity equations

$$\partial_t \phi_A = \Lambda \nabla^2 \mu_A, \quad (\text{C.2a})$$

$$\partial_t \phi_B = \Lambda \nabla^2 \mu_B. \quad (\text{C.2b})$$

We discuss the most simple case, constant mobility $\Lambda_{ii} = \Lambda$, no crossdiffusion $\Lambda_{ij} = 0$ for $i \neq j$ and same diffusivity for A and B . This does not change the qualitative behaviour, but it makes the calculations easier to interpret. Note that we expect quantitative shifts in the stability conditions for other mobility models. Linearize $\underline{\mu} = (\mu_A, \mu_B)^T$ around the homogeneous state $\bar{\phi} = (\bar{\phi}_A, \bar{\phi}_B)^T$ where we write the deviation from the homogeneous state as $\delta \underline{\phi} = \underline{\phi} - \bar{\phi}$ and get

$$\underline{\mu} \approx \underline{\mu}(\bar{\phi}) + \underline{M} \cdot \delta \underline{\phi} - \underline{K} \nabla^2 \delta \underline{\phi}. \quad (\text{C.3})$$

Where the matrix coefficients are given by $M_{ij} = (\partial_{\phi_j} \mu_i)|_{\bar{\phi}_A, \bar{\phi}_B}$ and $K_{ij} = (\chi_{ij} - \chi_{iC}) v_0^{2/d}$ for $i = A, B$. Accordingly the linearized dynamics are

$$\partial_t \delta \underline{\phi} = \Lambda [\underline{M} \nabla^2 - \underline{K} \nabla^4] \delta \underline{\phi} = \underline{L} \delta \underline{\phi}. \quad (\text{C.4})$$

Where the linear operator (matrix) \underline{L} determines the time evolution of the perturbations via $\delta \underline{\phi}(t) = e^{\underline{L}t} \delta \underline{\phi}(0)$ and to determine the stability of the homogeneous state we have to find the eigenvalues of \underline{L} . This is best done in terms of the eigenfunctions of ∇^2 , which are again the plane waves $\exp(i\mathbf{k}\mathbf{r})$ with wave vectors \mathbf{k} . As a result we get two eigenvalues $\omega_{1,2}$ for each wave vector \mathbf{k} by solving the characteristic polynomial and we get

$$\omega_{1,2} = \frac{1}{2} \left[-\text{Tr}(\underline{L}) \pm \sqrt{\text{Tr}(\underline{L})^2 - 4\text{Det}(\underline{L})} \right]. \quad (\text{C.5})$$

Obviously the result depends on the interaction matrix $\underline{\chi}$, but we can get some generic properties and then discuss the special cases important for our system. First there is a factor $-\Lambda k^2$ in all

terms of $\underline{\underline{L}}$, so $\underline{\underline{L}} = -\Lambda k^2 \underline{\underline{L}}'$ and we need to find the eigenvalues of $\underline{\underline{L}}'$ only. In ideal systems ($\chi_{ij} = 0$) those are always positive and thus all perturbations decay. But for strong interactions the eigenvalues can become negative, just like in the binary case, and the homogeneous state becomes unstable.

Including passive reactions

If we include a simple reaction $A \rightleftharpoons B$ and write the reaction flux using linear non-equilibrium thermodynamics, Eq. 2.25, $s_A = -s_B = s = -k(\mu_A - \mu_B)$, the resulting dynamical equations become

$$\partial_t \phi_A = \Lambda \nabla^2 \mu_A - k(\mu_A - \mu_B), \quad (\text{C.6a})$$

$$\partial_t \phi_B = \Lambda \nabla^2 \mu_B + k(\mu_A - \mu_B). \quad (\text{C.6b})$$

As seen in the main text, this can be rewritten in non-dimensional form as (see Eq. 3.23)

$$\partial_t \phi_A = \nabla^2 \mu_A - \xi^{-2}(\mu_A - \mu_B), \quad (\text{C.7a})$$

$$\partial_t \phi_B = \nabla^2 \mu_B + \xi^{-2}(\mu_A - \mu_B), \quad (\text{C.7b})$$

where $\xi^2 = \Lambda/k$ is the reaction diffusion length expressed in molecular volumes $v_0^{1/d}$. Note that we skip the hats, but all quantities in the non-dimensional form are dimensionless or expressed in terms of the characteristic length, time and energy scales. In this case we do not perturb around a generic homogeneous state, but the homogeneous case for which $\mu_A - \mu_B = 0$ for a given $\bar{\phi}_+$, so the reaction is in equilibrium. Besides the procedure is the same as discussed above and we get the perturbed dynamics

$$\partial_t \delta \phi = [\underline{\underline{M}}^* \nabla^2 - \underline{\underline{K}} \nabla^4 + \xi^{-2} \underline{\underline{R}}] \delta \phi = \underline{\underline{L}} \delta \phi. \quad (\text{C.8})$$

Here $R_{AA} = -R_{BA}$ and $R_{AB} = -R_{BA}$ and $R_{Aj} = -(\partial_{\phi_j}(\mu_A - \mu_B))|_{\bar{\phi}_A, \bar{\phi}_B}$. In addition, the non-local term in $\mu_A - \mu_B$ enters the matrix $\underline{\underline{M}}^* = \underline{\underline{M}} - \underline{\underline{T}} \cdot \underline{\underline{K}}$, where $T_{AA} = -T_{BA} = -1$ and $T_{BA} = -T_{BB} = 1$. Now, calculating the eigenvalues of $\underline{\underline{L}}$ gives the growth rates, which are shown in the main text.

D

Partition Coefficient

In this appendix we derive the partition coefficient in a ternary mixture of species i , B and C , where the solvent C is abundant $\bar{\phi}_C \gg \bar{\phi}_{B,i}$ and species B phase separates from C . The partition coefficient describes the ratio of concentrations between the two phases in equilibrium. Our aim is to derive the partition coefficient of the ‘client’ species only, i.e. the species that are not necessary for phase separation and not the solvent. These species partition into the two phases according to their interactions. In this example, we are interested in the partitioning of i only. The derivation is similar to the partition coefficient derived in Ref.[134].

Starting from a ternary regular solution free energy, so all molecular volumes are identical

$$\begin{aligned} \frac{fv_0}{k_B T} = & \phi_i \ln(\phi_i) + \phi_B \ln(\phi_B) + (1 - \phi_i - \phi_B) \ln(1 - \phi_i - \phi_B) + \\ & \chi \phi_B (1 - \phi_i - \phi_B) + \chi_{iB} \phi_i \phi_B + \chi_{iC} \phi_i (1 - \phi_i - \phi_B), \end{aligned} \quad (\text{D.1})$$

where $\phi_C = 1 - \phi_i - \phi_B$ has been applied already and χ_{iB}, χ_{iC} are the interaction strength of i with B and C . For low i fraction, $\phi_i \ll 1$, we can expand f up to first order in ϕ_i and get

$$\begin{aligned} \frac{fv_0}{k_B T} \approx & \phi_B \ln(\phi_B) + (1 - \phi_B) \ln(1 - \phi_B) + \chi \phi_B (1 - \phi_B) + \\ & \phi_i \left[\ln \frac{\phi_i}{1 - \phi_B} + (\chi_{iB} - \chi - \chi_{iC}) \phi_B + (\chi_{iC} - 1) \right]. \end{aligned} \quad (\text{D.2})$$

The result is a binary regular solution free energy with a correction linear in ϕ_i . From this free energy we can derive the (exchange) chemical potentials according to

$$\frac{\mu_i}{k_B T} = \ln \frac{\phi_i}{1 - \phi_B} + (e_{iB} - \chi - e_{iC}) \phi_B + e_{iC} \quad (\text{D.3a})$$

$$\frac{\mu_B}{k_B T} = \ln \frac{\phi_B}{1 - \phi_B} + \chi(1 - 2\phi_B) + \left(e_{iB} - \chi - e_{iC} + \frac{1}{1 - \phi_B} \right) \phi_i. \quad (\text{D.3b})$$

The equilibrium condition for the chemical potentials in a two phase system are $\mu_i^{\text{in}} = \mu_i^{\text{out}}$ and $\mu_B^{\text{in}} = \mu_B^{\text{out}}$, where in and out indicate the B -rich and B -poor phase respectively. From Eq.D.3 it is clear, that the equilibrium solution has to be determined numerically.

But we can discuss an approximation, assuming that phase separation is not affected by i at all and i partitions in the two phases according to $\mu_i^{\text{in}} = \mu_i^{\text{out}}$. In this case we drop the ϕ_i term in μ_B and get the binary phase separation discussed in App.B. Even this simplified case has to be solved numerically in general, but the problem is reduced to phase separation in a binary regular solution. The equilibrium fraction of B in droplet, ϕ_B^{in} , and solvent, ϕ_B^{out} , depend on χ only as discussed in the main text. Assuming, we know ϕ_B^{in} and ϕ_B^{out} from numerical calculations, we

can calculate the equilibrium condition for i from Eq. D.3a and get

$$\frac{\phi_i^{\text{in}}}{\phi_i^{\text{out}}} = \exp((e_{iB} - e_{iC})(\phi_B^{\text{out}} - \phi_B^{\text{in}})) \frac{1 - \phi_B^{\text{in}}}{1 - \phi_B^{\text{out}}} \exp(\chi(\phi_B^{\text{in}} - \phi_B^{\text{out}})). \quad (\text{D.4})$$

In the special case of symmetric free energy densities for equally sized molecules B and C , we get $\phi_B^{\text{in}} = \phi_C^{\text{in}}$ and $\phi_B^{\text{in}} = 1 - \phi_B^{\text{out}}$. Using this, we can rewrite the second part of Eq. D.4 as

$$\ln \left(\frac{1 - \phi_B^{\text{in}}}{1 - \phi_B^{\text{out}}} \right) + \chi(\phi_B^{\text{in}} - \phi_B^{\text{out}}) = \ln \left(\frac{\phi_B^{\text{out}}}{1 - \phi_B^{\text{out}}} \right) + \chi(1 - 2\phi_B^{\text{out}}) = \mu_B(\phi_B^{\text{out}}) = 0. \quad (\text{D.5})$$

As a result, we arrive at

$$\frac{\phi_i^{\text{in}}}{\phi_i^{\text{out}}} = \exp((e_{iB} - e_{iC})(\phi_B^{\text{out}} - \phi_B^{\text{in}})) = \exp(\chi_E(\phi_B^{\text{in}} - \phi_B^{\text{out}})) = \Gamma_i. \quad (\text{D.6})$$

Here, Γ_i is the partition coefficient of i between the two phases and $\chi_i = e_{iC} - e_{iB}$ is the interaction difference between i and C and i and B . Thus, for $\chi_i > 0$, i enriches in the B droplet, while for $\chi_i < 0$, i enriches in the solvent phase. Note that this result holds for every extra species i that is dilute, i.e. $\bar{\phi}_i \ll 1$.

We can use the partition coefficient and mass conservation to calculate the actual volume fraction in droplet and solvent phase. Therefore, we use mass and volume conservation

$$V_{\text{in}} + V_{\text{out}} = V_{\text{sys}}, \quad (\text{D.7a})$$

$$V_{\text{in}}\phi_i^{\text{in}} + V_{\text{out}}\phi_i^{\text{out}} = V\bar{\phi}_i. \quad (\text{D.7b})$$

Where V_{in} and V_{out} are the volumes of droplet and solvent phase. We call the droplet volume ratio $\psi = V_{\text{in}}/V_{\text{sys}}$, with this and $\Gamma_i = \phi_i^{\text{in}}/\phi_i^{\text{out}}$, we arrive at

$$\phi_i^{\text{out}} = \frac{1}{1 - \psi(1 - \Gamma_i)} \bar{\phi}_i \approx (1 + (1 - \Gamma_i)\psi) \bar{\phi}_i, \quad (\text{D.8})$$

$$\phi_i^{\text{in}} = \frac{\Gamma_i}{1 - \psi(1 - \Gamma_i)} \bar{\phi}_i \approx (1 + (1 - \Gamma_i)\psi) \Gamma_i \bar{\phi}_i, \quad (\text{D.9})$$

where the approximation is for small droplets, i.e. $\psi \ll 1$. Thus, to 0th order, we can approximate $\phi_i^{\text{out}} \approx \bar{\phi}_i$ and $\phi_i^{\text{in}} \approx \Gamma_i \bar{\phi}_i$.

Chemical Equilibrium ratio

In this appendix, we derive the analytical solution of the chemical equilibrium for a simple conversion reaction $A \rightleftharpoons B$. We start from a regular solution free energy given by

$$\frac{fv_0}{k_B T} = \sum_{i=A,B,C} \phi_i \ln(\phi_i) + (k_B T)^{-1} h(\phi_A, \phi_B, \phi_C), \quad (\text{E.1})$$

where $\sum_i \phi_i = 1$ and $h(\phi_A, \phi_B, \phi_C)$ contains the enthalpic contributions, i.e. the internal energies and interactions between particles. We assume pairwise interactions only and expand h up to second order in all ϕ_i and end up with

$$h \approx \sum_i e_i \phi_i + \sum_{ij} \frac{e_{ij}}{2} \phi_i \phi_j, \quad (\text{E.2})$$

where e_i are the internal energies and e_{ij} are the pairwise interactions between species i and j . Thus, the chemical potentials are given by

$$\frac{\mu_i}{k_B T} = \ln(\phi_i) + e_i + \sum_{j=A,B,C} e_{ij} \phi_j. \quad (\text{E.3})$$

We want to calculate the chemical equilibrium condition for the reaction $A \rightleftharpoons B$, i.e. $\mu_A - \mu_B = 0$, which results in the condition

$$\frac{\mu_A - \mu_B}{k_B T} = \ln \frac{\phi_A}{\phi_B} + e_A - e_B + \sum_j (e_{Aj} - e_{Bj}) \phi_j = 0. \quad (\text{E.4})$$

Using the incompressibility condition to replace species C via $\phi_C = 1 - \phi_A - \phi_B$, we end up with

$$\ln \frac{\phi_A}{\phi_B} + \Delta w + \chi_A \phi_A - \chi_B \phi_B = 0, \quad (\text{E.5})$$

where $\Delta w = e_A - e_B + e_{AC} - e_{BC}$, $\chi_A = e_{AA} - e_{BA} - e_{AC} + e_{BC}$, and $\chi_B = e_{BB} - e_{AB} + e_{AC} - e_{BC}$. We can rewrite this as

$$\phi_A \exp(\Delta w + \chi_A \phi_A) = \phi_B \exp(\chi_B \phi_B). \quad (\text{E.6})$$

Substituting $x = \chi_A \phi_A$, we end up with

$$x e^x = \chi_A \phi_B \exp(\chi_B \phi_B - \Delta w), \quad (\text{E.7})$$

here, we can use that $xe^x = y$ is solved by the Lambert W function, $x = W_n(y)$, where $n = 0$ or $n = -1$ for real x, y . And thus

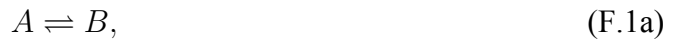
$$\phi_A = W_n(\chi_A \phi_B \exp(\chi_B \phi_B - \Delta w)) / \chi_A. \quad (\text{E.8})$$

This argument holds for general forms of the enthalpic interactions up to two body interactions. Indeed, it does work for specific three body interactions as well, but we have not investigated the case of general three body interactions.

F

Steady state of a reaction cycle

In this appendix we discuss the condition of vanishing total reaction flux for a reaction cycle with different kinetics. The reaction cycle is given by the two reactions (Eq. 4.5)



And the corresponding detailed balance conditions are (Eq. 4.6)

$$\frac{s_p^f}{s_p^b} = \exp \frac{\mu_A - \mu_B}{k_B T}, \quad (\text{F.2a})$$

$$\frac{s_a^f}{s_a^b} = \exp \frac{\mu_A - \mu_B - \Delta\mu}{k_B T}. \quad (\text{F.2b})$$

With $s_p = s_p^f - s_p^b$ and $s_a = s_a^f - s_a^b$, we can solve for the condition $s = s_p + s_a = 0$ or $s_p = -s_a$ in terms of external driving $\Delta\mu$ and backward rates s_i^b

$$s_p^b \left(\exp \frac{\mu_A - \mu_B}{k_B T} - 1 \right) + s_a^b \left(\exp \frac{\mu_A - \mu_B - \Delta\mu}{k_B T} - 1 \right) = 0. \quad (\text{F.3})$$

Rewriting this in terms of $\exp \frac{\mu_A - \mu_B}{k_B T}$, we get

$$\exp \frac{\mu_A - \mu_B}{k_B T} = \frac{s_p^b + s_a^b}{s_p^b + s_a^b e^{-\Delta\mu/(k_B T)}}. \quad (\text{F.4})$$

The important parameter are not the rates themselves, but the ratio between the two backward rates $\eta = s_a^b/s_p^b$

$$\frac{\mu_A - \mu_B}{k_B T} = \ln \frac{1 + \eta}{1 + \eta e^{-\Delta\mu/(k_B T)}}. \quad (\text{F.5})$$

It is convenient to write this as

$$\mu_A - \mu_B = \Delta\mu - k_B T \ln \frac{e^{\Delta\mu/(k_B T)} + \eta}{1 + \eta}. \quad (\text{F.6})$$

Importantly, this discussion uses detailed balance of the rates and is thus valid, independent of the functional form of $s_{a,p}^b$. For a generalization of this procedure to complex chemical reaction networks see for example Ref.[165].

If we assume inhomogeneously distributed enzymes that catalyze the driven reaction and in addition assume that the active rate scales linear with the amount of enzyme $s_a \propto \phi_E$, we end

up with

$$\mu_A - \mu_B = \Delta\mu - k_B T \ln \frac{e^{\Delta\mu/(k_B T)} + \phi_E \eta}{1 + \phi_E \eta}, \quad (\text{F.7})$$

which corresponds to Γ_E in the main text in the droplet phase.

G

Steady state of the non-equilibrium dynamics

In this appendix, we discuss the steady state chemical potential profiles for a non-equilibrium reaction cycle with enzymes that enrich in the droplet phase. We start with the binary system with linear non-equilibrium reactions and then extend it to the ternary case with reactions described by transition state theory, which are discussed in the main text. In both cases, we assume for simplicity, that the enzyme enriches in the droplet phase by a factor of Γ_E , i.e. the enzyme partition coefficient. This is valid if the total droplet volume is small compared to the system volume. Furthermore, we assume equal diffusivity Λ for all species and neglect cross-diffusion.

Binary active droplets

The dynamical equations to describe the binary active droplets in the effective droplet model (see main text) for a droplet of radius R are given by Eq. 4.22

$$\partial_t \phi_{\text{in}} = \nabla^2 \mu_{\text{in}} - \ell_{\text{in}}^{-2} \left(\mu_{\text{in}} + \frac{\Gamma_E \eta}{1 + \Gamma_E \eta} \Delta \mu \right), \quad r \leq R, \quad \text{and} \quad (\text{G.1a})$$

$$\partial_t \phi_{\text{out}} = \nabla^2 \mu_{\text{out}} - \ell_{\text{out}}^{-2} \left(\mu_{\text{out}} + \frac{\eta}{1 + \eta} \Delta \mu \right), \quad r > R, \quad (\text{G.1b})$$

here $\phi_{\text{in/out}}$ and $\mu_{\text{in/out}}$ are the volume fractions and chemical potentials in droplet (in) and solvent (out) phase. $\ell_{\text{in/out}}$ are the corresponding reaction diffusion lengths. $\eta = s_a^b/s_p^b$ is the reaction rate ratio and $\Delta \mu$ is the driving strength. The boundary conditions are no flux conditions at $r = 0/L$, $\mathbf{e}_r \partial_r \nabla \mu|_{r=0,L} = 0$, where L is the system size of the radial symmetric system. In addition, phase coexistence requires that $\mu_{\text{in}}(R) = \mu_{\text{out}}(R) = -\Delta w$, where Δw is the internal energy difference between A and B .

Notably, the right hand side depends on the chemical potential only, therefore, in the steady state we can solve the equation for the chemical potential as a function of r . In a first step, we introduce the steady state chemical potential in droplet and solvent phase as

$$\mu_{\text{in}}^* = \frac{\Gamma_E \eta}{1 + \Gamma_E \eta} \Delta \mu, \quad (\text{G.2a})$$

$$\mu_{\text{out}}^* = \frac{\eta}{1 + \eta} \Delta \mu. \quad (\text{G.2b})$$

Then, we substitute $\bar{\mu}_{\text{in/out}} = \mu_{\text{in/out}} + \mu_{\text{in/out}}^*$. The resulting steady state equations in a spheri-

cally symmetric system are

$$\partial_r^2 \bar{\mu}_{\text{in}} + \frac{2}{r} \partial_r \bar{\mu}_{\text{in}} - \ell_{\text{in}}^{-2} \bar{\mu}_{\text{in}} = 0, \quad r \leq R, \quad \text{and} \quad (\text{G.3a})$$

$$\partial_r^2 \bar{\mu}_{\text{out}} + \frac{2}{r} \partial_r \bar{\mu}_{\text{out}} - \ell_{\text{in}}^{-2} \bar{\mu}_{\text{out}} = 0, \quad r > R. \quad (\text{G.3b})$$

$$(\text{G.3c})$$

The general solution of this ODE, the Sturm-Liouville equation, is

$$\bar{\mu}(r) = \frac{a}{r} \exp(-r/\ell) + \frac{b\ell}{r} \exp(r/\ell), \quad (\text{G.4})$$

where a and b are constants related to the boundary conditions. For the solvent phase, the chemical potential has to remain finite for $r \rightarrow \infty$, thus $b = 0$ and for the droplet phase, $\partial_r \bar{\mu}|_0 = 0$ leads to $a = -b$. Thus, the solutions for solvent and droplet phase are

$$\mu_{\text{in}} = -\mu_{\text{in}}^* + \frac{a_{\text{in}}}{r} \sinh(r/\ell_{\text{in}}), \quad (\text{G.5a})$$

$$\mu_{\text{out}} = -\mu_{\text{out}}^* + \frac{a_{\text{out}}}{r} \exp(-r/\ell_{\text{out}}). \quad (\text{G.5b})$$

In a last step, we enforce $\mu_{\text{in/out}}(R) = -\Delta w$ and thus

$$a_{\text{in}} = (\mu_{\text{in}}^* - \Delta w) \frac{R}{\sinh(R/\ell_{\text{in}})}, \quad (\text{G.6a})$$

$$a_{\text{out}} = (\mu_{\text{out}}^* - \Delta w) R \exp(R/\ell_{\text{out}}). \quad (\text{G.6b})$$

Therefore, the final result is

$$\mu_{\text{in}} = -\mu_{\text{in}}^* + (\mu_{\text{in}}^* - \Delta w) \frac{R \sinh(r/\ell_{\text{in}})}{r \sinh(R/\ell_{\text{in}})}, \quad (\text{G.7a})$$

$$\mu_{\text{out}} = -\mu_{\text{out}}^* + (\mu_{\text{out}}^* - \Delta w) \frac{R}{r} \exp(-(r - R)/\ell_{\text{out}}), \quad (\text{G.7b})$$

which is the result we use in the main text.

Ternary active droplets

In the ternary system, which corresponds to Eq. 4.39, where we drop the enzyme species and just assume $\phi_E^{\text{in}} = \Gamma_E \bar{\phi}_E$ and $\phi_E^{\text{out}} = \bar{\phi}_E$, is given by

$$\partial_t \phi_+ = \Lambda \nabla^2 \mu_+, \quad (\text{G.8a})$$

$$\partial_t \phi_- = \Lambda \nabla^2 \mu_- - 2s. \quad (\text{G.8b})$$

While the first equation is independent of μ_- , the resulting steady state is $\mu_+ = \text{const}$. Therefore, only the second equation is of interest. To solve it, we need to specify the reaction flux. For TST kinetics (see main text), the total reaction flux is given by $s = s_a + s_p$ and the individual

reaction fluxes of active and passive reaction are (see Eq. 4.40 in the main text)

$$s_p = \lambda_p \left[\exp\left(\frac{\mu_A}{k_B T}\right) - \exp\left(\frac{\mu_B}{k_B T}\right) \right], \quad \text{and} \quad (\text{G.9a})$$

$$s_a = \lambda_a e^{\mu_F/k_B T} \frac{\phi_E}{\bar{\phi}_E} \left[\exp\left(\frac{\mu_A - \Delta\mu}{k_B T}\right) - \exp\left(\frac{\mu_B}{k_B T}\right) \right]. \quad (\text{G.9b})$$

We rewrite this in terms of the new variables, μ_- and μ_+ , as well as the steady state chemical potential μ_-^* as

$$s(\mu_+, \mu_-) = 2\lambda_p \left(1 + e^{\frac{-\Delta\mu}{k_B T}} \eta \frac{\phi_E}{\bar{\phi}_E} \right) e^{\frac{\mu_+ + \mu_-^*}{2k_B T}} \sinh \left[\frac{\mu_- - \mu_-^*}{2k_B T} \right]. \quad (\text{G.10})$$

Here, μ_-^* is given by

$$\mu_-^* = \Delta\mu - k_B T \ln \left[\frac{e^{\Delta\mu/k_B T} + \frac{\phi_E}{\bar{\phi}_E} \eta}{1 + \frac{\phi_E}{\bar{\phi}_E} \eta} \right]. \quad (\text{G.11})$$

Now we consider the effective droplet model, i.e. a droplet of radius R is present and the enzyme fraction in the droplet and solvent phase is $\Gamma_E \bar{\phi}_E$ and $\bar{\phi}_E$ respectively. We can thus distinguish the reaction flux and steady state chemical potential in droplet and solvent phase, i.e. $s_{\text{in/out}}$ and $\mu_{\text{in/out}}^*$. In addition, we assume that the reaction flux in the solvent phase is close to equilibrium and for strong driving, where $e^{\Delta\mu/k_B T} \gg \eta$. In this case, the steady state chemical potential can be approximated by $\mu_{\text{out}}^* \approx \ln(1 + \eta)$ and the reaction flux can be approximated by

$$s_{\text{out}} \approx \bar{\lambda}_p^{\text{out}} \left[\frac{\mu_-^{\text{out}}}{k_B T} - \ln(1 + \eta) \right], \quad (\text{G.12})$$

where we introduce the effective rate $\bar{\lambda}_p^{\text{out}} = \lambda_p \left(1 + \eta \right) e^{\frac{\mu_+}{k_B T}}$. Thus, in the solvent phase behaves like the linear non-equilibrium reaction kinetics with rescaled rate and steady state chemical potential. This approximation is not generally valid in the droplet phase as discussed in the main text. Instead, we assume that the chemical reaction changes only weakly in the droplet phase, i.e. the reaction diffusion length is large compared to R . Then, we can expand the hyperbolic sinus around the chemical potential at the interface, $\mu_{\text{in}}(R) = \mu_{\text{out}}(R) = \mu_R$. In this case, we end up with

$$s_{\text{in}} \approx \lambda_p \left(1 + e^{-\Delta\mu/k_B T} \eta \Gamma_E \right) e^{(\mu_+ + \mu_{\text{in}}^*)/(2k_B T)} e^{(\mu_{\text{in}}^* - \mu_R)/(2k_B T)} \left(\frac{\mu_-^{\text{in}} - \mu_R}{2k_B T} - 1 \right). \quad (\text{G.13})$$

Here, μ_{in}^* is given by Eq. G.11 for $\Gamma_E = \phi_E^{\text{in}}/\bar{\phi}_E$. For simplicity, we assume strong segregation, $\eta \Gamma_E \gg 1$ and end up with

$$s_{\text{in}} \approx \Gamma_E \bar{\lambda}_p^{\text{in}} \left(\frac{\mu_-^{\text{in}} - \mu_R}{k_B T} - 2 \right), \quad (\text{G.14})$$

where $\bar{\lambda}_p^{\text{in}} = \eta \lambda_p e^{(\mu_+ - \mu_R)/(2k_B T)}$. Although we expand around a state far away from the steady state chemical potential, we still end up with a linear expansion, thus the result is similar to linear non-equilibrium reactions.

Finally, we can calculate the steady state of Eq. G.8 in the effective droplet model:

$$\nabla^2 \mu_+^{\text{in}} = 0, \quad (\text{G.15a})$$

$$\nabla^2 \mu_-^{\text{in}} = \ell_{\text{in}}^{-2} (\mu_-^{\text{in}} - \mu_R - 2k_{\text{B}}T), \quad (\text{G.15b})$$

$$\nabla^2 \mu_+^{\text{out}} = 0, \quad (\text{G.15c})$$

$$\nabla^2 \mu_-^{\text{out}} = \ell_{\text{out}}^{-2} (\mu_-^{\text{out}} - k_{\text{B}}T \ln(1 + \eta)), \quad (\text{G.15d})$$

with $\ell_{\text{in/out}}^2 = \Lambda / \bar{\lambda}_p^{\text{in/out}}$ the reaction diffusion lengths. As a result, $\mu_+^{\text{in}} = \mu_+^{\text{out}} = \mu_+ = \text{const}$ and the two equations for μ_- in droplet and solvent phase are qualitatively the same as in the binary case; see Eq. G.3. The resulting chemical potential profiles as a function of r in the spherically symmetric system are

$$\mu_-^{\text{in}}(r) = \mu_R + 2k_{\text{B}}T \left(1 - \frac{R \sinh(r/\ell_{\text{in}})}{r \sinh(R/\ell_{\text{in}})} \right), \quad (\text{G.16a})$$

$$\mu_-^{\text{out}}(r) = k_{\text{B}}T \ln(1 + \eta) + (\mu_R - k_{\text{B}}T \ln(1 + \eta)) \frac{R}{r} \exp(-(r - R)/\ell_{\text{out}}). \quad (\text{G.16b})$$

Which is the form that is used to plot the analytical solution in fig. 4.19B. The only difference compared to the binary case is the chemical potential at the interface $\mu(R)$, which replaces the boundary condition $\mu = -\Delta w$. It can be calculated as follows: Assuming low total amount of A , we can calculate the phase equilibrium at the interface for B similar to the binary case and find $\mu_B(R) = -w_B$. In addition, we know that $\mu_+ = \text{const}$, although we do not know the value, and thus $\mu_R = \mu_+ - 2\mu_B(R) = \mu_+ - 2w_B$.

Stable droplet radius

Using Eq. G.16, we can calculate the total reaction flux in droplet and solvent phase and use them to calculate the steady state radius, similar to Eq. 4.29 for the binary system. First, we calculate the total reaction flux in the solvent phase S_{out} in an infinite system, i.e. $\ell_{\text{out}} \ll L$:

$$\begin{aligned} S_{\text{out}} &= -4\pi \int_R^\infty \bar{\lambda}_p^{\text{out}} (\mu_-^{\text{out}}(r) - k_{\text{B}}T \ln(1 + \eta)) r^2 dr \\ &= -4\pi \bar{\lambda}_p^{\text{out}} (\mu_R - k_{\text{B}}T \ln(1 + \eta)) \int_R^\infty R r e^{-(r-R)/\ell_{\text{out}}} dr. \end{aligned} \quad (\text{G.17})$$

The integral results in $\int_R^\infty R r e^{-(r-R)/\ell_{\text{out}}} dr = \ell_{\text{out}}^2 R (1 + R/\ell_{\text{out}})$

$$S_{\text{out}} = 4\pi \bar{\lambda}_p^{\text{out}} \ell_{\text{out}}^2 R (\mu_R - k_{\text{B}}T \ln(1 + \eta)) \left(\frac{R}{\ell_{\text{out}}} + 1 \right) \quad (\text{G.18})$$

The total reaction flux in the droplet S_{in} is given by

$$S_{\text{in}} = -4\pi \Gamma_E \bar{\lambda}_p^{\text{in}} \int_0^R (\mu_-^{\text{in}}(r) - \mu_R - 2k_{\text{B}}T) R r \frac{\sinh(r/\ell_{\text{in}})}{\sinh(R/\ell_{\text{in}})} dr, \quad (\text{G.19})$$

and the integral is given by $\int_0^R R r \frac{\sinh(r/\ell_{\text{in}})}{\sinh(R/\ell_{\text{in}})} dr = \ell_{\text{in}}^2 R (R/\ell_{\text{in}} \coth(R/\ell_{\text{in}}) - 1)$. Thus, the total

reaction flux in the droplet is

$$S_{\text{in}} = -4\pi\Gamma_E\bar{\lambda}_p^{\text{in}}\ell_{\text{in}}^2R\left(\frac{R}{\ell_{\text{in}}}\coth\left[\frac{R}{\ell_{\text{in}}}\right]-1\right)(2k_{\text{B}}T). \quad (\text{G.20})$$

Because we already assume that the reaction diffusion length in the droplet is large compared to the droplet radius, we might as well expand the hyperbolic cotangens and get

$$S_{\text{in}} \approx -\frac{4\pi R^3}{3}\Gamma_E\bar{\lambda}_p^{\text{in}}(2k_{\text{B}}T). \quad (\text{G.21})$$

Solving for $S_{\text{in}} + S_{\text{out}} = 0$, we get the steady state radius

$$R_* = \frac{3\ell_{\text{in}}^2}{2\ell_{\text{out}}}\left(\frac{\mu_R}{k_{\text{B}}T} - \ln(1 + \eta)\right) \propto \Gamma_E \approx e^{-\chi_E}. \quad (\text{G.22})$$

Bibliography

Here are the references in citation order.

1. Milo R and Phillips R. *Cell Biology by the Numbers*. Garland Science, 2015 (cited on pages 1, 17, 23, 29, 54, 57, 75, 79, 100, 108)
2. Hutchison CA, Chuang RY, Noskov VN, Assad-Garcia N, Deerinck TJ, Ellisman MH, Gill J, Kannan K, Karas BJ, Ma L, Pelletier JF, Qi ZQ, Richter RA, Strychalski EA, Sun L, Suzuki Y, Tsvetanova B, Wise KS, Smith HO, Glass JI, Merryman C, Gibson DG, and Venter JC. Design and synthesis of a minimal bacterial genome. *Science* 2016; 351. doi: [10.1126/science.aad6253](https://doi.org/10.1126/science.aad6253) (cited on page 1)
3. Alberts B, Johnson A, Lewis J, Raff M, Roberts K, and Walter P. *Molecular biology of the cell*. 4th ed. Garland Science, 2002 (cited on pages 1, 60, 72, 75)
4. Brangwynne CP, Eckmann CR, Courson DS, Rybarska A, Hoege C, Gharakhani J, Jülicher F, and Hyman AA. Germline P Granules Are Liquid Droplets That Localize by Controlled Dissolution/Condensation. *Science* 2009; 324. doi: [10.1126/science.1172046](https://doi.org/10.1126/science.1172046) (cited on pages 1, 2)
5. Banani SF, Lee HO, Hyman AA, and Rosen MK. Biomolecular condensates: organizers of cellular biochemistry. *Nature Reviews Molecular Cell Biology* 2017; 18. doi: [10.1038/nrm.2017.7](https://doi.org/10.1038/nrm.2017.7) (cited on pages 1, 2, 68, 88, 104)
6. Brangwynne CP, Tompa P, and Pappu RV. Polymer physics of intracellular phase transitions. *Nature Physics* 2015; 11. doi: [10.1038/nphys3532](https://doi.org/10.1038/nphys3532) (cited on pages 1, 6, 17, 27, 88)
7. Berry J, Brangwynne CP, and Haataja M. Physical principles of intracellular organization via active and passive phase transitions. *Reports on Progress in Physics* 2018; 81. doi: [10.1088/1361-6633/aaa61e](https://doi.org/10.1088/1361-6633/aaa61e) (cited on pages 1, 3, 6, 8, 59)
8. Goodsell DS. Integrative illustration of a JCVI syn3A minimal cell. 2022. doi: [10.2210/rcsb_pdb/goodsell-gallery-042](https://doi.org/10.2210/rcsb_pdb/goodsell-gallery-042) (cited on page 2)
9. Haldane JBS. The origin of life. *Ration. Annu.* 1929; 148 (cited on page 2)
10. Oparin AI. *Origin of Life*. Dover, 1952 (cited on page 2)
11. Marx S, Schilling J, Sackmann E, and Bruinsma R. Helfrich Repulsion and Dynamical Phase Separation of Multicomponent Lipid Bilayers. *Physical Review Letters* 2002; 88(13). doi: [10.1103/PhysRevLett.88.138102](https://doi.org/10.1103/PhysRevLett.88.138102) (cited on page 2)
12. Sabari BR, Dall'Agnesse A, Boija A, Klein IA, Coffey EL, Shrinivas K, Abraham BJ, Hannett NM, Zamudio AV, Manteiga JC, Li CH, Guo YE, Day DS, Schuijers J, Vasile E, Malik S, Hnisz D, Lee TI, Cisse II, Roeder RG, Sharp PA, Chakraborty AK, and Young RA. Coactivator condensation at super-enhancers links phase separation and gene control. *Science* 2018; 361. doi: [10.1126/science.aar3958](https://doi.org/10.1126/science.aar3958) (cited on pages 2, 9)
13. Sengupta P, Baird B, and Holowka D. Lipid rafts, fluid/fluid phase separation, and their relevance to plasma membrane structure and function. *Seminars in Cell & Developmental Biology* 2007; 18. doi: <https://doi.org/10.1016/j.semcdb.2007.07.010> (cited on page 2)

14. Cho WK, Spille JH, Hecht M, Lee C, Li C, Grube V, and Cisse II. Mediator and RNA polymerase II clusters associate in transcription-dependent condensates. *Science* 2018; 361. doi: [10.1126/science.aar4199](https://doi.org/10.1126/science.aar4199) (cited on pages 2, 9, 100)
15. Feric M and Brangwynne CP. A nuclear F-actin scaffold stabilizes ribonucleoprotein droplets against gravity in large cells. *Nature Cell Biology* 2013; 15. doi: [10.1038/ncb2830](https://doi.org/10.1038/ncb2830) (cited on pages 2, 100)
16. Fritsch AW, Diaz-Delgado AF, Adame-Arana O, Hoegge C, Mittasch M, Kreysing M, Leaver M, Hyman AA, Jülicher F, and Weber CA. Local thermodynamics govern formation and dissolution of *Caenorhabditis elegans* P granule condensates. 2021; 118. doi: [10.1073/pnas.2102772118](https://doi.org/10.1073/pnas.2102772118) (cited on pages 2, 6, 17, 29, 116)
17. Hyman AA, Weber CA, and Jülicher F. Liquid-Liquid Phase Separation in Biology. *Annual Review of Cell and Developmental Biology* 2014; 30. doi: [10.1146/annurev-cellbio-100913-013325](https://doi.org/10.1146/annurev-cellbio-100913-013325) (cited on pages 2, 3)
18. Riback JA, Zhu L, Ferrolino MC, Tolbert M, Mitrea DM, Sanders DW, Wei MT, Kriwacki RW, and Brangwynne CP. Composition-dependent thermodynamics of intracellular phase separation. *Nature* 2020; 581. doi: [10.1038/s41586-020-2256-2](https://doi.org/10.1038/s41586-020-2256-2) (cited on pages 2, 3, 5, 6, 27, 28, 38)
19. De Gennes PG. Dynamics of fluctuations and spinodal decomposition in polymer blends. *The Journal of Chemical Physics* 1980; 72. doi: [10.1063/1.439809](https://doi.org/10.1063/1.439809) (cited on pages 2, 30)
20. Shin Y and Brangwynne CP. Liquid phase condensation in cell physiology and disease. *Science* 2017; 357. doi: [10.1126/science.aaf4382](https://doi.org/10.1126/science.aaf4382) (cited on page 2)
21. Huggins ML. Solutions of Long Chain Compounds. *The Journal of Chemical Physics* 1941; 9. doi: [10.1063/1.1750930](https://doi.org/10.1063/1.1750930) (cited on pages 2, 27, 127)
22. Flory PJ. Thermodynamics of High Polymer Solutions. *The Journal of Chemical Physics* 1942; 10. doi: [10.1063/1.1723621](https://doi.org/10.1063/1.1723621) (cited on pages 2, 27, 71, 127, 130)
23. Flory PJ. Thermodynamics of Heterogeneous Polymers and Their Solutions. *The Journal of Chemical Physics* 1944; 12. doi: [10.1063/1.1723887](https://doi.org/10.1063/1.1723887) (cited on pages 2, 27, 127)
24. McSwiggen DT, Mir M, Darzacq X, and Tjian R. Evaluating phase separation in live cells: diagnosis, caveats, and functional consequences. *Genes & Development* 2019; 33. doi: [10.1101/gad.331520.119](https://doi.org/10.1101/gad.331520.119) (cited on page 2)
25. Musacchio A. On the role of phase separation in the biogenesis of membraneless compartments. *The EMBO Journal* 2022; 41. doi: <https://doi.org/10.15252/embj.2021109952> (cited on page 2)
26. Forman-Kay JD, Ditlev JA, Nosella ML, and Lee HO. What are the distinguishing features and size requirements of biomolecular condensates and their implications for RNA-containing condensates? *RNA* 2022; 28. doi: [10.1261/rna.079026.121](https://doi.org/10.1261/rna.079026.121) (cited on page 2)
27. Bracha D, Walls MT, and Brangwynne CP. Probing and engineering liquid-phase organelles. *Nature Biotechnology* 2019; 37. doi: [10.1038/s41587-019-0341-6](https://doi.org/10.1038/s41587-019-0341-6) (cited on page 3)

28. Deviri D and Safran SA. Physical theory of biological noise buffering by multicomponent phase separation. *Proc Natl Acad Sci USA* 2021; 118. doi: [10.1073/pnas.2100099118](https://doi.org/10.1073/pnas.2100099118) (cited on pages 3, 5)
29. Wang H, Kelley FM, Milovanovic D, Schuster BS, and Shi Z. Surface tension and viscosity of protein condensates quantified by micropipette aspiration. *Biophysical Reports* 2021; 1. doi: <https://doi.org/10.1016/j.bpr.2021.100011> (cited on pages 3, 4)
30. Jawerth LM, Ijavi M, Ruer M, Saha S, Jahnel M, Hyman AA, Jülicher F, and Fischer-Friedrich E. Salt-Dependent Rheology and Surface Tension of Protein Condensates Using Optical Traps. *Physical Review Letters* 2018; 121(25). doi: [10.1103/PhysRevLett.121.258101](https://doi.org/10.1103/PhysRevLett.121.258101) (cited on page 4)
31. Jawerth L, Fischer-Friedrich E, Saha S, Wang J, Franzmann T, Zhang X, Sachweh J, Ruer M, Ijavi M, Saha S, Mahamid J, Hyman AA, and Jülicher F. Protein condensates as aging Maxwell fluids. *Science* 2020; 370. doi: [10.1126/science.aaw4951](https://doi.org/10.1126/science.aaw4951) (cited on page 4)
32. Patel A, Lee HO, Jawerth L, Maharana S, Jahnel M, Hein MY, Stoyanov S, Mahamid J, Saha S, Franzmann TM, Pozniakovski A, Poser I, Maghelli N, Royer LA, Weigert M, Myers EW, Grill S, Drechsel D, Hyman AA, and Alberti S. A Liquid-to-Solid Phase Transition of the ALS Protein FUS Accelerated by Disease Mutation. *Cell* 2015; 162. doi: [10.1016/j.cell.2015.07.047](https://doi.org/10.1016/j.cell.2015.07.047) (cited on pages 4, 12)
33. Alberti S and Dormann D. Liquid–Liquid Phase Separation in Disease. *Annual Review of Genetics* 2019; 53. doi: [10.1146/annurev-genet-112618-043527](https://doi.org/10.1146/annurev-genet-112618-043527) (cited on page 4)
34. Alberti S, Gladfelter A, and Mittag T. Considerations and Challenges in Studying Liquid-Liquid Phase Separation and Biomolecular Condensates. *Cell* 2019; 176. doi: [10.1016/j.cell.2018.12.035](https://doi.org/10.1016/j.cell.2018.12.035) (cited on pages 4, 5, 7, 12, 64)
35. Hohenberg PC and Halperin BI. Theory of dynamic critical phenomena. *Rev. Mod. Phys.* 1977; 49(3). doi: [10.1103/RevModPhys.49.435](https://doi.org/10.1103/RevModPhys.49.435) (cited on pages 4, 12, 33, 37, 47, 50)
36. Wippich F, Bodenmiller B, Trajkovska MG, Wanka S, Aebersold R, and Pelkmans L. Dual Specificity Kinase DYRK3 Couples Stress Granule Condensation/Dissolution to mTORC1 Signaling. *Cell* 2013; 152. doi: [10.1016/j.cell.2013.01.033](https://doi.org/10.1016/j.cell.2013.01.033) (cited on pages 4, 6, 10, 87, 88, 112, 117, 118)
37. Alberti S and Carra S. Quality Control of Membraneless Organelles. *Journal of Molecular Biology* 2018; 430. doi: [10.1016/j.jmb.2018.05.013](https://doi.org/10.1016/j.jmb.2018.05.013) (cited on pages 4, 54)
38. Zhao YG and Zhang H. Phase Separation in Membrane Biology: The Interplay between Membrane-Bound Organelles and Membraneless Condensates. *Developmental Cell* 2020; 55. doi: [10.3389/fcell.2020.618733](https://doi.org/10.3389/fcell.2020.618733) (cited on page 4)
39. Jaqaman K and Ditlev JA. Biomolecular condensates in membrane receptor signaling. *Current Opinion in Cell Biology* 2021; 69. doi: [10.1016/j.ceb.2020.12.006](https://doi.org/10.1016/j.ceb.2020.12.006) (cited on page 4)
40. Peebles W and Rosen MK. Mechanistic dissection of increased enzymatic rate in a phase-separated compartment. *Nature Chemical Biology* 2021; 17. doi: [10.1038/s41589-021-00801-x](https://doi.org/10.1038/s41589-021-00801-x) (cited on pages 5, 6, 116, 118)
41. Lyon AS, Peebles WB, and Rosen MK. A framework for understanding the functions of biomolecular condensates across scales. *Nature Reviews Molecular Cell Biology* 2020; 21. doi: [10.1038/s41580-020-00303-z](https://doi.org/10.1038/s41580-020-00303-z) (cited on page 5)

42. Woodruff JB, Ferreira Gomes B, Widlund PO, Mahamid J, Honigmann A, and Hyman AA. The Centrosome Is a Selective Condensate that Nucleates Microtubules by Concentrating Tubulin. *Cell* 2017; 169. doi: [10.1016/j.cell.2017.05.028](https://doi.org/10.1016/j.cell.2017.05.028) (cited on pages 5, 7)
43. Setru SU, Gouveia B, Alfaro-Aco R, Shaevitz JW, Stone HA, and Petry S. A hydrodynamic instability drives protein droplet formation on microtubules to nucleate branches. *Nature Physics* 2021; 17. doi: [10.1038/s41567-020-01141-8](https://doi.org/10.1038/s41567-020-01141-8) (cited on pages 5, 6)
44. Eeftens JM, Kapoor M, Michieletto D, and Brangwynne CP. Polycomb condensates can promote epigenetic marks but are not required for sustained chromatin compaction. *Nature Communications* 2021; 12. doi: [10.1038/s41467-021-26147-5](https://doi.org/10.1038/s41467-021-26147-5) (cited on page 5)
45. Feric M and Misteli T. Function moves biomolecular condensates in phase space. *BioEssays*. n/a. doi: [10.1002/bies.202200001](https://doi.org/10.1002/bies.202200001) (cited on page 5)
46. Klosin A, Oltch F, Harmon T, Honigmann A, Jülicher F, Hyman AA, and Zechner C. Phase separation provides a mechanism to reduce noise in cells. *Science* 2020; 367. doi: [10.1126/science.aav6691](https://doi.org/10.1126/science.aav6691) (cited on page 5)
47. Böddeker TJ, Rosowski KA, Berchtold D, Emmanouilidis L, Han Y, Allain FHT, Style RW, Pelkmans L, and Dufresne ER. Non-specific adhesive forces between filaments and membraneless organelles. *bioRxiv* 2021. doi: [10.1101/2021.07.22.453380](https://doi.org/10.1101/2021.07.22.453380) (cited on pages 5, 12)
48. Feric M, Vaidya N, Harmon TS, Mitrea DM, Zhu L, Richardson TM, Kriwacki RW, Pappu RV, and Brangwynne CP. Coexisting Liquid Phases Underlie Nucleolar Subcompartments. *Cell* 2016; 165. doi: [10.1016/j.cell.2016.04.047](https://doi.org/10.1016/j.cell.2016.04.047). [Accessed on: 2021 Apr 14] (cited on page 5)
49. Zwicker D and Laan L. Evolved interactions stabilize many coexisting phases in multi-component liquids. 2022. doi: [10.48550/arXiv.2201.10898](https://doi.org/10.48550/arXiv.2201.10898) (cited on pages 5, 7, 117)
50. Schmit JD, Feric M, and Dunder M. How Hierarchical Interactions Make Membraneless Organelles Tick Like Clockwork. *Trends in Biochemical Sciences* 2021; 46. doi: [10.1016/j.tibs.2020.12.011](https://doi.org/10.1016/j.tibs.2020.12.011) (cited on page 6)
51. Nicolis G and Prigogine I. *Self-Organization in Nonequilibrium Systems*. Wiley Interscience, 1977 (cited on pages 6, 91)
52. Vidal-Henriquez E and Zwicker D. Cavitation controls droplet sizes in elastic media. *Proceedings of the National Academy of Sciences* 2021; 118. doi: [10.1073/pnas.2102014118](https://doi.org/10.1073/pnas.2102014118) (cited on pages 6, 7, 12)
53. Das S, Lin YH, Vernon RM, Forman-Kay JD, and Chan HS. Comparative roles of charge, π , and hydrophobic interactions in sequence-dependent phase separation of intrinsically disordered proteins. *Proceedings of the National Academy of Sciences* 2020; 117. doi: [10.1073/pnas.2008122117](https://doi.org/10.1073/pnas.2008122117) (cited on page 6)
54. Regy RM, Dignon GL, Zheng W, Kim YC, and Mittal J. Sequence dependent phase separation of protein-polynucleotide mixtures elucidated using molecular simulations. *Nucleic Acids Research* 2020; 48. doi: [10.1093/nar/gkaa1099](https://doi.org/10.1093/nar/gkaa1099) (cited on page 6)

55. Wang J, Choi JM, Holehouse AS, Lee HO, Zhang X, Jahnel M, Maharana S, Lemaitre R, Pozniakovskiy A, Drechsel D, Poser I, Pappu RV, Alberti S, and Hyman AA. A Molecular Grammar Governing the Driving Forces for Phase Separation of Prion-like RNA Binding Proteins. *Cell* 2018; 174. doi: [10.1016/j.cell.2018.06.006](https://doi.org/10.1016/j.cell.2018.06.006) (cited on pages 6, 8)
56. Ruff KM, Dar F, and Pappu RV. Ligand effects on phase separation of multivalent macromolecules. *Proc Natl Acad Sci USA* 2021; 118. doi: [10.1073/pnas.2017184118](https://doi.org/10.1073/pnas.2017184118) (cited on pages 6, 29, 31)
57. Zhang Y, Xu B, Weiner BG, Meir Y, and Wingreen NS. Decoding the physical principles of two-component biomolecular phase separation. *eLife* 2021; 10. doi: [10.7554/eLife.62403](https://doi.org/10.7554/eLife.62403) (cited on page 6)
58. Farr SE, Woods EJ, Joseph JA, Garaizar A, and Collepardo-Guevara R. Nucleosome plasticity is a critical element of chromatin liquid–liquid phase separation and multivalent nucleosome interactions. *Nat Commun* 2021; 12. doi: [10.1038/s41467-021-23090-3](https://doi.org/10.1038/s41467-021-23090-3) (cited on page 6)
59. Espinosa JR, Joseph JA, Sanchez-Burgos I, Garaizar A, Frenkel D, and Collepardo-Guevara R. Liquid network connectivity regulates the stability and composition of biomolecular condensates with many components. *Proc Natl Acad Sci USA* 2020; 117. doi: [10.1073/pnas.1917569117](https://doi.org/10.1073/pnas.1917569117) (cited on page 7)
60. Weber CA, Zwicker D, Jülicher F, and Lee CF. Physics of active emulsions. *Reports on Progress in Physics* 2019; 82. doi: [10.1088/1361-6633/ab052b](https://doi.org/10.1088/1361-6633/ab052b) (cited on pages 7, 12, 18, 27, 28, 30, 32, 36, 37, 55, 57, 91, 94, 95, 98, 100–102, 106, 115)
61. Weber CA, Lee CF, and Jülicher F. Droplet ripening in concentration gradients. *New Journal of Physics* 2017; 19. doi: [10.1088/1367-2630/aa6b84](https://doi.org/10.1088/1367-2630/aa6b84) (cited on page 7)
62. Jacobs WM and Frenkel D. Phase Transitions in Biological Systems with Many Components. *Biophys J* 2017; 112. doi: [10.1016/j.bpj.2016.10.043](https://doi.org/10.1016/j.bpj.2016.10.043) (cited on page 7)
63. Jacobs WM. Self-Assembly of Biomolecular Condensates with Shared Components. *Physical Review Letters* 2021; 126(25). doi: [10.1103/PhysRevLett.126.258101](https://doi.org/10.1103/PhysRevLett.126.258101) (cited on pages 7, 117)
64. Graf IA and Machta BB. Thermodynamic stability and critical points in multicomponent mixtures with structured interactions. 2021. doi: [10.48550/arXiv.2110.11332](https://doi.org/10.48550/arXiv.2110.11332) (cited on page 7)
65. Mao S, Kuldinow D, Haataja MP, and Košmrlj A. Phase behavior and morphology of multicomponent liquid mixtures. *Soft Matter* 2019; 15(6). doi: [10.1039/C8SM02045K](https://doi.org/10.1039/C8SM02045K) (cited on pages 7, 20, 22, 27, 30, 36, 38, 50, 117, 130)
66. Mao S, Chakraverti-Wuerthwein MS, Gaudio H, and Košmrlj A. Designing the Morphology of Separated Phases in Multicomponent Liquid Mixtures. *Physical Review Letters* 2020; 125. doi: [10.1103/PhysRevLett.125.218003](https://doi.org/10.1103/PhysRevLett.125.218003) (cited on pages 7, 30, 38)
67. Zwicker D, Decker M, Jaensch S, Hyman AA, and Jülicher F. Centrosomes are autocatalytic droplets of pericentriolar material organized by centrioles. *Proceedings of the National Academy of Sciences* 2014; 111. doi: [10.1073/pnas.1404855111](https://doi.org/10.1073/pnas.1404855111) (cited on pages 7, 12, 118)
68. Zwicker D, Baumgart J, Redemann S, Müller-Reichert T, Hyman AA, and Jülicher F. Positioning of Particles in Active Droplets. *Physical Review Letters* 2018; 121(15). doi: [10.1103/PhysRevLett.121.158102](https://doi.org/10.1103/PhysRevLett.121.158102) (cited on pages 7, 12)

69. Henninger JE, Oksuz O, Shrinivas K, Sagi I, LeRoy G, Zheng MM, Andrews JO, Zamudio AV, Lazaris C, Hannett NM, Lee TI, Sharp PA, Cissé II, Chakraborty AK, and Young RA. RNA-Mediated Feedback Control of Transcriptional Condensates. *Cell* 2021; 184. doi: <https://doi.org/10.1016/j.cell.2020.11.030> (cited on pages 7, 62, 66)
70. Zwicker D, Hyman AA, and Jülicher F. Suppression of Ostwald ripening in active emulsions. *Physical Review E* 2015; 92(1). doi: [10.1103/PhysRevE.92.012317](https://doi.org/10.1103/PhysRevE.92.012317) (cited on pages 7, 77, 93, 94, 99, 101, 102, 113, 115)
71. Wurtz JD and Lee CF. Chemical-Reaction-Controlled Phase Separated Drops: Formation, Size Selection, and Coarsening. *Physical Review Letters* 2018; 120(7). doi: [10.1103/PhysRevLett.120.078102](https://doi.org/10.1103/PhysRevLett.120.078102) (cited on pages 7, 12, 77, 91, 93, 94, 99, 101, 102, 113, 115, 117)
72. Turing AM. The chemical basis of morphogenesis. *Philosophical Transactions of the Royal Society of London. Series B, Biological Sciences* 1952; 237. doi: [10.1098/rstb.1952.0012](https://doi.org/10.1098/rstb.1952.0012) (cited on pages 7, 12, 118)
73. Söding J, Zwicker D, Sohrabi-Jahromi S, Boehning M, and Kirschbaum J. Mechanisms for Active Regulation of Biomolecular Condensates. *Trends in Cell Biology* 2020; 30. doi: [10.1016/j.tcb.2019.10.006](https://doi.org/10.1016/j.tcb.2019.10.006) (cited on pages 7–11, 63, 75, 78, 81, 87, 112, 113, 115, 118)
74. Giamb Bruno R, Grzybowska EA, Fawzi NL, and Dormann D. Editorial: The Role of Protein Post-Translational Modifications in Protein-RNA Interactions and RNP Assemblies. *Frontiers in Molecular Biosciences* 2022; 8. doi: [10.3389/fmolb.2021.831810](https://doi.org/10.3389/fmolb.2021.831810) (cited on page 8)
75. Snead WT and Gladfelter AS. The Control Centers of Biomolecular Phase Separation: How Membrane Surfaces, PTMs, and Active Processes Regulate Condensation. *Molecular Cell* 2019; 76. doi: [10.1016/j.molcel.2019.09.016](https://doi.org/10.1016/j.molcel.2019.09.016) (cited on page 8)
76. Hofweber M and Dormann D. Friend or foe—Post-translational modifications as regulators of phase separation and RNP granule dynamics. *The Journal of Biological Chemistry* 2019; 294. doi: [10.1074/jbc.TM118.001189](https://doi.org/10.1074/jbc.TM118.001189) (cited on page 8)
77. Bah A and Forman-Kay JD. Modulation of Intrinsically Disordered Protein Function by Post-translational Modifications. *Journal of Biological Chemistry* 2016; 291. doi: <https://doi.org/10.1074/jbc.R115.695056> (cited on page 8)
78. Rai AK, Chen JX, Selbach M, and Pelkmans L. Kinase-controlled phase transition of membraneless organelles in mitosis. *Nature* 2018; 559. doi: [10.1038/s41586-018-0279-8](https://doi.org/10.1038/s41586-018-0279-8) (cited on pages 8, 88)
79. Hondele M, Sachdev R, Heinrich S, Wang J, Vallotton P, Fontoura BMA, and Weis K. DEAD-box ATPases are global regulators of phase-separated organelles. *Nature* 2019; 573. doi: [10.1038/s41586-019-1502-y](https://doi.org/10.1038/s41586-019-1502-y) (cited on page 8)
80. Boehning M, Dugast-Darzacq C, Rankovic M, Hansen AS, Yu T, Marie-Nelly H, McSwiggen DT, Kokic G, Dailey GM, Cramer P, Darzacq X, and Zweckstetter M. RNA polymerase II clustering through carboxy-terminal domain phase separation. *Nature Structural & Molecular Biology* 2018; 25. doi: [10.1038/s41594-018-0112-y](https://doi.org/10.1038/s41594-018-0112-y) (cited on pages 8, 9)
81. Sing CE and Perry SL. Recent progress in the science of complex coacervation. *Soft Matter* 2020; 16(12). doi: [10.1039/D0SM00001A](https://doi.org/10.1039/D0SM00001A) (cited on pages 8, 27, 117)

82. Mountain GA and Keating CD. Formation of Multiphase Complex Coacervates and Partitioning of Biomolecules within them. *Biomacromolecules* 2020; 21. doi: [10.1021/acs.biomac.9b01354](https://doi.org/10.1021/acs.biomac.9b01354) (cited on page 8)
83. Aumiller WM and Keating CD. Phosphorylation-mediated RNA/peptide complex coacervation as a model for intracellular liquid organelles. *Nature Chem* 2016; 8. doi: [10.1038/nchem.2414](https://doi.org/10.1038/nchem.2414) (cited on page 9)
84. Nakashima KK, Baaij JF, and Spruijt E. Reversible generation of coacervate droplets in an enzymatic network. *Soft Matter* 2018; 14. doi: [10.1039/C7SM01897E](https://doi.org/10.1039/C7SM01897E) (cited on pages 9, 40)
85. Donau C, Späth F, Sosson M, Kriebisch BAK, Schnitter F, Tena-Solsona M, Kang HS, Salibi E, Sattler M, Mutschler H, and Boekhoven J. Active coacervate droplets as a model for membraneless organelles and protocells. *Nature Communications* 2020; 11. doi: [10.1038/s41467-020-18815-9](https://doi.org/10.1038/s41467-020-18815-9) (cited on page 9)
86. Chong S, Dugast-Darzacq C, Liu Z, Dong P, Dailey GM, Cattoglio C, Heckert A, Banala S, Lavis L, Darzacq X, and Tjian R. Imaging dynamic and selective low-complexity domain interactions that control gene transcription. *Science* 2018; 361. doi: [10.1126/science.aar2555](https://doi.org/10.1126/science.aar2555) (cited on page 9)
87. Ostwald W. Studien über die Bildung und Umwandlung fester Körper. *Zeitschrift für Physikalische Chemie* 1897; 22U. doi: [10.1515/zpch-1897-2233](https://doi.org/10.1515/zpch-1897-2233) (cited on pages 9, 37, 55)
88. Cates M. Complex fluids: the physics of emulsions. *Soft Interfaces: Lecture Notes of the Les Houches Summer School: Volume 98, July 2012*. Oxford Scholarship Online, 2017. doi: [10.1093/oso/9780198789352.001.0001](https://doi.org/10.1093/oso/9780198789352.001.0001) (cited on page 9)
89. Wang JT, Smith J, Chen BC, Schmidt H, Rasoloson D, Paix A, Lambrus BG, Calidas D, Betzig E, and Seydoux G. Regulation of RNA granule dynamics by phosphorylation of serine-rich, intrinsically disordered proteins in *C. elegans*. *eLife* 2014; 3. doi: [10.7554/eLife.04591](https://doi.org/10.7554/eLife.04591) (cited on page 10)
90. Milovanovic D, Wu Y, Bian X, and Camilli PD. A liquid phase of synapsin and lipid vesicles. *Science* 2018; 361. doi: [10.1126/science.aat5671](https://doi.org/10.1126/science.aat5671) (cited on page 10)
91. Langelier MF, Planck JL, Roy S, and Pascal JM. Structural Basis for DNA Damage-Dependent Poly(ADP-ribosylation) by Human PARP-1. *Science* 2012; 336. doi: [10.1126/science.1216338](https://doi.org/10.1126/science.1216338) (cited on page 11)
92. Chen C, Ding X, Akram N, Xue S, and Luo SZ. Fused in Sarcoma: Properties, Self-Assembly and Correlation with Neurodegenerative Diseases. *Molecules* 2019; 24. doi: [10.3390/molecules24081622](https://doi.org/10.3390/molecules24081622) (cited on page 11)
93. Altmeyer M, Neelsen KJ, Teloni F, Pozdnyakova I, Pellegrino S, Grøfte M, Rask MBD, Streicher W, Jungmichel S, Nielsen ML, and Lukas J. Liquid demixing of intrinsically disordered proteins is seeded by poly(ADP-ribose). *Nature Communications* 2015; 6. doi: [10.1038/ncomms9088](https://doi.org/10.1038/ncomms9088) (cited on page 11)
94. Rosowski KA, Sai T, Vidal-Henriquez E, Zwicker D, Style RW, and Dufresne ER. Elastic ripening and inhibition of liquid-liquid phase separation. *Nature Physics* 2020; 16. doi: [10.1038/s41567-019-0767-2](https://doi.org/10.1038/s41567-019-0767-2) (cited on page 12)

95. Garaizar A, Espinosa JR, Joseph JA, and Collepardo-Guevara R. Kinetic interplay between droplet maturation and coalescence modulates shape of aged protein condensates. *Scientific Reports* 2022; 12. doi: [10.1038/s41598-022-08130-2](https://doi.org/10.1038/s41598-022-08130-2) (cited on page 12)
96. Kondo S and Miura T. Reaction-Diffusion Model as a Framework for Understanding Biological Pattern Formation. *Science* 2010; 329. doi: [10.1126/science.1179047](https://doi.org/10.1126/science.1179047) (cited on page 12)
97. Soh S, Byrska M, Kandere-Grzybowska K, and Grzybowski BA. Reaction-diffusion systems in intracellular molecular transport and control. *Angew Chem Int Ed Engl* 2010; 49. doi: [10.1002/anie.200905513](https://doi.org/10.1002/anie.200905513) (cited on page 12)
98. Halatek J and Frey E. Rethinking pattern formation in reaction–diffusion systems. *Nature Phys* 2018; 14. doi: [10.1038/s41567-017-0040-5](https://doi.org/10.1038/s41567-017-0040-5) (cited on page 12)
99. Glock P, Brauns F, Halatek J, Frey E, and Schwille P. Design of biochemical pattern forming systems from minimal motifs. *eLife* 2019; 8. doi: [10.7554/eLife.48646](https://doi.org/10.7554/eLife.48646) (cited on page 12)
100. Harrison LG. *Kinetic Theory of Living Pattern*. Cambridge University Press, 1993 (cited on pages 12, 118)
101. Gross P, Kumar KV, Goehring NW, Bois JS, Hoegge C, Jülicher F, and Grill SW. Guiding self-organized pattern formation in cell polarity establishment. *Nature Physics* 2019; 15. doi: [10.1038/s41567-018-0358-7](https://doi.org/10.1038/s41567-018-0358-7) (cited on pages 12, 118)
102. Cross MC and Hohenberg PC. Pattern formation outside of equilibrium. *Rev. Mod. Phys.* 1993; 65(3). doi: [10.1103/RevModPhys.65.851](https://doi.org/10.1103/RevModPhys.65.851) (cited on pages 12, 50)
103. Wurtz JD and Lee CF. Stress granule formation via ATP depletion-triggered phase separation. *New Journal of Physics* 2018; 20. doi: [10.1088/1367-2630/aab549](https://doi.org/10.1088/1367-2630/aab549) (cited on pages 12, 55, 113, 117)
104. Zwicker D, Seyboldt R, Weber CA, Hyman AA, and Jülicher F. Growth and division of active droplets provides a model for protocells. *Nature Physics* 2016; 13. doi: [10.1038/nphys3984](https://doi.org/10.1038/nphys3984) (cited on pages 12, 93, 103)
105. Kirschbaum J and Zwicker D. Controlling biomolecular condensates via chemical reactions. *Journal of The Royal Society Interface* 2021; 18. doi: [10.1098/rsif.2021.0255](https://doi.org/10.1098/rsif.2021.0255) (cited on pages 13, 43, 48, 54, 55, 77, 80, 85, 88, 104–106, 108)
106. Bauermann J, Laha S, McCall PM, Jülicher F, and Weber CA. Chemical Kinetics and Mass Action in Coexisting Phases. 2021. doi: [10.48550/arXiv.2112.07576](https://doi.org/10.48550/arXiv.2112.07576) (cited on pages 13, 48, 53)
107. De Groot S and Mazur P. *Non-Equilibrium Thermodynamics*. Dover Publications, 1984 (cited on pages 15, 17, 18, 20, 79, 111, 113)
108. Adame-Arana O, Weber CA, Ziburdaev V, Prost J, and Jülicher F. Liquid Phase Separation Controlled by pH. *Biophysical Journal* 2020; 119. doi: [10.1016/j.bpj.2020.07.044](https://doi.org/10.1016/j.bpj.2020.07.044) (cited on page 15)
109. Doi M. *Soft Matter Physics*. Oxford University Press, 2013 (cited on pages 16, 27)
110. Ben-Naim A. On the Validity of the Assumption of Local Equilibrium in Non-Equilibrium Thermodynamics. 2018. doi: [10.48550/arXiv.1803.03398](https://doi.org/10.48550/arXiv.1803.03398) (cited on page 17)

111. Qian D, Welsh TJ, Erkamp NA, Qamar S, Nixon-Abell J, Krainer G, George-Hyslop PS, Michaels TCT, and Knowles TPJ. Tie-lines reveal interactions driving heteromolecular condensate formation. *bioRxiv* 2022. doi: [10.1101/2022.02.22.481401](https://doi.org/10.1101/2022.02.22.481401) (cited on pages 17, 40)
112. Turlier H, Fedosov DA, Audoly B, Auth T, Gov NS, Sykes C, Joanny JF, Gompper G, and Betz T. Equilibrium physics breakdown reveals the active nature of red blood cell flickering. *Nature Physics* 2016; 12. doi: [10.1038/nphys3621](https://doi.org/10.1038/nphys3621) (cited on page 17)
113. Mabillard J, Weber CA, and Jülicher F. Heat Fluctuations in Chemically Active Systems. 2022. doi: [arXiv:2203.04574](https://arxiv.org/abs/2203.04574) (cited on page 17)
114. Kramer EJ, Green P, and Palmstrøm CJ. Interdiffusion and marker movements in concentrated polymer-polymer diffusion couples. *Polymer* 1984; 25. doi: [https://doi.org/10.1016/0032-3861\(84\)90205-2](https://doi.org/10.1016/0032-3861(84)90205-2) (cited on pages 20, 22, 50)
115. Jülicher F, Grill SW, and Salbreux G. Hydrodynamic theory of active matter. *Reports on Progress in Physics* 2018; 81. doi: [10.1088/1361-6633/aab6bb](https://doi.org/10.1088/1361-6633/aab6bb) (cited on pages 22, 24, 75, 79)
116. Carati D and Lefever R. Chemical freezing of phase separation in immiscible binary mixtures. *Physical Review E* 1997; 56(3). doi: [10.1103/PhysRevE.56.3127](https://doi.org/10.1103/PhysRevE.56.3127) (cited on pages 25, 26)
117. Pagonabarraga I, Pérez-Madrid A, and Rubí J. Fluctuating hydrodynamics approach to chemical reactions. *Physica A: Statistical Mechanics and its Applications* 1997; 237. doi: [10.1016/S0378-4371\(96\)00377-9](https://doi.org/10.1016/S0378-4371(96)00377-9) (cited on page 25)
118. Hänggi P, Talkner P, and Borkovec M. Reaction-rate theory: fifty years after Kramers. *Reviews of Modern Physics* 1990; 62. doi: [10.1103/RevModPhys.62.251](https://doi.org/10.1103/RevModPhys.62.251) (cited on page 25)
119. De Gennes PG. *Scaling Concepts in Polymer Physics*. Cornell University Press, 1979 (cited on page 27)
120. Li YI and Cates ME. Non-equilibrium phase separation with reactions: a canonical model and its behaviour. *Journal of Statistical Mechanics: Theory and Experiment* 2020; 2020. doi: [10.1088/1742-5468/ab7e2d](https://doi.org/10.1088/1742-5468/ab7e2d) (cited on pages 27, 50, 76)
121. Semenov AN and Rubinstein M. Thermoreversible Gelation in Solutions of Associative Polymers. 1. Statics. *Macromolecules* 1998; 31. doi: [10.1021/ma970616h](https://doi.org/10.1021/ma970616h) (cited on page 29)
122. Rubinstein M and Semenov AN. Thermoreversible Gelation in Solutions of Associating Polymers. 2. Linear Dynamics. *Macromolecules* 1998; 31. doi: [10.1021/ma970617](https://doi.org/10.1021/ma970617) (cited on page 29)
123. Cahn JW and Hilliard JE. Free Energy of a Nonuniform System. I. Interfacial Free Energy. *The Journal of Chemical Physics* 1958; 28. doi: [10.1063/1.1744102](https://doi.org/10.1063/1.1744102) (cited on pages 29, 30, 35, 36, 50)
124. Müller M. 1.15 - Polymers at Interfaces and Surfaces and in Confined Geometries. *Polymer Science: A Comprehensive Reference*. Ed. by Matyjaszewski K and Möller M. Elsevier, 2012. doi: <https://doi.org/10.1016/B978-0-444-53349-4.00006-6> (cited on page 30)

125. De Gennes PG. Wetting: statics and dynamics. *Rev. Mod. Phys.* 1985; 57(3). doi: [10.1103/RevModPhys.57.827](https://doi.org/10.1103/RevModPhys.57.827) (cited on page 30)
126. Müller M and Binder K. Wetting and Capillary Condensation in Symmetric Polymer Blends: A Comparison between Monte Carlo Simulations and Self-Consistent Field Calculations. *Macromolecules* 1998; 31. doi: [10.1021/ma980052x](https://doi.org/10.1021/ma980052x) (cited on page 30)
127. Schmid F. Theory and Simulation of Multiphase Polymer Systems. 2010. doi: [10.48550/arXiv.1001.1265](https://doi.org/10.48550/arXiv.1001.1265) (cited on page 33)
128. Frenkel J. A General Theory of Heterophase Fluctuations and Pretransition Phenomena. *The Journal of Chemical Physics* 1939; 7. doi: [10.1063/1.1750484](https://doi.org/10.1063/1.1750484) (cited on pages 35, 109)
129. O'Shaughnessy B and Sawhney U. Polymer Reaction Kinetics at Interfaces. *Physical Review Letters* 1996; 76(18). doi: [10.1103/PhysRevLett.76.3444](https://doi.org/10.1103/PhysRevLett.76.3444) (cited on page 37)
130. Zwicker D. py-pde: A Python package for solving partial differential equations. *Journal of Open Source Software* 2020; 5. doi: [10.21105/joss.02158](https://doi.org/10.21105/joss.02158) (cited on pages 40, 41)
131. Van Kampen NG. *Stochastic Processes in Physics and Chemistry*. 3rd ed. Elsevier, 2007 (cited on page 41)
132. Atkins P, Depaula, and J. Keeler J. *Physical Chemistry*. 11th ed. Oxford University Press, 2018 (cited on page 44)
133. Zwicker D. The intertwined physics of active chemical reactions and phase separation. 2022. doi: [10.48550/arXiv.2202.13646](https://doi.org/10.48550/arXiv.2202.13646) (cited on pages 48, 49, 115)
134. Weber C, Michaels T, and Mahadevan L. Spatial control of irreversible protein aggregation. *eLife* 2019; 8. doi: [10.7554/eLife.42315](https://doi.org/10.7554/eLife.42315) (cited on pages 48, 68, 88, 135)
135. Choi S, Bevilacqua PC, and Keating CD. Phase-specific RNA accumulation and duplex thermodynamics in multiphase coacervate models for membraneless organelles. *bioRxiv* 2021. doi: [10.1101/2021.05.15.444314](https://doi.org/10.1101/2021.05.15.444314) (cited on page 49)
136. Bazant MZ. Thermodynamic stability of driven open systems and control of phase separation by electro-autocatalysis. *Faraday Discussions* 2017; 199. doi: [10.1039/C7FD00037E](https://doi.org/10.1039/C7FD00037E) (cited on page 50)
137. Allen SM and Cahn JW. Coherent and incoherent equilibria in iron-rich iron-aluminum alloys. *Acta Metallurgica* 1975; 23. doi: [10.1016/0001-6160\(75\)90106-6](https://doi.org/10.1016/0001-6160(75)90106-6) (cited on page 50)
138. Dewey JA, Azizi SA, Lu V, and Dickinson BC. A System for the Evolution of Protein-Protein Interaction Inducers. *ACS Synth. Biol.* 2021; 10. doi: [10.1021/acssynbio.1c00276](https://doi.org/10.1021/acssynbio.1c00276) (cited on pages 54, 55)
139. Wheeler JR, Matheny T, Jain S, Abrisch R, and Parker R. Distinct stages in stress granule assembly and disassembly. *eLife* 2016; 5. doi: [10.7554/eLife.18413](https://doi.org/10.7554/eLife.18413) (cited on pages 54, 71)
140. Johnson LN, Noble ME, and Owen DJ. Active and Inactive Protein Kinases: Structural Basis for Regulation. *Cell* 1996; 85. doi: [10.1016/S0092-8674\(00\)81092-2](https://doi.org/10.1016/S0092-8674(00)81092-2) (cited on page 55)
141. Kirschbaum J and Zwicker D. Python code for figures in 'Controlling biomolecular condensates with chemical reactions'. *Zenodo* 2021. doi: [10.5281/zenodo.4893526](https://doi.org/10.5281/zenodo.4893526) (cited on page 55)

142. Nozawa RS, Boteva L, Soares DC, Naughton C, Dun AR, Buckle A, Ramsahoye B, Bruton PC, Saleeb RS, Arnedo M, Hill B, Duncan RR, Maciver SK, and Gilbert N. SAF-A Regulates Interphase Chromosome Structure through Oligomerization with Chromatin-Associated RNAs. *Cell* 2017; 169. doi: <https://doi.org/10.1016/j.cell.2017.05.029> (cited on pages 56, 64, 72)
143. Molliex A, Temirov J, Lee J, Coughlin M, Kanagaraj AP, Kim HJ, Mittag T, and Taylor JP. Phase Separation by Low Complexity Domains Promotes Stress Granule Assembly and Drives Pathological Fibrillization. *Cell* 2015; 163. doi: <https://doi.org/10.1016/j.cell.2015.09.015> (cited on page 56)
144. Aguzzi A and Altmeyer M. Phase Separation: Linking Cellular Compartmentalization to Disease. *Trends in Cell Biology* 2016; 26. doi: [10.1016/j.tcb.2016.03.004](https://doi.org/10.1016/j.tcb.2016.03.004) (cited on page 56)
145. Michieletto D and Gilbert N. Role of nuclear RNA in regulating chromatin structure and transcription. *Current Opinion in Cell Biology* 2019; 58. *Cell Nucleus*. doi: <https://doi.org/10.1016/j.ccb.2019.03.007> (cited on pages 56, 72)
146. Sharma D, Zagore LL, Brister MM, Ye X, Crespo-Hernández CE, Licatalosi DD, and Jankowsky E. The kinetic landscape of an RNA-binding protein in cells. *Nature* 2021; 591. doi: [10.1038/s41586-021-03222-x](https://doi.org/10.1038/s41586-021-03222-x) (cited on pages 57, 60)
147. Braga J, McNally JG, and Carmo-Fonseca M. A Reaction-Diffusion Model to Study RNA Motion by Quantitative Fluorescence Recovery after Photobleaching. *Biophysical Journal* 2007; 92. doi: [10.1529/biophysj.106.096693](https://doi.org/10.1529/biophysj.106.096693) (cited on page 59)
148. Deng L, Yang W, and Liu H. PredPRBA: Prediction of Protein-RNA Binding Affinity Using Gradient Boosted Regression Trees. *Frontiers in Genetics* 2019; 10. doi: [10.3389/fgene.2019.00637](https://doi.org/10.3389/fgene.2019.00637) (cited on pages 59, 66)
149. Hubatsch L, Jawerth LM, Love C, Bauermann J, Tang TD, Bo S, Hyman AA, and Weber CA. Quantitative theory for the diffusive dynamics of liquid condensates. *eLife* 2021; 10. doi: [10.7554/eLife.68620](https://doi.org/10.7554/eLife.68620) (cited on pages 64, 65)
150. Kanaan NM, Hamel C, Grabinski T, and Combs B. Liquid-liquid phase separation induces pathogenic tau conformations in vitro. *Nature Communications* 2020; 11. doi: [10.1038/s41467-020-16580-3](https://doi.org/10.1038/s41467-020-16580-3) (cited on page 65)
151. Michaels TCT, Mahadevan L, and Weber CA. Liquid condensates increase potency of amyloid fibril inhibitors. *bioRxiv* 2020. doi: [10.1101/2020.10.29.360206](https://doi.org/10.1101/2020.10.29.360206) (cited on page 68)
152. Ditlev JA, Case LB, and Rosen MK. Who's In and Who's Out—Compositional Control of Biomolecular Condensates. *Journal of Molecular Biology* 2018; 430. doi: [10.1016/j.jmb.2018.08.003](https://doi.org/10.1016/j.jmb.2018.08.003) (cited on pages 68, 88, 104)
153. Qian H. Phosphorylation Energy Hypothesis: Open Chemical Systems and Their Biological Functions. *Annual Review of Physical Chemistry* 2007; 58. doi: [10.1146/annurev.physchem.58.032806.104550](https://doi.org/10.1146/annurev.physchem.58.032806.104550) (cited on pages 75, 112)
154. Knowles JR. Enzyme-Catalyzed Phosphoryl Transfer Reactions. *Annual Review of Biochemistry* 1980; 49. doi: [10.1146/annurev.bi.49.070180.004305](https://doi.org/10.1146/annurev.bi.49.070180.004305) (cited on page 75)
155. Jülicher F and Prost J. Cooperative Molecular Motors. *Physical Review Letters* 1995; 75(13). doi: [10.1103/PhysRevLett.75.2618](https://doi.org/10.1103/PhysRevLett.75.2618) (cited on page 75)

156. Jülicher F, Ajdari A, and Prost J. Modeling molecular motors. *Rev. Mod. Phys.* 1997; 69(4). doi: [10.1103/RevModPhys.69.1269](https://doi.org/10.1103/RevModPhys.69.1269) (cited on pages 75, 79)
157. Junge W and Nelson N. ATP Synthase. *Annual Review of Biochemistry* 2015; 84. doi: [10.1146/annurev-biochem-060614-034124](https://doi.org/10.1146/annurev-biochem-060614-034124) (cited on page 75)
158. Reece J, Urry L, Cain M, Wasserman S, Minorsky P, and Jackson R. *Campbell Biology*. 10th ed. Pearson, 2014 (cited on pages 75, 77)
159. Hofweber M and Dormann D. Friend or foe—Post-translational modifications as regulators of phase separation and RNP granule dynamics. *Journal of Biological Chemistry* 2019; 294. doi: <https://doi.org/10.1074/jbc.TM118.001189> (cited on page 75)
160. Cates ME and Tailleur J. Motility-Induced Phase Separation. *Annual Review of Condensed Matter Physics* 2015; 6. doi: [10.1146/annurev-conmatphys-031214-014710](https://doi.org/10.1146/annurev-conmatphys-031214-014710) (cited on page 76)
161. Cates ME and Tailleur J. When are active Brownian particles and run-and-tumble particles equivalent? Consequences for motility-induced phase separation. *EPL* 2013; 101. doi: [10.1209/0295-5075/101/20010](https://doi.org/10.1209/0295-5075/101/20010) (cited on page 76)
162. Wittkowski R, Tiribocchi A, Stenhammar J, Allen RJ, Marenduzzo D, and Cates ME. Scalar ϕ^4 field theory for active-particle phase separation. *Nature Communications* 2014; 5. doi: [10.1038/ncomms5351](https://doi.org/10.1038/ncomms5351) (cited on page 76)
163. Tjhung E, Nardini C, and Cates ME. Cluster Phases and Bubbly Phase Separation in Active Fluids: Reversal of the Ostwald Process. *Physical Review X* 2018; 8(3). doi: [10.1103/PhysRevX.8.031080](https://doi.org/10.1103/PhysRevX.8.031080) (cited on page 76)
164. Marchetti MC, Joanny JF, Ramaswamy S, Liverpool TB, Prost J, Rao M, and Simha RA. Hydrodynamics of soft active matter. *Rev. Mod. Phys.* 2013; 85(3). doi: [10.1103/RevModPhys.85.1143](https://doi.org/10.1103/RevModPhys.85.1143) (cited on pages 76, 77)
165. Rao R and Esposito M. Nonequilibrium Thermodynamics of Chemical Reaction Networks: Wisdom from Stochastic Thermodynamics. *Physical Review X* 2016; 6(4). doi: [10.1103/PhysRevX.6.041064](https://doi.org/10.1103/PhysRevX.6.041064) (cited on pages 77, 139)
166. Bowen WJ and Martin HL. The diffusion of adenosine triphosphate through aqueous solutions. *Archives of Biochemistry and Biophysics* 1964; 107. doi: [https://doi.org/10.1016/0003-9861\(64\)90265-6](https://doi.org/10.1016/0003-9861(64)90265-6) (cited on page 77)
167. de Graaf RA, van Kranenburg A, and Nicolay K. In Vivo ³¹P-NMR Diffusion Spectroscopy of ATP and Phosphocreatine in Rat Skeletal Muscle. *Biophysical Journal* 2000; 78. doi: [https://doi.org/10.1016/S0006-3495\(00\)76717-8](https://doi.org/10.1016/S0006-3495(00)76717-8) (cited on page 77)
168. Glotzer SC, Di Marzio EA, and Muthukumar M. Reaction-Controlled Morphology of Phase-Separating Mixtures. *Physical Review Letters* 1995; 74(11). doi: [10.1103/PhysRevLett.74.2034](https://doi.org/10.1103/PhysRevLett.74.2034) (cited on page 77)
169. Mendelsohn BA, Bennett NK, Darch MA, Yu K, Nguyen MK, Pucciarelli D, Nelson M, Horlbeck MA, Gilbert LA, Hyun W, Kampmann M, Nakamura JL, and Nakamura K. A high-throughput screen of real-time ATP levels in individual cells reveals mechanisms of energy failure. *PLOS Biology* 2018; 16. doi: [10.1371/journal.pbio.2004624](https://doi.org/10.1371/journal.pbio.2004624) (cited on page 79)

170. Glansdorff P, Nicolis G, and Prigogine I. The Thermodynamic Stability Theory of Non-Equilibrium States. *Proceedings of the National Academy of Sciences* 1974; 71. doi: [10.1073/pnas.71.1.197](https://doi.org/10.1073/pnas.71.1.197) (cited on page 82)
171. Qian H. Open-System Nonequilibrium Steady State: Statistical Thermodynamics, Fluctuations, and Chemical Oscillations. *J. Phys. Chem. B* 2006; 110. doi: [10.1021/jp061858z](https://doi.org/10.1021/jp061858z) (cited on page 82)
172. Qian H and Beard DA. Metabolic futile cycles and their functions: a systems analysis of energy and control. *Systems biology* 2006; 153. doi: [10.1049/ip-syb:20050086](https://doi.org/10.1049/ip-syb:20050086) (cited on page 86)
173. Samoilov M, Plyasunov S, and Arkin AP. Stochastic amplification and signaling in enzymatic futile cycles through noise-induced bistability with oscillations. *Proceedings of the National Academy of Sciences* 2005; 102. doi: [10.1073/pnas.0406841102](https://doi.org/10.1073/pnas.0406841102) (cited on page 86)
174. Avanzini F, Falasco G, and Esposito M. Thermodynamics of non-elementary chemical reaction networks. *New Journal of Physics* 2020; 22. doi: [10.1088/1367-2630/abafea](https://doi.org/10.1088/1367-2630/abafea) (cited on page 86)
175. Ubersax JA and Ferrell Jr JE. Mechanisms of specificity in protein phosphorylation. *Nature Reviews Molecular Cell Biology* 2007; 8. doi: [10.1038/nrm2203](https://doi.org/10.1038/nrm2203) (cited on pages 87, 112)
176. Briggs GE and Haldane JBS. A Note on the Kinetics of Enzyme Action. *Biochemical Journal* 1925; 19. doi: [10.1042/bj0190338](https://doi.org/10.1042/bj0190338) (cited on pages 87, 88, 112)
177. Sanchez-Burgos I, Joseph JA, Collepardo-Guevara R, and Espinosa JR. Size conservation emerges spontaneously in biomolecular condensates formed by scaffolds and surfactant clients. *Scientific Reports* 2021; 11. doi: [10.1038/s41598-021-94309-y](https://doi.org/10.1038/s41598-021-94309-y) (cited on page 89)
178. Nelson DL, Cox M, and Lehninger A. *Lehninger Principles of Biochemistry*. 7th ed. Freeman and Company, 2017 (cited on pages 97, 118)
179. Schavemaker PE, Boersma AJ, and Poolman B. How Important Is Protein Diffusion in Prokaryotes? *Frontiers in Molecular Biosciences* 2018; 5. doi: [10.3389/fmolb.2018.00093](https://doi.org/10.3389/fmolb.2018.00093) (cited on pages 100, 108)
180. Anderson P and Kedersha N. Stress granules. *Current Biology* 2009; 19. doi: [10.1016/j.cub.2009.03.013](https://doi.org/10.1016/j.cub.2009.03.013) (cited on page 100)
181. De Gennes P, Brochard-Wyart F, and Quere D. *Capillarity and Wetting Phenomena*. Springer, 2004 (cited on page 100)
182. Shimobayashi SF, Ronceray P, Sanders DW, Haataja MP, and Brangwynne CP. Nucleation landscape of biomolecular condensates. *Nature* 2021; 599. doi: [10.1038/s41586-021-03905-5](https://doi.org/10.1038/s41586-021-03905-5) (cited on page 109)
183. Weyer H, Brauns F, and Frey E. Coarsening and wavelength selection far from equilibrium: a unifying framework based on singular perturbation theory. 2022. doi: [10.48550/arXiv.2203.03892](https://doi.org/10.48550/arXiv.2203.03892) (cited on page 114)
184. Testa A, Dindo M, Rebane AA, Nasouri B, Style RW, Golestanian R, Dufresne ER, and Laurino P. Sustained enzymatic activity and flow in crowded protein droplets. *Nature Communications* 2021; 12. doi: [10.1038/s41467-021-26532-0](https://doi.org/10.1038/s41467-021-26532-0) (cited on page 116)

185. Wu C and Wang X. Globule-to-Coil Transition of a Single Homopolymer Chain in Solution. *Physical Review Letters* 1998; 80(18). doi: [10.1103/PhysRevLett.80.4092](https://doi.org/10.1103/PhysRevLett.80.4092) (cited on page 116)
186. Sherman E and Haran G. Coil-globule transition in the denatured state of a small protein. *Proceedings of the National Academy of Sciences* 2006; 103. doi: [10.1073/pnas.0601395103](https://doi.org/10.1073/pnas.0601395103) (cited on page 116)
187. Zeng X, Holehouse AS, Chilkoti A, Mittag T, and Pappu RV. Connecting Coil-to-Globule Transitions to Full Phase Diagrams for Intrinsically Disordered Proteins. *Biophysical Journal* 2020; 119. doi: <https://doi.org/10.1016/j.bpj.2020.06.014> (cited on page 116)
188. Stroberg W and Schnell S. Do Cellular Condensates Accelerate Biochemical Reactions? Lessons from Microdroplet Chemistry. *Biophysical Journal* 2018; 115. doi: <https://doi.org/10.1016/j.bpj.2018.05.023> (cited on page 116)
189. Swain P and Weber SC. Dissecting the complexity of biomolecular condensates. *Biochemical Society Transactions* 2020; 48. doi: [10.1042/BST20200351](https://doi.org/10.1042/BST20200351) (cited on page 116)
190. Overbeek J and Voorn M. Phase separation in polyelectrolyte solutions. Theory of complex coacervation. *Journal of Cell. and Comp. Phys.* 1957; 49(S1). doi: [10.1002/jcp.1030490404](https://doi.org/10.1002/jcp.1030490404) (cited on page 117)
191. Avanzini F, Penocchio E, Falasco G, and Esposito M. Nonequilibrium thermodynamics of non-ideal chemical reaction networks. *The Journal of Chemical Physics* 2021; 154. doi: [10.1063/5.0041225](https://doi.org/10.1063/5.0041225) (cited on page 118)
192. Harmon TS and Jülicher F. Molecular Assembly Lines in Active Droplets. *Physical Review Letters* 2022; 128(10). doi: [10.1103/PhysRevLett.128.108102](https://doi.org/10.1103/PhysRevLett.128.108102) (cited on page 119)
193. Lafontaine DLJ, Riback JA, Bascetin R, and Brangwynne CP. The nucleolus as a multiphase liquid condensate. *Nature Reviews Molecular Cell Biology* 2020; 21. doi: [10.1038/s41580-020-0272-6](https://doi.org/10.1038/s41580-020-0272-6) (cited on page 119)

Jan Kirschbaum

Date of Birth 24. September 1991
Place of Birth Münster
Citizenship German

Education

- 07.2018 – 04.2022 **Ph.D. (expected 04.2022)**, *Max Planck Institute for Dynamics and Self-Organization*, Göttingen, Germany.
Supervisors: **Dr. David Zwicker**, Prof. Dr. Karen Alim, Prof. Dr. Marcus Müller
- 04.2017 – 04.2018 **Research Assistant**, *Department of Physics, University of Münster*, Münster, Germany.
Institute of Materials Physics, AG Bracht
- 10.2014 – 11.2016 **Master of Science, Physics**, *University of Münster*, Münster, Germany.
Focus: Materials Physics and Non-linear Physics, Final Grade: 1.1
Thesis: Experimental and Numerical Investigation of Self-Diffusion in Amorphous Silicon. (Institute of Materials Physics, Supervisor : Apl. Prof. Dr. H. Bracht)
- 10.2011 – 09.2014 **Bachelor of Science, Physics**, *University of Münster*, Münster, Germany.
Final Grade: 2.3
Thesis: Coupled Cubic Maps: Period Doubling vs Torus Breakdown Mechanisms (Institute of Theoretical Physics, Supervisor: Prof. Dr. Stefan Linz)

Publications

- [1] J. Kirschbaum, D. Zwicker; Controlling biomolecular condensates via chemical reactions; *J. R. Soc. Interface.* 18, 20210255 (2021)
- [2] J. Söding, D. Zwicker, S. Sohrabi-Jahromi, M. Boehning, J. Kirschbaum; Mechanism for active regulation of biomolecular condensates; *Trends in Cell Bio.* 30, 4-14 (2020)
- [3] S. Hilke, J. Kirschbaum, V. Hieronymus-Schmidt, M. Radek, H. Bracht, M. Peterlechner; Analysis of medium-range order based on simulated segmented ring detector STEM-images: Amorphous Si; *Ultramicroscopy* 200, 169-179(2019)
- [4] J. Kirschbaum, T. Teuber, A. Donner, M. Radek, A. N. Larsen, D. Bougeard, M. Posselt, H. Bracht; Self-diffusion in amorphous silicon by local bond rearrangements; *Phys. Rev. Lett.* 120, 225902 (2018)

Selected Conferences

- July 2021 **Fundamental Problems in Statistical Physics XV**, *Bruneck, Italy*, Poster Presentation.
- June 2021 **Physics of Living Systems**, *EMBO Workshop, Virtual*, Poster Presentation.
- March 2021 **Fundamentals of Growing Active Matter**, *Higgs Center for Theoretical Physics, Virtual*, Poster Presentation.
- March 2021 **American Physical Society Meeting**, *Virtual*, Talk.
- December 2020 **Statistical Biological Physics**, *ICTS Workshop, Bangalore, Virtual*.
- July 2019 **European Biophysics Conference**, *Madrid, Spain*, Poster Presentation (Best Poster Award).
- February 2019 **Phase Transitions in Polymeric and Protein Systems**, *MPIPKS, Dresden, Germany*, Poster Presentation.
- June 2018 **European Materials Research Society Spring Meeting**, *Strasbourg, France*, Poster Presentation (Best Poster Award).
- May 2016 **European Materials Research Society Spring Meeting**, *Lille, France*, Poster Presentation (Best Poster Award).

Computer Skills

- OS Microsoft Windows, Linux (Ubuntu), MacOS
- Primary Use PYTHON
- Basic Knowledge C/C++, FORTRAN, OPENMP, CUDA C, MPI
- Other L^AT_EX, Bash Shell Scripting, LAMMPS

Languages

- German Mother tongue
- English Fluent
- Latin Latinum
- Spanish Basic knowledge (A1)